



# Challenges and advances in nanocomposite processing techniques

V. Viswanathan<sup>a</sup>, T. Laha<sup>b</sup>, K. Balani<sup>b</sup>, A. Agarwal<sup>b</sup>, S. Seal<sup>a,\*</sup>

<sup>a</sup>Advanced Materials Processing and Analysis Center, Department of Mechanical, Materials and Aerospace Engineering, Nanoscience and Technology Center, University of Central Florida, Orlando, FL 32826, USA

<sup>b</sup>Mechanical and Materials Engineering, Florida International University, Miami, FL 33174, USA

Available online 6 February 2007

## Abstract

Of late, nanotechnology seems to be rapidly thrusting its applications in all aspects of life including engineering and medicine. Materials science and engineering has experienced a tremendous growth in the field of nanocomposite development with enhanced chemical, mechanical, and physical properties. A wide array of research has been conducted in the processing of nanocomposites. Consolidation of these systems from loose particles to bulk free form entities has always been a challenge. To name a few, traditional consolidation techniques such as cold pressing and sintering at high temperatures, hot pressing, and hot isostatic pressing have strong limitations of not being able to retain the nanoscale grain size due to the excessive grain growth during processing. This article reviews in detail the results from numerous studies on various methods for manufacturing nanocomposites with improved properties and retained nanostructures. Both challenges and recent advances are discussed in detail in this review.

© 2006 Elsevier B.V. All rights reserved.

**Keywords:** Nanostructures; Processing techniques; Mechanical properties; Processing challenges

## Contents

1. Introduction . . . . .	123
2. Mechanical processing . . . . .	124
2.1. Severe plastic deformation. . . . .	124
2.1.1. Introduction . . . . .	124
2.1.2. Advantages . . . . .	124
2.2. Equal-channel angular pressing . . . . .	126
2.2.1. Introduction . . . . .	126
2.2.2. Fundamental principles . . . . .	126
2.2.3. Nanoconsolidation . . . . .	128
2.3. High pressure torsion . . . . .	130
2.3.1. Introduction . . . . .	130
2.3.2. Fundamental principles . . . . .	130
2.3.3. Nanoconsolidation . . . . .	134
2.4. Shock wave consolidation . . . . .	135
2.4.1. Introduction . . . . .	135

\* Corresponding author. Tel.: +1 407 882 1119; fax: +1 407 882 1462.  
E-mail address: [sseal@mail.ucf.edu](mailto:sseal@mail.ucf.edu) (S. Seal).

2.4.2.	Fundamental principles . . . . .	137
2.4.3.	Advantages . . . . .	137
2.4.4.	Equipment—process and mechanism . . . . .	138
2.4.5.	Nanoconsolidation . . . . .	138
2.5.	Transformation assisted consolidation . . . . .	141
2.5.1.	Introduction . . . . .	141
2.5.2.	Fundamental principles . . . . .	141
2.5.3.	Advantages . . . . .	141
2.5.4.	Equipment—process and mechanism . . . . .	141
2.5.5.	Nanoconsolidation . . . . .	142
3.	Thermo-mechanical processing . . . . .	142
3.1.	Hot pressing . . . . .	142
3.1.1.	Introduction . . . . .	142
3.1.2.	Fundamental principles . . . . .	144
3.1.3.	Advantages . . . . .	144
3.1.4.	Equipment—process and mechanism . . . . .	144
3.1.5.	Nanoconsolidation . . . . .	145
3.2.	Hot isostatic pressing . . . . .	156
3.2.1.	Introduction . . . . .	156
3.2.2.	Fundamental principles . . . . .	158
3.2.3.	Advantages . . . . .	158
3.2.4.	Equipment—process and mechanism . . . . .	158
3.2.5.	Nanoconsolidation . . . . .	160
3.3.	Hot extrusion . . . . .	169
3.3.1.	Introduction . . . . .	169
3.3.2.	Fundamental principles . . . . .	169
3.3.3.	Advantages . . . . .	170
3.3.4.	Equipment—process and mechanism . . . . .	171
3.3.5.	Nanoconsolidation . . . . .	171
3.4.	Sintering . . . . .	180
3.4.1.	Introduction . . . . .	180
3.4.2.	Fundamental principles . . . . .	181
3.4.3.	Advantages . . . . .	181
3.4.4.	Equipment—process and mechanism . . . . .	182
3.4.5.	Nanoconsolidation . . . . .	182
3.5.	Sinter forging . . . . .	185
3.5.1.	Introduction . . . . .	185
3.5.2.	Fundamental principles . . . . .	185
3.5.3.	Advantages . . . . .	186
3.5.4.	Equipment—process and mechanism . . . . .	187
3.5.5.	Nanoconsolidation . . . . .	187
4.	Non-equilibrium processing . . . . .	195
4.1.	Microwave sintering . . . . .	195
4.1.1.	Introduction . . . . .	195
4.1.2.	Fundamental principles . . . . .	196
4.1.3.	Advantages . . . . .	197
4.1.4.	Equipment—process and mechanism . . . . .	197
4.1.5.	Nanoconsolidation . . . . .	197
4.2.	Thermal spray processing . . . . .	206
4.2.1.	Introduction . . . . .	206
4.2.2.	Fundamental principles . . . . .	206
4.2.3.	Types of thermal spray techniques . . . . .	206
4.2.4.	Advantages . . . . .	207
4.3.	Plasma spraying . . . . .	207
4.3.1.	Introduction . . . . .	207
4.3.2.	Fundamental principles . . . . .	207

4.3.3.	Equipment—process and mechanism . . . . .	209
4.3.4.	Nanoconsolidation . . . . .	210
4.4.	High velocity oxyfuel spraying . . . . .	220
4.4.1.	Introduction . . . . .	220
4.4.2.	Fundamental principles . . . . .	221
4.4.3.	Nanoconsolidation . . . . .	221
4.5.	Cold spraying . . . . .	226
4.5.1.	Introduction . . . . .	226
4.5.2.	Fundamental principles . . . . .	226
4.5.3.	Nanoconsolidation . . . . .	227
4.6.	Spark plasma sintering . . . . .	229
4.6.1.	Introduction . . . . .	229
4.6.2.	Fundamental principles . . . . .	229
4.6.3.	Advantages . . . . .	229
4.6.4.	Equipment—process and mechanism . . . . .	230
4.6.5.	Nanoconsolidation . . . . .	231
4.7.	Laser-based techniques . . . . .	242
4.7.1.	Introduction . . . . .	242
4.7.2.	Fundamental principles . . . . .	242
4.7.3.	Advantages . . . . .	243
4.7.4.	Disadvantages . . . . .	244
4.7.5.	Equipment—process and mechanism . . . . .	244
4.7.6.	Nanoconsolidation . . . . .	246
5.	Room temperature processing . . . . .	255
5.1.	Electrodeposition . . . . .	255
5.1.1.	Introduction . . . . .	255
5.1.2.	Fundamental principles . . . . .	256
5.1.3.	Advantages . . . . .	256
5.1.4.	Equipment—process and mechanism . . . . .	256
5.1.5.	Nanoconsolidation . . . . .	258
5.2.	Nanoconsolidation for self-assembling structures . . . . .	268
5.2.1.	Introduction . . . . .	268
5.2.2.	Fundamental principles . . . . .	269
5.2.3.	Nanoconsolidation . . . . .	271
6.	Future challenges . . . . .	276
7.	Concluding remarks . . . . .	276
	Acknowledgements . . . . .	277
	References . . . . .	277

## 1. Introduction

Nanocrystalline materials are characterized by a grain size or particulate size of up to about 100 nm. These materials exhibit enhanced mechanical [1–3], magnetic [1], elevated temperature [4], optical [5,6], and excellent catalytic properties [7]. The commercial applications of nanocomposite beyond the boundaries of *Materials Science Laboratories* lie on the successful consolidation of these materials into bulk-sized components preserving the nanostructures. The traditional consolidation techniques have a strong limitation of not being able to retain the nanograin size due to the problem of grain growth.

The density of the green compact depends on the frictional forces of the powder particles that are originated from electrostatic, van der Waals, and surface adsorption forces. These forces are significantly high in nanoparticles forming hard agglomerates and interagglomerate which are relatively large. Based on the thermodynamic treatment of the shrinkage of the pore, Mayo [8] suggested that the finest pore size usually yields the highest densification rate. Such large pores require not only higher temperature but also prolong sintering times for their successful elimination; consequently, it becomes difficult to retain the grain size in the nanometer domain. Large pores undergo

pore–boundary separation that restricts attaining the full density in the consolidated nanoparticles [6,9]. During sintering of nanoparticles, pores smaller than the critical size shrink [10], while larger pores undergo the pore–boundary separation. The fraction of grain boundaries in nanomaterials is large compared to that for coarse-grained materials. The density of the grain boundary regions is less than the grain interior due mainly to the relaxation of atoms in the grain boundaries, and they also contain other lattice defects. Therefore, consolidated nanoparticles with retained nanostructure is expected to exhibit a density lower than the theoretical density of the bulk counterpart. There are numerous conflicting views on the sintering behavior of the nanoparticles. Nanoparticles show depressed onset of sintering temperature to the range of  $0.2T_m$ – $0.3T_m$  compared to that of conventional powders that normally exhibit a range of  $0.5T_m$ – $0.8T_m$ , where  $T_m$  is the melting point (K). Such results possibly attributed to the structural instability of these particles due to the presence of high surface area. Synthesis of nanoparticles of ceramic, metallic, and their mixture has made a substantial progress in the last decade, however, consolidation of such nanoparticles into fully densified *bulk* components with retained nanostructures remains a difficult problem. A brief review of the various consolidation processes is presented herein.

In this review paper, latest developments, advances and challenges in processing, microstructural details, physical, and mechanical properties of nanocrystalline materials, and coatings will be dealt with. Relative merits of each processing techniques and equipment infrastructure required to do research on specific techniques have been discussed at length. Fig. 1 represents a layout of various consolidation techniques discussed in the following sections.

## 2. Mechanical processing

### 2.1. Severe plastic deformation

#### 2.1.1. Introduction

Nano and submicrocrystalline materials, consisting of large amount of grain boundary area, have simulated considerable attention in the research field of advanced materials attributed to their exceptional changes in mechanical, physical, and electronic properties [11–15]. One of the efficient methods to induce ultrafine grain structure in materials is deforming it to large strains below recrystallization temperature without intermediate thermal treatment [16–19]. Traditional techniques for introducing deformation of higher strains, such as forging, extrusion, drawing, or rolling do have the inevitable limitation on required equipments in exerting enough load or pressure to cause uniform submicron level grain refinement [16,17,20–22]. More recently developed techniques for producing ultrafine grain structure, viz. inert gas condensation and high energy ball milling are not yet capable of producing large bulk samples of uniform dense structure [16,17,20,21,23–25]. In recent years, various severe plastic deformation (SPD) techniques have been practiced towards synthesizing bulk nanostructured materials attributed to the multifarious advantages of these techniques [20,21,26–35]. Besides achieving uniform grain refinement, reduction in residual porosity and impurities in compacted samples can also be accomplished in the various SPD methods [26,27,29,33,35–39].

#### 2.1.2. Advantages

Severe plastic deformation, where processing of materials is being carried out by applying high amount of strain to the material, has its own advantages over other nanoconsolidation processes by plastic deformation which are reported below.

- It is difficult to achieve a uniform microstructure throughout the whole sample by processing materials by conventional plastic deformation techniques like cold rolling, drawing, forging, or extrusion. Processing materials by SPD methods with special mechanical scheme can attain grain refinement and microstructural uniformity simultaneously.
- The problems associated with porosity and impurity incorporation are predicaments in consolidation by plastic deformation. Porosity reduction and lowering of impurity level can greatly be accomplished by various SPD methods.
- It is not desirable to have any mechanical damage or cracks while samples are exposed to large plastic deformations. The mold design and mode of load application in SPD techniques takes care of this problem.
- Fabrication of bulk structure with induced nanostructure is extremely difficult by conventional processing routes, whereas, comparatively larger bulk components can be fabricated by assuming SPD techniques.

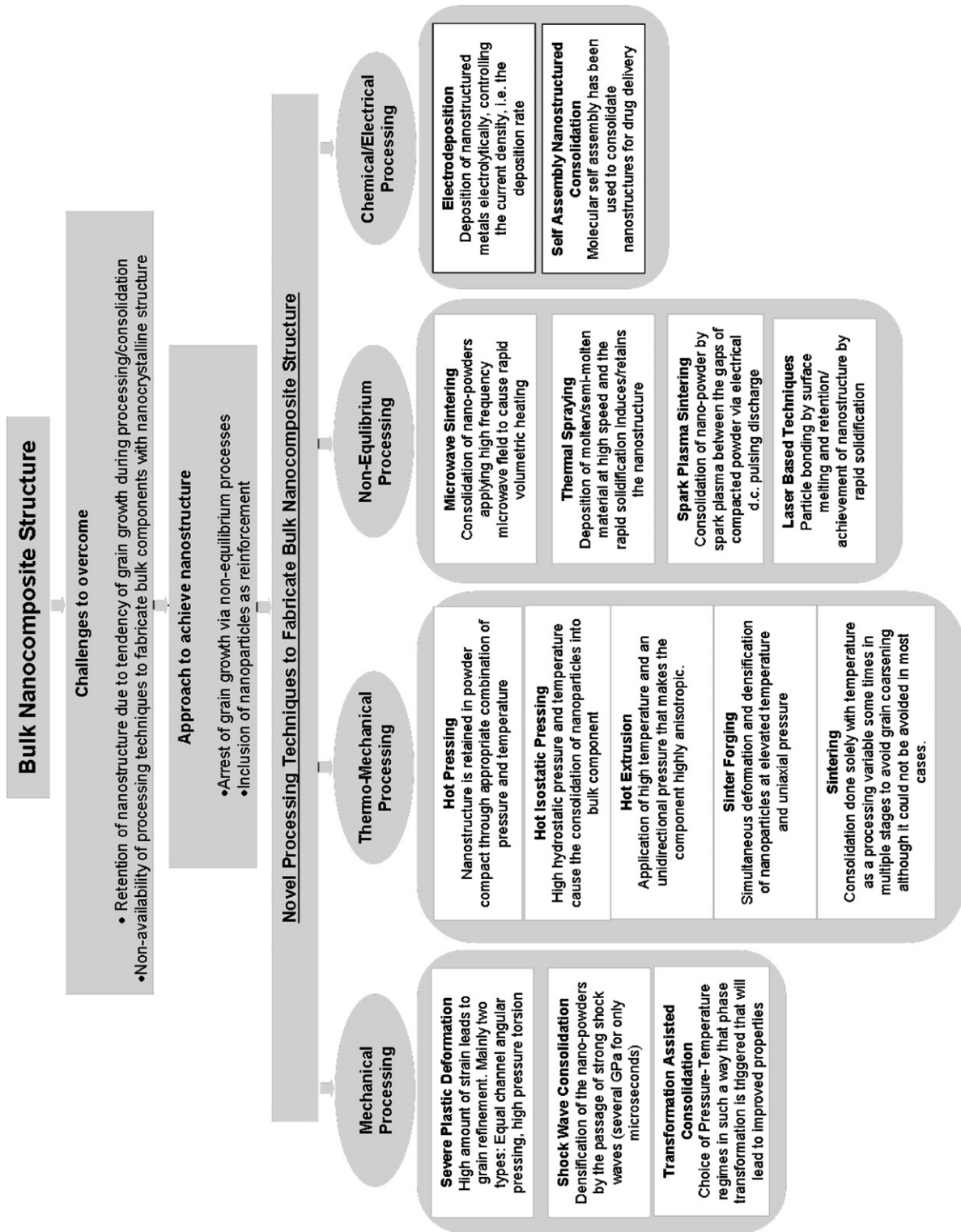


Fig. 1. Overview of different consolidation techniques.

Therefore, synthesis of bulk materials with ultrafine and uniform microstructure is feasible by various SPD methods, where the processed materials contain no or very minimum porosity and impurity.

The earliest developments and investigations of nanostructured materials processed by SPD methods were carried out by Valiev and co-workers more than 15 years ago [19,40]. Several SPD methods such as equal-channel angular pressing (ECAP), high pressure torsion (HPT), accumulative roll bonding (ARB), cyclic extrusion–compression, torsion–compression, and multi-axial forging have been evolved till then towards obtaining bulk nanostructured materials. Equal-channel angular pressing and high pressure torsion are the most well-known methods and has been considered the most prospective techniques among the various severe plastic deformation techniques. The principles, fundamentals, and applications of these two techniques are communicated below with details.

## 2.2. Equal-channel angular pressing

### 2.2.1. Introduction

Segal et al. introduced the method of ECAP in 1980s, deformation of billets were carried out under pure shear to introduce intense plastic strain into materials without changing the cross-sectional area of billets. In the early 1990s, the method was further developed and applied as an SPD method for processing of structures with submicron and nanometric grain sizes by Valiev et al. [40–43]. In these experiments the initial billets with a round or square cross-section were cut from rods, from 70 to 100 mm in length. The cross-section diameter or its diagonal did not exceed 20 mm, as a rule [40,41].

### 2.2.2. Fundamental principles

Equal-channel angular pressing, also termed as equal-channel angular extrusion is the most widely practiced among the various severe plastic deformation techniques, in which a well lubricated metallic billet or ingot is pressed by a ram through a die constrained within two intersecting channels which are placed at an abrupt angle that is equal to, or very close to  $90^\circ$  (Fig. 2) [21,22,31,32,44–47]. Contrary to conventional extrusion method, the cross-sectional areas of the intersecting channels in ECAP are identical in diameter. During the pressing, the billet moves inside the channel as a rigid body and deformation is achieved by simple shear in successive thin layers at the crossing planes of the channels. In this way, the complete billet undergoes deformation of uniform strain, except the small end regions. The ram retreats after the extrusion stroke, and the deformed billet is withdrawn from the second channel. The billets can be subjected to multiple pressing and entry at following passes is performed by rotating the billets around the longitudinal axis at different angles of  $0^\circ$ ,  $90^\circ$ , and  $180^\circ$ . ECAP is also conducted at elevated temperatures for several materials which do not possess malleability at normal temperature.

The ECAP parameters, viz. amount of deformation shear strain ( $\varepsilon$ ), number of passes ( $N$ ), rotation angle between each repetitive pressing, the strain rate monitored by movement of punch, and the temperature in process greatly influence the final microstructure and thus the properties of the final product in ECAP [21,22,31,44,46]. A schematic of the process is exhibited in Fig. 2, where  $\phi$  and  $\psi$  are the channel intersection angle and the arc curvature angle. The magnitude of these angles along with the number of passes determines the shear strain induced into the sample. The strain increment ( $\varepsilon$ ) that the material undergoes after each pass can be expressed in terms of punch pressure ( $P$ ) and the flow stress of the material ( $\sigma_{f.s.}$ ) and depends on the intersection angle ( $\phi$ ) between two channels as follows [22,42,48]:

$$\text{Strain increment after each pass, } \Delta\varepsilon = \frac{P}{\sigma_{f.s.}} = \frac{2}{\sqrt{3}} \cot \phi \quad (1)$$

The shear strain value greatly depends on the number of passes ( $N$ ) and the curvature angle at the channel intersection and can be generalized as follows [22,49,50]:

$$\text{Shear strain, } \varepsilon = \frac{N}{\sqrt{3}} \left[ 2 \cot \left( \frac{\phi}{2} + \frac{\psi}{2} \right) + \phi \operatorname{cosec} \left( \frac{\phi}{2} + \frac{\psi}{2} \right) \right] \quad (2)$$

From the above equation it can be inferred that the deformed billet experiences a shear strain value of nearly equal to 1, considering the frequently practiced values of  $\phi = 90^\circ$  and  $\psi = 20^\circ$ . The strain rate in ECAP depends on the diameter (for round cross-section) or width (for square cross-section) of the billet and the ram speed during the deformation. As plastic deformation is a dynamic process governed by dislocation mobility, the strain rate in ECAP also affects the

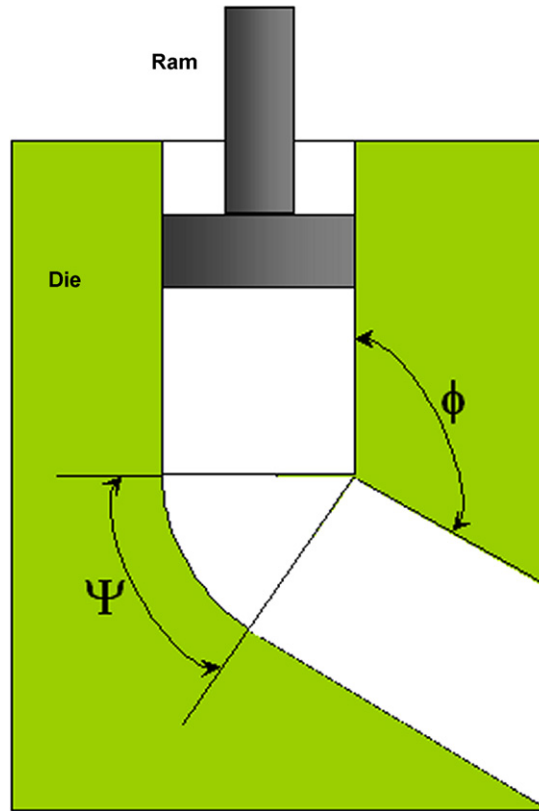


Fig. 2. Schematic of equal-channel angular pressing process.

properties of final product and can be expressed by the following relationship [22,49]:

$$\text{Strain rate, } \dot{\epsilon} = \frac{N}{\sqrt{3}} \left[ 2 \cot \left( \frac{\phi}{2} + \frac{\psi}{2} \right) + \phi \operatorname{cosec} \left( \frac{\phi}{2} + \frac{\psi}{2} \right) \right] \frac{V\sqrt{2}}{\phi L}, \quad (3)$$

where ‘ $V$ ’ is the ram speed and ‘ $L$ ’ is the width or diameter of the billet. The optimum property evolution by ECAP technique can be envisaged by minimum contact friction, sharp corner channels, and square long or flat billet.

The degree of grain refinement in ECAP method depends on various factors like processing parameters, phase composition, and initial microstructure of a material. The interdependent relationship of nanostructure evolution and mechanical properties of various material system processed by ECAP has been discussed below.

Equal-channel angular pressing provides a simple procedure for obtaining a homogenous ultrafine grain size in polycrystalline materials [45,51,52]. High purity (99.99%) aluminum, with an initial grain size of  $\sim 1$  mm, exhibited grain size reduction to the micrometer level ( $\sim 4 \mu\text{m}$ ) after a single pressing with approximate strain of 1.05. The microstructure consists of parallel bands of subgrains further divided by many boundaries having very low angles of misorientation. Moreover, the hardness increased significantly by a factor of  $>2$  only after a single pass [51].

Langdon and co-workers studied the effect of severe plastic deformation by the method of ECAP on 6061Al alloy, where the feedstock billets were deformed to a strain of approximately 1, a homogeneous hardness distribution was observed in the processed materials with continuous hardness increase (Fig. 3) [39]. Purcek investigated the effect of multi-pass equal-channel angular pressing on commercially used zinc–aluminum alloy at a temperature of about  $75^\circ\text{C}$  [53]. The ductility decreased gradually with successive passes, however, extensive increase in strength was observed.

Low carbon steel, processed by ECAP for up to a maximum of 10 passes at room temperature exhibited non-equilibrium microstructure with poorly defined boundaries and high densities of dislocation tangles [34]. The as-pressed microstructure exhibited nearly parallel bands of elongated grains having a width of the order of  $\sim 0.2\text{--}0.3 \mu\text{m}$

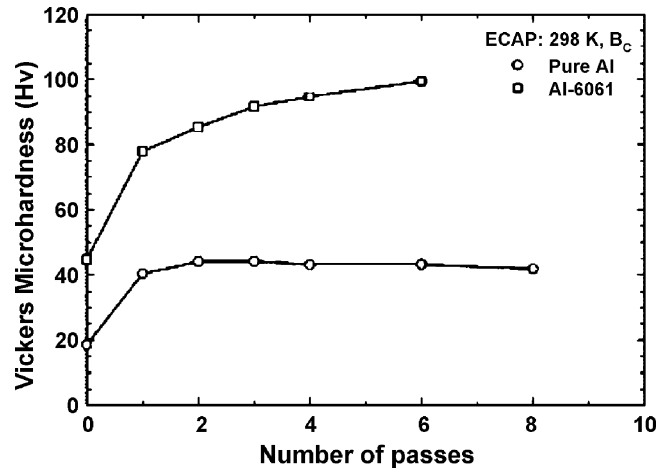


Fig. 3. The average Vickers microhardness (HV), vs. the number of passes in ECAP for pure aluminum and an 6061Al alloy processed at room temperature. (Reprinted from [52] with permission from Elsevier.)

(Fig. 4). Annealing for 1 h at 773 K of the deformed sample resulted in reasonably recovered microstructure with equiaxed grains, consisting of only fewer intragranular dislocations and more equiaxed grains, which is only slightly larger than the widths of the elongated grains in the as-pressed condition (Fig. 4).

### 2.2.3. Nanoconsolidation

ECAP is a well-established procedure for achieving extensive grain refinement in polycrystalline metallic systems, which has been discussed in the earlier section. However, the application of ECAP in synthesizing nanocomposite material is rather restricted. The distribution of reinforcement should have homogenous distribution throughout the matrix in order to perceive isotropic property in the composite. Traditional secondary deformation processes such as rolling, forging, and extrusion are not very efficient in achieving uniform distribution of second phase particles [54,55]. The problem becomes more aggravated in case of finer second phase particles, as it requires very high amount of strain to accomplish homogenous dispersion in the matrix. As a huge amount of deformation can be induced, ECAP can be useful in synthesizing metal matrix composites with uniform distribution of second phase particles in the matrix. Recently, researchers have started working on metal matrix composites, which will be discussed in the later section, but, absolutely no information is available regarding ECAP of ceramic and polymer matrix composite, primarily due to the malleability issue of the matrices.

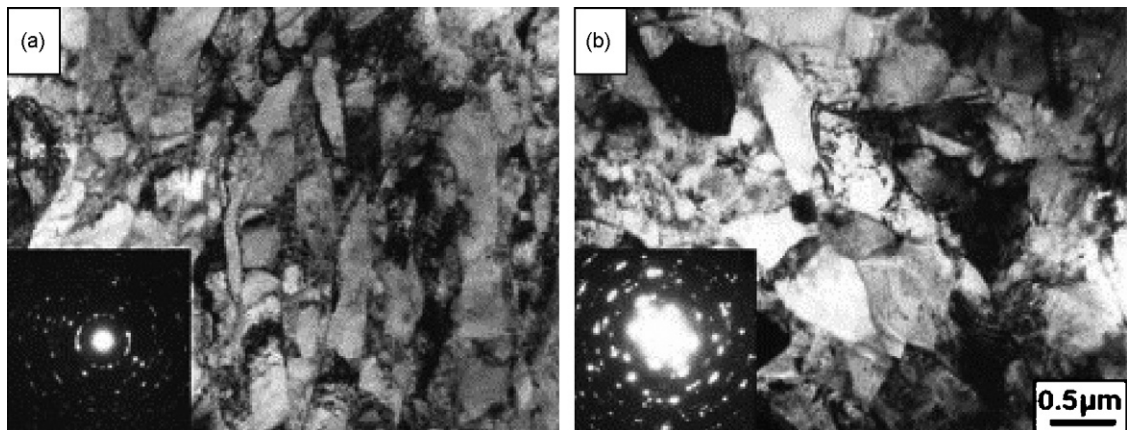


Fig. 4. Observations by TEM: (a) after processing by 10 passes of ECAP at room temperature and (b) after 10 passes of ECAP and annealing for 1 h at 773 K. (Reprinted from [52] with permission from Elsevier.)

**2.2.3.1. Al–Al<sub>2</sub>O<sub>3</sub> composite.** A metal matrix composite, consisting of 6061Al matrix alloy reinforced with 10 vol.% of fine Al<sub>2</sub>O<sub>3</sub> particulates, was processed by Langdon and co-workers by equal-channel angular pressing [56]. The diameter and the length of the composite billets were 10 and 60 mm, respectively. The intersection angle ( $\phi$ ) and the outer arc curvature angle ( $\psi$ ) between the two channels in the solid die was 90° and 20°, respectively, which imposed a strain of approximately 1 on each single pass of the billet. The billets were pressed through the die for 1 pass at room temperature and additional 11 passes at 473 K with the total imposed strain of  $\sim$ 12. The grain size reduced from  $\sim$ 3.5 to  $\sim$ 1.9  $\mu\text{m}$  after the severe plastic deformation. However, there was no change in the average size of the particulates ( $\sim$ 270 nm) (Fig. 5). The difficulty in attaining significant grain refinement in this material, comparing with 6061Al alloy, is attributed to the presence of the fine Al<sub>2</sub>O<sub>3</sub> particulates. For example, un-reinforced 6061Al alloy has experienced grain refinement due to ECAP from initial grain sizes of  $\sim$ 50  $\mu\text{m}$  to ultrafine sizes of 0.2–0.4  $\mu\text{m}$  [39]. Tensile testing on both the as-received and ECAP composite samples was conducted at different high strain rate at 873 K, which showed higher flow stress in as-received samples (Fig. 6).

Sabirov et al. conducted equal-channel angular pressing on an 6061Al–20% Al<sub>2</sub>O<sub>3</sub> composite produced by powder metallurgy route [57]. Twenty-five millimeter diameter and 100 mm length billets were pressed at a temperature of 370 °C for various number of passes with imposed strain of  $\sim$ 1 in each passes. The samples were rotated in the same direction by 90° between successive passes. It was shown that the severe plastic deformation gradually improved the uniformity of the particle distribution (Fig. 7). The diffuse particle clusters resolved completely and only dense particle

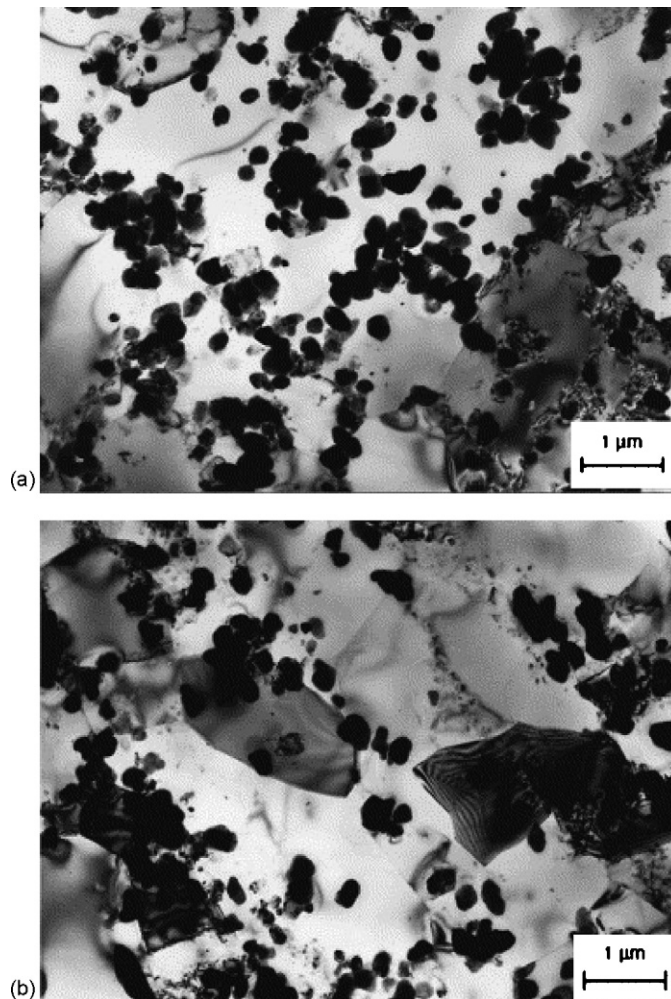


Fig. 5. Transmission electron micrograph of the 6061Al–10 vol.% Al<sub>2</sub>O<sub>3</sub> composite (a) in as-received condition and (b) after processing by ECAP through 1 pass at 298 K and 11 passes at 473 K. (Reprinted from [56] with permission from Elsevier.)

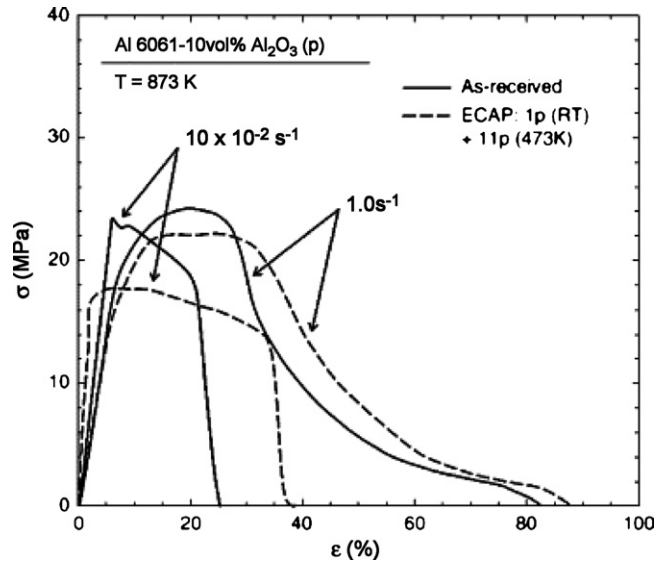


Fig. 6. Stress–strain curves at 873 K for the 6061Al–10 vol.%  $\text{Al}_2\text{O}_3$  composite tested in the as-received and pressed condition at two different strain rates. (Reprinted from [56] with permission from Elsevier.)

clusters with no matrix material between the particles were visible after seven passes. Tensile test was carried out on the under-aged ECAP processed samples to understand the effect of particle homogenization in the composite. The uniform particle distribution resulted in improving the fracture toughness and the total crack growth resistance. However, the deformation process did not influence the global tensile properties of the composite.

**2.2.3.2. Al–TiAl composites.** The effect of equal-channel angular pressing on extruded Al–TiAl composites has been studied by Morris and co-workers in evolution of microstructure and mechanical properties as a function of reinforcement particle size and distribution [58]. The 20 mm diameter billets were given a maximum number of passes with a strain value of 0.7 per pass and without any rotation after each pass, until cracks appeared at the surface of the samples. The composite after undergoing ECAP, showed fully dense microstructure with excellent cohesion at the interfaces between the Al matrix and the TiAl particles (Fig. 8). The matrix grain size decreased from about  $4\ \mu\text{m}$  in the extruded matrix to about 600–500 nm after two to four ECAP passes. However, ECAP does not lead to refinement in TiAl particle size or spacing, since the intermetallic particles neither deform nor fracture (Fig. 8). The strength of the composites increased and the ductility decreased gradually with increase in number of passes. Tensile stress carried out at higher temperature exhibited lower strength of the composite (Fig. 9). The reduction of ductility in the composites is attributed to the loss of cohesion by weakening of the Al–TiAl interface during ECAP.

### 2.3. High pressure torsion

#### 2.3.1. Introduction

The first high pressure torsion device of its kind is the Bridgeman anvil type device [59], which was further modified for severe plastic torsion straining under high pressure [60,61]. These devices were used for investigation of phase transformations during heavy deformation [62] as well as evolution of structure and changes in temperature of recrystallization after large plastic deformations [60]. Successful formation of homogeneous nanostructures with high angle grain boundaries via severe torsion straining [19,63] was a very important step allowing one to consider this procedure as a new method of processing nanostructured materials.

#### 2.3.2. Fundamental principles

In HPT process, an ingot is held between anvils and strained in torsion under the applied pressure ( $P$ ) of several GPa. A lower holder rotates and surface friction forces deform the ingot by shear (Fig. 10). Due to the specific geometric shape of the sample, the main volume of the material is strained in conditions of quasihydrostatic

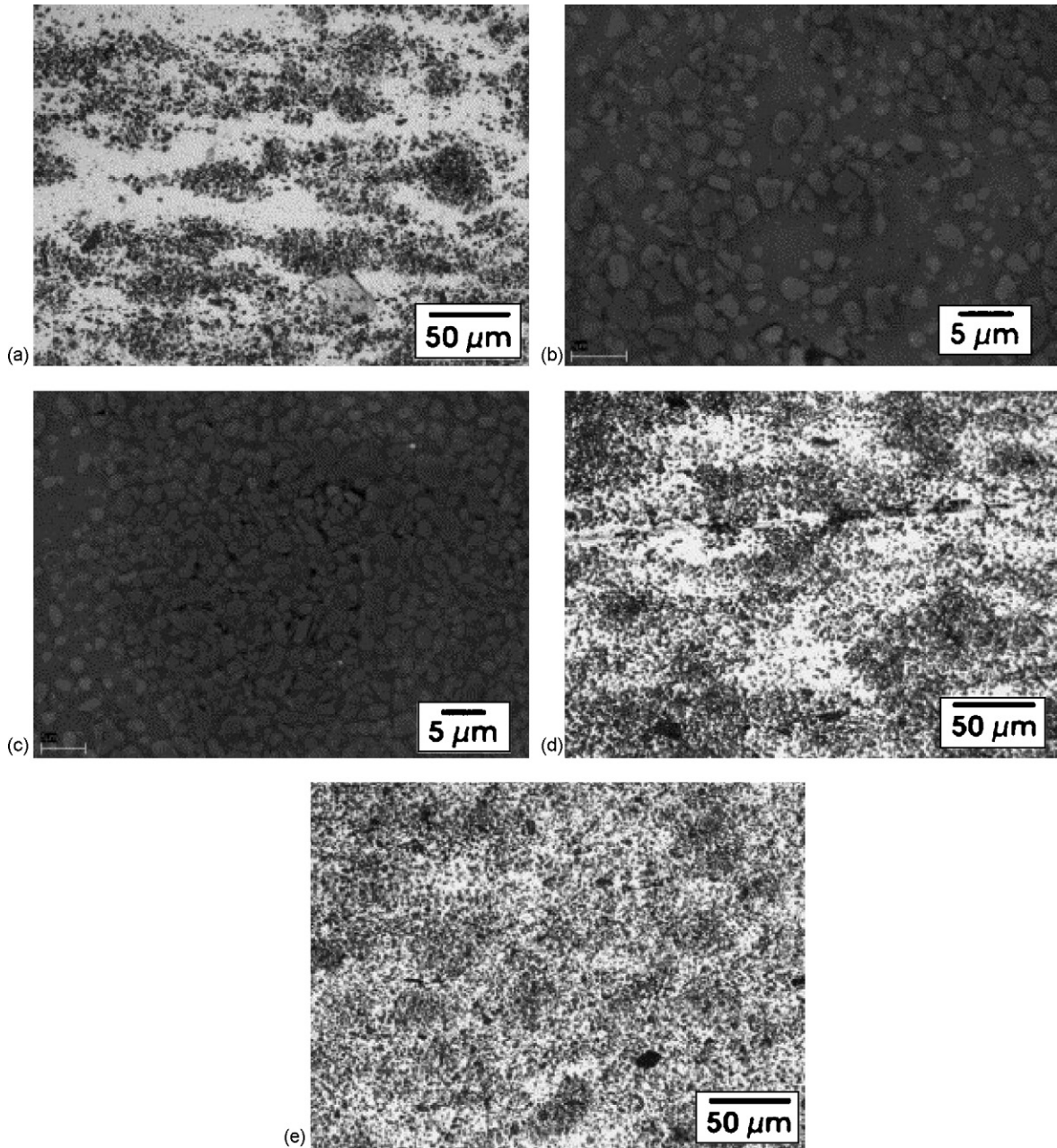


Fig. 7. Microstructure of the MMC: (a) as-fabricated condition, (b) as-fabricated condition (a dense particle cluster), (c) as-fabricated condition (diffused particle clusters), (d) after four ECAP passes, and (e) after seven ECAP passes. (Reprinted from [57] with permission from Elsevier.)

compression under the applied pressure. As an effect the deformed sample does not get destroyed in spite of large strain values.

The shear strain ( $\gamma$ ) value due to the torsional effect at a distance ' $R$ ' from the center of disk-shaped sample with thickness ' $t$ ' can be estimated from the following equation:

$$\gamma = \frac{2\pi RN}{t}, \quad (4)$$

where ' $N$ ' is the number of rotation of the lower anvil during HPT process. The diameter and thickness of the disk-shaped samples in HPT process varies in the range of 10–20 and 0.2–0.5 mm, respectively.

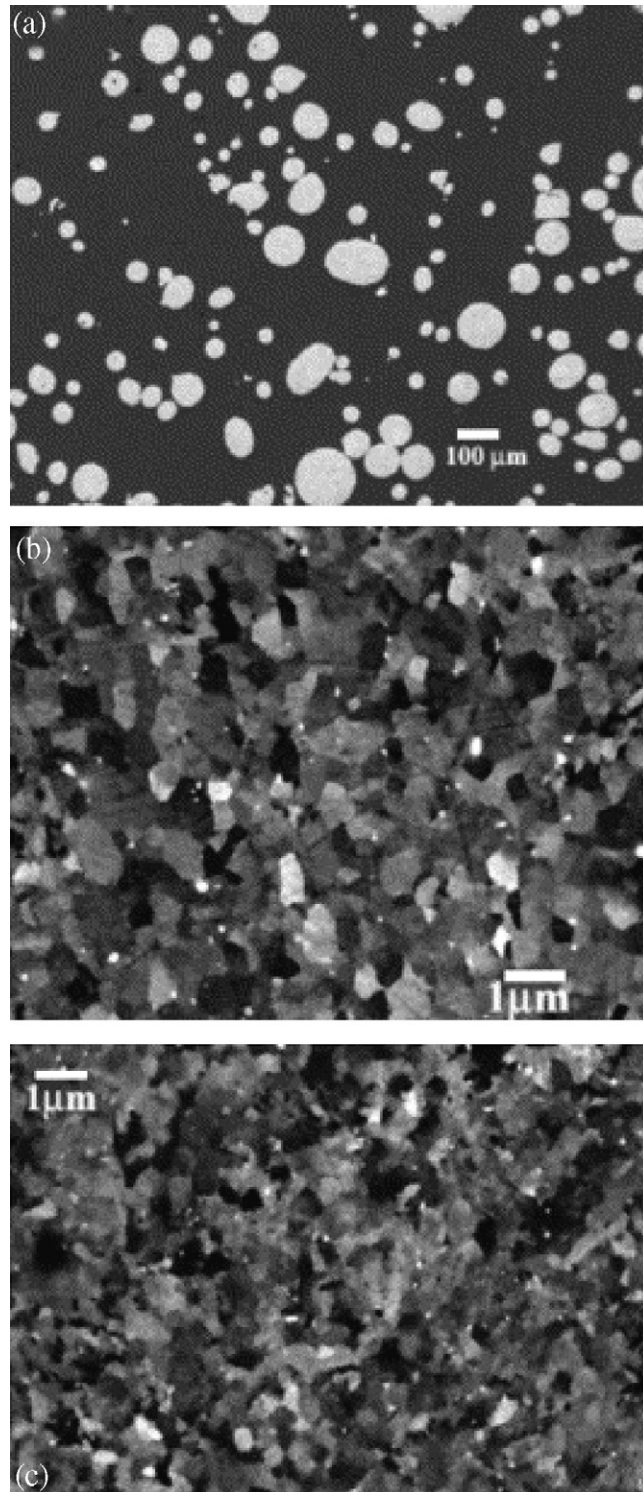


Fig. 8. Typical microstructures observed by SEM from the composite materials containing 25% TiAl atomised particles. (a) TiAl particles distribution within the Al matrix after four ECAP passes. (b and c) Grain size distribution obtained by crystallographic contrast from the Al matrix after two and four ECAP passes, respectively. (Reprinted from [58] with permission from Elsevier.)

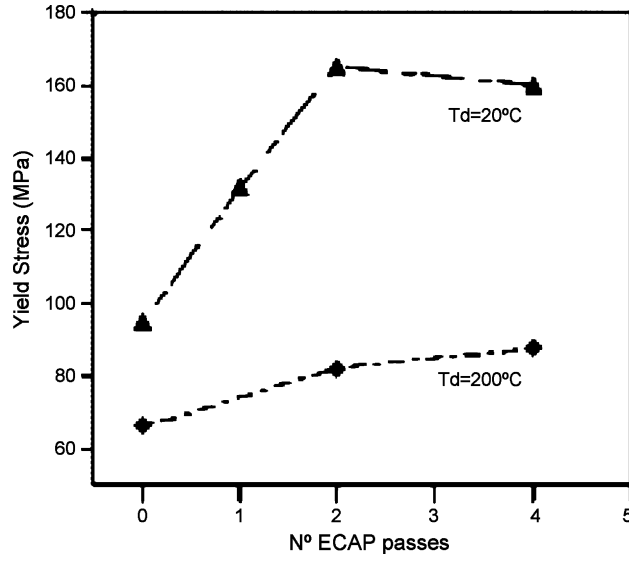


Fig. 9. Yield stress variation as a function of the number of ECAP passes in Al–25% TiAl composite at room temperature and at 200 °C. (Reprinted from [181] with permission from Elsevier.)

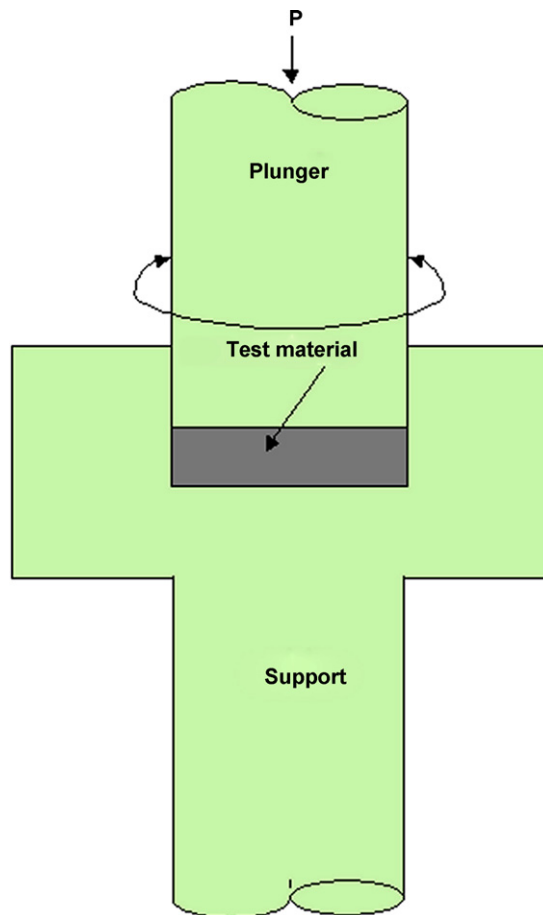


Fig. 10. Schematic of high pressure torsion.

It is obvious from the above formula that the strain value should exhibit a linear behavior from zero at the center to its maximum value at the edge of the samples. However, as the thickness ' $l$ ' changes approximately to its half value under high compression pressure, the calculated strain value does not exactly match with the true strain value. Thus, considering the number of rotations ' $N$ ' is more rational, than relying on the computed strain value while carrying out microstructural investigation.

High pressure torsion method is very efficient in synthesizing uniformly nanostructured materials using torsional strain. The efficiency of the process primarily influenced by the number of rotation ( $N$ ) in Eq. (2) and the load applied. The grain refinement also depends largely on the material system undergoing the processing. The commonly practiced material systems in HPT technique have been discussed below.

Commercial aluminum alloy synthesized by Islamgaliev et al. assuming HPT method under 6 GPa pressure in order to attain high strength by achieving nanostructure in the material [64]. The HPT processed alloy exhibited a uniform microstructure with lowering of grain size to 100 nm from 10  $\mu\text{m}$  at initial stage. The alloy exhibited advanced combination of high tensile strength (up to 800 MPa) and enhanced ductility (up to 25%) resulted from several contributions, i.e. the very small grain size (375 MPa), solid solution in Al matrix (255 MPa), and the presence of dispersoids (80 MPa).

The effect of degree of deformation and subsequent annealing on microstructural evaluation in copper has been studied by Jiang et al. [65]. At the initial stage of deformation the sample exhibited formation of subgrains of  $\sim 565$  nm with low angle grain boundaries (Fig. 11a). Subsequently, the low angle grain boundaries transformed into high angle boundaries with increase in deformation strain and continuous decrease in grain size with preferred crystallographic orientation (Fig. 11b). However, high densities of small defects and dislocation debris from dynamic recovery are observed. The microhardness of the processed alloy increased radially with amount of deformation.

Disk-shaped annealed high purity nickel (99.99%), with diameters of  $\sim 10$  mm and thickness of  $\sim 0.3$  mm was subjected to HPT straining under different applied pressures and with different number of revolutions at room temperature [66]. The processing of nickel by HPT leads to an increase in the microhardness due to significant microstructural refinement that is strongly influenced by the processing parameters. The microhardness values of the HPT processed Ni show higher than that of the unprocessed nickel ( $\sim 1.4$  GPa). An increase of pressure from 1 to 9 GPa leads to an increase in the microhardness values, especially in the center of the disk (Fig. 12a). Fig. 12b reveals that the microhardness increases with increase in applied load and the edge region experiences higher hardness. However, the hardness profile at higher loads becomes almost linear justifying the uniformity of microstructure at higher load during HPT.

### 2.3.3. Nanoconsolidation

**2.3.3.1. W–Cu composite.** A coarse-grained W–25% Cu composite is subjected to high pressure torsion at different temperatures and at different degree of deformation [67]. The initial equiaxed W particles in the composite were 2–10  $\mu\text{m}$ . A continuous increase in the degree of homogenization with breaking of W particles is shown with increase in the applied strain (Fig. 13). At lower strain values a layered microstructure can be observed (Fig. 12a, b), but the composite shows very homogenize microstructure with a W particle size of 10–20 nm deformed at room temperature to a strain of  $\geq 256$ . It can also be envisaged from Fig. 13 that the kinetics of microstructure homogenization becomes faster at higher temperatures (see also, Fig. 14).

**2.3.3.2. Cu–Fe composite.** A Cu–Fe composite synthesized by cold drawing was processed by high pressure and torsion by Sauvage et al. The initial composite material was produced by cold drawing of Cu (99.5% purity) and Fe (99.5% purity) together [68]. The HPT process on the cold drawn composite leads to a layered nanostructure. The grain size of copper regions was 100–200 nm while regions containing the  $\alpha$ -Fe phase exhibit a much smaller grain size in the range of 20–80 nm. This confirms the ability of multi-phase materials to produce structures with a grain size of several tens of nanometers using SPD. Both TEM and X-ray diffraction data show that both the fcc copper and the bcc  $\alpha$ -Fe phases are preserved after the HPT deformation.

Severe plastic deformation techniques such as equal-channel angular pressing and high pressure torsion are proven to be very much successful in achieving ultrafine grain structure in various material systems. Although there is a considerable progress attained by these processing methods, exercise of nanocomposite fabrication is still limited to few material systems.

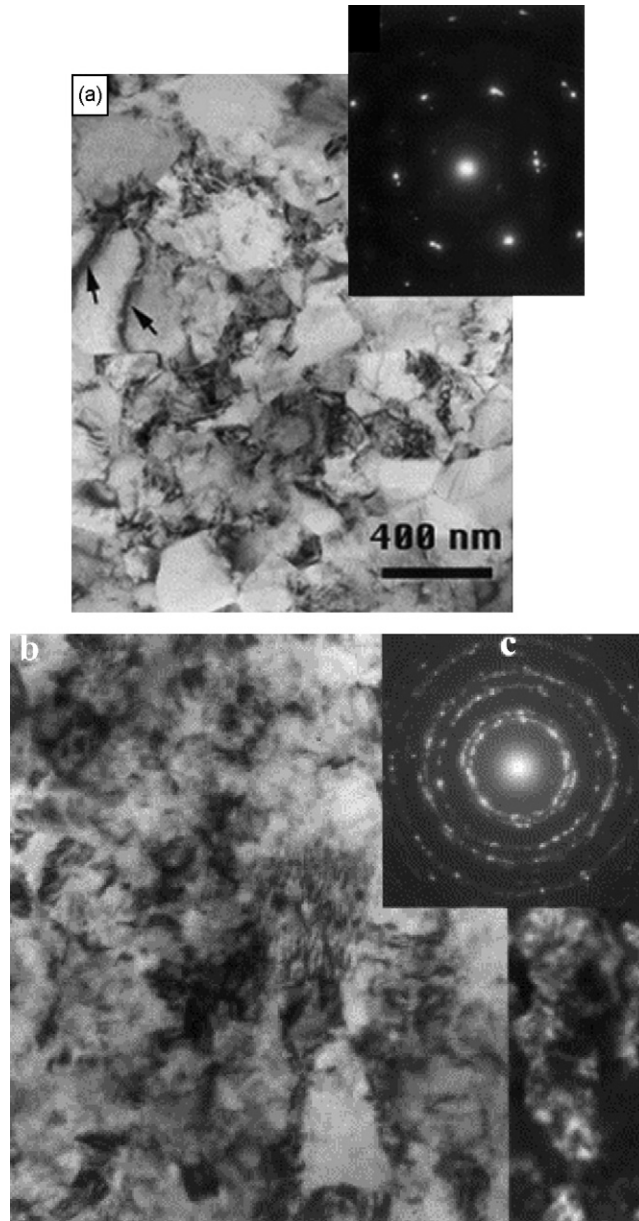


Fig. 11. Grain refinement in copper by HPT: (a) evolution of low angle grain boundaries and (b) dissolution of dislocations. (Reprinted from [65] with permission from Elsevier.)

## 2.4. Shock wave consolidation

### 2.4.1. Introduction

Shock wave consolidation also termed as dynamic consolidation is used to densify powdered materials without inducing thermal activated microstructural and compositional changes that are normal in conventional thermo-mechanical processing. Such densification is possible because of the interparticle bonding due to localized melting at the interfaces between the particles. High pressure and rapid loading rates which create high plastic deformation finally leads to high shock initiated chemical reaction totally different from the conventional ones. Metallic or alloy powders are usually processed through this route due to the fact that plastic deformation in metal is quite easier compared to the ceramics. For example, magnetic materials processed using compaction and sintering have now been

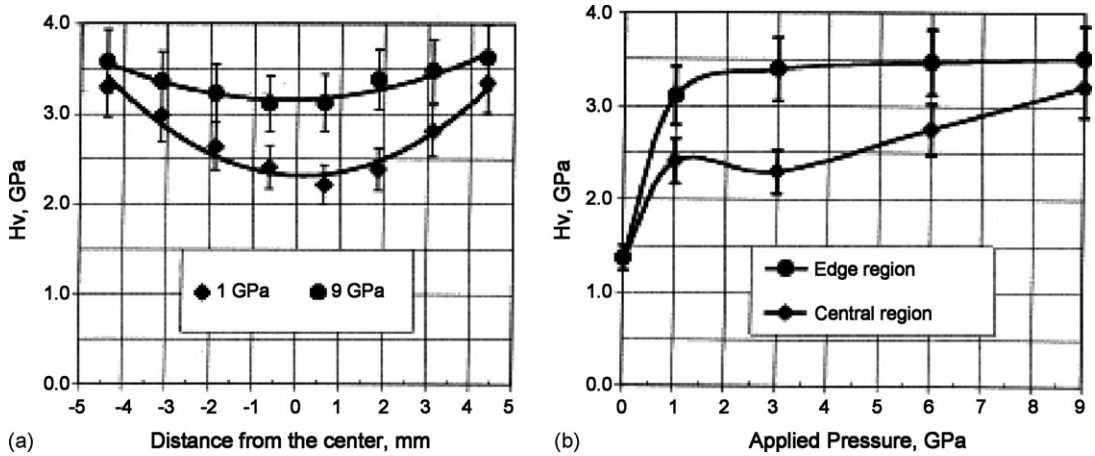


Fig. 12. Microhardness profile of HPT processed nickel at two different applied pressures (a), and average microhardness for the central and edge regions of HPT nickel as a function of applied pressure (b). Samples were subjected to HPT pressing at room temperature through five whole turns. (Reprinted from [66] with permission from Elsevier.)

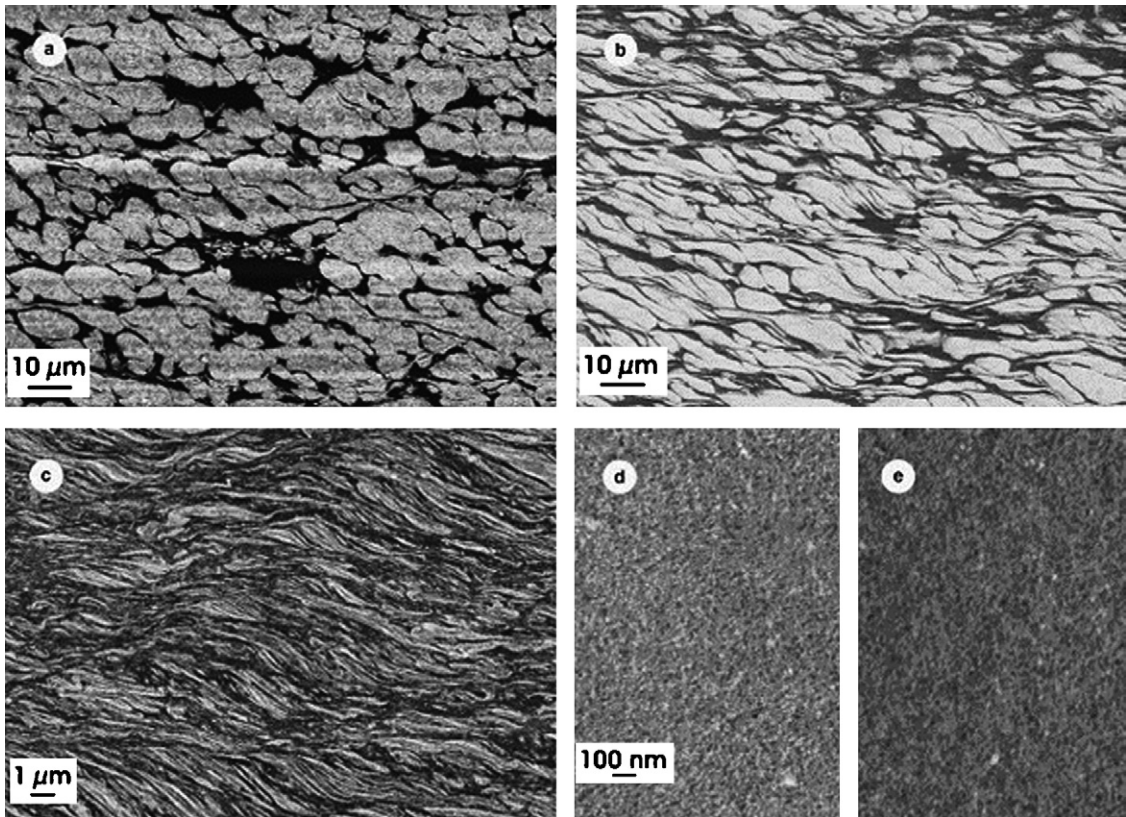


Fig. 13. The microstructure of the W-25% Cu composite subjected to HPT at room temperature to strains of: (a) 4, (b) 16, (c) 64, (d) 256, and (e) 512. (Reprinted from [67] with permission from Elsevier.)

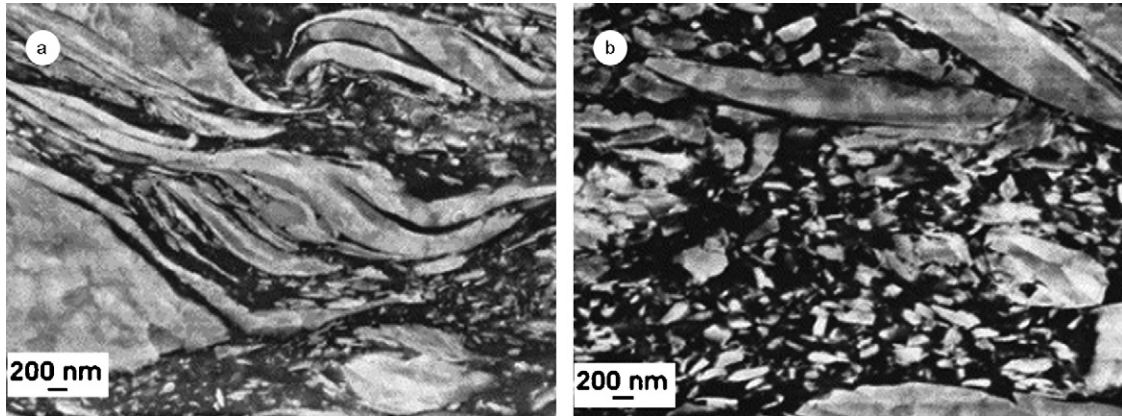


Fig. 14. The microstructure of the W–25% Cu composite subjected to HPT to a strain of 64: (a) at 200 °C and (b) at 400 °C. (Reprinted from [67] with permission from Elsevier.)

processed using shock consolidation [69]. A typical laboratory shock wave setup and a schematic of the equipment are shown in Fig. 15.

#### 2.4.2. Fundamental principles

If a metal powder at atmospheric pressure, ambient temperature, and initial packing density is subjected to a shock wave of energy  $E$ , then consolidation is all about how much energy is being used along the interfaces of the particles in order for the lot to be densified properly. Energy is absorbed by the packing material or spent towards creating a loud noise. Net shock energy spent in the interfaces is inversely proportional to the surface area of the particles [70]. It is obvious that less energy is needed to consolidate nanoparticles compared to coarse-grained particle which is a merit indeed. Different models have been proposed to describe the solid-state chemistry involved during shock wave processing and several experiments have been conducted to correlate those models with the experiments [71].

#### 2.4.3. Advantages

- The critical processes happening during the microsecond time duration of shock compression loading, involve the heterogeneous deposition of shock energy, resulting in interparticle bonding, and configurational changes in the particles due to the annihilation of voids via plastic flow and dispersion of fragments. Hence, with shock

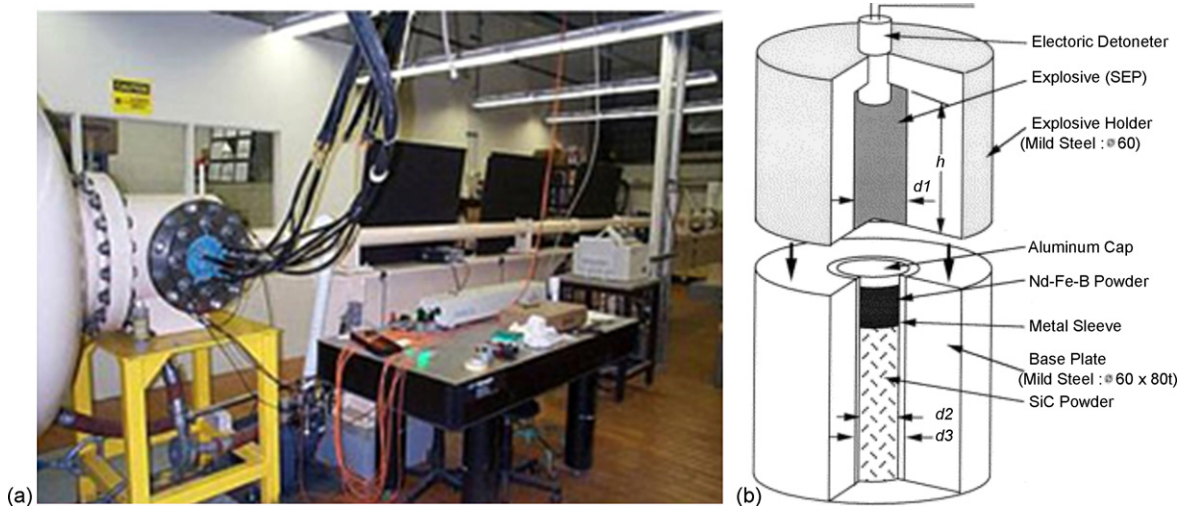


Fig. 15. (a) Picture of 80 mm diameter single stage gas gun being used for shock wave consolidation (Photo source: [www.mse.gatech.edu](http://www.mse.gatech.edu)) and (b) schematic of a consolidation process showing the experimental setup. (Reproduced from [72] with permission from Elsevier.)

compression, it is possible to fabricate nanocomposite bulk magnets without grain growth since the heating is limited to the particle surface regions and it occurs in microseconds.

- Microstructural modifications and a high density of defects produced under such conditions generate a highly activated dense-packed state which can result in improvements in properties of bulk shock-consolidated materials, or even alter the thermodynamics and kinetics of post-shock crystallization and precipitation treatments to permit retention of metastable phases or nanoscale size of crystallites or precipitates.

#### 2.4.4. Equipment—process and mechanism

Shock wave consolidation involves the typical parts mentioned in Fig. 15b [72]. Particles are enclosed in a steel block that looks similar to a cold compaction chamber which is covered using a plate, on top of which a driver plate usually bears the brunt of explosion and drives the shock wave towards the sample. The driver plate is usually made out of a highly conductive, highly ductile material. Both the conditions are satisfied by copper. Explosives are packed on top of this plate carefully and the spillage if any, needs to be removed. Detonator is set on top of the explosive and the setup is ready for processing to start. Ammonium nitrate is usually used as an explosive. Explosives involved in experiments need federal authorities' (Homeland Security in US) approval in order to be bought as individuals are not allowed to manufacture explosives. Once the processing is completed, extreme care needs to be exercised to look for unexploded explosive material. Of late, gas guns are widely used in performing shockwave consolidation. Gas gun looks similar to a canon. It has a breach filled with gun powder that triggers a piston which compresses hydrogen gas. Hydrogen gas activates the projectile which travels all the way through the Barrel and hits the target which in this case is the powder sample. The small projectile screams down the barrel at a whopping  $8 \text{ km s}^{-1}$  which is three-quarter of the velocity needed to escape earth's gravity. When the projectile hits its target, the pressure of the resulting shock wave is over 600 GPa, 6 million times the pressure of air at earth's surface. Present day gas guns are equipped to monitor shock-initiated events with nanosecond resolution employing piezoelectric and piezoresistive stress gauges, velocity interferometry, and high speed digital imaging, coupled with microstructural characterization to study the mechanisms of phase transformations, chemical reactions, deformation, and fracture initiation processes in metallic and ceramic materials. Different shock wave assemblies have been published [73,74].

#### 2.4.5. Nanoconsolidation

Shock compaction of powders is a dynamic consolidation technique [75] which provides a viable method for densification of amorphous [76] as well as ultrafine powders [77]. The pressures and its duration are important. Fe base, Ni base, Ti base alloys have been studied more often using this technique. For magnetic materials this method seems to be a more suitable consolidation technique. Process parameters of some of the materials compacted has been listed in Table 1.

Pure metals and alloys with retained nanostructures could be consolidated using this technique. Some of the systems that have been investigated are:  $\text{Fe}_{73.5}\text{Cu}_1\text{Nb}_3\text{Si}_{13.5}\text{B}_9$  [78], Fe [79], Fe–Al [80], diamond–Si [81], Al [82],  $\text{Pr}_2\text{Fe}_{14}\text{B}/\alpha\text{-Fe}$  [83],  $\text{Ti}_5\text{Si}_3$  [84], NiAl [85]. Some of the systems will be discussed at length in the next section.

**2.4.5.1. FINEMET magnetic alloy [78].** Amorphous ribbon of  $\text{Fe}_{73.5}\text{Cu}_1\text{Nb}_3\text{Si}_{13.5}\text{B}_9$  produced by melt spinning technique is crushed in a ball mill and subjected to shockwave compaction. Upon annealing of the as compacted amorphous alloy, nanocrystalline microstructure could be produced which changed the magnetic properties altogether. Hysteresis curve (Fig. 16) of the as compacted alloy is being compared with the ones after annealing at 550 and 650 °C. The observed behavior of  $H_c$  (coercive force) and  $B_{\text{max}}$  (flux density) in compacted samples can be explained on the

Table 1  
Experimental parameters used for consolidation using shockwave compaction

No.	Material	Pressure (GPa)	Velocity ( $\text{m s}^{-1}$ )
1	$\text{Fe}_{73.5}\text{Cu}_1\text{Nb}_3\text{Si}_{13.5}\text{B}_9$ [78]	0.65	–
2	Fe–Al [80]	10–11	5000
3	Al [82]	2–3.6	890
4	$\text{Ti}_5\text{Si}_3$ [84]	11–12	300–700
5	NiAl [85]	4–6	400

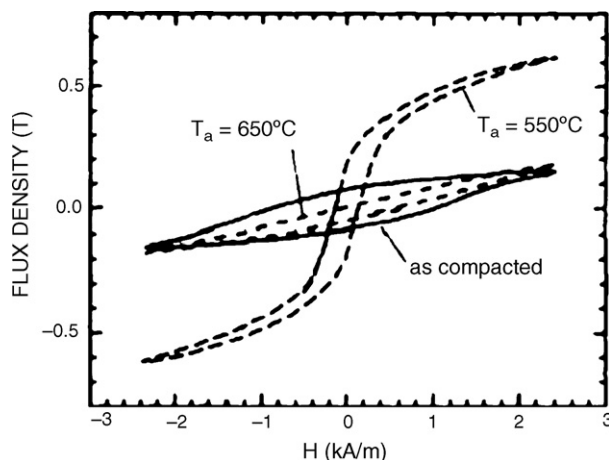


Fig. 16. Hysteresis loop of  $\text{Fe}_{73.5}\text{Cu}_1\text{Nb}_3\text{Si}_{13.5}\text{B}_9$  FINEMET alloy. (Reproduced from [78] with permission from Elsevier.)

basis of the stress anisotropy and the creep-induced anisotropy. After ball milling and shock compaction the material is highly stressed and plastically deformed. Lattice defects, dislocations and dislocation arrangements cause short- and long-range internal stress fields in the material which subsequently alter the total energy balance within the material and the entire domain structure. The magnetic properties of a bulk nanocrystalline material are better than those measured from permalloy Fe/50% Ni materials [86]. The total core losses in Fe/50% Ni materials is  $10 \text{ W kg}^{-1}$  corresponding to a flux density of  $B = 0.6 \text{ T}$  at a magnetizing frequency of 50 Hz. Total losses in the same material are  $600 \text{ W kg}^{-1}$ , corresponding to a flux density of 0.6 T and a magnetization frequency of 1 kHz. Difference in electrical resistivity is attributed to the difference. The electrical resistivity for Fe/50% Ni is  $0.50 \mu\Omega \text{ m}$  [86] and the electrical resistivity for a nanocrystalline, rapidly solidified FINEMET is  $1.35 \mu\Omega \text{ m}$  [87]. The resistivities for FINEMET materials compacted using shock wave technology were measured as  $5 \mu\Omega \text{ m}$  in the as-compacted condition,  $2 \mu\Omega \text{ m}$  in a nanocrystalline state annealed at  $550^\circ\text{C}$ , and  $3 \mu\Omega \text{ m}$  in a crystalline state following annealing at  $650^\circ\text{C}$ .

**2.4.5.2.  $\text{Pr}_2\text{Fe}_{14}\text{B}-\alpha\text{-Fe}$  [83].**  $\alpha\text{-Fe}$  (20 wt.%) mixed with  $\text{Pr}_2\text{Fe}_{14}\text{B}$  and prepared in the form of ribbons by melt spinning technique and subsequently subjected to comminution using packed steel capsules. The powder is then statically pressed to different densities 64 and 76%. Cold compacted samples were then shock-consolidated with a projectile velocity of  $880 \text{ m s}^{-1}$  using a single stage gas gun. The compacts after processing had a density of 97.5 and 99%, respectively. The grains have a size range of 20–25 nm as shown in Fig. 17a. The nanograin size morphology of the  $\text{Pr}_2\text{Fe}_{14}\text{B}$  phase is also confirmed by the HRTEM micrograph shown in Fig. 17b. Large  $\alpha\text{-Fe}$  grains which are prevalent before compaction could not be seen after shock wave consolidation because of the fragmentation. Hysteresis behavior of the sample after consolidation revealed that the higher densification could make the material suitable to behave like a hard magnet (high remanence and high coercivity; Fig. 18). These shock compacted nanocomposite magnets possess not only larger density ( $\rho$ ) but also better magnetic properties than those of commercially available resin-bonded magnets ( $\rho$ :  $\sim 80\%$  TMD,  $\text{BH}_{\text{max}}$ :  $88 \text{ kJ m}^{-3}$  for compression molded bonded magnet; and  $\rho$ :  $\sim 68\%$  TMD,  $\text{BH}_{\text{max}}$ :  $62 \text{ kJ m}^{-3}$  for injection molded bonded magnet) since non-magnetic resins in those bonded magnets results in the decrease of bulk density and therefore the degradation of magnetization and energy products.

**2.4.5.3. Ti–Si alloy [84].** Amorphous Ti–Si alloy powder has been shock compacted at velocities of 300, 500, and  $700 \text{ m s}^{-1}$ . The dense compacts were subsequently crystallized at temperatures between 800 and  $1200^\circ\text{C}$ , for time periods of 1–12 h. The compacts were observed to crystallize as a single-phase  $\text{Ti}_5\text{Si}_3$  compound and an ultrafine grain microstructure. TEM micrograph of the compact shock-densified at  $500 \text{ m s}^{-1}$  revealed the presence of 10–40 nm crystallites in the amorphous matrix. Vickers microhardness measurements showed values of 1200–1400  $\text{kg mm}^{-2}$  for grain size ranging from  $\sim 60$  to 160 nm (Fig. 19b). The microhardness values are  $\sim 80\%$  higher than those for microcrystalline shock-densified  $\text{Ti}_5\text{Si}_3$  alloy.

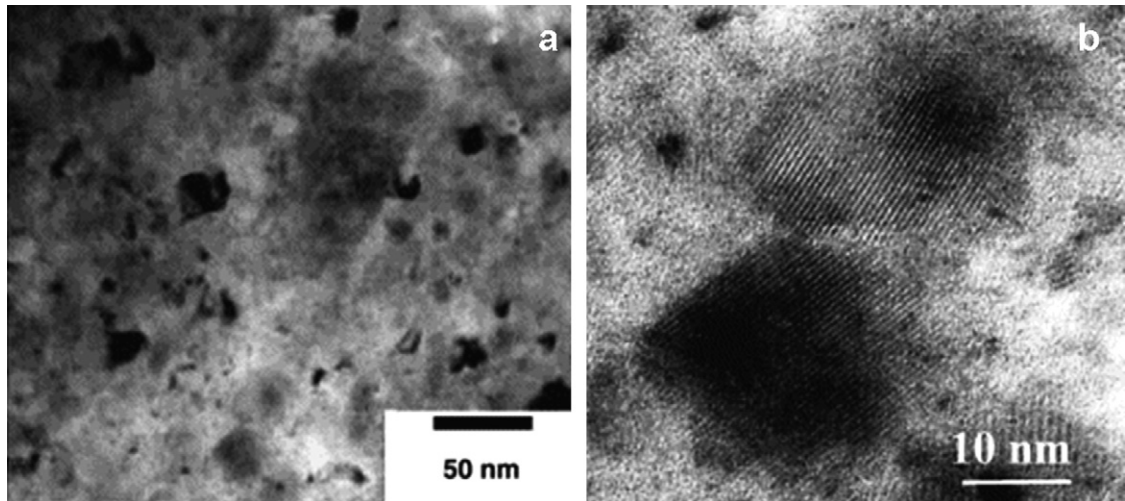


Fig. 17. (a) TEM bright field micrograph of recovered shock compressed specimen and (b) HRTEM micrograph of  $\text{Pr}_2\text{Fe}_{14}\text{B}$  grain morphology of recovered shock compacted specimens. (Reproduced from [83] with permission from Elsevier.)

Shock wave compaction is suitable for achieving high densification in very less time without appreciable grain growth. Most of the applications that require better magnetic properties and high hardness can utilize this processing technique with considerable ease. It has been found that high velocities of impact are quite favorable to breakdown coarse particles to nanosize range that even annealing does not coarsen the grain structure unlike other processing techniques. Lattice straining and plastic deformation are so high that the thermal energy is spent only on relieving the strains. The technique is not suitable for processing materials of pyrophoric nature. Skilled personnel are essential to operate these equipments.

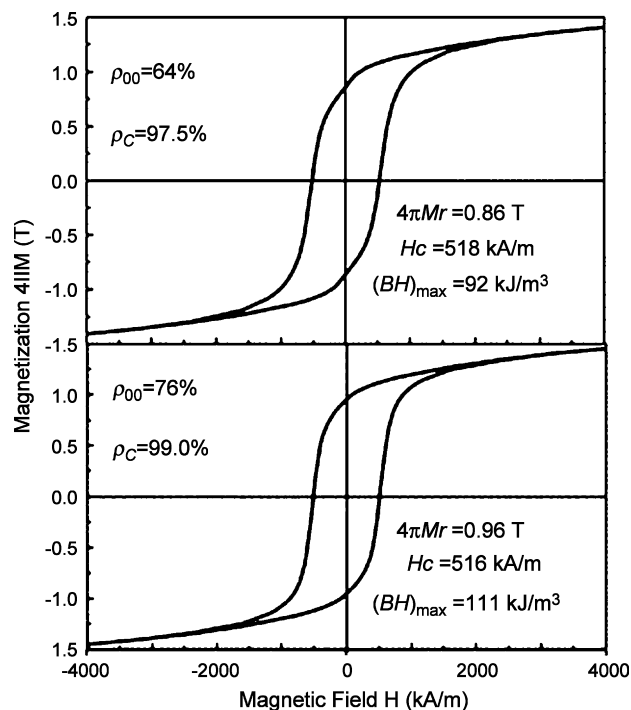


Fig. 18. Hysteresis behavior of  $\text{Pr}_2\text{Fe}_{14}\text{B}$ - $\alpha$ -Fe nanocomposites with different starting densities and different final densities. (Reproduced from [83] with permission from Elsevier.)

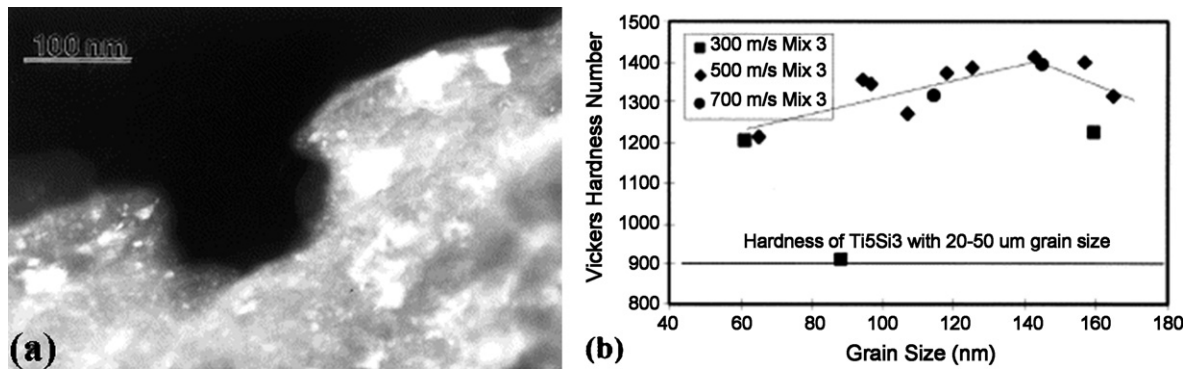


Fig. 19. (a) Dark field TEM micrograph showing presence of 10–40 nm crystallites ( $\text{Ti}_5\text{Si}_3$ ) in amorphous matrix and (b) Vickers hardness values of the composite as a function of grain size of the crystallite. (Reproduced from [84] with permission from Elsevier.)

## 2.5. Transformation assisted consolidation

### 2.5.1. Introduction

Pressureless sintering for consolidation of nanoparticles does not serve the purpose of nanostructure retention and the property amelioration associated. Experiments to consolidate such nanoscale powders especially at high temperatures [88–90] by conventional sintering were always thwarted by the abnormal grain growth due to the unusually high interfacial area between the grains. Sintering assisted with pressure in the range of  $\sim 1$ –8 GPa resulted in consolidation being achieved without appreciable grain growth and densification close to the theoretical density could also be achieved. Several factors have been ascribed to the retention of nanostructures during such processing. Phase transformation triggered by the application of temperature and pressure is one of the factors for such resistance to growth. Open pore structure [10] also is thought to be resisting grain growth by arresting the grain boundary migration. Driving forces in the form of temperature are used only to diffuse atoms in to the prevailing pores rather than the simple grain boundary migration. Transformation assisted consolidation is advantageous as it favors co-nucleation of two or more phases and limits their growth, thus creating a uniform nanocomposite structure.

### 2.5.2. Fundamental principles

Due to the presence of two degree of freedom, pressure, and temperature, there is a phase transformation associated with the volume reduction that is irreversible. High pressure reduces the nucleation activation energy thereby increasing the nucleation rate of the phases that is being transformed. Application of hydrostatic pressure also increases the nucleation rate. Similar to the realization of equiaxed fine grain structure during casting of metals near to the mold walls where nucleation rate is higher, presence of too many nuclei will have no room to grow further which will result in small grain size in the absence of phase transformation. Alumina and titania are classic examples which could retain the nanostructures as a result of phase transformation. More theory related to the transformation assisted consolidation could be found in reference [91].

### 2.5.3. Advantages

For allotropic materials, processing comes at no extra processing cost as application of small pressures and temperatures will help in retention of nanostructures. However, the method will not be suitable if the starting material is in the stable crystalline form.

### 2.5.4. Equipment—process and mechanism

Fig. 20 reveals the toroidal-type high pressure apparatus for carrying out transformation assisted consolidation experiments. The green compacted sample are wrapped up in an inert, high temperature resistant foil and then kept in a graphite crucible. The crucible is enclosed in a container with limestone or lava which serves as both insulator and the pressure transmitting medium. The reaction cell is then placed in between the anvils of high pressure apparatus and subjected to pressures of 1–8 GPa between 400 and 800 °C for about 30 min.

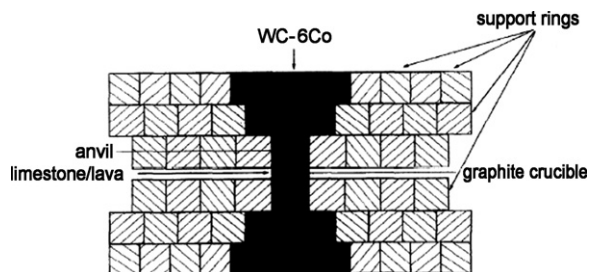


Fig. 20. Schematic of the toroidal type high pressure apparatus for transformation assisted consolidation. (Reproduced from [96] with permission from Elsevier.)

### 2.5.5. Nanoconsolidation

Typical materials systems that have been explored for consolidation using pressure assisted sintering are oxide ceramics ( $ZrO_2$  and  $Y_2O_3$ ), nitrides ( $Si_3N_4$  and  $AlN$ ), carbides ( $SiC$  and  $WC$ ) and nanocomposites ( $Al_2O_3-ZrO_2$ ,  $Al_2O_3-Si_3N_4$ ,  $Al_2O_3-SiC$ ) [92], nanocrystalline  $TiO_2$  [93–95], and nano-alumina [96].

**2.5.5.1. Nanocrystalline  $TiO_2$ .**  $TiO_2$  has two important phases that is stable at different temperature and pressure. Anatase transforms to rutile in the temperature regime between 400 and 1200 °C. If the transformation is carried out at atmospheric pressure, transformation temperature increases as a result of low nucleation rate of the new phase. On the other hand, higher the pressure, lower is the transformation start temperature. Table 2 [92] concisely gives the data that is being used to process the nano- $TiO_2$ . It has been found that chances of achieving 100% rutile is more when the pressure is 2.5 GPa and above. Nucleation rate of the rutile phase increases with an increase in pressure. This makes the bulk part denser due to the ability of the material to fill in the pores easily.

Field emission scanning electron microscope (FESEM) investigations revealed decrease in grain size with the increase in pressure. Fig. 21 shows the grain size between 33 and 25 nm at 2.5 and 4.5 GPa, respectively.

Another study [93] also confirmed that pressure assisted sintering (Fig. 22a) leads to a transformation assisted consolidation that could retain nanostructures with better wear properties [94]. Fig. 22b compares the wear properties of nano- $TiO_2$  with micron grain-sized  $TiO_2$  and showed that there is one-tenth reduction in the magnitude of the wear rate of nano- $TiO_2$  compared to the micron counterpart. This could be due to the nanostructure induced by phase transformation.

Phase transformation assisted consolidation could prove efficient and economical for allotropic materials. It does not require much hi-tech infrastructure to consolidate the nanomaterials. However, the process is not suitable for stable crystalline structures.

## 3. Thermo-mechanical processing

### 3.1. Hot pressing

#### 3.1.1. Introduction

Hot pressing is a process used to consolidate metal powder and ceramic compacts to full density with controlled microstructures. Hot pressing has evolved as an alternative route to sintering to achieve high densification. Si-Ge [97]

Table 2  
Effect of pressure on the sintering process and the grain size variation

Sample #	Pressure (GPa)	Temperature (°C)	Time (min)	Density ( $g\ cm^{-3}$ )	Density (percent of theoretical)	Grain size (nm)	Phase (s)
1	1.5	400	60	4.01	94.8	A = 59, R = 44	R + A (~5 wt.%)
2	2.5	400	60	4.07	95.8	33	R
3	4.5	400	60	4.10	96.5	25	R
4	5.5	400	60	4.11	96.4	R = 20, S = 33	R + S (~14 wt.%)
5	8	400	60	4.12	94.7	44	S

Reproduced from [92] with permission from Elsevier. R: rutile; A: anatase; S: srilankite.

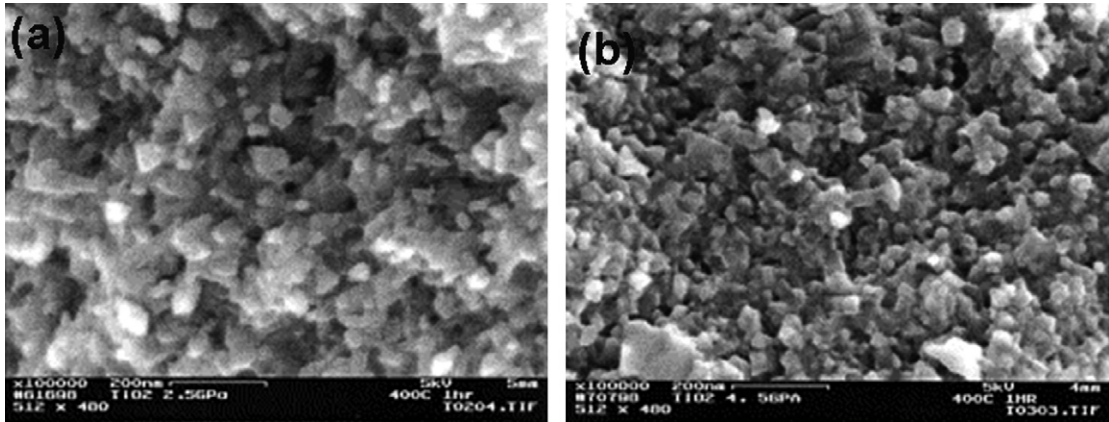


Fig. 21. FESEM micrographs of nano-TiO<sub>2</sub> sintered at: (a) 2.5 GPa and (b) 4.5 GPa. (Reprinted from [92] with permission from Elsevier.)

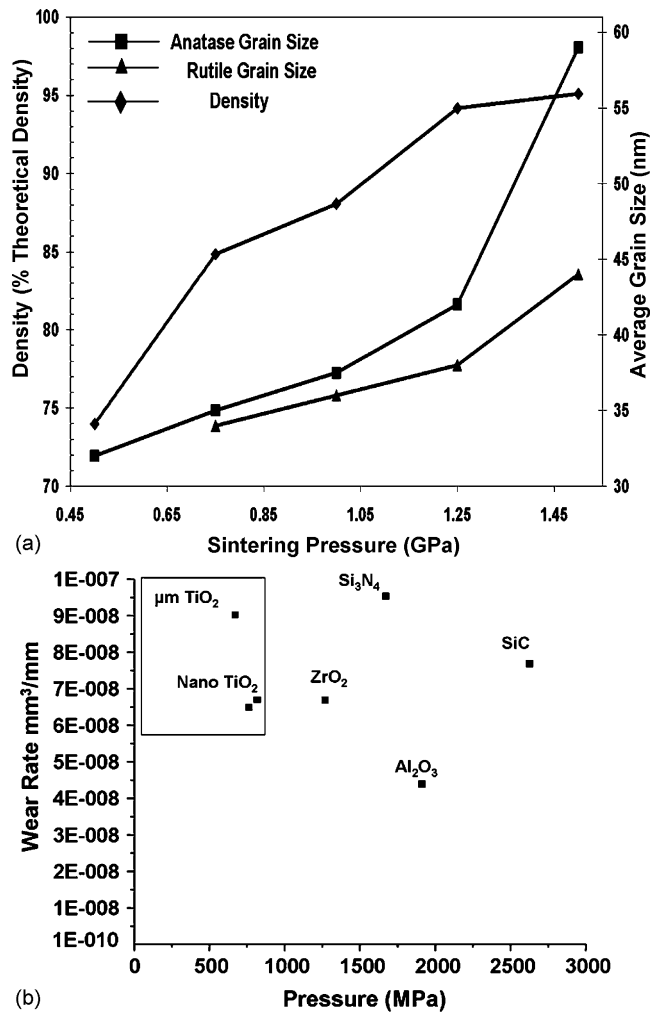


Fig. 22. (a) Densification as a function of sintering pressure in both anatase and rutile phases and (b) wear rate of nano-TiO<sub>2</sub> compared to micron TiO<sub>2</sub> and other ceramic systems. (Reprinted from [93,94], respectively, with permission from Elsevier.)

metal powders and SiC–Si<sub>3</sub>N<sub>4</sub> composites [98] have been consolidated for high strength. Inserts based on carbide and nitrides [99,100] have been processed using hot pressing as a result of the long life of the tool inserts.

### 3.1.2. Fundamental principles

In hot pressing, there are two degrees of freedom in terms of varying the temperature and pressure during processing. The process involves the simultaneous application of pressure and heat to a ‘green’ component. Pressure is applied statically or dynamically to the heated component in one or two opposing directions along a single axis as indicated in Fig. 23a. As an option, a vacuum or controlled atmosphere is required to prevent oxidation in case of metals or other sensitive materials. During hot pressing, a mold provides the component with the desired shape. Heat can be applied directly (induction or resistance heating) or indirectly (convection or radiation). Fig. 23b is an actual photograph of a laboratory at Fuji Denpa located at AIST, Japan.

### 3.1.3. Advantages

- Reduction in processing time of the nanoparticles as a result of the application of pressure.
- Reduction in temperature of processing as compared to sintering because of the enhanced kinetics associated with the densification.

### 3.1.4. Equipment—process and mechanism

Hot presses are designed for high temperature, high pressure consolidation of powder materials. Operating temperatures as high as 2250 °C and uniaxial loads up to 25 tonne, are available. Hot presses are capable of densifying all known ceramic materials. The vacuum furnaces are available with graphite, tungsten mesh, molybdenum mesh, or silicon carbide hot zones to meet specific process requirements. Atmospheres ranging from high vacuum to inert to reducing to oxidizing can be accommodated. The basic models of hot pressing systems include the vacuum furnace, press load frame with rams, manual power supply with water-cooled flexible power leads, and manually controlled hydraulic force system. High purity, high strength technical ceramics can be fabricated. A variety of accessories such as temperature sensors, automatic temperature control, automatic power control, etc., are available.

Resistance heating elements are positioned to allow adequate clearance between the die body and the element. The work zone may be used for pressureless sintering or heat treating applications with load train removed and insulation plugs and hearth plate installed. The standard graphite hot zone is constructed with thermally stable high temperature graphite insulation and machined graphite heating elements. Sufficient insulation and power is provided to attain 2250 °C in inert gas or vacuum. Sustained operation in high vacuum over 2000 °C is not recommended due to sublimation of graphite heating elements. Graphite hot zones are ideally suited for processing of carbides and other ceramics where carbon contamination is not a critical issue.

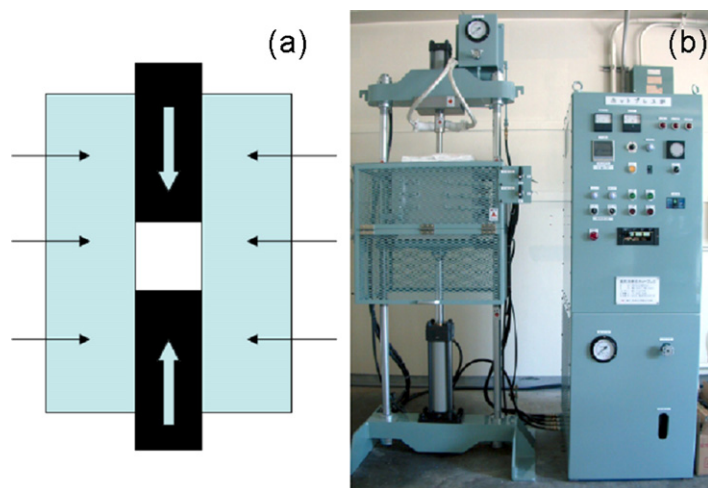


Fig. 23. (a) Schematic of a hot pressing setup and (b) hot pressing equipment with temperature and pressure controller. (Photo source: AIST, Japan.)

Refractory metal hot zones are recommended when high purity or low thermal mass is required. Tungsten or molybdenum mesh heating elements provide greater radiating surface area than rod heating elements, lowering element watt density and hence lowering element operating temperature. The lower element operating temperature for a given hot zone temperature assures less distortion, longer life, better uniformity, and greater reliability. When combined with tungsten or molybdenum radiation shielding, all-metal hot zones provide an ultraclean environment. The fully dense metal contains no porosity that could outgas contaminants, and the low thermal mass of the complete hot zone permits rapid heat up and cool down. Refractory metal hot zones are used for processing of silicon nitride and other technical ceramics when all contamination must be avoided. Refractory metal is also called for when a rapid process cycle is required to minimize time between the production runs or experimental procedures. When equipped with a suitable power supply, tungsten hot zones can be used to 2500 °C and molybdenum hot zones to 1700 °C in either high vacuum, inert, or hydrogen atmospheres.

For operation in air, oxidizing, or high purity inert gases to 1500 °C, a furnace utilizing silicon carbide heating elements and alumina/silica insulation is available. Typical applications include production of PZT and ferrite materials requiring accurate partial oxygen pressures to control stoichiometric composition. Full or partial pressure air atmospheres can be used for processing oxide ceramics and other compositions requiring a reactive oxidizing environment (1200–1350 °C).

### 3.1.5. Nanoconsolidation

Hot pressing technique has been considered only from the perspective of densification until the 1990s. One of the concerns during the consolidation of nanostructures has been the unrestricted grain coarsening with just temperature as a processing variable. Appropriate combination of pressure and temperature gave encouraging results in the retention of nanostructures. Hot pressing is material specific and does not work well for all material systems. Some of the systems that have been studied extensively so far are MgO [101], TiN–Si<sub>3</sub>N<sub>4</sub> [102], alumina–SiC [103–105], Ni–alumina [1,106], YSZ–SiC [107], Cu–Al<sub>2</sub>O<sub>3</sub> [108], Si<sub>3</sub>N<sub>4</sub>–SiC [109,110], Al<sub>2</sub>O<sub>3</sub>–ZrO<sub>2</sub>–SiC [111], Mo–Al<sub>2</sub>O<sub>3</sub> [112], YAG–Al<sub>2</sub>O<sub>3</sub> [113], Al–CuAl<sub>2</sub>–Al<sub>2</sub>O<sub>3</sub>–Al<sub>4</sub>C<sub>3</sub> [114], Ag–Ni [115], WC–Co [116], nano–micro Al<sub>2</sub>O<sub>3</sub> [117], Al–Ti [118], Si<sub>3</sub>N<sub>4</sub>–SiC–BN [119,120], Al<sub>2</sub>O<sub>3</sub>–BN [121], 3Y–ZrO<sub>2</sub>–BN [122], AlN–BN [123], Al<sub>2</sub>O<sub>3</sub>–Cr [124], TiN–Al<sub>2</sub>O<sub>3</sub> [125], Ni–Al–M [126], Al<sub>2</sub>O<sub>3</sub>–Co [127]. Before hot pressing, powder preparation is important for making nanostructured particles. Some of the known powder processing routes are ball milling, precipitation, calcination and pyrolysis. Predominantly, these methods are used either stand-alone or in combination in a particular sequence. Precipitation methods are usually followed by drying and calcination.

**3.1.5.1. Alumina–SiC nanocomposites.** These composites have been extensively studied [103–105] for hardness, strength and fracture toughness (mode I). SiC reinforced in alumina matrix was found to strengthen the grain boundaries due to compressive residual stresses, thus increasing the fracture toughness by a change in the fracture mode. SiC particle size has been varied [103] to control the microstructures and thereby controlling the properties. Four different nanocomposite materials, all containing 5 vol.% SiC with different average SiC particle sizes in alumina matrix were prepared. Polymer-derived SiC particles were found to exhibit uniquely small SiC particles with homogenous distribution compared to other sources. The SiC powder has been ball milled along with alumina powder and subsequently hot pressed with a graphite die at 1700 °C, 20 MPa for 1 h under Ar atmosphere. For monolithic alumina and UF 45 material, hot pressing temperature has been reduced to 1500 °C to keep the grain size similar to other nanocomposites. TEM micrographs from all the four nanocomposites have been presented in Fig. 24. When comparing the SiC particle size on all these micrographs, the differences in nanostructures are evident. It is believed that due to low sintering temperature for standard UF 45 material (Fig. 24C), the degree of coarsening of SiC particles seem to be less. A striking contrast in microstructure between monolithic alumina and all other nanocomposites was the presence of subgrain boundaries (small angle grain boundaries) which are absent in the monolithic alumina. The property variation as a result of this microstructure is being realized and the properties are presented in Table 3. Hardness measurement using Vickers indentation and fracture toughness using both Vickers and Hertzian indentation methods have been reported. Fracture strength is determined by four point bend testing. The strength of polymer-derived nanocomposite as well as the UF 15 material is higher than that of alumina to the tune of 50 and 40%, respectively. Sedimented and standard UF 45 nanocomposites showed a minor increase. Although, fracture toughness determined using Vickers indentation portrayed UF 15 nanocomposites to possess a higher value compared to other composites, a more accurate fracture toughness measurement has been obtained using Hertzian indentation. Hertzian

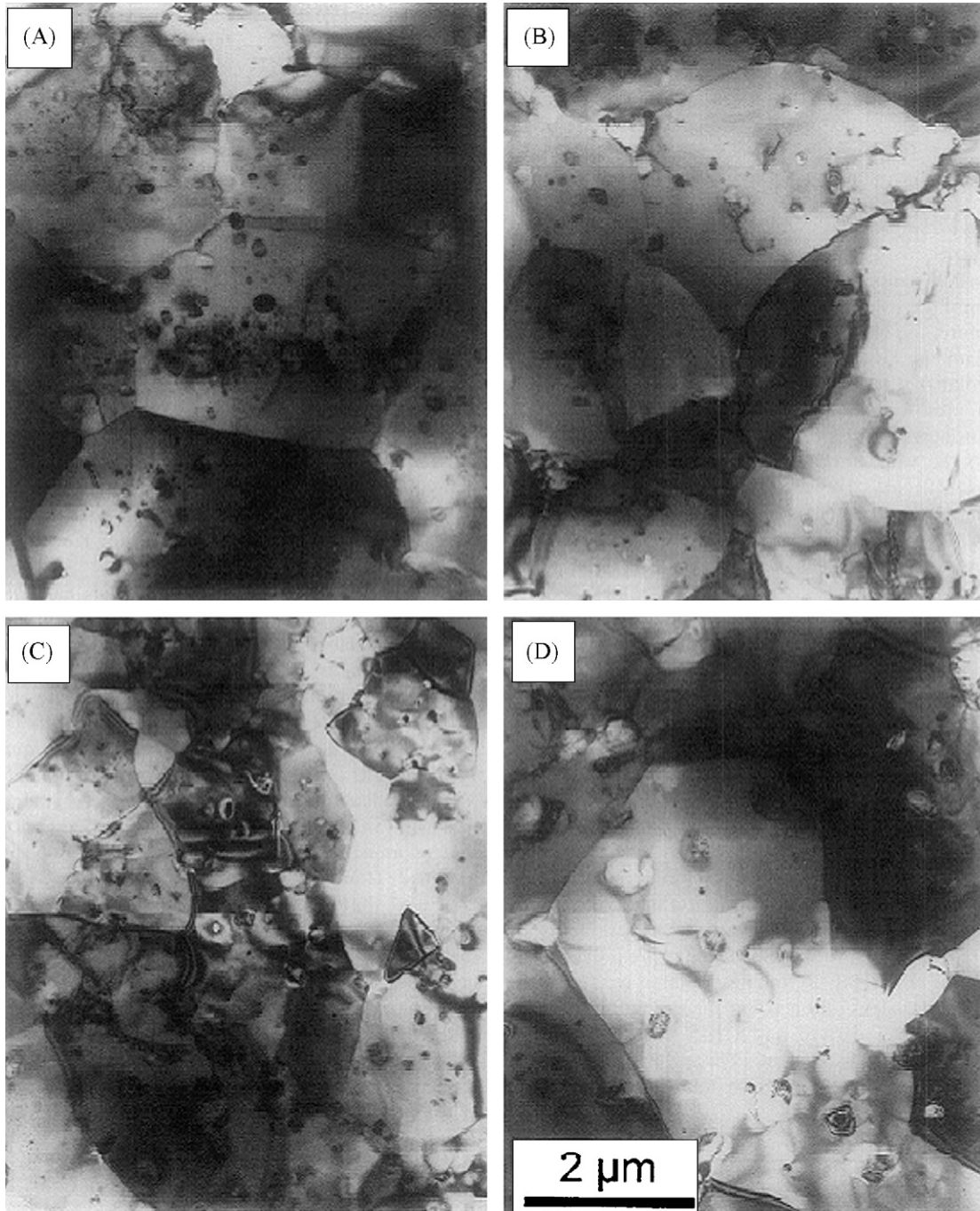


Fig. 24. TEM micrograph of  $\text{Al}_2\text{O}_3$ -SiC (5 vol.%) nanocomposites from various sources: (A) polymer-derived, (B) sedimented UF 45, (C) UF 45, and (D) UF 15. (Reprinted from [103] with permission from Elsevier.)

indentation uses cumulative fracture load distribution to get the fracture toughness. It has also been shown [104] that by varying the processing route, the predominant location of SiC particles in alumina matrix can be changed. Wang et al. [105] achieved a fracture toughness of  $4.7 \text{ MPa m}^{1/2}$  using Vickers indentation method for the same composition (5 vol.% SiC) used by Carroll et al. [103]. The microstructures shown in Fig. 25 confirmed the presence of nano-SiC particulates throughout the alumina matrix. Most of the SiC particles were distributed inside the alumina grains and therefore can be classified as intergranular nanocomposites.

Table 3  
Mechanical property data for Al<sub>2</sub>O<sub>3</sub>–SiC nanocomposites [103]

Material	Hardness (GPa)	Strength (MPa)	$K_{IC}$ (MPa m <sup>1/2</sup> )	
			Hertzian	Vickers
Alumina	17.5 (1.6)	491 (63)	3.53 (2)	3.25 (27)
Polymer (12 nm SiC)	17.8 (1.0)	738 (115)	4.32 (15)	3.02 (21)
Sedimented UF 45 (55 nm SiC)	18.3 (1.3)	549 (125)	4.00 (8)	2.76 (31)
UF 45 (90 nm SiC)	18.5 (1.8)	593 (95)	3.71 (5)	3.04 (39)
UF 15 (15 nm SiC)	18.8 (1.7)	689 (80)	3.63 (5)	3.47 (61)

Fracture toughness of alumina–5 vol.% SiC obtained by [105] using hot pressing is 4.7 MPa m<sup>1/2</sup> (obtained using Vickers indentation). Numbers in parentheses represent S.D.  $3.79 (2) = 3.79 \pm 0.02$ .

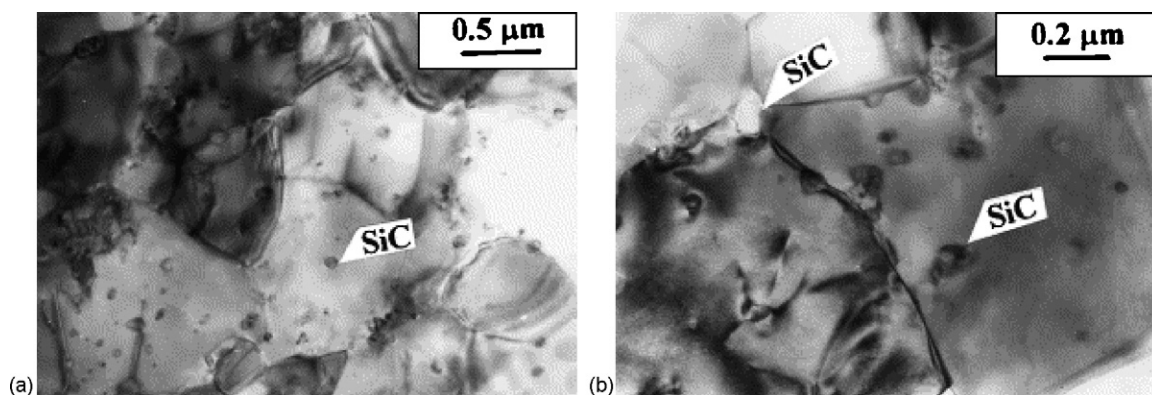


Fig. 25. TEM micrograph of Al<sub>2</sub>O<sub>3</sub>–5 vol.% SiC sample hot pressed at 1700 °C for 1 h depicting (a) the location of SiC particles in the alumina grains and (b) on the grain boundaries. (Reprinted from [105] with permission from Elsevier.)

**3.1.5.2. Ni–alumina.** Metallic particle reinforced alumina matrices has been found to possess certain mechanical and magnetic properties. Sekino et al. [1] fabricated bulk, dense Ni–Al<sub>2</sub>O<sub>3</sub> nanocomposites with improved fracture toughness, fracture strength and good magnetic properties. Calcined Ni–Al<sub>2</sub>O<sub>3</sub> powder mixture has been ball milled and hot pressed at 1450 °C for 1 h after hydrogen reduction at a pressure of 30 MPa. Magnetization studies on the nanocomposite system showed hysteresis behavior thereby clearly exhibiting ferromagnetism. The coercive force was 3.1 kA m<sup>-1</sup>, which is approximately two orders of magnitude larger than that of pure Ni metal. Coercive force is very sensitive to the particle size and the increase in coercive force will help in enhancing the behavior of Ni–Al<sub>2</sub>O<sub>3</sub> nanocomposite as hard magnets. Li et al. [106] processed Ni–Al<sub>2</sub>O<sub>3</sub> nanocomposites through an unique coating technique followed by hot pressing at 1400 °C. Mechanical properties of Ni–Al<sub>2</sub>O<sub>3</sub> nanocomposites have been presented in Table 4. Fig. 26 shows the TEM picture of Ni–Al<sub>2</sub>O<sub>3</sub> where most of the Ni particles are present at the grain boundaries.

**3.1.5.3. Yttria-stabilized zirconia.** Yttria-stabilized zirconia (YSZ) is a well-known solid electrolyte that has high oxygen ionic conductivity over a wide range of temperatures and oxygen partial pressures. In an effort to strengthen zirconia, Bamba et al. [107] dispersed nanosized SiC particulates in 8YSZ matrix and studied the mechanical properties. Fig. 27a presents the TEM micrograph of 5 vol.% SiC dispersed in 8YSZ matrix. The variation in fracture

Table 4  
Fracture strength and fracture toughness values for Ni–alumina nanocomposite

Composition	Fracture strength (MPa)	Fracture toughness (MPa m <sup>1/2</sup> )
Ni–4 vol.% [106]	502 ± 10	3.92 ± 0.1
Ni–5 vol.% [1]	1090	3.5

Reproduced from [1,106] with permission from Elsevier.

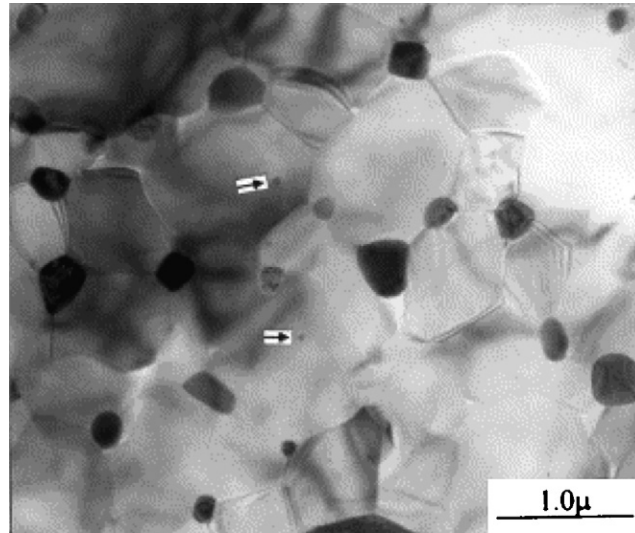


Fig. 26. Alumina-4 vol.% Ni nanocomposite imaged under TEM [106]. (Reprinted from [106] with permission from Elsevier.)

strength for different compositions has been explained in Fig. 27b based on the grain size variation. Even though 20 vol.% SiC has been processed at a higher temperature (1700–1900 °C) abnormal grain growth did not occur and the mean grain size was 1 μm while for 5 vol.% SiC sample, the average grain size was 2 μm. For monolithic alumina sample, the grain size after processing was ~23 μm. Thus, the fracture strength of 20 vol.% SiC nanocomposites has

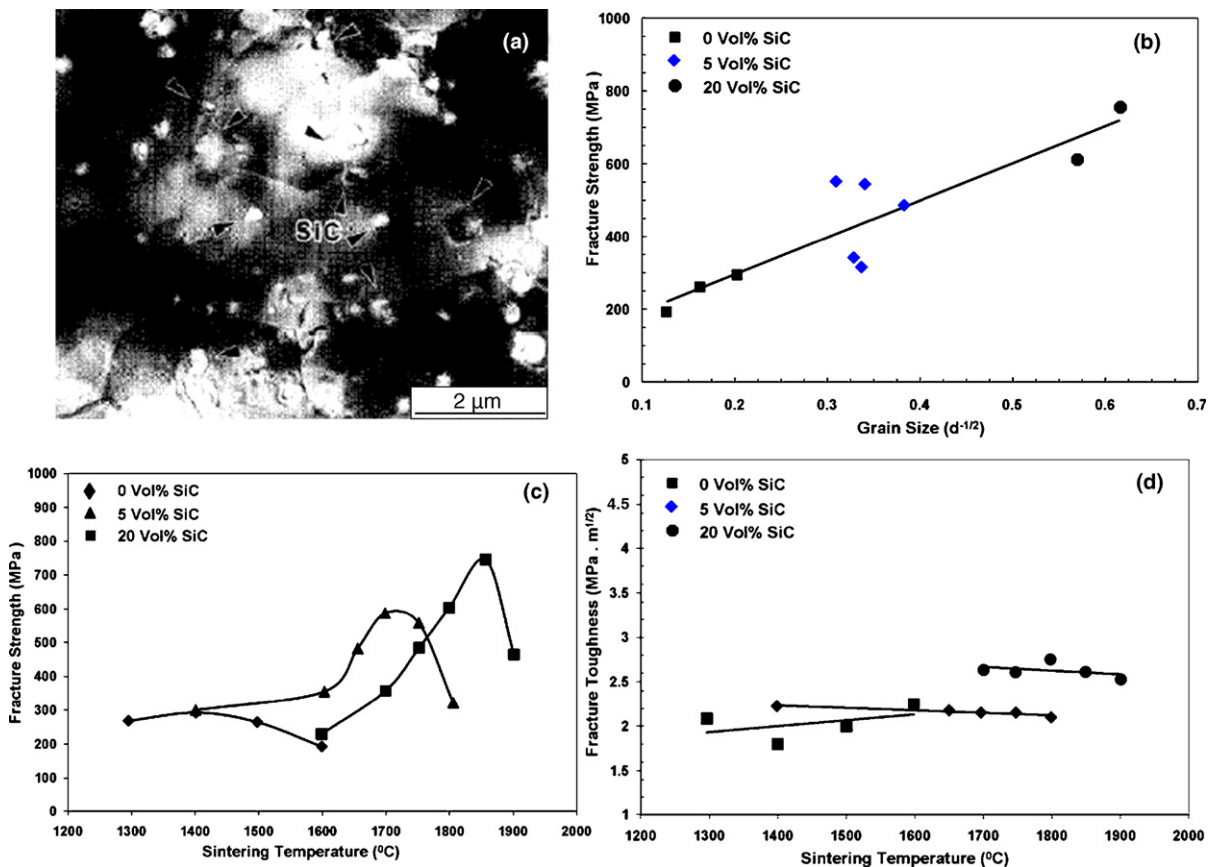


Fig. 27. Microstructure and mechanical properties of YSZ-SiC nanocomposites. (Reprinted from [107] with permission from Elsevier.)

been higher than any of the other composition as shown in Fig. 27b. Fig. 27c reveals the fracture strength as a function of sintering temperature which in turn affects the grain size. Due to the grain size variation, fracture toughness of 20 vol.% SiC nanocomposites is higher than that of the compositional variants (Fig. 27d).

**3.1.5.4. Cu–alumina.** Cu–alumina is another metal reinforced ceramic matrix nanocomposite of general interest [108]. The starting powders were micron-sized  $\alpha$ -alumina and CuO. Ball milled powders were hot pressed in a rectangular graphite die and heated in the flowing  $H_2$  gas to a temperature of 350 °C. Both fracture toughness and fracture strength showed improvement compared to the monolithic alumina. Fig. 28 presents the mechanical property data. As the Cu content increases, the strength of the nanocomposite increased due to the reduction in the average grain size of the matrix after processing. A 2.5 vol.% Cu nanocomposite had an average grain size of 0.68  $\mu\text{m}$  (680 nm) compared to a 10 vol.% Cu nanocomposite, the growth restriction being made possible by fine Cu dispersion. Crack deflection around coalesced Cu particles has been attributed to the high fracture toughness values.

**3.1.5.5. SiC– $\text{Si}_3\text{N}_4$  nanocomposite.**  $\text{Si}_3\text{N}_4$  is an ideal material for heat engine components because of its excellent mechanical properties. But due to the covalent bonding between the Si–N,  $\text{Si}_3\text{N}_4$  is difficult to densify without sintering additives such as  $\text{Al}_2\text{O}_3$ ,  $\text{Y}_2\text{O}_3$ , MgO. However, such additives remain as a glassy phase in grain boundaries of  $\text{Si}_3\text{N}_4$  which reduce the high temperature strength above 1200 °C. SiC is added as reinforcement in  $\text{Si}_3\text{N}_4$  matrix [109,110] for improvement of high temperature strength. SiC (20 vol.%) has been reinforced with  $\text{Si}_3\text{N}_4$  with different additives 2 wt.% alumina, 8 wt.%  $\text{Y}_2\text{O}_3$ , and 4 wt.%  $\text{Y}_2\text{O}_3$  and called as ST–AY, ST–8Y, ST–4Y have been tested for fracture strength from room temperatures till 1400 °C. The fracture strength results are presented in Fig. 29a. Among all the samples, the sample with alumina additive (ST–AY) showed high fracture strength up to 1000 °C and later plummeted with increasing temperatures. However, the ST–4Y sample showed fracture strength almost constant from room temperature to 1400 °C. Based on the operating temperatures of the actual application, a suitable additive combination can be selected. TEM micrograph of ST–4Y sample is shown in Fig. 29b wherein the SiC particulates seem to be present both at the grain boundaries as well as inside the matrix. Such high fracture strength is attributed to the good lattice matching between the SiC and the  $\text{Si}_3\text{N}_4$  interfaces as revealed in Fig. 29c.

**3.1.5.6. Toughened alumina.** Alumina being used in structural applications generally lacks in mechanical properties for which reinforcements such as SiC particulates are quite useful for strength enhancement. However, the fracture toughness of zirconia toughened alumina ceramic has been found to be much better than that of pure alumina. Such ZTA ceramics has been reinforced with SiC [111]. Alumina–15 wt.%  $\text{ZrO}_2$ –5 wt.% SiC has been processed using precipitation–calcination–hot pressing route. Hot pressing has been performed between 1650 and 1700 °C. SiC particulates have been found to be reinforced along with  $\text{ZrO}_2$  on the elongated alumina grains (Fig. 30). Table 5 presents the mechanical properties, bending strength, fracture toughness, and hardness. The sample processed at 1650 °C exhibits low strength compared to that processed at 1550 °C. Such higher strength may be explained based on the smaller grain size in the matrix.

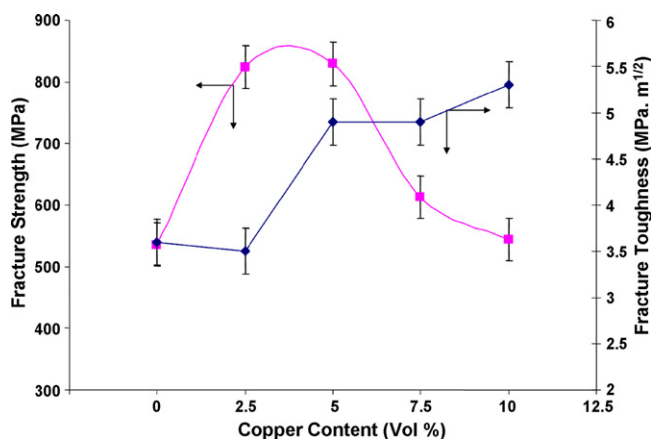


Fig. 28. Fracture toughness and fracture strength of Cu–alumina as a function of copper content [108].

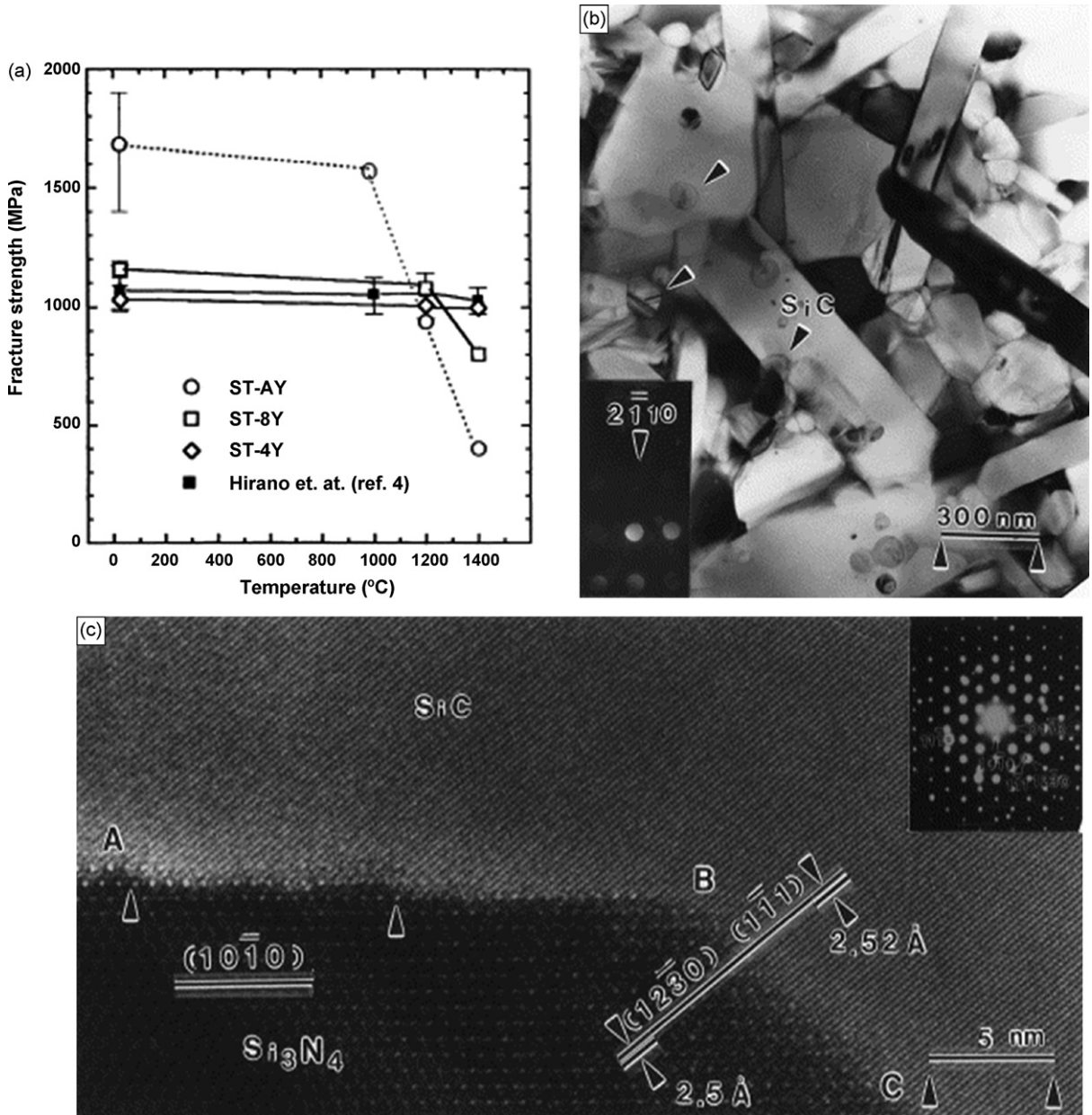


Fig. 29. Fracture strength of the ST-4Y nanocomposites are higher at high temperatures and good lattice matching is explained as a reason. (Reprinted from [109] with permission from Elsevier.)

**3.1.5.7. Transition metal reinforcements.** Transition metals such as Ni, Cr, Mo reinforced in ceramic matrix have been found to possess high fracture toughness and hardness. One such nanocomposite system that has been processed by Lin et al. [112] is the reinforcement of Mo in  $\text{Al}_2\text{O}_3$ . The nanocomposite is fabricated by metal–organic chemical vapor deposition (MOCVD) followed by hot pressing at  $1400 \text{ }^\circ\text{C}$  for 1 h in vacuum. The wear rate of this nanocomposite is compared (Table 6) to that of the sample processed using pressureless sintering (MA3-1 and MA3-2), along with pure alumina (Al6-SG) sample. The wear resistance of MA3-2HP is superior to pure  $\text{Al}_2\text{O}_3$ .

**3.1.5.8. YAG– $\text{Al}_2\text{O}_3$ .** Yttrium aluminum garnet [113] (YAG)– $\text{Al}_2\text{O}_3$  was investigated for strength characteristics at room temperature using a coprecipitation–hot pressing route. Hot pressing has been performed at  $1400 \text{ }^\circ\text{C}$  for 1 h at a pressure of 30 MPa. Microstructural evaluation using TEM (Fig. 31) showed that intergranular YAG grains of

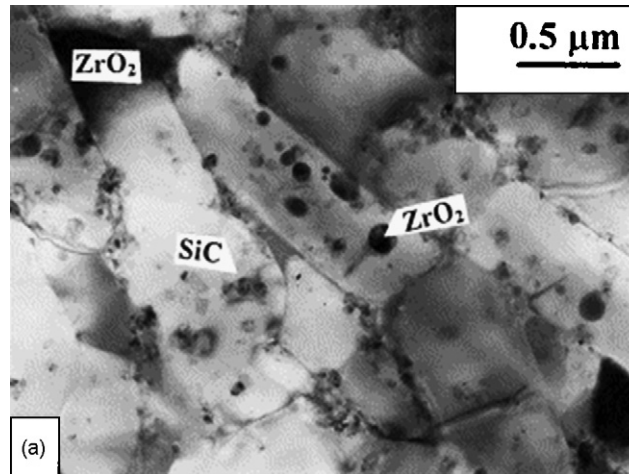


Fig. 30. TEM micrograph of  $\text{Al}_2\text{O}_3\text{-ZrO}_2\text{-SiC}$  nanocomposites. (Reprinted from [111] with permission from Elsevier.)

Table 5  
Mechanical properties of 80 wt.%  $\text{Al}_2\text{O}_3\text{-15 wt.% ZrO}_2\text{-5 wt.% SiC}$  nanocomposites

Sample	Bending strength (MPa)	Fracture toughness ( $\text{MPa m}^{1/2}$ )	Hardness (GPa)
Sample sintered at 1550 °C	555	3.4	16.9
Sample sintered at 1650 °C	448	3.8	16.8

Reproduced from [111] with permission from Elsevier.

micrometer size ( $\sim 800$  nm) were dispersed at the grain boundaries of a dense alumina matrix and mostly fine-grained YAG grains of nanometric size ( $\sim 100$  nm) were entrapped within the alumina grains in the composite. The mechanical properties achieved through such processing route are listed in Table 7. It is being proposed that the improvement of mechanical properties of hot pressed nanocomposites has been due to the grain size reduction of the matrix and the improved strength of the grain boundaries in 25 vol.% YAG- $\text{Al}_2\text{O}_3$  nanocomposite.

**3.1.5.9. Ceramic particulates in aluminum matrix.** Particles reinforced aluminum matrix composites exhibit high specific elastic modulus, high specific strength, good wear resistance, and excellent properties at elevated temperatures over conventional aluminum alloys. As a major step towards cutting costs and to attain ameliorated properties, oxides such as CuO,  $\text{TiO}_2$  has been used to react in situ with Al matrix to obtain particle reinforcements, which yields a cleaner interface and thereby stronger binding strength with the Al matrix. One such example [114] is nanocomposite obtained naturally by mechanically driven reduction reaction of CuO and Al powder mixture consolidated using hot pressing at 540 °C at a pressure of 800 MPa for 2 h. After processing, a nearly full density nanostructured aluminum matrix composite reinforced with  $\text{CuAl}_2$  (100–500 nm in size) and  $\text{Al}_2\text{O}_3$ ,  $\text{Al}_4\text{C}_3$  (10–50 nm in size) is obtained. Stress strain plots of the nanocomposite tested under compression were shown in Fig. 32. Fig. 32a reveals the stress strain curves at different temperatures wherein at high temperatures, a nearly steady state flow stress was reached over the strain range of 0.025–0.1. The steady state flow stress at the strain of 0.20 as a function of test temperature is revealed

Table 6  
The fabrication conditions, wear test parameters, and wear rate of Mo/ $\text{Al}_2\text{O}_3$  composites and pure  $\text{Al}_2\text{O}_3$

Sample	Deposition conditions	Sintering conditions	Bulk density ( $\text{g cm}^{-3}$ )	Wear rate ( $\text{mm}^3 \text{N}^{-1} \text{m}^{-1}$ )
Al6-SG	1 h at 325 °C	1600 °C/1 h	3.92	$5.47 \times 10^{-4}$
MA3-1	1 h at 325 °C	1600 °C/1 h	3.59	$2.66 \times 10^{-4}$
MA3-2	2 h at 325 °C	1600 °C/1 h	3.31	$2.52 \times 10^{-4}$
MA3-1	2 h at 325 °C	1400 °C/1 h + HP	3.92	$5.47 \times 10^{-4}$

Reproduced from [112] with permission from Elsevier.

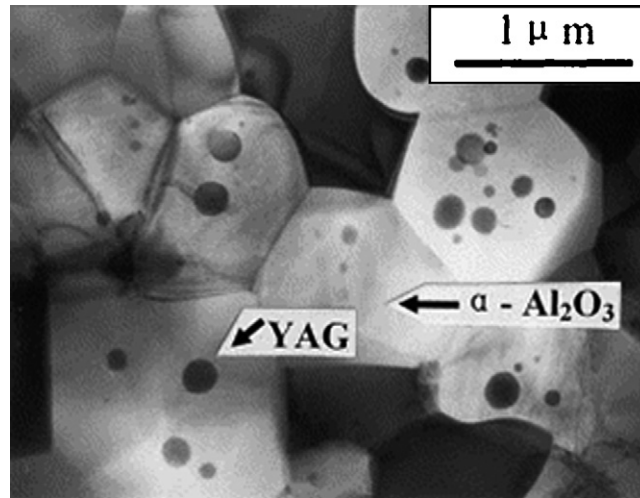


Fig. 31. TEM micrograph of 25 vol.% YAG–alumina nanocomposite. (Reprinted from [113] with permission from Elsevier.)

Table 7

Mechanical properties of 25 vol.% YAG–Al<sub>2</sub>O<sub>3</sub> nanocomposites compared with other systems

Composition	Sintering temperature (°C)	Vickers hardness	Fracture strength (MPa)	Fracture toughness (MPa m <sup>1/2</sup> )
Monolithic Al <sub>2</sub> O <sub>3</sub>	1500	14.26	392	3.62
25 vol.% YAG Al <sub>2</sub> O <sub>3</sub>	1400	16.25	611.6	4.54
Eutectic	–	–	373	4.3
Monolithic YAG	1600	–	190	2.2

Reproduced from [113] with permission from Elsevier.

in Fig. 32b. It can be seen that the flow stress of the composites decreases with increasing temperatures. However, the strength of the nanostructured Al–5CuO composite is much higher than that of the Al–Ti alloys [128,129] at the same test temperatures. Fine crystallinity of the Al matrix and fine dispersoids is attributed to this property enhancement.

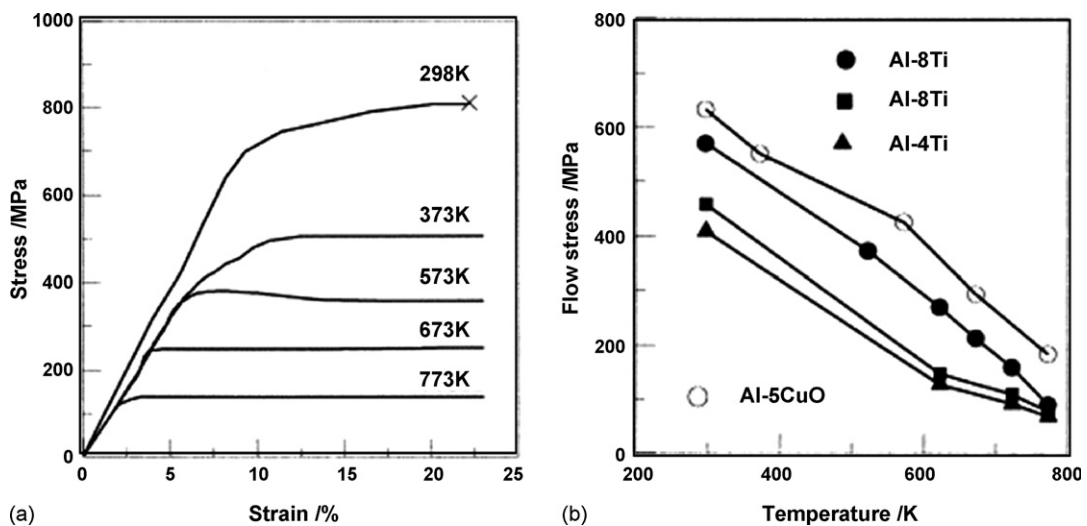


Fig. 32. (a) Stress vs. strain behavior of the nanocomposite at various temperatures and (b) flow stress vs. temperature of the Al–5CuO nanocomposite compared with other materials. (Reprinted from [114] with permission from Elsevier.)

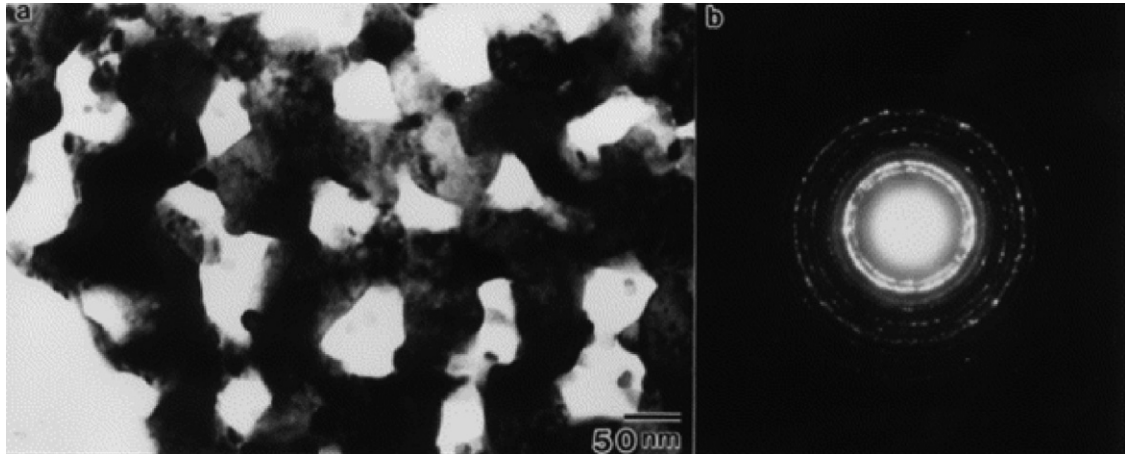


Fig. 33. TEM micrograph of as hot pressed WC–14 wt.% Co at 1973 K with a pressure of 1 GPa. (Reprinted from [116] with permission from Elsevier.)

**3.1.5.10. WC–Co nanocomposites.** WC–Co nanocomposites [116] have been made using ball milling–vacuum hot pressing technique to attain a high fracture toughness component. Hot pressing is performed at a pressure of 1.5 GPa at 1973 K for 43 ks without the addition of any binding materials. Fig. 33 shows the TEM micrograph of the WC–14 wt.% Co nanocomposite hot pressed at 1973 K. The micrograph reveals a homogenous distribution of the nanograins of WC. It can be seen that a density of the bulk material is considerably higher. The SADP revealed that the consolidated powders contain hcp-WC and hcp-Co with no other phases. Also, the ring pattern reveals the retention of nanostructures. The fracture toughness (Fig. 34) as a function of Co content is increased. The increased fracture toughness is due to the crack bridging capability of Co nanoparticulates. The increase in Poisson’s ratio as a function of Co content indicates the improvement in the isotropic nature of the bulk nanocomposite.

**3.1.5.11. Nanocrystalline Al–Ti.** The consolidation of Al–5 at.% Ti powders using an ultra high pressure hot pressing method has been carried out by Moon et al. [118]. Hot pressing was done for 250 s at 120 °C under 4.8 GPa and the grain size was less than 50 nm. Random orientation assured that the properties are uniform throughout the sample. Hot pressing parameters, viz. pressure, temperature, time has been varied and the result revealed that higher processing temperatures coarsened the grain size which reflected in the reduction in hardness (HV and HR<sub>B</sub>). The results are shown in Table 8 and the processing parameters are optimized to achieve the desired mechanical properties.

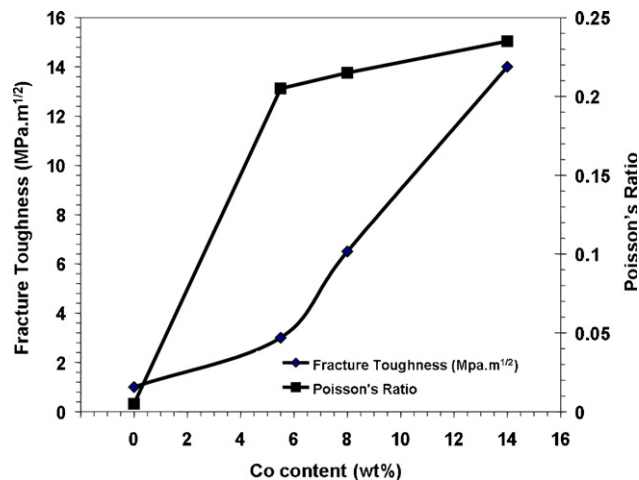


Fig. 34. Mechanical properties of WC–Co nanocomposite with Co content (wt.%).

Table 8  
Hardness and grain size of Al–Ti alloys for different hot pressing pressure, temperature, and time

Specimen	Hot pressing conditions			Grain size (TEM and FESEM) (nm)	HV	HR	Abnormal grain growth
	Pressure (GPa)	Temperature (°C)	Time (s)				
1	4.5	240	50	90	176.7	91.7	N
2	4.8	300	50	90/300	156.3	83.8	Y
3	4.8	240	250	120	166	87.3	N
4	4.8	300	250	150/300	144.3	74.2	Y
5	4.8	360	250	150/500	140.5	70.5	Y
6	4.8	120	250	50	243.7	105.5	N
7	5.3	240	250	140	149.3	85.1	N
8	5.3	360	250	160/600	124	66.8	Y

Reprinted from [118] with permission from Elsevier.

**3.1.5.12. Machinable ceramics.** From the point of view of machinability, hot pressing has been found to be a promising consolidation technique for processing Al<sub>2</sub>O<sub>3</sub>–BN nanocomposite ceramics with nanosized BN dispersions ranging from 0 to 30 vol.%. BN content more than 20 vol.% exhibited excellent machinability, which could be drilled using conventional hard metal alloy drills (Fig. 35a). SEM picture (Fig. 35b) of the polished and etched surface of the hot pressed body revealed BN grains of 100–200 nm in diameter. Also, club-shaped BN grains 400–600 nm in length, 100–200 nm in width are present at the grain boundaries for pinning action. Fracture toughness of the nanocomposite showed an increasing trend with increase in BN content as indicated in Fig. 35c. Another nanocomposite system fabricated using hot pressing route is 3Y–ZrO<sub>2</sub>–BN [122] in which BN dispersoids range in composition from 0 to 30 vol.%. The starting materials were prepared by an in situ reaction between boric acid and urea on the surface of 3Y–ZrO<sub>2</sub> particles in nitrogen gas. Hot pressing has been carried out at 1400–1500 °C in nitrogen, holding for 1 h under 30 MPa pressure. The bending strength and the fracture toughness as a function of BN content has been determined using three point bend test and Vickers indentation, respectively. Fig. 36 reveals the mechanical property data of these nanocomposites. It is to be noted that, although both the bending strength and the fracture toughness shows a decreasing trend with increasing BN content, the properties are much better compared to the micron-sized counterpart. Also, comparing the fracture toughness of Al<sub>2</sub>O<sub>3</sub>–BN and 3Y–ZrO<sub>2</sub>–BN, the fracture toughness of the latter is much higher (~8 MPa m<sup>1/2</sup>) than the former (5.5 MPa m<sup>1/2</sup>).

**3.1.5.13. Metallic reinforcements in alumina.** Reinforcement of metallic second phase in alumina matrices seems to improve the fracture toughness. Ji et al. [124] reinforced Cr (5 vol.%) in alumina matrix and consolidated using hot pressing at 1000 °C at a pressure of 35 MPa. The properties such as fracture toughness, strength and hardness have been compared for these nanocomposites with pure Al<sub>2</sub>O<sub>3</sub> hot pressed at 1400 °C (Table 9). It is to be noted that processing condition for A, B, and C are different with A being consolidated at a lower temperature compared to C with B in between. Due to the lower temperature processing of sample A (1450 °C), the strength, hardness, and fracture toughness values are much higher than that of B (1450 °C) and C (1450 °C). This can be explained based on the grain coarsening at higher processing temperatures and subsequent property degradation.

**3.1.5.14. TiN–Al<sub>2</sub>O<sub>3</sub>.** TiN–Al<sub>2</sub>O<sub>3</sub> nanocomposites have been known to exhibit electroconductivity along with good fracture toughness and bending strength [125]. TiN (5–25 vol.%) have been reinforced with Al<sub>2</sub>O<sub>3</sub> and hot pressed between 1400 and 1650 °C at a pressure of 30 MPa for 1 h. The mechanical properties and electrical resistivity as a function of TiN content is presented in Fig. 37. The electrical resistivity values have been found to decrease with increase in TiN content and uniform distribution of nano-TiN particulates. Presence of nanoparticulates has been suggested as a key reason to improved electroconductivity in a less conductive alumina matrix. As expected, the bending strength and the fracture toughness values also found to be increasing with increase in the TiN content.

**3.1.5.15. Magnetic nanocomposites.** Hot pressing has also been used to consolidate magnetic nanocomposites [127,128]. Al<sub>2</sub>O<sub>3</sub>–Co nanocomposite has been synthesized by dispersion of Co particles in Al<sub>2</sub>O<sub>3</sub> matrix by vacuum hot pressing technique. The effects of Co particulates incorporated in the alumina matrix on the magnetic properties were investigated. Fig. 38a presents a TEM picture of Al<sub>2</sub>O<sub>3</sub>–10 wt.% Co nanocomposites in which Co particulates

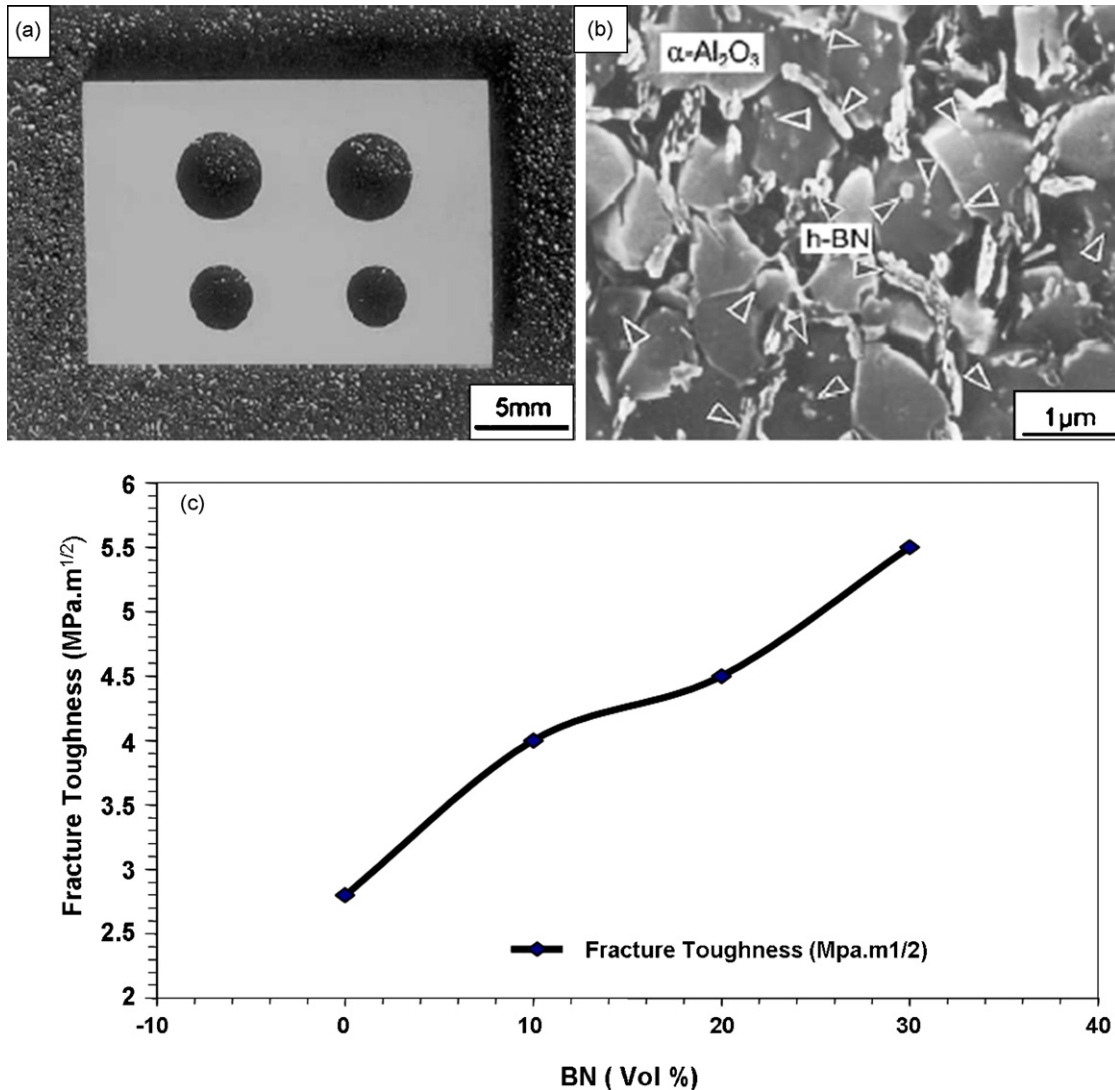


Fig. 35. (a) Manifestation of machinability of the  $\text{Al}_2\text{O}_3$ -BN nanocomposite material. (b) SEM micrograph confirming the presence of 400–600 nm BN grains. (c) Mechanical properties of WC-Co nanocomposite with Co content (wt.%). (Figures reprinted from [121] with permission from Elsevier.)

(50–150 nm) seem to be uniformly distributed all over alumina matrix mostly along the grain boundaries. Fig. 38b indicates how Co content can vary the magnetic property such as coercivity ( $H_c$ ), magnetization (both saturation and remnant). The saturation magnetization is the magnetization required to align all the magnetic domains in a particular direction seems to be increasing with increase in cobalt content. It is to be noted that nanosized Co particulates makes it a lot difficult to align these domains. Similarly, remnant magnetization increases with Co content. Such a behavior will lead to the formation of hard magnets. Thus composition can be varied at will to choose between hard and soft magnets. Coercive force depends strongly on the grain size, residual stress, and dislocation density. When the particle size of the magnetic materials decreases, the magnetic structure varies from a multi-domain to a single domain state to reduce the total energy of the system thus leading to high  $H_c$ . Fig. 39 is a testimony of the fact that how Co content can manipulate the area of the hysteresis loop thereby varying the magnetic properties.

Hot pressing technique utilizes pressure to expedite the densification of nanocomposites before appreciable grain growth occurs. Unlike hot isostatic pressing which will be discussed next, the process leaves the material with an anisotropic condition which further needs some sort of heat treatment to induce uniform mechanical properties in all directions. This may lead to grain growth.

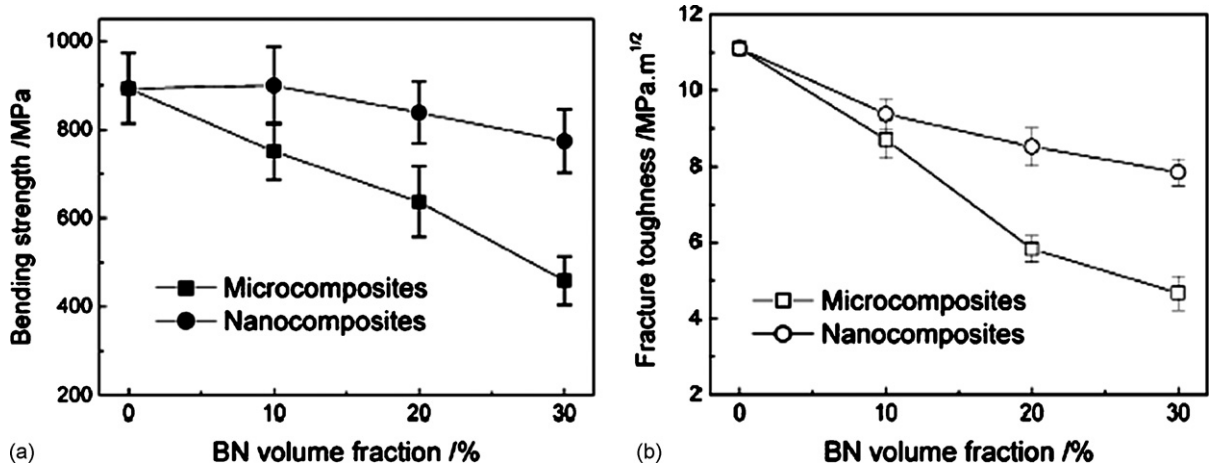


Fig. 36. Effect of BN content on: (a) bending strength and (b) fracture toughness of the 3Y-ZrO<sub>2</sub> nanocomposite. (Reprinted from [122] with permission from Elsevier.)

Table 9

Mechanical properties of Al<sub>2</sub>O<sub>3</sub>-Cr nanocomposites for different processing conditions

Processing condition	Specimen	Indentation toughness (MPa m <sup>1/2</sup> )	Hardness (MPa)	Strength (MPa)
Hot pressed 1400 °C	Alumina	3.6 ± 0.2	17.2 ± 0.4	474 ± 12
Nano, A	Alumina-Cr	4.0 ± 0.2	17.9 ± 0.5	736 ± 29
Nano, B	Alumina-Cr	3.8 ± 0.2	17.7 ± 0.4	640 ± 20
Nano, C	Alumina-Cr	3.8 ± 0.2	16.8 ± 0.5	540 ± 44

Reprinted from [124] with permission from Elsevier.

### 3.2. Hot isostatic pressing

#### 3.2.1. Introduction

The process of using high hydrostatic pressure and high temperature to compress fine particles into coherent parts is termed as ‘hot isostatic pressing’. The mention of the term hydrostatic pressure is crucial which if not indicated will be considered as hot pressing. In this process, if just hydrostatic pressure is used and no heating is done, then the process is called ‘cold isostatic pressing’ (CIP). In 1976, Howmet Corporation became the first company to offer hot isostatic

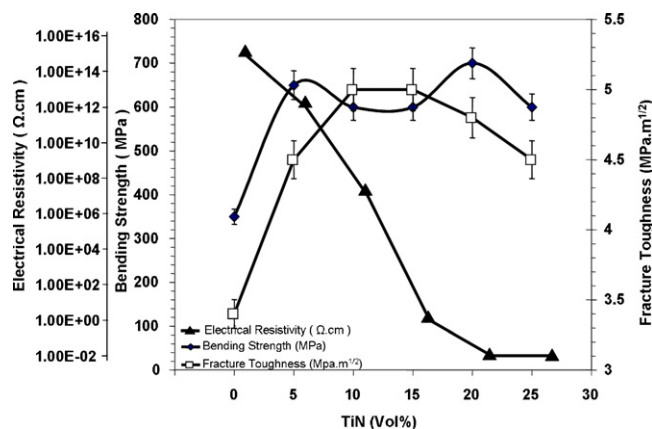


Fig. 37. Fracture toughness, bending strength, and resistivity of the nanocomposite as a function of the TiN content. (Reprinted from [125] with permission from Elsevier.)

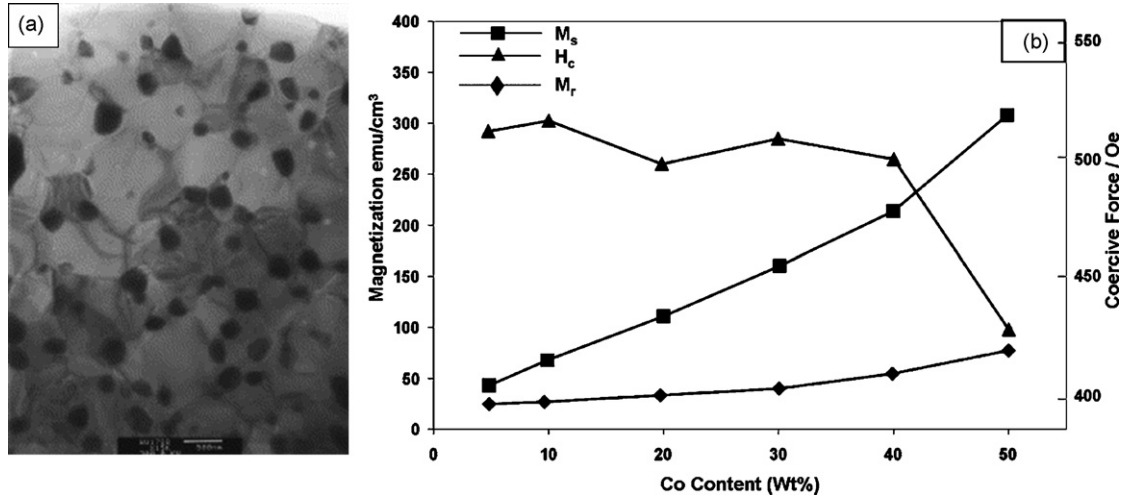


Fig. 38. (a) TEM micrograph of Al<sub>2</sub>O<sub>3</sub>-10 wt.% Co nanocomposite with Co nanoparticles dispersed on the alumina matrix. (b) Magnetic properties achieved with different Co content. (Reprinted from [127] with permission from Elsevier.)

pressing (HIP) services to the aerospace industry. The HIP process, which subjects a component to elevated temperatures and pressures to eliminate internal microshrinkage, helped engineers respond to the aerospace industry’s increasingly stringent regulations. HIP enabled engineers to design components so they could meet specifications for use in critical, highly stressed applications.

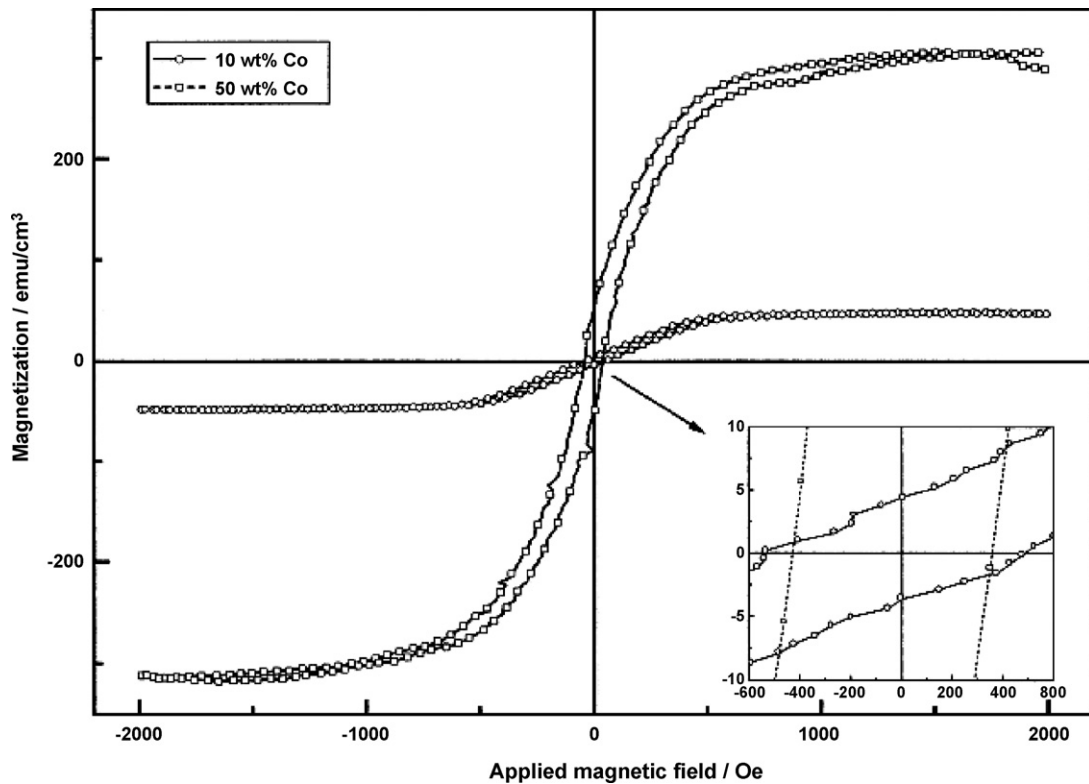


Fig. 39. Hysteresis loops for the Al<sub>2</sub>O<sub>3</sub>-10 wt.% Co and Al<sub>2</sub>O<sub>3</sub>-50 wt.% Co nanocomposites. (Reprinted from [127] with permission from Elsevier.)

### 3.2.2. Fundamental principles

The HIP process provides a method for producing components from diverse powdered materials, including metals and ceramics. During the manufacturing process, a powder mixture of several elements is placed in a container, typically steel can. The container is subjected to elevated temperature and a very high vacuum to remove air and moisture from the powder. The container is then sealed and HIPed. The application of high inert gas pressures and elevated temperatures results in the removal of internal voids and creates a strong bond throughout the material. The result is a clean homogeneous material with a uniformly fine grain size and a near 100% density [130,131].

Cold isostatic pressing applies pressure from multiple directions for achieving greater uniformity of compaction (high quality parts) and increased shape capability, compared to uniaxial pressing. There are two methods in isostatic pressing. In wet-bag isostatic pressing, powder is encased in a rubber sheath that is immersed in a liquid which transmits the pressure uniformly to the powder. In dry-bag isostatic pressing, rather than immerse the tooling in a fluid, the tooling itself is built with internal channels into which high pressure fluid is pumped.

### 3.2.3. Advantages

- The reduced porosity of HIPed materials enables improved mechanical properties and increased workability. The HIP process eliminates internal voids and creates clean, firm bonds and fine, uniform microstructures. These characteristics are not possible with welding or casting.
- The virtual elimination of internal voids enhances part performance and improves fatigue strength. The process also results in significantly improved non-destructive examination ratings. One of the primary advantages of the HIP process is its ability to create near-net shapes that require little machining.
- Conventional manufacturing methods use only 10–30% of the material purchased in the final product, the rest is removed during machining. A HIPed near-net shape part typically uses 80–90% of the material. As a result, machining time and costs are significantly reduced.
- Because powder metals do not have the directional property characteristics of forgings, the HIP process can produce materials from metallic compositions that are difficult or impossible to forge or cast. HIP powder compaction is used in the manufacture of abrasive tips.
- Abrasive tips are uniquely layered compacts of ceramic and metallic powders which are used for turbine blade wear protection.

### 3.2.4. Equipment—process and mechanism

A schematic of the HIP process and a photograph of the actual equipment are shown in Fig. 40. The HIP equipment is commercially available in the market with various technical specifications to suit the needs. The equipment (Type ASEA QIH 10) is operated under argon atmosphere and allows the following process parameters:

- maximum operating temperature 1400 °C;
- maximum pressure 1250 bar;
- volume of hot zone to be used: diameter 200 mm, height 400 mm.

The gas (argon) used for the compression process is taken from buffer gas cylinders for each compression cycle. After completion of the pressure cycle the gas is transferred and stored again in the buffer tank. This procedure leads to a considerable reduction of the gas consumption. The equipment can be used for applications such as:

- post-densification of powder metallurgical products;
- pressure sintering of ceramics;
- production of sputtering targets;
- infiltration of components;
- joining of components;
- healing of microstructural defects;
- stabilization of microstructural features in cellular solids with open porosity;
- pressure controlled reactions.

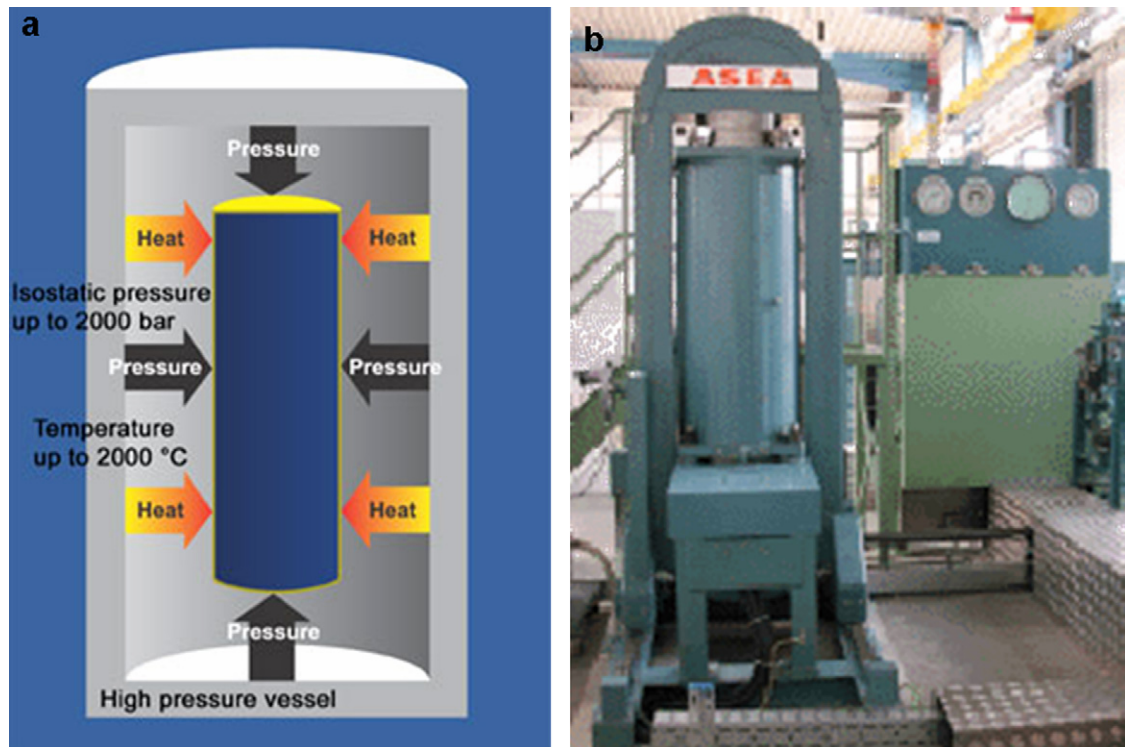


Fig. 40. (a) Schematic of a hot isostatic pressing setup and (b) hot pressing equipment with temperature and pressure controller. (Photo source: University of Bremen, Germany.)

A numerical simulation program has been installed to calculate the road map of the pressure assisted densification process; temperature and pressure programs are to be determined with their optimal effects on the final densification under simultaneous evolution of the microstructure with minimized grain growth and flow sizes. The microstructural evolution of submicron oxide ceramics has been successfully provided by this model and the experimental results could be predicted by the program.

The HIP process is now not only used for densifying castings, but in many other applications such as diffusion bonding of dissimilar materials, component repair and powder metal consolidation. Predominant applications include:

- consolidation of powder metals (PM);
- creation of PM shapes;
- production of near-net shapes;
- cladding.

Cladding is the selective bonding of hardfacing materials onto various substrate surfaces. A less expensive material is coated with a thin layer of powdered metal, creating a buffer on its wear surface. This reduces costs by placing expensive, wear resistant materials only where they are needed. As a result, wear resistant properties are improved without incurring unnecessary cost penalties. An additional benefit of cladding is that it can create bonds between otherwise incompatible materials such as metal, intermetallic, and ceramic powders. Most notably, cladding is used in the production of diesel engine valve lifters. Here, the hardfacing material (tungsten carbide) is bonded to a lower cost material such as an alloy steel.

Today, HIP has expanded well beyond aerospace products and is finding new applications in a range of industries, including automotive (turbocharger wheels and diesel engine valve lifters), medical (prosthetic devices), petroleum (valve bodies), and chemical processing. HIP offers engineers in these industries greater design freedom than was previously possible with conventional processes such as forging and casting. Parts which cannot be made by the more conventional processes are now possible using HIP. An example of this is the dual alloy wheel. In this the hub, which is

made of a HIP consolidated powder metal, is bonded to a cast outer ring through the use of the HIP process. The resulting part has excellent tensile properties in the hub and high stress rupture properties on the outer ring. A rapid rise in the use of the HIP process followed the intensification of standards within the gas turbine industry. These standards required the elimination of shrinkage porosity in investment cast components, such as increasingly complex airfoils. Conventional foundry technology was not up to the task. By developing HIP, Howmet met mechanical property requirements and eliminated shrinkage porosity defects. HIP provided the means to produce the desired high density, fine grain material.

Since its inception in 1955, the use of the HIP has grown steadily in the powder metal and casting densification fields. During the last 25 years, HIP has become a proven process in the production of aerospace and industrial gas turbine parts, and the future looks bright. New markets have developed for rocket engines, satellites and aerospace airframe castings. HIP continues to be used more frequently in the production of powder metal parts and shapes. Cladding and near-net shape technologies are on the rise with significant growth expected in the production of sputtering targets.

### 3.2.5. Nanoconsolidation

With this background, HIP and CIP seem to be promising techniques for development of bulk nanostructured metals and ceramic components that have superior mechanical properties compared to their conventional counterparts. Some of the material systems that have been experimented with these processing technique are TiC [132], TiCN [132], SiC [133],  $\text{Si}_3\text{N}_4\text{-Y}_2\text{O}_3\text{-Al}_2\text{O}_3$  [134,135],  $\text{Si}_3\text{N}_4$  [136], intermetallic TiAl [137,138],  $\text{MgAl}_2\text{O}_4$  [139], Ni-Fe [140],  $\text{Y}_2\text{O}_3$ ,  $\text{MgAl}_2\text{O}_4$  dispersed steels [141], Al [142], carbon nanotube reinforced  $\text{Si}_3\text{N}_4$  [143]. There have been instances where HIP is used as an add-on processing to CIP to increase the densification and thereby the mechanical properties such as the example of consolidation of Fe [144]. Using CIP as a primary consolidation technique works well for a micron-sized particle where as a nanoparticle might need some sort of secondary consolidation process to form a bulk part as the nanoparticles are friable and can crumble even if crushed with a hand. The only solution is to either use sintering after CIPing or use HIPing. It has been found that [144] HIPing leads to better densification at a lesser time compared to the time required for sintering to achieve the same density. CIP has also been used as a stand-alone consolidation process for  $\text{Al}_2\text{O}_3\text{-SiC}$  [145], Y-TZP [146,147],  $\text{CeO}_2$  [148], tri-aluminides [149].

**3.2.5.1. Non-oxide ceramics.** Both the variants in isostatic pressing, hot and cold led to improvement of properties such as hardness, fracture toughness, alteration in thermal conductivity behavior, tensile strength. During HIPing [132], the temperature and pressures required to consolidate the material and duration of HIPing dictates the final grain size of the component, which remained a crucial parameter in accomplishing good mechanical properties. As it can be seen in Table 10, different HIP temperatures of 1600 and 1000 °C at same pressure of 350 MPa led to different grain sizes with the grain size of the SiC turned out to be higher than that of TiC and TiCN. This is reflected in the SEM micrograph shown in Fig. 41 which reveals the grain size after HIPing. Hardness property, a measure of the resistance offered by the material to scratch or to indentation is generally higher for carbide and nitride materials. Within these materials, grain size plays an important role in determining the hardness value of the material. It has been proved (Fig. 42a) that a SiC with 130–150 nm exhibited high hardness than the conventional micron grained SiC. Similarly, TiN with a grain size of 30–40 nm showed highest hardness value of 27 GPa compared to other higher grain-sized TiN. As the grain size decreases, the amount of dislocation inside the grain decreases the dislocation density along the grain boundary provide more resistance to indentation which leads to high hardness values. Below a certain threshold level, 40 nm in case of TiN and 130 nm in case of SiC,  $\text{Si}_3\text{N}_4$  with 200 and 300 nm exhibited significantly higher hardness than conventional  $\text{Si}_3\text{N}_4$  [135]. Fig. 42b shows the effect of grain size on thermal diffusivity of SiC at room

Table 10  
Grain size data of different materials after HIP processing

No.	Material	HIP conditions	Grain size after HIP (nm)
1	SiC	1600 °C, 350 MPa, 1 h	160
2	Pieper SiC	1600 °C, 350 MPa, 1 h	150
3	MA TiC	1000 °C, 350 MPa, 3 h	Bimodal: 100–200
4	TiCN	1000 °C, 350 MPa, 3 h	100

Reproduced from [132] with permission from Elsevier.

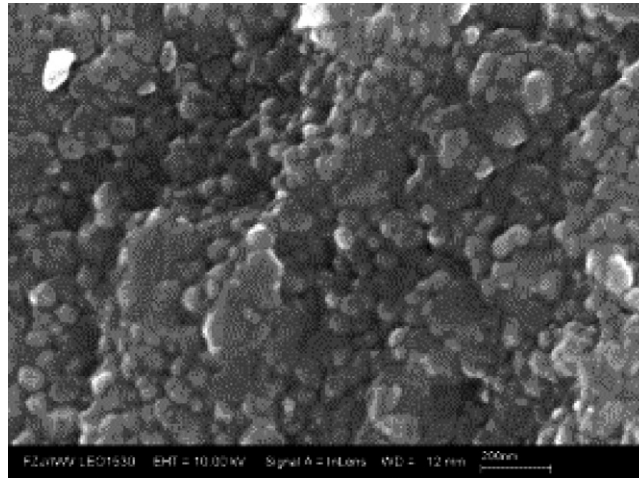


Fig. 41. SEM micrograph of the fractured surface of SiC HIPed at 1600 °C, 350 MPa, 1 h. (Reproduced with permission from Elsevier from [132].)

temperature. For a nanostructured SiC, the thermal diffusivity is reduced by a factor of 8 due to high phonon scattering at the grain boundaries. At higher temperatures, the difference between a conventional and nanostructured SiC got narrowed down as the influence of grain boundaries is reduced. Fig. 42c reveals the thermal conductivity values of the conventional SiC along with nanostructured SiC. An interesting concept in this thermal conductivity study is that the thermal conductivity of conventional SiC plummeted sharply after irradiation with neutrons, while in nanostructured SiC the reduction is not much significant. Conventional SiC being defect free, the production of point defects will have a pronounced effect compared to the production of point defects in a nanostructured material full of defects. Such behavior is crucial to situations where the material has to perform under irradiated conditions. Table 11 summarized the properties exhibited by non-oxide ceramics that has been HIPed. Silicon nitride exhibits high fracture toughness among all other candidates listed in the table due to the presence of elongated grain structure. This leads to the crack deflection or crack bridging.

**3.2.5.2. Intermetallic compounds.** Fine-grained intermetallic compounds based on TiAl [137,138] remained effective in controlling the grain growth of the matrix grains at high temperature. The presence of uncoarsened grain structure led to the improvement of superplastic property of the alloy. Ti–Al–Si alloys have been processed using high energy milling and HIP. The intermetallic/ceramic compounds thus produced were very homogenous and consists of equiaxed  $\gamma$ -TiAl grains and  $\xi$ -Ti<sub>5</sub>(Si,Al)<sub>3</sub> particles. Fig. 43a reveal a bimodal grain size distribution for Ti–45Al–2.4Si with a majority of  $\gamma$ -TiAl surrounded by smaller particles of the  $\xi$ -Ti<sub>5</sub>(Si,Al)<sub>3</sub>. Fig. 43b portrays a situation for Ti–36Al–10Si where there is no difference between the mean grain size of the  $\xi$ -Ti<sub>5</sub>(Si,Al)<sub>3</sub> and the  $\gamma$ -TiAl phase. These microstructures have an effect on the tensile behavior of the alloy and hence the superplastic properties. The flow stress (Fig. 44a) which should be as low as possible for the material to be superplastic is compared for materials with different processing histories. It can be seen that Ti–48Al processed [150] using mechanical alloying and HIPing, the flow stress seems to fall sharply in a very short processing temperature. Ti alloys processed with casting/forging [151] has maintained almost constant trajectory of flow stress with temperature. One more factor worth noting is that the grain size of the HIPed component is smaller than that of other materials plotted in the graph. Fine-grained intermetallic compounds keep the grain from growing at high temperatures and Hall–Petch reversal can be explained as a reason for reduction in the flow stress with such small grain-sized structures. In an effort to confirm whether these intermetallic compounds control the grain growth of the alloy, annealing has been performed on Ti–46Al–5Si, Ti–45Al–2.4Si, Ti–48.9Al alloys and found that the former has been able to restrict the grain growth to 12% as opposed to 80% grain growth detected with a 0 vol.% silicide phase material, i.e. Ti–48.9Al (Fig. 44b). It is indeed a testimony of the fact that the silicide phase controls the grain growth and retains the superplastic behavior of the material at high temperature. High temperature tensile tests at 800 °C have been conducted on Ti–45Al–2.4Si and fracture strains were found to be ~175% which shows that the material is fairly soft to yield to that level. TEM micrograph from the necked region of the yielded sample showed a slight grain coarsening from 120 to 248 nm as

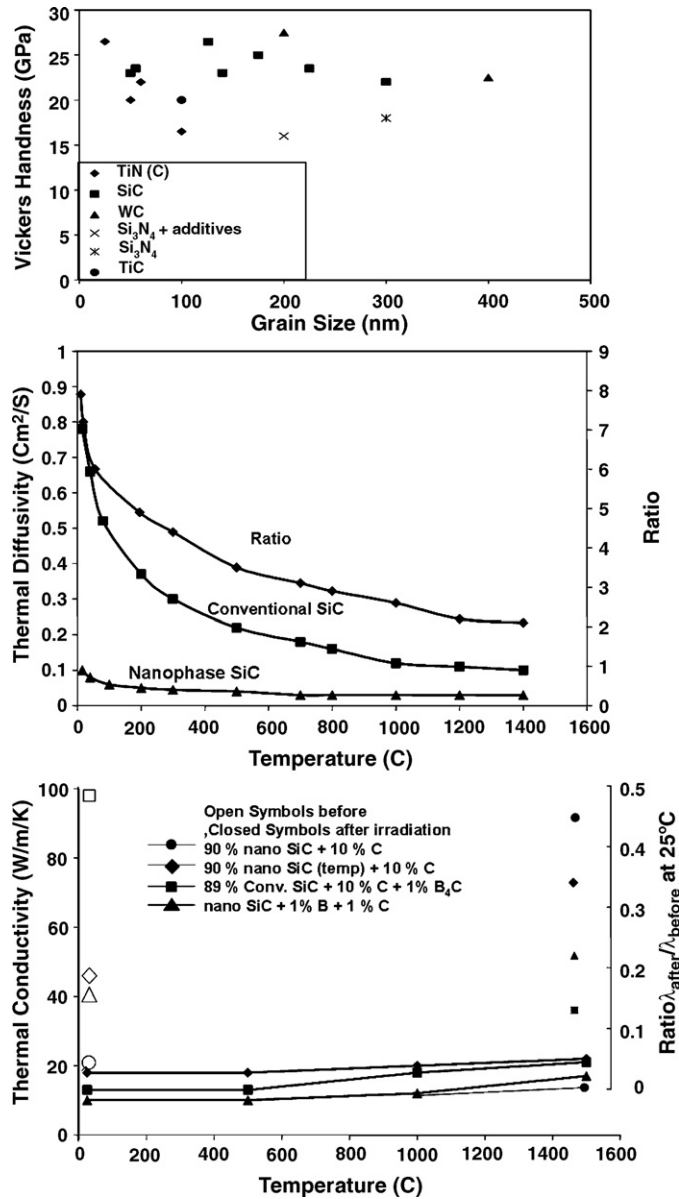


Fig. 42. (a) Vickers hardness as a function of grain size and (b and c) thermal properties of the nanoceramic as a function of temperature. (Reproduced with permission from Elsevier from [132].)

evident from Fig. 45. The beneficial effect of adding Si in bringing down the HIP consolidation temperature has been extensively studied in [152].

**3.2.5.3. Spinels.** Spinels were investigated widely for fracture toughness, hardness and creep with micron grain structures. However, nanostructured spinels have also been consolidated using HIP technique and both hardness and fracture toughness values have been reported [139]. Magnesium aluminate spinels have been developed from auto-ignition processing followed by CIP and HIP to enhance the densification of the bulk nanocomposite. Samples with four different compositions (14, 20, 40, and 50 mol.% MgO with the rest alumina) have been HIPed 1200–1300 °C for 2–4 h. Hardness and fracture toughness of the as HIPed samples are shown in Fig. 46a. Sample with 14 mol.% MgO exhibited high fracture toughness and hardness compared to all other compositions. High fracture toughness could be attributed to the presence of nano-alumina which reduced the grain growth of MgO. Hot hardness measured using a

Table 11  
Mechanical properties of certain non-oxide ceramics along with the mechanical properties

No.	Material	Powder preparation	HIP parameters	Mechanical properties	Reference
1	SiC	Laser synthesis	1500–1650 °C, 350 MPa, grain size: 70 nm	HV10 = 24–25 GPa, $K_{IC} = 3\text{--}4.2 \text{ MPa m}^{1/2}$	[4]
2	Si <sub>3</sub> N <sub>4</sub> + 6% Y <sub>2</sub> O <sub>3</sub> + 2% Al <sub>2</sub> O <sub>3</sub>	Plasma processing	1750 °C, 186 MPa, grain size: 100–250 nm	$\sigma = 1000 \text{ MPa}$ , $K_{IC} = 4.6\text{--}4.8 \text{ MPa m}^{1/2}$	[5]
3	Si <sub>3</sub> N <sub>4</sub> + 6% Y <sub>2</sub> O <sub>3</sub> + 2% Al <sub>2</sub> O <sub>3</sub>	Pieper procured	1750 °C, 350 MPa, grain size: 200–300 nm	HV10 = 15.4 GPa, $K_{IC} = 7.2 \text{ MPa m}^{1/2}$	[6]
4	Si <sub>3</sub> N <sub>4</sub>	Pieper procured	1900 °C, 350 MPa, grain size: 300–400 nm	HV10 = 18.4 GPa, $K_{IC} = 4.5 \text{ MPa m}^{1/2}$	[7]
5	TiNC	Plasma chemical	1000 °C, 350 MPa, grain size: 100 nm	HV10 = 16 GPa, $K_{IC} = 3.5 \text{ MPa m}^{1/2}$	[3]
6	TiC	Mechanically alloyed	1000 °C, 350 MPa, grain size: 100–1000 nm	HV10 = 21 GPa, $K_{IC} = 2.9 \text{ MPa m}^{1/2}$	[3]

Nikon QM-1 hot hardness indenter revealed a drop in hardness at 1000 °C which might be due to grain coarsening. Nevertheless, the material can be considered for possible superplastic deformation thereby exploiting the soft nature of the spinel at that temperature (Fig. 46b).

**3.2.5.4. Oxide dispersed steels.** Oxide dispersed steels (ODS) have been found to be used in applications with increased working temperatures above 650 °C especially in fusion nuclear reactors. Tensile and creep properties have been found to have improved which validates the use of these materials in such applications. This improvement is attributed to the dislocation pinning by a dispersion of nano-oxides. The oxides that are widely used for dispersion are Y<sub>2</sub>O<sub>3</sub> and MgAl<sub>2</sub>O<sub>4</sub>. ODS steels can be consolidated to the final shape using hot working or HIP. Hot working leads to undesirable anisotropy in the material and the grain size after processing often remains small which is not good for creep resistance. However, HIP avoids any formability or anisotropy problems [153]. Cayron et al. [141] dispersed

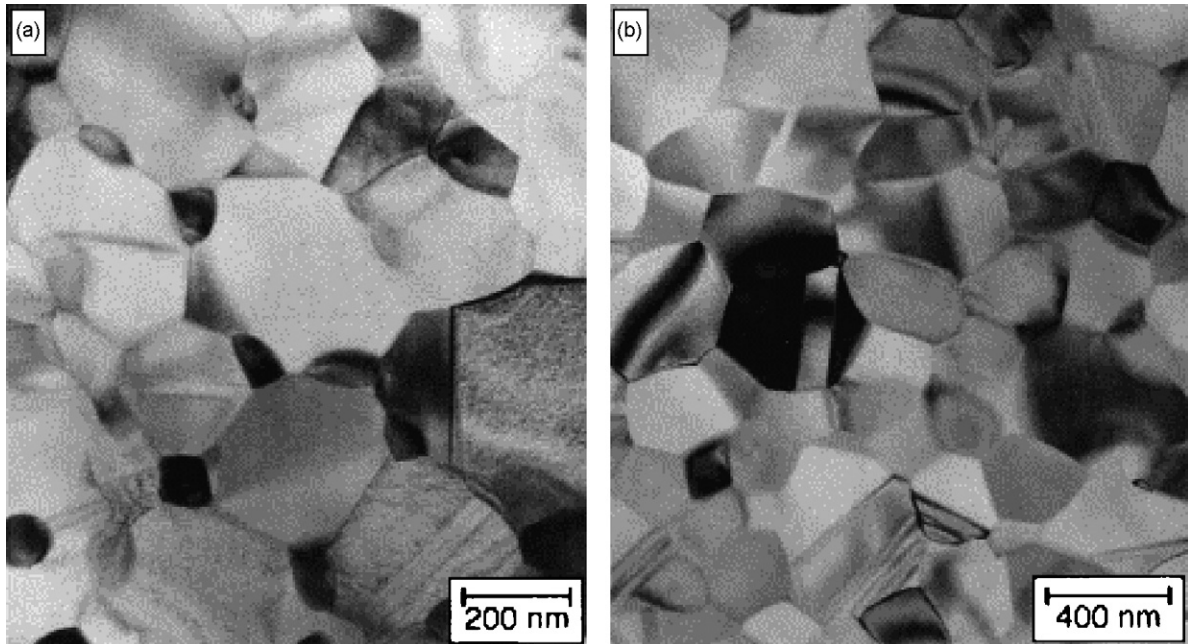


Fig. 43. TEM micrograph of TiAlSi compounds after HIP. (a) Ti–45Al–2.4Si consolidated at 875 °C and (b) Ti–36Al–10Si consolidated at 1000 °C. (Reproduced with permission from Elsevier from [137].)

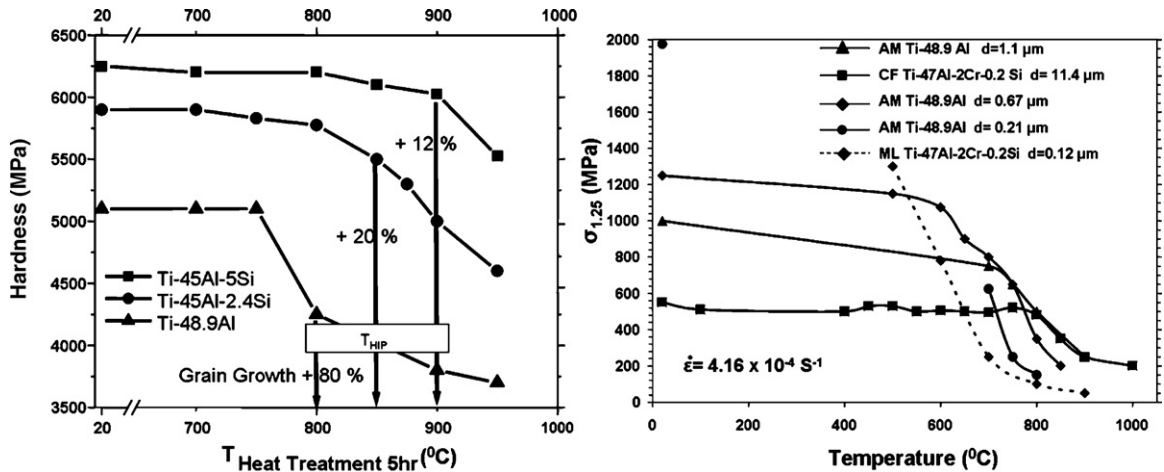


Fig. 44. (a) Hardness data for different compounds as a function of annealing temperature and (b) temperature-dependent flow stress of different compounds. (Reproduced with permission from Elsevier from [137].)

$\text{Y}_2\text{O}_3$  and  $\text{MgAl}_2\text{O}_4$  in EUROFER steel, a steel variety with a composition of 8.9 wt.% Cr, 1.1 wt.% W, 0.1 wt.% C, and balance Fe. A forged bar of EUROFER steel has been atomized to get steel powders and sieved to less than 45  $\mu\text{m}$ . Four different compositions 0, 0.2, 1%  $\text{Y}_2\text{O}_3$ , and 1%  $\text{MgAl}_2\text{O}_4$  (10–100 nm crystallite size) has been mixed with the steel powder and mechanically milled and HIPed subsequently at 1020 °C at 1000 bar under argon followed by furnace cooling. TEM micrograph of 1%  $\text{Y}_2\text{O}_3$  dispersed steel in the as HIPed condition (Fig. 47a) revealed a bimodal structure with micron grains ( $\sim 3 \mu\text{m}$ ) surrounded by nanograins ( $\sim 200 \text{ nm}$ ). The proportion of grains with a

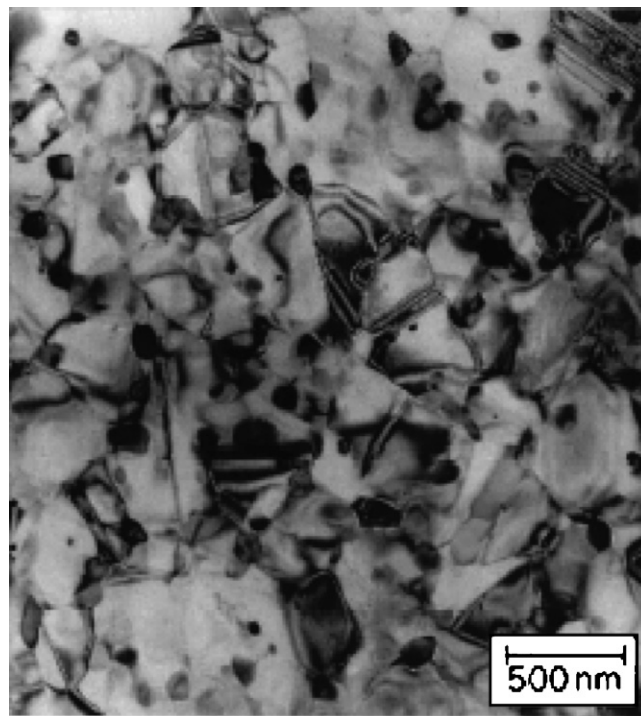


Fig. 45. TEM micrograph taken in the necked region of the Ti-45Al-2.4Si tensile sample with a slight grain coarsening from 170 to 248 nm. (Reproduced with permission from Elsevier from [137].)

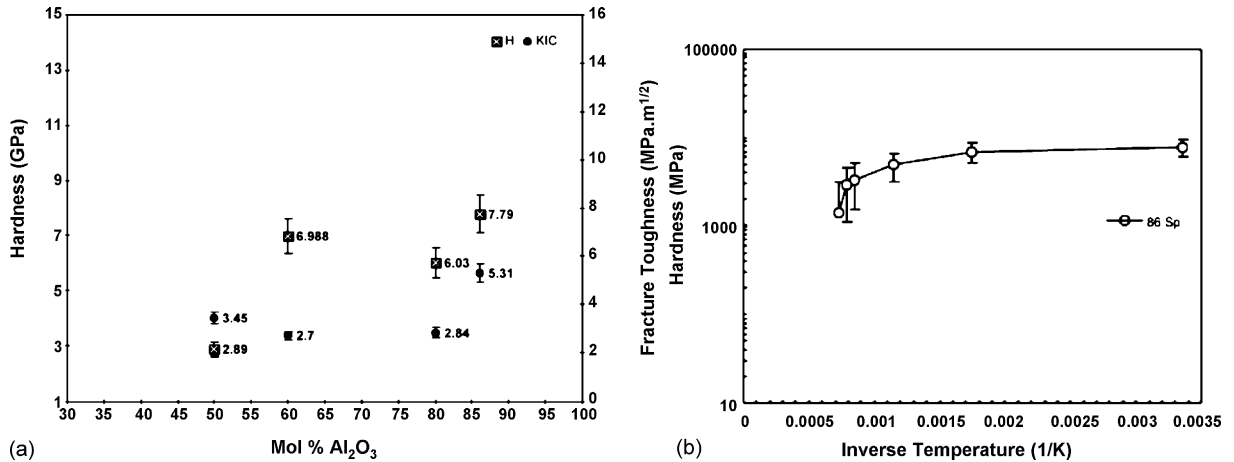


Fig. 46. (a) Hardness and fracture toughness as a function of alumina content and (b) hot hardness of the spinel. (Reproduced with permission from Elsevier from [139].)

nanometric grain size was 70% in this case. It is quite undesirable for this application to leave the material in the as HIPed state because of the absence of martensitic phase. So, the material has been heated up to 130 °C for 2 h followed by 115 °C for 1 h and then water quenched to retain the martensitic phase. The microstructure for post-heat-treated sample is shown in Fig. 47b, revealing the presence of nanograins. Also, the sample attained a higher density compared to the as HIPed condition. Yield and tensile strength data for different composition and heat treatment conditions are presented in (Table 12). It is evident that the tensile strength of the steel (no oxide dispersion) in the HIPed state is much higher than the forged state. Also, with oxide dispersions, the UTS still increased attaining a maximum of 1300 MPa for 1% Y<sub>2</sub>O<sub>3</sub> steel in the heat-treated condition.

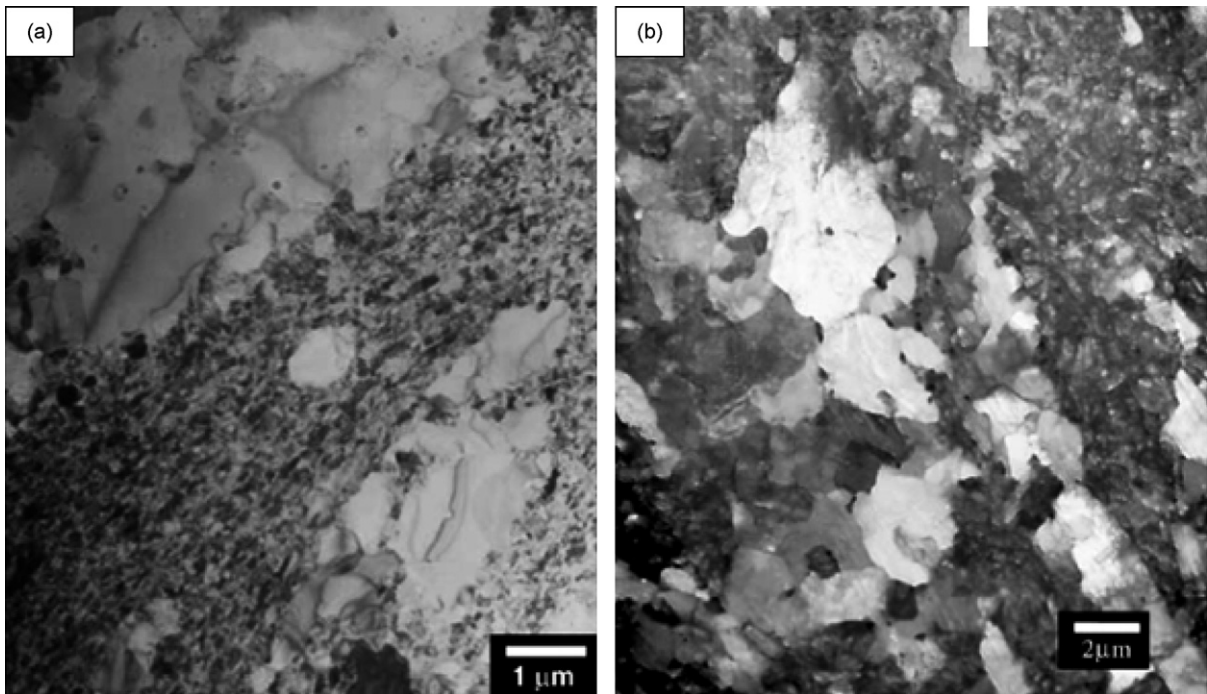


Fig. 47. TEM images 1% Y<sub>2</sub>O<sub>3</sub> EUROFER steel in (a) as HIPed condition and (b) heat-treated at 1300 °C/3 h 1100 °C/1 h furnace cooled. (Reproduced with permission from Elsevier from [141].)

Table 12  
Tensile test data of ODS EUROFER steels at different temperatures

No.	Tensile test temperature	Composition	Condition	Yield strength (MPa)	Ultimate tensile strength (MPa)
1	RT	EUROFER	Forged	533	673
2	RT	EUROFER	HIP	493	725
3	RT	0.2% Y <sub>2</sub> O <sub>3</sub> EUROFER	HIP	956	1063
4	RT	1% Y <sub>2</sub> O <sub>3</sub> EUROFER	HIP	945	1168
5	RT	1% Y <sub>2</sub> O <sub>3</sub> EUROFER	HIP + heat treatment 950 °C, 1 h/WQ tempering at 75 °C, 2 h	1164	1297
6	RT	1% Y <sub>2</sub> O <sub>3</sub> EUROFER	HIP + heat treatment 130 °C, 3 h, 1150 °C, 1 h/WQ tempering at 75 °C, 2 h	935	1061
7	550 °C	EUROFER	Forged	360	360
8	550 °C	0.2% Y <sub>2</sub> O <sub>3</sub> EUROFER	HIP	614	690

Reproduced from [141] with permission from Elsevier.

**3.2.5.5. Nano-aluminum.** Nano-aluminum [142] is processed by HIP from a commercial purity aluminum nanopowder. A temperature of 550 °C and pressure of 200 MPa is used to consolidate the powders using HIP. The microstructure consisted of fine dispersion of the oxide phase heterogeneously distributed inside an ultrafine-grained (ufg) matrix (average grain size of about 150 nm) and also contains negligible fraction of microcrystalline (mc) grains. Compression test has been done on to study the macroscopic mechanical properties. Microstructure of ufg-Al consisted of equiaxed grains about 150 nm in size (Fig. 48a). Some large grains (Fig. 48b) are also seen with a very low dislocation density ( $d$ ) and a fine dispersion of particles/oxides ( $p$ ). EFTEM analysis (Fig. 48c) of the HIPed samples demonstrates the presence of an oxide phase in the form of lathes or plates. These are mostly  $\gamma$ -alumina and appear from the crystallization of the native oxide layer that occurs at about 500 °C and as observed by high resolution electron microscopy studies. The mechanical property data from compression testing has been presented in (Table 13). The most notable feature for the ufg-Al material is that yield and fracture strength are higher compared to the mc-Al. Such an increase can be attributed to the sole effect of grain refinement through the well-known Hall–Petch relationship.

**3.2.5.6. Multiwalled carbon nanotube reinforced Si<sub>3</sub>N<sub>4</sub>.** Multiwalled carbon nanotubes reinforced silicon nitride has been processed using HIP [143]. The high elastic modulus, tensile strength, electrical, and thermal conductivity of carbon nanotubes make them very attractive for ceramic-based nanocomposite applications. 1% MWCNT has been mixed with silicon nitride, 4% Al<sub>2</sub>O<sub>3</sub>, 6% Y<sub>2</sub>O<sub>3</sub> and HIPed at 1700 °C at 2 MPa pressure for 1 h in high purity nitrogen using BN embedding powder. Fracture surface of HIP sample are presented in Fig. 49. In Fig. 49a, well developed  $\beta$ -Si<sub>3</sub>N<sub>4</sub> grains evolved during the hot isostatic pressing. More detailed view of the fracture surface and microstructure are shown in Fig. 49b–d. In some parts, web-like connected MWCNTs can be found in the structure, but individual MWCNTs, properly attached to  $\beta$ -Si<sub>3</sub>N<sub>4</sub> surfaces can also be observed. Mechanical properties such as bending strength (both four and three point bend strength) and elastic modulus have been measured for the HIPed samples (Fig. 50). It is found that all these properties have improved compared to the reference samples with no MWCNT reinforcements.

**3.2.5.7. Nano-iron.** Nanoscale iron has been subjected to both CIP and HIP. The starting powders have been classified in to four distinct varieties based on the size. They are nano–nano (NN), nano–micro (NM), micron–micron (MMa) atomized, and micron–micron (MMb) ground powders. All the samples were CIPed initially and later on sintered or HIPed. In all the cases, HIPed sample exhibited higher density compared to that of other processing techniques. The densities achieved are 8.5, 7.2, and 7 g cm<sup>-3</sup>, respectively, for MMa, NM, and NN, respectively. Vickers hardness of these variants is plotted in Fig. 51. It is found that HIPed samples showed increased hardness compared to all other consolidation technique attempted. The yield strength of these samples is improved (Fig. 52) at a processing temperature of 800 °C. Vickers hardness as a function of grain size for different processing routes revealed that NM Fe provided higher hardness compared with the NN and MM (Fig. 53). It is to be believed that nanograin Fe fills the pores effectively left by the micron-sized Fe and thereby providing the optimized hardness values.

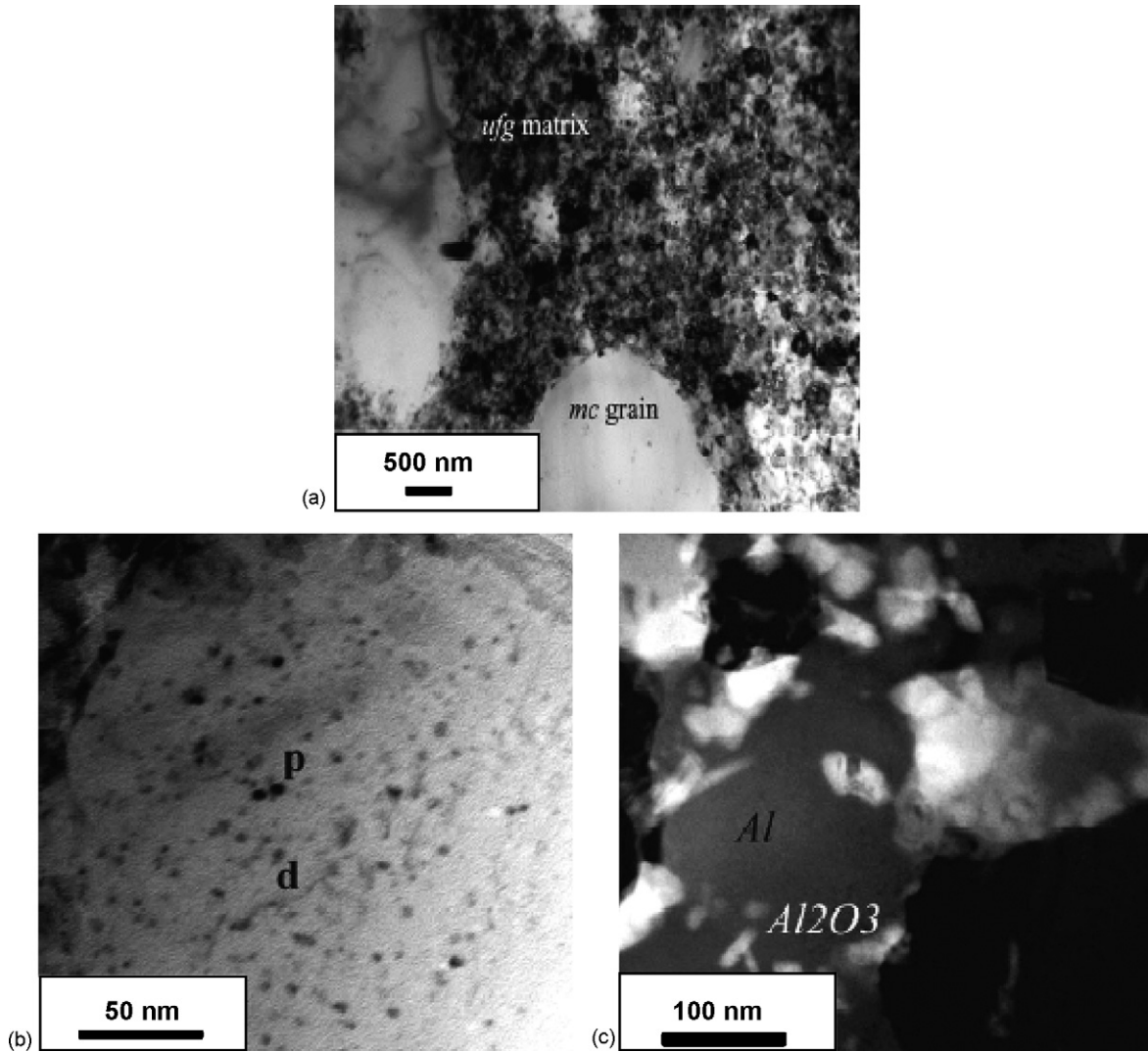


Fig. 48. The as-processed microstructure of the HIPed materials. (a) TEM bright field images showing the ufg matrix and embedded mc grains, (b) some mc grains contains a fine dispersion of second phase particles (*p*) and individual dislocations (*d*) that are pinned by the dispersoids, and (c) an EFTEM image illustrating the presence of alumina particles (white contrast) within the microstructure. (Reproduced with permission from Elsevier from [142].)

Table 13  
Mechanical properties of the HIPed samples

Properties	ufg-Al	mc-Al
Yield strength (MPa)	390	40
Yield strength at 0.2% offset (MPa)	440	50
Maximum stress (MPa)	490	120
Maximum strain	0.2	>0.4
Linear hardening value	-200	100

Reproduced from [142] with permission from Elsevier.

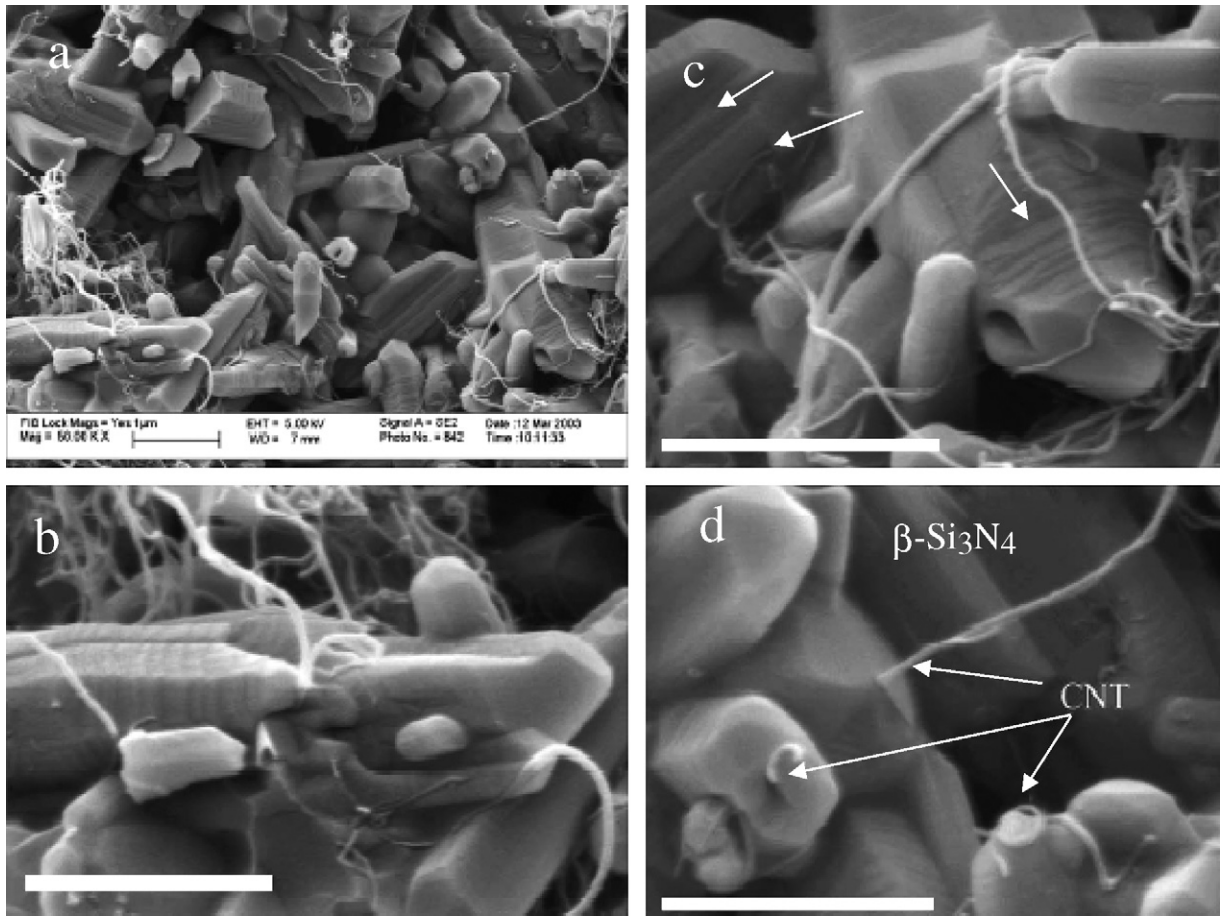


Fig. 49. Fracture surface of composite HIP-2: (a) a general view and (b–d) details about MWNT/grain surface interaction. (b–d) Bar is 1 μm. (Reproduced with permission from Elsevier from [143].)

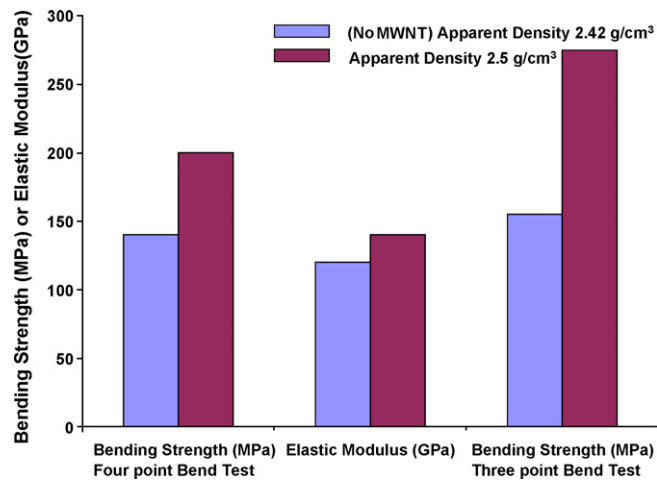


Fig. 50. Bending strength and elastic modulus data for CNT reinforced Si<sub>3</sub>N<sub>4</sub> as a function of apparent density [143].

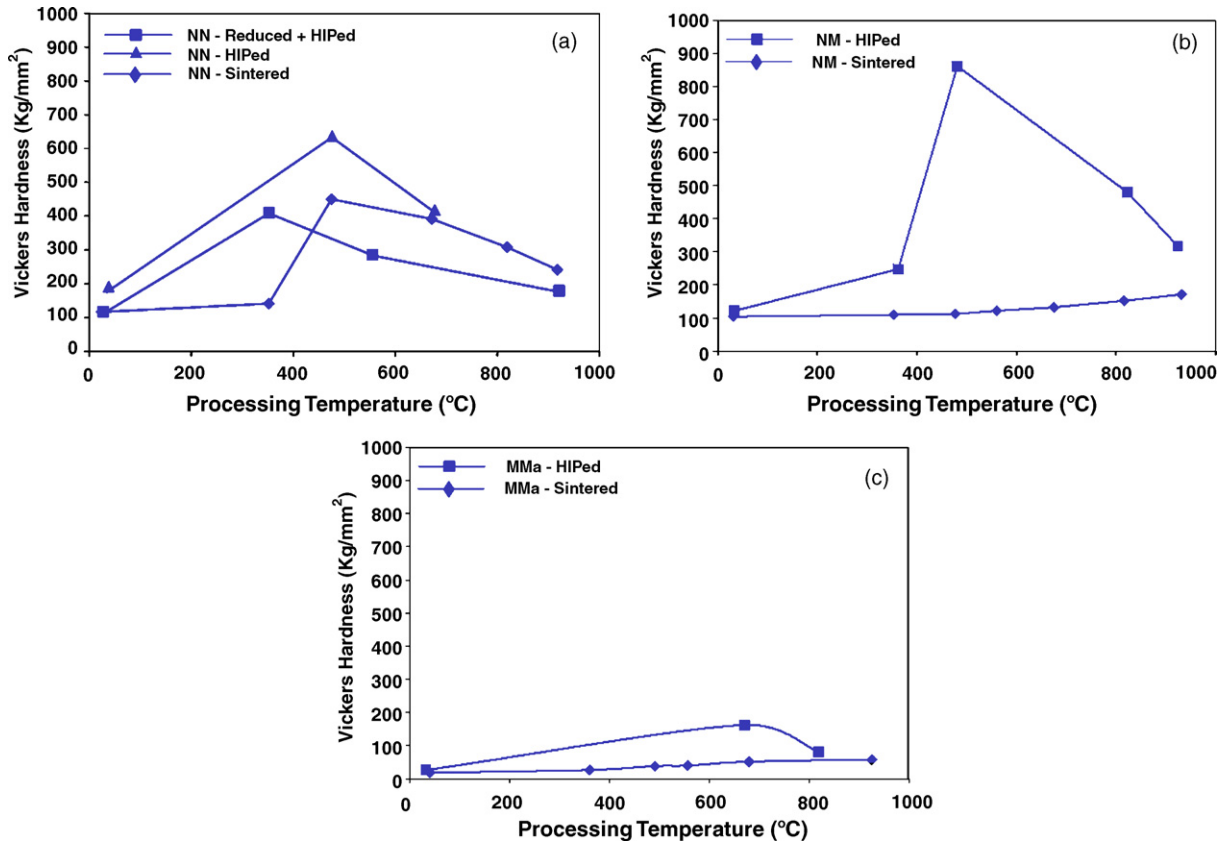


Fig. 51. Hardness of the nano–nano, nano–micro, and micro–micro Fe compacts with different processing variables. (Reproduced from [144] with permission from Elsevier.)

Hot isostatic pressing could lead to uniform mechanical properties achieved due to the uniform pressure applied in all directions. Metals, ceramics and composites (both metal matrix composites and ceramic matrix composites) could be processed through this technique with relative ease. The process however, is costlier than hot pressing.

### 3.3. Hot extrusion

#### 3.3.1. Introduction

Extrusion has been a conventional forming technique to process cast billets of both ferrous and non-ferrous metals. Hot extrusion has been used to fabricate different shapes such as rods, strips, tubes with desirable lengths. Extrusion is usually performed at high temperatures above the recrystallization temperature, in order to achieve more strength and area reduction simultaneously. The process has been gradually extended in the fabrication of making ceramic parts such as clays. While conventional ceramic extrusion processes are based on plasticity developed from the use of wet clay at ambient temperatures, the Ceramext extrusion process<sup>TM</sup> [154] derives plasticity by the formation of a liquid phase in the material at high temperature (Fig. 54A). It can therefore utilize a very wide variety of raw materials, including those that would otherwise be considered waste materials, such as coal fly ash and incinerated garbage ash, which would otherwise have to be placed in expensive landfills.

#### 3.3.2. Fundamental principles

Extrusion is the process by which the material is reduced in cross-section by forcing it to flow through a die orifice under high pressure. Initially, extrusion is viewed as a processing technique from the perspective of achieving a wide variety of shapes. While extrusion may not be suitable for processing ceramics that are inherently brittle in nature, it is

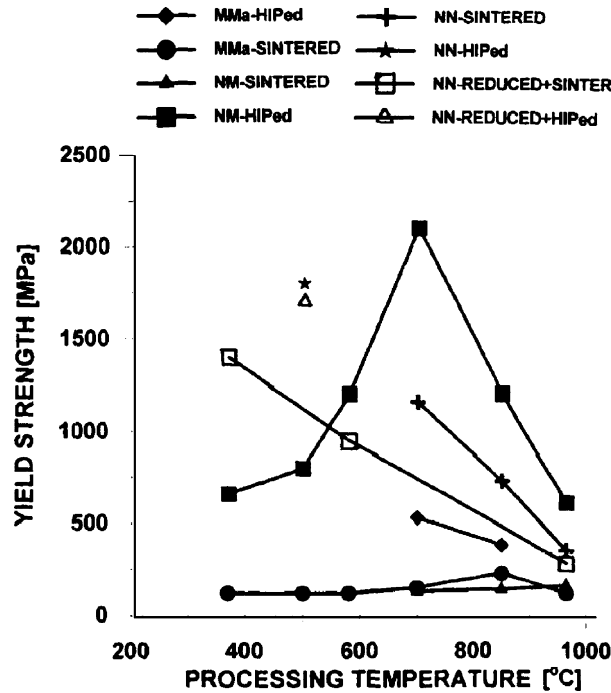


Fig. 52. Yield strength during compression of the iron compacts. (Reproduced from [144] with permission from Elsevier.)

envisioned that extrusion will at least densify the ceramics. Extrusion can be visualized as a hot pressing technique with the material being subjected to compressive stresses which will annihilate any crack that will develop during processing.

3.3.3. Advantages

Hot extrusion is a hot working technology that is versatile from the point of view of processing metals or ceramics. Hot extrusion has the following advantages:

- Hot working makes use of compressive stresses to process the material. So, any possibility of a pore getting transformed in to a crack and eventual failure is remote.

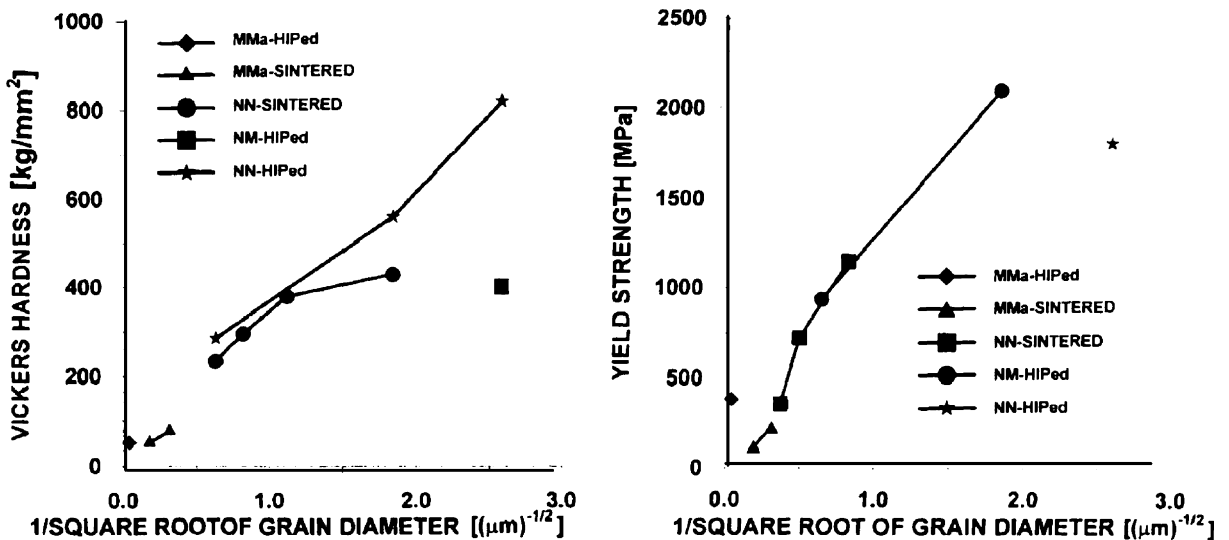


Fig. 53. Vickers hardness and yield strength as a function of grain size. (Reproduced from [144] with permission from Elsevier.)

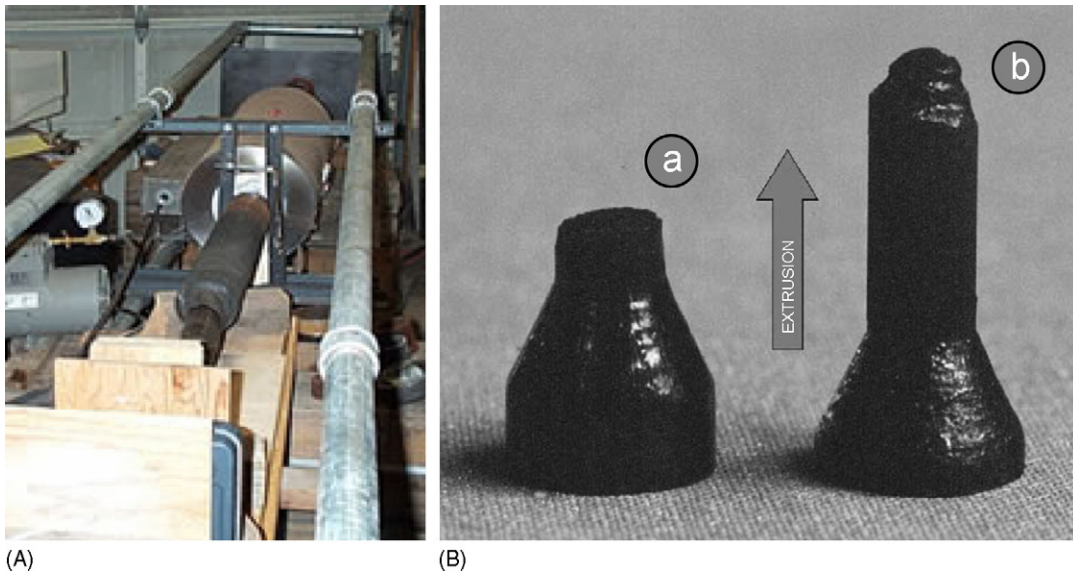


Fig. 54. (A) Ceramic extrusion setup (Photo source: [www.ceramext.com](http://www.ceramext.com)) and (B) picture illustration of how the material looks like before (a) and after extrusion (b). (Reprinted from [161] with permission from Elsevier.)

- The process can be used to maximize the densification of the component to be fabricated.
- Except for initial preheating of the material to be processed, the process takes less operation time especially with sophisticated hydraulic rams available in market in terms of speed and load.

#### 3.3.4. Equipment—process and mechanism

Most extrusion processing is done with hydraulic press. The press has a capacity of 15–50 MN. Dies that are used to create different shapes are usually designed in such a way that the angle at the entrance decides how much extrusion pressure needs to be applied. Smaller die angle increases the homogeneity of deformation and lowers the extrusion pressure. Extrusion is done both hot [155] and cold [156,157] (above and below recrystallization temperature of the material). The process makes the use of different die design to suit the dimension of the end product. The extruded products are cold drawn later for required finish. Extrusion ratio describes the efficacy of the whole extrusion process. Extrusion ratio is the ratio of the initial cross-section area of the material before extrusion to that after the event. Extrusion ratio depends upon the ductility of the material as well as the efficiency of the hydraulic ram [158].

#### 3.3.5. Nanoconsolidation

Extrusion process has been innovatively applied to the consolidation of nanomaterials ranging from metallic powders to ceramic matrix composites. It can be thought of as an extension to hot pressing, but nowadays, hydrostatic extrusion [159] has also been used to process such materials to achieve homogenous mechanical properties all over the consolidated bulk composites. Based on the material to be consolidated, the extrusion temperature is selected. Based on the fact that the material to be extruded is a ceramic, a metal or a composite, the extrusion ratio and the extrusion temperatures are decided. Table 14 illustrates the extrusion experiment parameters that have been adopted for different materials. It is to be seen that, among the members listed in the table, there are alloy systems, carbon nanotubes (CNT) reinforced ceramics, metal reinforced ceramics. It is to be noted that extrusion ratios are high for Al-based systems compared to the others. This is due to the fact that Al has more slip systems compared to other crystal structures. Also, the extrusion temperatures are decided based on the recrystallization temperature of the material. CNT reinforced alumina has a higher extrusion temperature because of the presence of MgO and alumina in the system which has high melting points. Similar to the conventional extrusion, die design and manufacturing is crucial for nanoconsolidation. Kellett et al. [160] presented a new die design for consolidation of zirconia-based ceramics. Fig. 54B illustrates the evaluation of shape and form of the component by incorporating innovative die designs in the extrusion process.

Table 14  
Extrusion parameters for different material systems

No.	Material	Temperature (K)	Ratio	Reference
1	Mg–Zn–Y	523	1:10	[170]
2	Mg–alumina	523	1:20.25	[162]
3	CNT–Mg–alumina	1750–2000	NA	[161]
4	Mg–Al–Nd	673	1:25	[164]
5	Al–nano–ZrO <sub>2</sub>	873	1:44	[169]
6	Al–Ti	723–773	1:25	[165]
7	Mg–alumina	623	1:25	[163]
8	Mg–graphite	623	NA	[167]
9	Al–Ni–Y	700	1:25	[168]

Various materials processed by extrusion are, CNT–metal oxide nanocomposites [161], Mg–alumina [162,163], Mg–Al–Nd [164], Al–Ti alloys [165,166], graphite strengthened Mg [167], Al–Ni–Y [168], Al–ZrO<sub>2</sub> [169], Mg–Zn–Y [170], Al–Mg [171,172], nano–micro composites.

**3.3.5.1. CNT–metal oxide nanocomposites.** High temperature extrusion is carried out on carbon nanotube–metal oxide nanocomposites [161]. The presence of CNTs enables superplastic forming of the nanocomposite. CNTs could be aligned easily along any direction in the ceramic matrix, which are bulk materials rather than fibers or thin films. These CNTs withstand the extreme shear stresses occurring during the extrusion. Dense composites were prepared by high temperature extrusion in a graphite die, under primary vacuum. The composites were partially densified under a mild load (8.6 MPa) and the materials were then extruded under a 43 MPa load. Al<sub>2</sub>O<sub>3</sub> and MgAl<sub>2</sub>O<sub>4</sub> matrix materials were extruded at 1500 °C but the extrusion of MgO matrix materials were required to increase the temperature up to 1730 °C. Cylindrical extruded rods, 6.7 mm in diameter and 20 mm in length were produced. The electrical conductivity of the specimens was measured at room temperature, both in the longitudinal and transverse direction of extrusion. The current densities used were found to be less than 160 mA cm<sup>-2</sup>. Anisotropy of the electrical conductivity has been observed. Electron microscopy revealing the alignment (Fig. 55), the materials show an anisotropy of the electrical conductivity ( $r$ ) (Fig. 56), which could be adjusted by controlling the amount of CNTs. The CNTs seem to be aligned (Fig. 55) but it should be noted that the alignment is more or less pronounced in different areas, which was dictated by the ability of the CNTs to relocate within the die during the extrusion. The low values measured for CNT–Co–MgO (Fig. 56a) reflect the almost total destruction of the CNTs, in both the non-extruded (upper) and extruded (lower) parts of the material. For the CNT–Fe–Al<sub>2</sub>O<sub>3</sub> and CNT–Fe/Co–MgAl<sub>2</sub>O<sub>4</sub> composites (Fig. 56b and c), the values measured in the non-extruded part are similar to those measured on hot pressed specimens. The alignment of the remaining CNTs must lead to an increase in the electrical conductivity along the extrusion

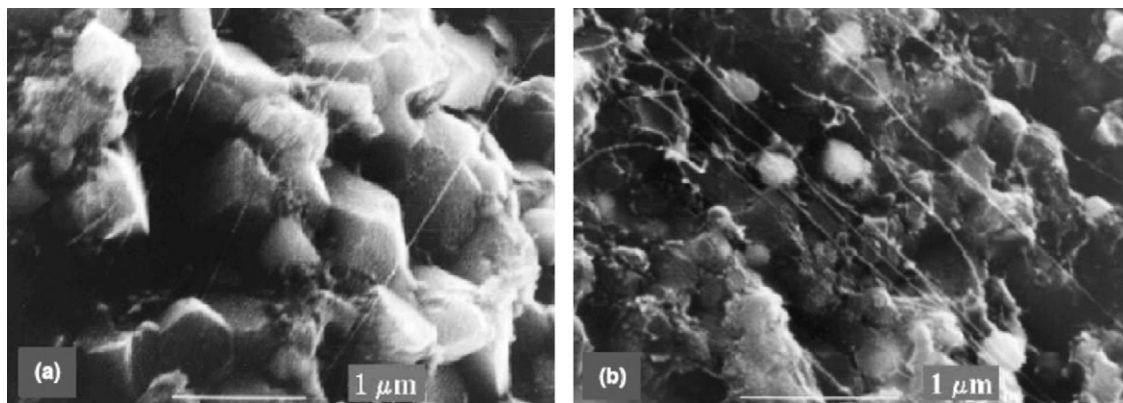


Fig. 55. SEM images of fracture surfaces of: (a) CNT–Fe–Al<sub>2</sub>O<sub>3</sub> and (b) CNT–Fe/Co–MgAl<sub>2</sub>O<sub>4</sub>. (Reprinted from [161] with permission from Elsevier.)

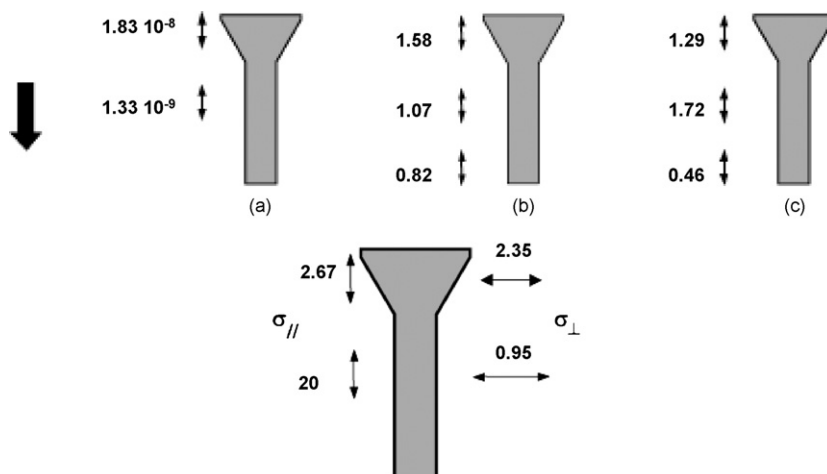


Fig. 56. Electrical conductivity measurements on: (a) CNT–Co–MgO, (b) CNT–Fe–Al<sub>2</sub>O<sub>3</sub>, and (c) CNT–Fe/Co–MgAl<sub>2</sub>O<sub>4</sub>. (d) Same as (c) but contains twice that of CNT arrow indicates the extrusion direction. (Reprinted from [161] with permission from Elsevier.)

direction. The values measured for ‘*r*’ in the non-extruded part, along the extrusion direction and in the transverse direction (Fig. 56d), are similar to each other (ca. 2.5 S cm<sup>-1</sup>) and only slightly higher than those obtained for the previous composite. In the extruded part, there is a strong increase in the electrical conductivity measured along the extrusion direction (20 S cm<sup>-1</sup>) whereas much lower values are measured in the transverse direction (0.6 S cm<sup>-1</sup>). CNTs thus can be aligned in a preferred direction to selectively raise the electrical conductivity.

**3.3.5.2. Mg–alumina nanocomposites.** Magnesium-based composites containing 2.5 wt.% of nanosized Al<sub>2</sub>O<sub>3</sub> (50 nm) particulates reinforcement were synthesized using disintegrated melt deposition (DMD) technique and blend–press–sinter powder metallurgy technique followed by hot extrusion [162]. In another study [163], magnesium powder of 98.5% purity with a size range of 60–300 μm was used as the matrix material. Alumina powder of 0.3 μm and 50 nm in size were used as the reinforcements. Mechanical alloying followed by microwave assisted sintering and compaction. Further densification is achieved by densification using extrusion.

Detailed material characterization [162] revealed that the presence of nano-Al<sub>2</sub>O<sub>3</sub> particulates led to an increase in dimensional stability, hardness, elastic modulus, 0.2% yield strength, UTS, and ductility of pure magnesium. Between the composites (DMD and powder metallurgy route), the ingot metallurgy processed material exhibited superior modulus and ductility while powder metallurgy processed material exhibited superior yield strength and ultimate tensile strength (Tables 15a and 15b). The results further revealed that the overall combination of tensile properties of these materials remained superior when compared to the pure Mg [173] and high strength magnesium alloy AZ91 [174] reinforced with much higher weight percentage of SiC.

Addition of micron and nanosized particulate reinforcements in magnesium matrix [163] leads to a significant increase in the hardness, elastic modulus, 0.2% yield strength, ultimate tensile strength and a decrease in ductility

Table 15a  
Mechanical properties of extruded Mg/Al<sub>2</sub>O<sub>3</sub> nanocomposite

Materials	CTE ( $\times 10^{-6}$ K)	Hardness 15 HRT	<i>E</i> (GPa)	0.2% YS (MPa)	UTS (MPa)	Ductility (%)
Mg (PM)	29.4 ± 0.3	43 ± 0	41.2	132 ± 7	193 ± 2	4.2 ± 0.1
Mg (DMD)	28.4 ± 0.3	37 ± 1	42.8	97 ± 2	173 ± 1	7.4 ± 0.2
Mg/2.5Al <sub>2</sub> O <sub>3</sub> (PM)	28.4 ± 0.7	60 ± 1	44.5	194 ± 5	250 ± 3	6.9 ± 1.0
Mg/2.5Al <sub>2</sub> O <sub>3</sub> (DMD)	25.1 ± 0.3	65 ± 1	52.7	175 ± 3	246 ± 3	14.0 ± 2.4
Pure Mg	–	–	40–44	69–105	165–205	5–8
AZ91/16.1SiC	–	–	47.5	191	236	2
Mg/16.0SiC	–	–	44 ± 2	120 ± 5	181 ± 6	4.7 ± 1.3

Reprinted from [162] with permission from Elsevier.

Table 15b  
Mechanical properties of extruded Mg/Al<sub>2</sub>O<sub>3</sub> nanocomposite

Materials	Work of fracture (J m <sup>-3</sup> )	$\sigma$ 0.2% YS/ $\rho$	$\sigma$ UTS/ $\rho$
Mg (PM)	7.1 ± 0.3	76	111
Mg (DMD)	11.1 ± 0.3	56	99
Mg/2.5Al <sub>2</sub> O <sub>3</sub> (PM)	15.5 ± 2.6	110	142
Mg/2.5Al <sub>2</sub> O <sub>3</sub> (DMD)	31.7 ± 6.3	99	140
AZ91/16.1SiC	–	102	126
Mg/16.0SiC	8.8 ± 2	65	98

Reprinted from [162] with permission from Elsevier.

when compared to pure magnesium. With an increase in nanosized alumina particulates from 0.75 to 1%, the overall mechanical properties of the hybrid composites were enhanced with an increase in the elastic modulus, 0.2% yield strength and ductility of the composites. Further density and porosity measurements indicate that near dense monolithic and composite formulations can be achieved using the extrusion technology (see Table 16). CTE measurements in the range of 50–400 °C revealed that addition of submicron and nanosized Al<sub>2</sub>O<sub>3</sub> reinforcements led to the reduction in the coefficient of thermal expansion values of the magnesium matrix (Table 17). The reduction in CTE values can be attributed to the presence of submicron and nano-Al<sub>2</sub>O<sub>3</sub> reinforcements which exhibit a lower CTE value of  $7.0 \times 10^{-6} \text{ }^\circ\text{C}^{-1}$  [174] when compared to pure magnesium ( $28.6 \times 10^{-6} \text{ }^\circ\text{C}^{-1}$ ) and the ability of these reinforcements to effectively constraint the expansion of the matrix.

Elastic modulus measurements revealed that the addition of submicron and nanosize Al<sub>2</sub>O<sub>3</sub> leads to an increase in the elastic modulus of the magnesium matrix. The results further revealed that an increase in the relative proportion of nanosize Al<sub>2</sub>O<sub>3</sub> particulates were more instrumental in increasing the elastic modulus of magnesium when compared to submicron size particulates [175–178] (Table 18). The increase in the elastic modulus of composite samples is due to the reinforcement of alumina which has high modulus ( $E_{\text{alumina}} = 416 \text{ GPa}$  [179]).

An increase in 0.2% YS of the hybrid composites when compared to pure magnesium is ascribed to (i) the Orowan strengthening mechanism triggered by nanosized Al<sub>2</sub>O<sub>3</sub> particulates, (ii) decrease in the grain size, and (iii) increase in dislocation density around the particulates due to different thermal expansion behavior of the matrix and particulates. An increase of 35% in 0.2% YS and 26% in UTS over pure magnesium could be achieved with the addition of 4 vol.%

Table 16  
Results of density and porosity measurements of Mg–Al<sub>2</sub>O<sub>3</sub>

Materials	Reinforcement (vol.%)		Theoretical density ( $\rho$ )	Experimental density ( $\rho$ )	Porosity (%)
	50 nm	0.3 $\mu\text{m}$			
Mg	–	–	1.740	1.738 ± 0.001	0.07
Mg/Al <sub>2</sub> O <sub>3</sub>	0.5	4.5	1.851	1.840 ± 0.003	0.58
Mg/Al <sub>2</sub> O <sub>3</sub>	0.75	4.25	1.851	1.837 ± 0.005	0.75
Mg/Al <sub>2</sub> O <sub>3</sub>	1.0	4.0	1.851	1.831 ± 0.005	1.04

Reprinted from [163] with permission from Springer.

Table 17  
Results of grain size study and CTE measurements of Mg–Al<sub>2</sub>O<sub>3</sub>

Materials	Reinforcement (vol.%)		Grain size ( $\mu\text{m}$ )	Aspect ratio ( $\rho$ )	CTE ( $\times 10^{-6} \text{ }^\circ\text{C}^{-1}$ )
	50 nm	0.3 $\mu\text{m}$			
Mg	–	–	36 ± 4	1.65 ± 0.45	28.6 ± 0.8
Mg/Al <sub>2</sub> O <sub>3</sub>	0.5	4.5	24 ± 8	2.26 ± 0.91	27.2 ± 1.2
Mg/Al <sub>2</sub> O <sub>3</sub>	0.75	4.25	27 ± 9	1.83 ± 0.51	25.7 ± 0.6
Mg/Al <sub>2</sub> O <sub>3</sub>	1.0	4.0	31 ± 7	1.65 ± 0.42	25.8 ± 0.8

Reprinted from [163] with permission from Springer.

Table 18  
Results of room temperature tensile properties of Mg–Al<sub>2</sub>O<sub>3</sub>

Materials	Reinforcement (vol.%)		Elastic modulus (GPa)	0.2% YS (MPa)	UTS (MPa)	Ductility (%)
	Submicron	Nano				
Mg	–	–	45	116 ± 11.1	168 ± 10	9.0 ± 0.3
Mg/Al <sub>2</sub> O <sub>3</sub>	4.5	0.5	50.5	139 ± 26.5	187 ± 28	1.9 ± 0.2
Mg/Al <sub>2</sub> O <sub>3</sub>	4.25	0.75	51.9	138 ± 13.2	189 ± 15	2.4 ± 0.6
Mg/Al <sub>2</sub> O <sub>3</sub>	4.0	1	54.4	157 ± 20.3	211 ± 21	3.0 ± 0.3
Mg/SiC <sub>p</sub> <sup>a</sup>	10	–	45	120	160	2
AZ91/SiC <sup>b</sup>	10	–	44.7	135	152	0.8
Mg/21.3SiC <sup>c</sup>	21.3	–	50	128 ± 1.9	176 ± 3.5	1.4 ± 0.1
Mg/SiC/Al <sub>2</sub> O <sub>3</sub> /SiO <sub>2</sub> <sup>d</sup>	8	–	53.4	–	201.3	2.13

Reprinted from [163] with permission from Springer.

<sup>a</sup> Data obtained from [175].

<sup>b</sup> Data obtained from [176].

<sup>c</sup> Data obtained from [177].

<sup>d</sup> Data obtained from [178].

submicron and 1 vol.% nanosize Al<sub>2</sub>O<sub>3</sub> particulates. The addition of Al<sub>2</sub>O<sub>3</sub> particulates led to a reduction in the ductility of the magnesium matrix. However, it should be noted that within hybrid composites increasing addition of nanosize Al<sub>2</sub>O<sub>3</sub> particulates led to an increase in the ductility. The overall combination of mechanical properties exhibited by hybrid composite formulations synthesized in this study is found to be better than that of conventional Mg-based composites containing higher volume fraction of reinforcement and synthesized using other processing routes [175–178] (see Table 18).

**3.3.5.3. Alloys of magnesium.** There are Mg-based alloys that are also processed through extrusion and some interesting properties have been recorded [164,170]. Mg–Al–Nd [164] and Mg–Zn–Y [170] alloy systems are investigated. The former system has been prepared by mechanical alloying route followed by cold compaction and sintering. The compacts were later extruded. The extrusion parameter details were laid out in Table 14. Tensile tests on extruded samples were carried out and the data is listed in Table 19. It should be noted that the strength of the mechanically alloyed specimens is larger than those of unmilled ones. Ductility of the mechanically alloyed specimen is larger than those of unmilled samples. Strength of specimens is also dependent on Nd composition. In addition to slip and twinning of Mg, other mechanisms such as low temperature creep may play a very important role in enhancing the ductility of the samples. Also, the yield strength of alloys with high Nd content (C series) is higher than that of the samples A and B series (low Nd content). Such increase is attributed to the reduction in the grain size as well as enhanced diffusion after mechanical activation.

Table 19  
Tensile properties of Mg–5% Al–Nd alloys

Specimen	0.2% YS (MPa)		Elongation (%)	
	zzz = 400 °C	zzz = 500 °C	zzz = 400 °C	zzz = 500 °C
A0-zzz	227	216	4.6	4.9
A20-zzz	276	223	10.8	17.4
A30-zzz	297	217	2.2	5.8
B0-zzz	212	208	3.9	5.1
B20-zzz	351	331	9.2	5.6
B30-zzz	346	225	3.6	12.3
C0-zzz	190	311	2.7	3.3
C20-zzz	422	436	1.7	2.6
C30-zzz	271	333	1.6	5.9

Reprinted from [164] with permission from Elsevier. zzz: sintering temperature; 0, 20, 30: milling time (h); A: Mg–5% Al–0.5% Nd; B: Mg–5% Al–1% Nd; C: Mg–5% Al–5% Nd.

$Mg_{95}Zn_{4.2}Y_{0.8}$  [170] alloys were prepared by melting ingredient elements together in an electric arc furnace. The cast alloy was homogenized by annealing at 673 K for 10 h and then extruded. TEM micrograph from extruded alloy ( $Mg_{95}Zn_{4.2}Y_{0.8}$ ) after testing at 473 K shows very fine precipitates (nano) inside grains. The matrix zone axis is found to be  $[0\ 1\ 0]$ . Irregular-shaped large particles of the icosahedral phase, small precipitates and long rods of  $\beta'_1$  phase were found. Icosahedral phase particles seem to be irregularly shaped with over 100 nm in size and were located inside the grains, as shown in Fig. 57. Ultrafine nanometer-sized particles are retained in the matrix. Lengthening of these precipitates apparently occurred during tensile testing at this temperature.

The tensile strength data of as-extruded alloys are given in Fig. 58a. It could be seen that due to softening the yield strength and UTS decreases gradually as temperature is increased and more elongation could be achieved. The as-extruded samples were given isothermal treatment at 673 K for 1 h followed by water quenching in order for the precipitates to dissolve in the matrix and then reprecipitate, without affecting the icosahedral phase. The icosahedral grains became rounded. Fine precipitation of  $\tau_1$  phase is also detected. The stress–strain plot at room temperature for the alloy is given in Fig. 58b. The yield strength is reduced and it could be improved by ageing at 473 K by which lengthening of the  $\beta_1$  rods occurred. Fig. 58d shows the bright field micrograph of a matrix grain viewed along  $[0\ 0\ 1]$  zone axis after heat treatment, in a sample tensile tested at room temperature. A network of dislocations is observed, the dislocation lines terminating at icosahedral phase particles of 200 nm. The diffraction from one such surrounding phase, marked in the micrograph, is inset. The diffraction pattern suggests that this phase is the  $\tau_1$  phase. Fig. 58c shows the curves for tensile tests at 473 K. The yield strength and the UTS are improved on heat treatment. The icosahedral phase particles appear to be acting as strong pinning centers thereby leading to the improved strength. It also exhibited strength comparable to AZ61, while maintaining a better stability and a high failure stress.

**3.3.5.4. Aluminum-based alloys.** Nanocrystalline Al–Ti alloy [165] powders were produced by reactive ball milling (RBM) in a hydrogen atmosphere and its microstructure consisted of nanosized Al and nanosized  $TiH_2$ . The powders were consolidated by hot extrusion at 500 °C. The grain size of as-extruded specimens was about 50–100 nm. The grain sizes of the reactive ball milled specimens in  $H_2$  and hot extruded were much smaller than those of the specimen mechanically alloyed in Ar and hot extruded. The average grain size was 150–400 nm, as shown in Fig. 59a.  $Al_2O_3$  and  $Al_4C_3$  that were formed by reactions between Al and C and O in the process control agent also existed as dispersoids. The oxides, as indicated in Fig. 59b, had a round shape with 10 nm in diameter found inside the grain. Though  $Al_2O_3$  and  $Al_4C_3$  were not uniformly distributed through out the matrix, they may be the primary dispersoid strengthening phases because they were very small compared to  $Al_3Ti$ . Table 20 lists four samples processed from different extrusion conditions. Hardness along with the relative densities of as-extruded specimens is listed. The relative densities of all the specimens were 99% and above.

Al–10 wt.% Ti alloy [166] has been consolidated using the mechanical alloying–hydrostatic extrusion method and tested for their tensile properties. Different extrusion temperatures have been used to consolidate three different samples of same composition and the tensile data gathered is shown in Fig. 60. It is to be noted that, for the sample

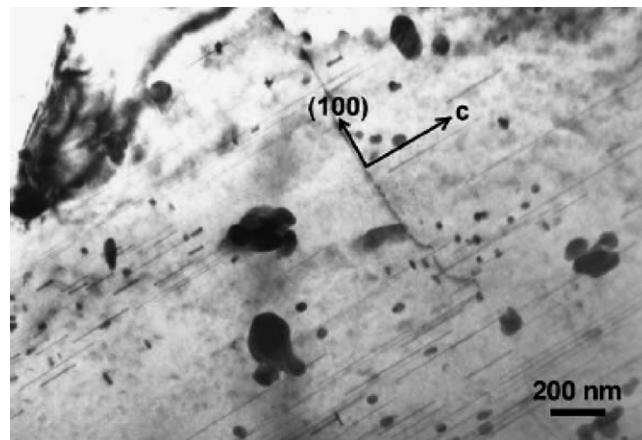


Fig. 57. TEM micrograph of alloy  $Mg_{95}Zn_{4.2}Y_{0.2}$  showing fine precipitates within grains (extruded at 473 K). (Reproduced from [170] with permission from Elsevier.)

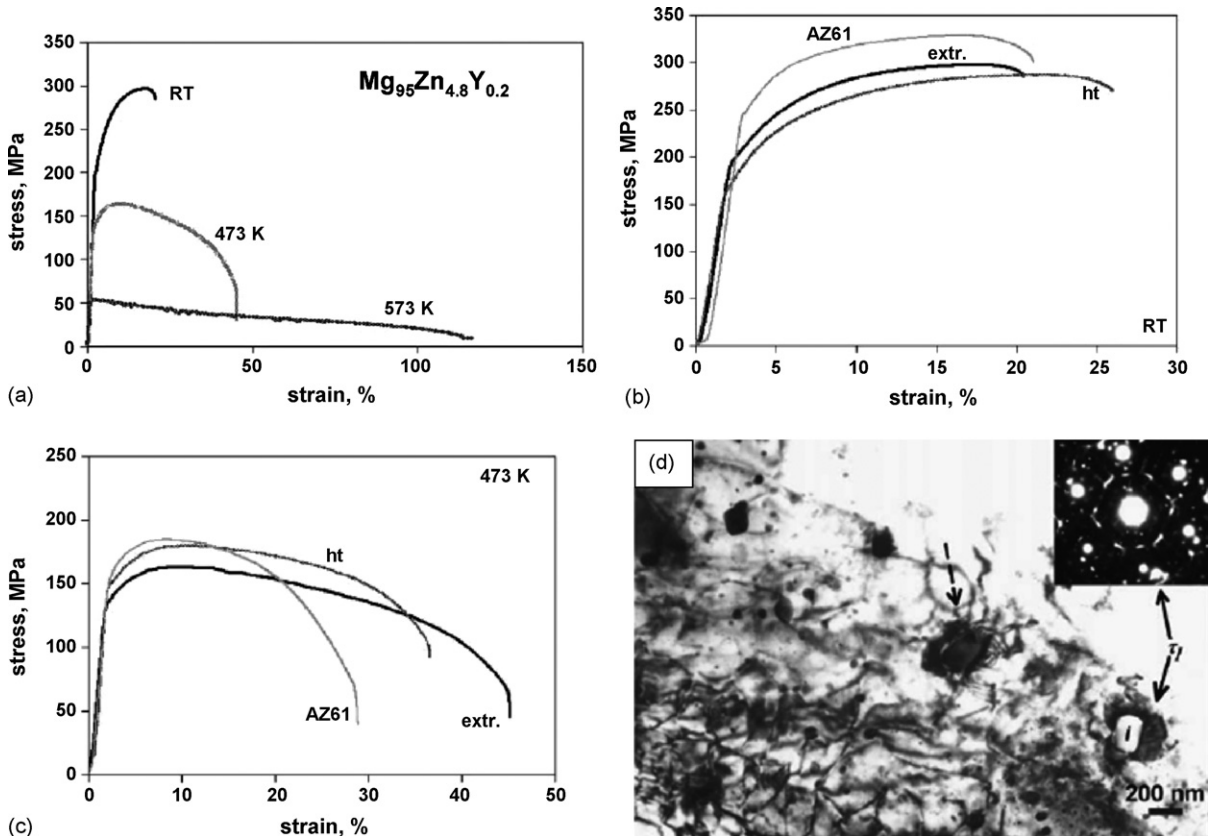


Fig. 58. (a) Tensile test data of as-extruded alloy at different temperatures, (b and c) room temperature and high temperature tensile data of the alloy in heat-treated condition, and (d) TEM micrograph of the heat-treated alloy after tensile test. (Reprinted from [170] with permission from Elsevier.)

processed at 300 °C extrusion temperature, the material behaved in a brittle manner during tensile testing, while for 350 °C processed sample, the ductility showed improvement with increased UTS. For the samples extruded at temperatures higher than 400 °C, elongation of about 24% is achieved. Temperature of extrusion plays a role in the tensile properties because of the fact that mechanical alloying leads to harder particles. Ball milling leads to lattice strains thereby leading to high hardness of particles which will fail to bind together unless there is a driving force, such as, temperature.

Al–Ni–Y-based alloys ( $\text{Al}_{85}\text{Ni}_{10}\text{Y}_5$ ) [168] have been processed using melt spinning technique followed by cold compaction, hot pressing and hot extrusion. TEM micrographs imaged in the region perpendicular to the extrusion direction of the alloy have been shown in Fig. 61a–c. In Fig. 61a, the unstable nanograins ( $\sim 20$  nm) with few dislocations are observed in the AlNiY alloy. Besides, the amorphous phase is frequently observed in the remaining matrix even though the consolidation temperatures are higher than the transition temperature of  $\text{Al}_{85}\text{Ni}_{10}\text{Y}_{95}$  amorphous alloy. For the AlNiY-250 alloy, the grains are relatively non-uniform and become more stable after annealing treatment as shown in Fig. 61b. In Fig. 61b and c, the grains with  $\sim 100$  nm containing fine intermetallic compounds indicated by arrow are obtained, while the grains below 100 nm without any precipitates and dislocations are obtained in the AlNiY-250 and AlNiY-400 alloys during the processing. It was found that the precipitates within grains of the AlNiY-400 alloy are somewhat larger than the AlNiY-250 alloy, resulting in an increase in the flow stress during high temperature deformation. Flow stress and strain data for these samples have been listed in Table 21. High strain rates could be achieved for nanostructured materials as a result of their high flow stresses, these materials could withstand. Flow stresses are increased due to an increase in grain boundary area that acts as impediments to dislocation movements.

**3.3.5.5. Mg–graphite nanocomposites.** Mg and its alloys are known for its automotive applications because of its light weight. In order to achieve high strength, Mg-based nanocomposites have evolved. Graphite (3 vol.%) is used as reinforcement using powder metallurgy route and hot extruded [167]. TEM micrograph showed an average grain size

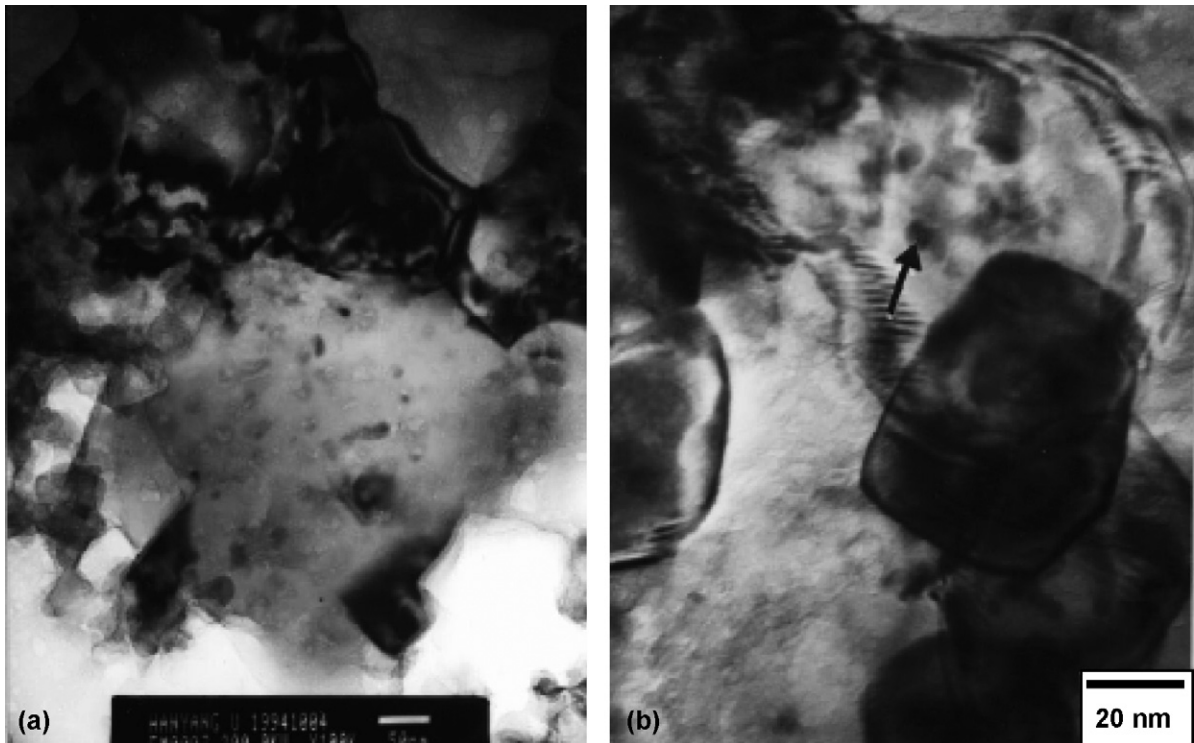


Fig. 59. (a) Bright field image of Al–8 wt.% Ti extruded at 500 °C and (b) Al–5 at.% Ti hot extruded at 450 °C. (Reprinted from [165] with permission from Elsevier.)

of 200 nm (Fig. 62a). The creep properties of pure Mg are compared to Mg–3 vol.% graphite (Fig. 62b). The tests are conducted at 200 °C. It is evident, these nanocomposites could withstand higher stresses than a pure Mg billet. Graphite particles might help in annihilating grain boundary diffusion which is responsible for good creep properties in these nanocomposites.

**3.3.5.6. Al–ZrO<sub>2</sub> nanocomposites.** Pure aluminum matrix nanocomposites reinforced with fine needle-like Al<sub>3</sub>Zr phase (100 nm width, 400 nm length) were synthesized by the reaction between nanocrystalline ZrO<sub>2</sub> particles and

Table 20  
Mechanical properties of as-extruded Al–Ti alloys

Specimen #	Hot extrusion conditions	Grain size (by TEM) (nm)	Relative density (%)	HV	HR <sub>B</sub>
1	Degassing condition: 500 °C for 3 h Pre-heat treating condition: 500 °C for 2 h Extrusion temperature: 500 °C	50–100	99.8	231.7	97.1
2	Degassing condition: 500 °C for 3 h Pre-heat treating condition: 550 °C for 2 h Extrusion temperature: 550 °C	100	99.8	197.5	87.6
3	Degassing condition: 500 °C for 1 h Pre-heat treating condition: 450 °C for 1 h Extrusion temperature: 450 °C	50	99.5	206.0	91.1
4	Degassing condition: 500 °C for 1 h Pre-heat treating condition: 500 °C for 1 h Extrusion temperature: 500 °C	<50	99.6	287.0	102.6

Reprinted from [165] with permission from Elsevier. Extrusion velocity, 6 mm s<sup>-1</sup>; extrusion ratio, 25:1; load, 1.5 GPa; specimen #4 produced by using a Cu scan.

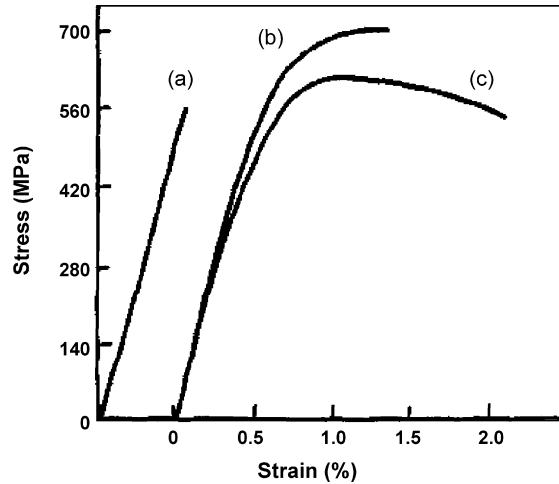


Fig. 60. Tensile stress–strain curves of Al–Ti: (a) hot pressed at 300 °C and extruded at 300 °C, (b) hot pressed at 350 °C and extruded at 350 °C, and (c) hot pressed at 400 °C and extruded at 450 °C. (Reprinted from [166] with permission from Elsevier.)

pure aluminum using powder metallurgy followed by extrusion and hot rolling [169]. After extrusion, the composite fabricated with 5 vol.%  $\text{ZrO}_2$  had strain rate sensitivity ( $m$  value) of 0.31 and a total elongation of 156% at 650 °C and  $1.3 \times 10^{-1} \text{ s}^{-1}$ . The high strain rate superplasticity was improved by hot rolling. After hot rolling, the  $m$  (strain rate sensitivity) value of the composite fabricated with 10%  $\text{ZrO}_2$  particles was 0.4 and the total elongation was 204% at 640 °C and  $1.3 \times 10^{-1} \text{ s}^{-1}$ . A TEM image as shown in Fig. 63 in the hot extruded condition of the composite shows a

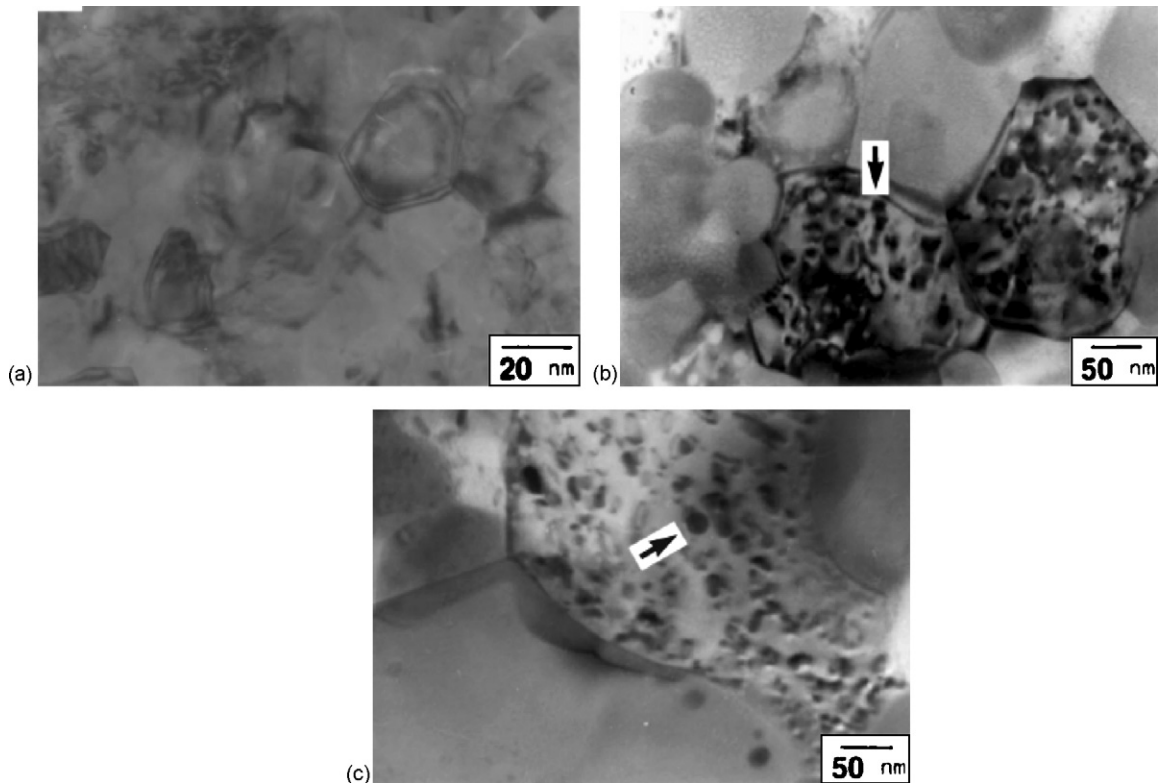


Fig. 61. (a–c) TEM micrograph of: sample 1 (AlNiY), sample 2 (AlNiY250), and sample 3 (AlNiY400) after extrusion. Table 21 showing the tensile test data for sample 1 (AlNiY), sample 2 (AlNiY250), and sample 3 (AlNiY400) at 450 °C. (Reprinted from [168] with permission from Kluwer.)

Table 21

The tensile test data for sample 1 (AlNiY), sample 2 (AlNiY250), sample 3 (AlNiY400) at 450 °C

Sample	Flow stress	Flow strain
1	161	1.14
2	142	1.07
3	190	1.73

Reproduced from [168] with permission from Kluwer.

needle-like phase (A) and an equiaxed phase (50 nm) (B). Strain rate and temperature at which maximum total elongation is attained for various aluminum matrix composites reinforced with fiber-like phase (see Tables 22 and 23). It is to be noted that the Al–ZrO<sub>2</sub> nanocomposites need lower temperature to achieve maximum elongation compared to other alloy systems [180–185] listed in the table. Grain boundary sliding coupled with interfacial sliding is found to dominate which is a contributing factor to the higher elongation.

In summary, non-ferrous light weight metals such as Al and Mg alloys have been investigated either with ceramic reinforcements or as nanocrystalline alloy for enhanced mechanical properties such as UTS, yield strength, superplasticity, and hardness. Very few processes are capable of processing nanostructured materials to bulk form with retention of nanostructures and hot extrusion seems to be one of the promising technology. Some of the reasons for the retention could be the time involved in processing and lower processing temperatures to achieve highest possible density.

### 3.4. Sintering

#### 3.4.1. Introduction

Sintering is a consolidation method to compact loose powders to a bulk component. During this process, particles bond together and annihilate the voids, resulting in dense structures with complex shapes. Ancient sintering practice for pottery making and ceramic art objects remain in vogue even today. Most ceramic materials have a lower affinity for water and a lower plasticity index than clay, requiring organic additives in the stages before sintering. The general procedure of creating ceramic objects via sintering of powders has been mixing water, binder, anti-flocculant and ceramic powder to form slurry, spray drying, putting the spray-dried powder in to a mold and pressing it to form a

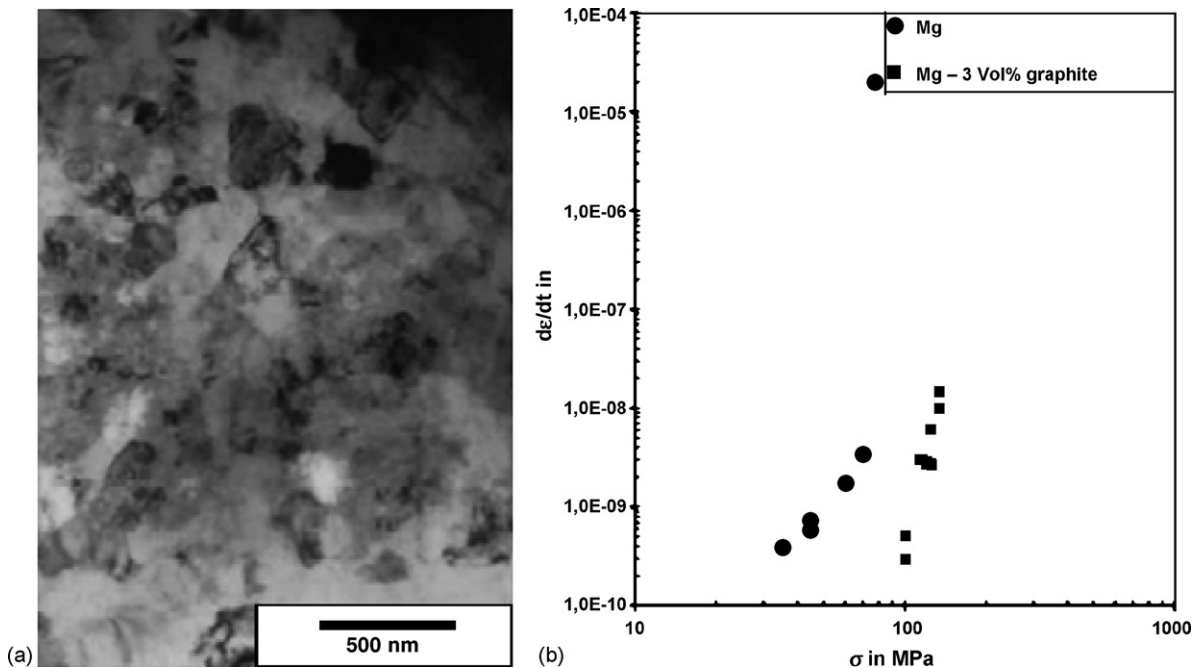


Fig. 62. (a) TEM image of Mg–3 vol.% graphite in extruded condition and (b) steady state creep rates as a function of applied compressive stresses. (Reprinted from [167] with permission from Wiley.)

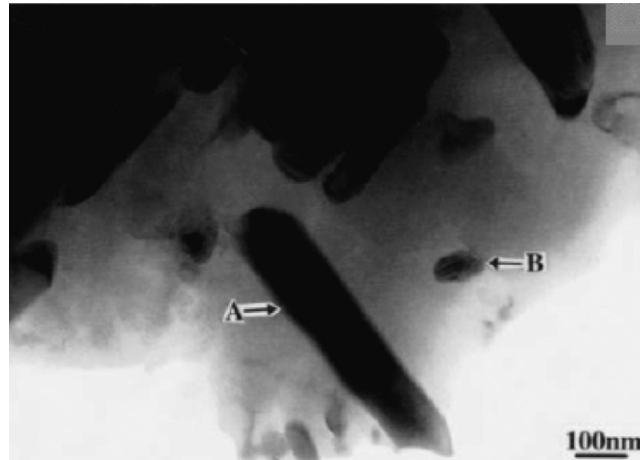


Fig. 63. TEM micrograph of hot extruded Al-ZrO<sub>2</sub> composite. (Reprinted from [169] with permission from Manny.)

Table 22

The tensile data for two different composition variants of Al-ZrO<sub>2</sub>

Sample	$m$	Elongation
Al-5% ZrO <sub>2</sub>	0.31	156
Al-10% ZrO <sub>2</sub>	0.4	204

Reproduced from [168] with permission from Kluwer.

green body (an unsintered ceramic entity). This is followed by heating the green body at lower temperatures to burn off the binder and sintering at high temperature. Metals could be processed to complex shapes using this technique as well. One classic example is the development of self-lubricated bearing used in almost all rotors.

### 3.4.2. Fundamental principles

A schematic drawing of how particles fuse together by application of thermal energy is shown in Fig. 64. Such process is dependent on diffusion of atoms that combine distinct powder particles into one cohesive material. Fusion occurs well below the melting point of the material, but at a temperature sufficiently high enough to allow an acceptable rate of diffusion to occur, usually at greater than one-half of the melting point on a Kelvin scale. The powder particles are thus compacted together thereby forming a compacted mass of powder particles that resembles a close packed crystal structure, with the powder particles being analogous to the atoms of the crystal.

### 3.4.3. Advantages

- The purity of the material is guaranteed due to very few processing steps.
- The processing can be done in controlled environment.
- Easy to achieve complex shapes.

Table 23

Mechanical properties of extruded Al-ZrO<sub>2</sub> nanocomposites

No.	Sample	Strain rate (s <sup>-1</sup> )	$T_{sp} - T_i$ (°C)
1	$\alpha$ -Si <sub>3</sub> N <sub>4</sub> (w)-2124Al [27]	0.5	23
2	SiC (w)-2009Al [28–30]	0.3	22
3	Si <sub>3</sub> N <sub>4</sub> (w)-2124Al [31]	0.2	23
4	$\beta$ -Si <sub>3</sub> N <sub>4</sub> (w)-2124Al [32]	0.2	23
5	Al-5% ZrO <sub>2</sub> [16]	0.1	-5
6	Al-10% ZrO <sub>2</sub> [16]	0.1	-20

Reproduced from [169] with permission from Manny.  $T_i$ : incipient melting point of matrix;  $T_{sp}$ : temperature at which maximum elongation is achieved.

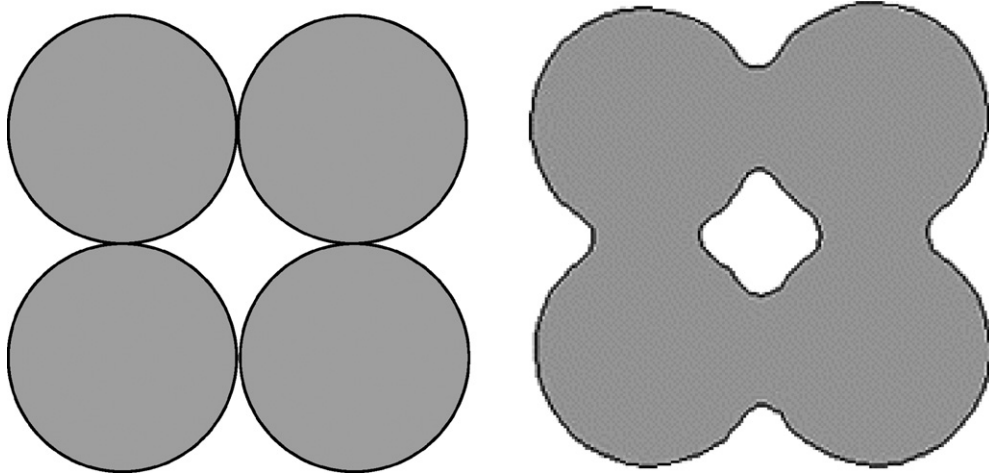


Fig. 64. A schematic showing individual particles fusing together and annihilating the voids.

#### 3.4.4. Equipment—process and mechanism

The characteristics of the raw materials (powders) such as particle size and % purity are very important as they affect the microstructural and mechanical properties of the final component. Since strength increases with decreasing grain size, most starting powders are milled (or ground) to produce a fine powder. Since dry powders are difficult to be compacted, processing additives such as water, polymers, etc., are added to improve their plasticity. Consolidation involves forming the ceramic mixture into the specified shape. There are many techniques available for this step. Some of the techniques are described schematically in Fig. 65.

Sintering is the final step in the process. Sintering at high temperatures (800–1800 °C) can be carried out through high temperature furnaces that are equipped with the programmable PLCs so that heat treatment cycles can be programmed. Vacuum sintering could also be done with chambers equipped for controlled environment.

#### 3.4.5. Nanoconsolidation

While sintering could be used to consolidate the micron-sized grains, the kinetics of densification is not quite suitable for consolidating nanostructured materials. Enhanced sintering techniques such as spark plasma sintering

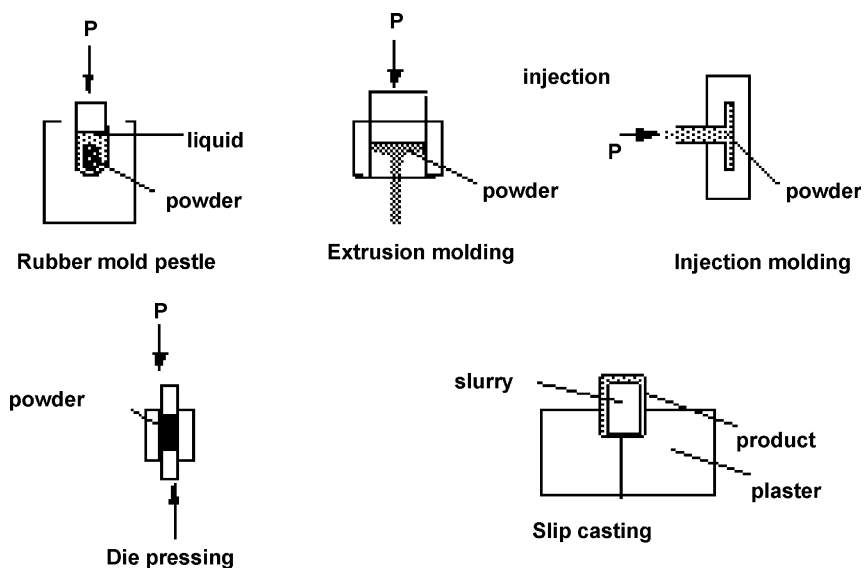


Fig. 65. Some of the ceramic compaction techniques available before sintering. (Source: <http://matse1.mse.uiuc.edu/~tw/ceramics/prin.html>.)

have been introduced to restrict the grain growth and enhance the densification kinetics [186,187]. Chen and Wang [187] proved that by two stage sintering process, it could be possible to achieve retained nanostructures (cubic  $Y_2O_3$ ) without any applied pressure.

Sintering is being used to successfully consolidate the following systems without application of external forces such as pressure.  $Y_2O_3$  [187],  $Si_3N_4$  [188],  $Mg-MgO-Mg_2Cu$  [101,189],  $W_2C-Si_3N_4$  [190],  $BaTiO_3$  [191],  $MgTiO_3$  [192],  $ZrO_2$  [193],  $WC-Co$  [194],  $Al_2O_3-SiC$  [195],  $Cu-Al_2O_3$  [196]. While most of the systems could effectively retain their nanostructures, some were able to achieve maximum densification with little grain growth.

**3.4.5.1.  $Y_2O_3$ .** Two stage sintering has been first reported by Chen and Wang [187] for consolidation of nano- $Y_2O_3$  powders without appreciable grain growth compared to a single stage sintering. Sintering has been carried out at 1000 °C without applied pressure. During the first stage itself, a high starting density needs to be achieved. Densities up to 75% should be sufficient for effective results in the second stage. Grain boundary diffusion will enable to fill in the rest of the pores left during the first stage. Second stage sintering appears to take place in an already ‘frozen microstructure’ created during the first stage as a result, the kinetics of grain growth are retarded but enough to fill in the rest of the pores. Fig. 66 compares the grain growth sequence during normal sintering and two stage sintering. With dopants such as Mg, grain coarsening could be further restricted and a maximum grain size of 60 nm could be seen in the microstructure as shown in Fig. 66b.

**3.4.5.2.  $Si_3N_4$  nanoceramics [188].** Two stage sintering is also being used for processing silicon nitride ceramics known for its high temperature applications. The 6 wt.%  $Y_2O_3$ –3 wt.%  $Al_2O_3$  additives is used to carryout sintering in two stages with a peak temperature of 1750 °C during the first stage and a peak temperature of 1450 °C during the second stage with a holding time of 20 h that yielded a 97% theoretical density as shown in Fig. 67b. It should be noted that for the same theoretical density of the nanoceramics during two stage sintering, there is no appreciable grain growth as observed in conventional sintering. The corresponding SEM microstructure reveals  $\beta$ - $Si_3N_4$  grains with an average grain size of 67 nm (Fig. 67a).

**3.4.5.3.  $Mg-Mg_2Cu-MgO$  nanocomposite [101].** Nanoparticles of magnesium oxide (MgO) effectively kill bacteria, including *E. coliform* and *anthrax* [197]. The biocidal action is due to the fact that nanowires have an opposite electrical charge from bacteria. The bacteria become attracted to the nanoparticles, which have a sharp edge that penetrate the bacteria’s tough outershell, causing death within 5 min. The MgO nanowires in Mg–MMCs have been found to have the property inducing biocidal actions. A ternary powder mixture with 80 wt.% Mg, 10 wt.% Cu, 10 wt.% CuO has been ground, cold pressed and sintered in argon atmosphere at 450 °C. MgO is located mainly along

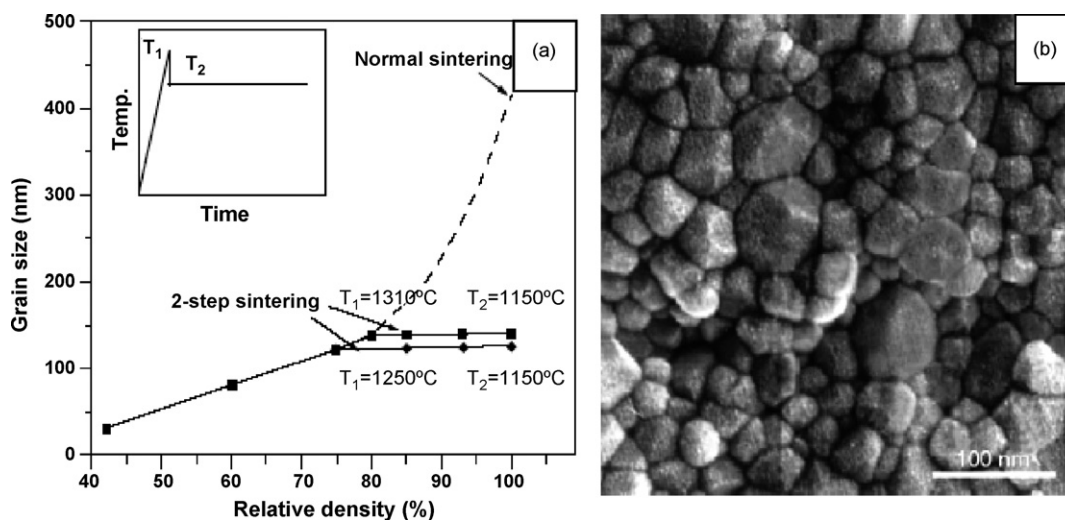


Fig. 66. (a) Grain growth as a function of relative density during normal sintering and two step sintering and the (b) 60 nm grains in  $Y_2O_3$ –1% Mg microstructure. (Reprinted from [187] with permission from Macmillan Publishers.)

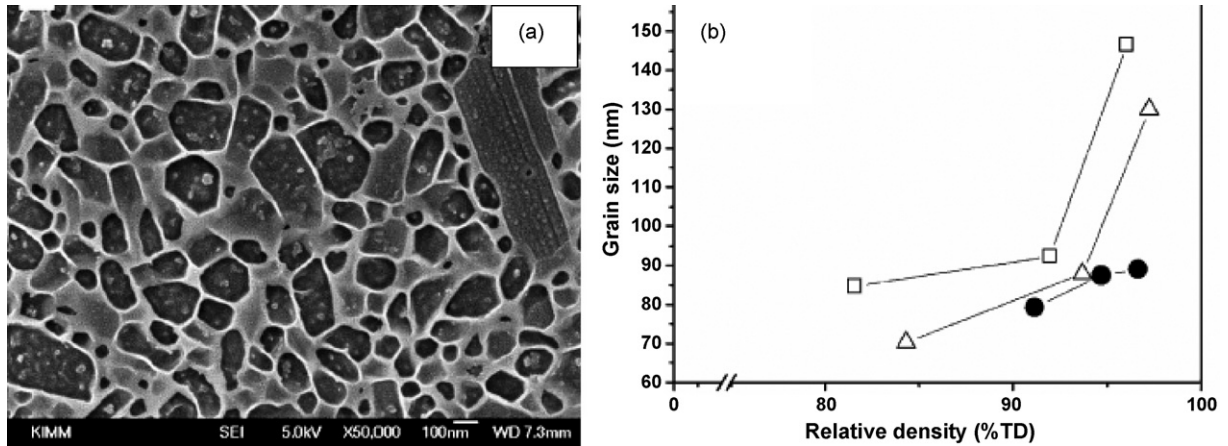


Fig. 67. (a) Nano-Si<sub>3</sub>N<sub>4</sub> processed using double stage sintering showed little coarsening especially in the second stage and (b) high densification could be achieved with grain growth rate much lower compared to the conventional sintering. (Reprinted from [188] with permission from Elsevier.)

the grain boundaries (light) along with few Cu particles (dark) as shown in Fig. 68. As an application to exploit its anti-bacterial property, the samples containing MgO was exposed to air for more than 48 h, the MgO nanowires absorbed some chlorine in their surface which facilitated the biocidal action of the bacteria. Due to the large surface area of the MgO nanowires they could potentially be used in building electronic packaging materials that contain anti-bacterial properties to exploit in hospitals and potential locations of biological attack.

**3.4.5.4. W<sub>2</sub>C–Si<sub>3</sub>N<sub>4</sub> matrix [190].** W<sub>2</sub>C nanoparticle reinforced Si<sub>3</sub>N<sub>4</sub> matrix composite has been sintered from tungsten solution-infiltrated porous Si<sub>3</sub>N<sub>4</sub> and the sliding wear and micro-tribological behaviors of W<sub>2</sub>C–Si<sub>3</sub>N<sub>4</sub> composite and sulfided W<sub>2</sub>C–Si<sub>3</sub>N<sub>4</sub> composite were studied. Due to the presence of W<sub>2</sub>C nanoparticles into the grain boundary phases of Si<sub>3</sub>N<sub>4</sub> the tribological properties are significantly improved. The W<sub>2</sub>C–Si<sub>3</sub>N<sub>4</sub> composite exhibited lower friction resistance when compared to the Si<sub>3</sub>N<sub>4</sub>. The average friction coefficient and specific wear rate of the sulfided W<sub>2</sub>C–Si<sub>3</sub>N<sub>4</sub> composite were 0.41 and  $5.6 \times 10^{-6} \text{ mm}^3 \text{ N}^{-1} \text{ m}^{-1}$ , under dry condition, 34 and 47% lower than those for the Si<sub>3</sub>N<sub>4</sub>, respectively. TEM micrograph of W<sub>2</sub>C–Si<sub>3</sub>N<sub>4</sub> nanocomposite sintered at 1850 °C for 4 h showed nanometer-sized spherical W<sub>2</sub>C particles dispersed along the grain boundary junctions (Fig. 69a). Fig. 69b reveals the cross-section of the wear tested samples of Si<sub>3</sub>N<sub>4</sub>, W<sub>2</sub>C–Si<sub>3</sub>N<sub>4</sub>, and sulfided W<sub>2</sub>C–Si<sub>3</sub>N<sub>4</sub> after a sliding distance of 1000 m. More wear scars could be seen for pure silicon nitride samples compared to the other two. The formation of the solid lubricant WS<sub>2</sub> on the surface of the W<sub>2</sub>C–Si<sub>3</sub>N<sub>4</sub> composite lowered both the friction coefficient and specific wear rate, and showed self-lubricated behavior during the sliding wear.

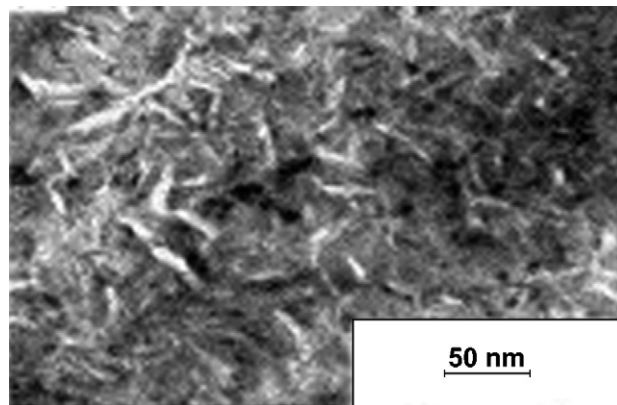


Fig. 68. MgO nanowires located on the grain boundaries of the Mg matrix nanocomposite potential anti-bacterial agent. (Reprinted from [189] with permission from Elsevier.)

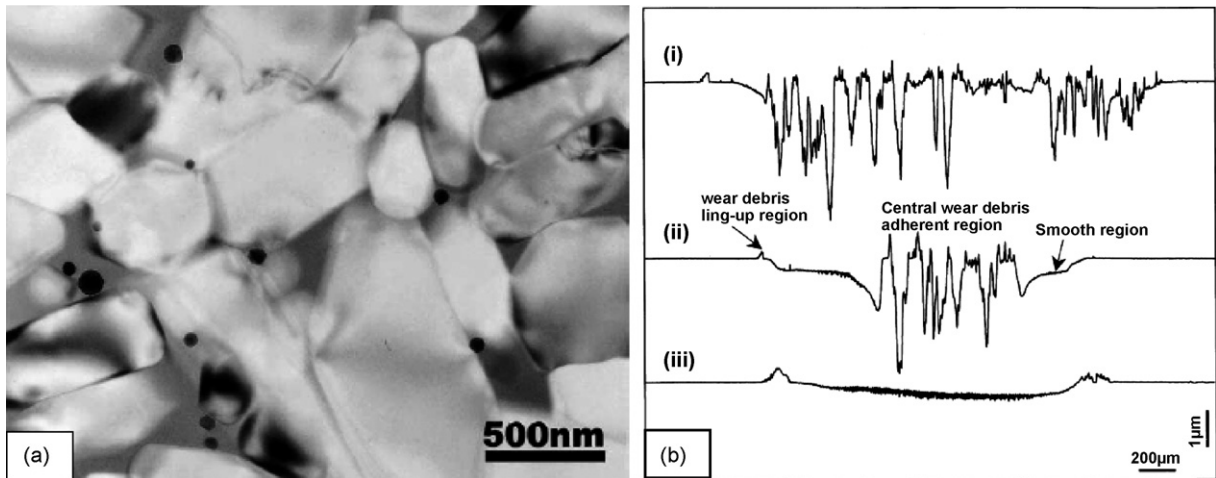


Fig. 69. (a) TEM pictures of the revealing  $W_2C$  particles in  $Si_3N_4$  matrix. (b) Cross-sectional profiles of wear scars from: (i)  $Si_3N_4$ , (ii)  $W_2C-Si_3N_4$ , and (iii) sulfided  $W_2C-Si_3N_4$  after a sliding distance of 1000 m. (Reproduced from [190] with permission from Elsevier.)

Sintering has been the first ever fundamental technique that was put forth to consolidate nanomaterials but then due to its inherent disadvantages in the form of grain growth, several variants of sintering including two stage sintering have been innovated. All the subsequent processings such as microwave and spark plasma sintering have gained a significant interest in the consolidation of nano and micromaterials.

### 3.5. Sinter forging

#### 3.5.1. Introduction

High strength, fracture resistance, dense microstructure, chemical inertness, and structural stability are the requirements of many structural ceramics. To enhance superplasticity in ceramics, glassy grain boundary can be introduced, which often results in inferior bulk properties, hence process of consolidating nanocrystalline grains is main attraction of research for producing nanocomposite ceramics [198]. Hence, in the past decade numerous advanced techniques have been mastered to produce bulk nanocrystalline powders to experience such advantages [199]. But high specific surface, extremely low bulk densities, and high reactivity is observed by non-oxide powders. Therefore, to potentially tap the exotic mechanical and microstructural properties of nanopowders, special consolidation techniques are required without incurring grain growth [200]. Conventional powder metallurgy techniques often leave porosity after sintering, whereas sinter forging serves as a convenient way of reducing or eliminating porosity in the consolidated nanocomposites [201]. Deformations via sinter forging can accelerate disappearance of agglomerated pores, acquire rapid densification and achieve consolidation with limited grain growth [202]. Moreover, anisotropy can also be introduced to take advantage of directional properties of the nanocomposites via sinter forging [203]. Sinter forging strongly reduces time and temperature for densification during consolidation of nanocomposites without incurring exaggerated grain growth [198].

#### 3.5.2. Fundamental principles

Sinter forging is simultaneous deformation, consolidation, and densification of porous ceramic nanocomposite at elevated temperature and uniaxial pressure [199,204]. High pressure application helps reducing the free volume, thereby facilitating atomic jumps across grain boundary, slowing down grain growth and achieving higher densification [205]. Limiting the sintering temperatures (200–300 °C less than that used for hot isostatic pressing) used in the consolidation help retaining the grains in desirable nanosize as that of the starting powders. Moreover, contamination, compositional changes, stresses and cracking can also be reduced with reduced processing temperature [206].

Dense compacts are produced by the stress assisted diffusion [199,207,208] or strain-controlled elimination of pore [199,209,210]. Sinter forging utilizes high shear strain to plastically deform rapidly and reduces coarse pores quickly.

Densification is directed both by applied stress and internal sintering stress to help pore closure and compaction of ceramic nanopowders. Intrinsic sintering stress germinates because of surface curvature ( $\kappa = 2\gamma/r$ , where  $\gamma$  is the surface energy and  $r$  is the pore radius).

In nanocrystalline material, sintering stress becomes dominant and cannot be neglected in determining overall stress. Apart from stress experienced by sintering particles, strain controls the deformation behavior for powder compaction. Material flow into the pore or closure of the pore is decided by strain-controlled densification. Kuhn and Ferguson model is widely accepted for densification mechanism [209]. Hence, mainly strain driven densification via pore closure, applied stress plastic deformation, and diffusion controlled pore curvature are impetus for densification of consolidated nanocomposites via sinter forging. Sinter forging suppresses grain growth during nanoconsolidation due to limited exposure to high temperature and rapid densification to theoretical density [205]. Consolidation of nanoparticles can considerably result in reduction of sintering temperature [211].

Fine initial microstructure helps plastic deformation of ceramics when the crystallite size is much smaller than the particle size, in other words, diffusional densification will be slower and fine grain size will be retained after sinter forging nanoconsolidation technique. Contribution from pore curvature and applied stress contribute to the total driving force for sinter densification (Fig. 70) [211].

### 3.5.3. Advantages

In order to improve fracture toughness, damage tolerance, and reducing weight and cost of ceramics, many approaches of introducing controlled porosity in the microstructure have been attempted. Few of the advantages of sinter forging of nanocomposites include:

- Control of grain boundary composition, grain size distribution, and porosity control can be achieved by manipulating the processing conditions [212].
- Grain alignment can be achieved using the directional uniaxial stress application.
- Disappearance of large defects result in improved strength of consolidated nanocomposite.
- Hot consolidation using conventional techniques is usually a challenging problem, which could be avoided in sinter forging [213].
- Since the processing is usually short and in under protective environment, contamination from light elements such as oxygen and carbon, is very low [213].
- Reduction of residual flaws and improved mechanical properties can be expected from sinter-forged consolidation [198].
- With application of compressive stress, more necks form in an early sintering stage leading to rapid sintering of consolidated nanocomposite [214].

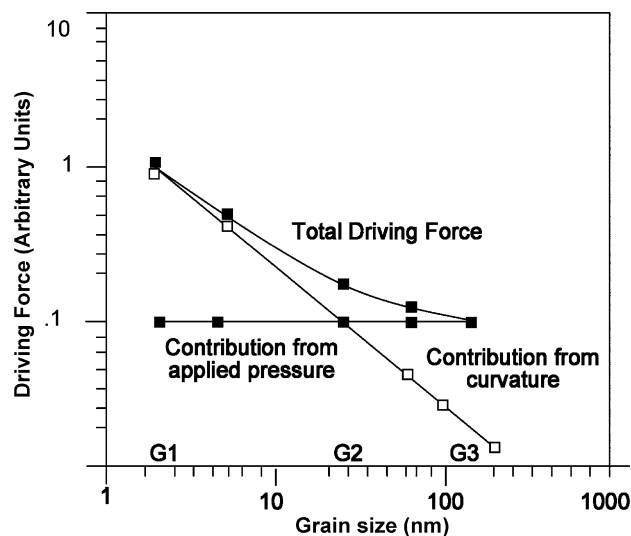


Fig. 70. Contribution of pore curvature and applied stress towards consolidation of nanocomposite.

### 3.5.4. Equipment—process and mechanism

Sinter forging has very simple experimental setup requiring conventional hot pressing equipment and graphite/WC die for compaction. Hot press (such as HP20-4560-20, Thermal Technology Inc., Santa Barbara, CA) can be used for consolidating the green compact at elevated pressures.

Sinter forging is carried out as a two-step process. Initially, a preform is compacted near room temperature using graphite/tungsten carbide die at pressures ranging  $\sim 1$  GPa for a few hours. Resultant green density ranges between 70 and 80% of the theoretical density. Then this green compact is hot pressed at high pressures (1–1000 MPa) and elevated temperatures (350–1850 °C) for duration of 1 min to 1 h. This hydrostatic state helps closure of cracks, thereby improving the ductility and surface finish of the fabricated nanocomposite. This process holds tremendous potential of consolidating nanocomposites and retaining the nanostructure in the bulk component [205]. Fig. 71 represents a schematic of the sinter forging process, i.e. from formation of green presintered compact followed by sinter forging to result densified nanocomposite. Grain boundary property is the critical factor in deciding the mechanical and toughness properties of the consolidated nanocomposite. Elimination or reduction of continuous amorphous phase along the grain boundary, and resulting thinner and distributed second phase bonding the adjacent grains can significantly improve the bulk properties [205].

Agglomeration and distribution of pores can have significant effect on deciding the consolidation of the sintered structure. Nanostructure pore model can be represented by pore diameter and distances between pore interfaces, elucidating the agglomeration tendency of pores (Fig. 72) [200]. Open pore network transforms to closed/isolated pore structure as the sintering reaches final stage of densification.

Difference between pressureless sintering and sinter forging are represented by grain boundary consolidation since thin and regular grain boundary results via sinter forging (Fig. 73) [215–217]. Along with physical–chemical grain boundary, interface is presented in the cartoon depicting amorphous films (Fig. 74) [215].

As a function of time, axial strain decreases monotonically at specified temperature due to densification and grain growth. Fig. 75 shows an initial density of 68% for  $n$ -TiO<sub>2</sub> (with grain size of 10 nm) at 700 °C, which densifies to 91% theoretical density and final grain size of 60 nm [218].

### 3.5.5. Nanoconsolidation

3.5.5.1. ZrO<sub>2</sub>/Al<sub>2</sub>O<sub>3</sub>. Alumina possesses high grain boundary mobility, hence grain rapidly coalesce to result large grain sizes after sintering. Secondly, low grain boundary cohesion results cavitation in sintered alumina ceramic.

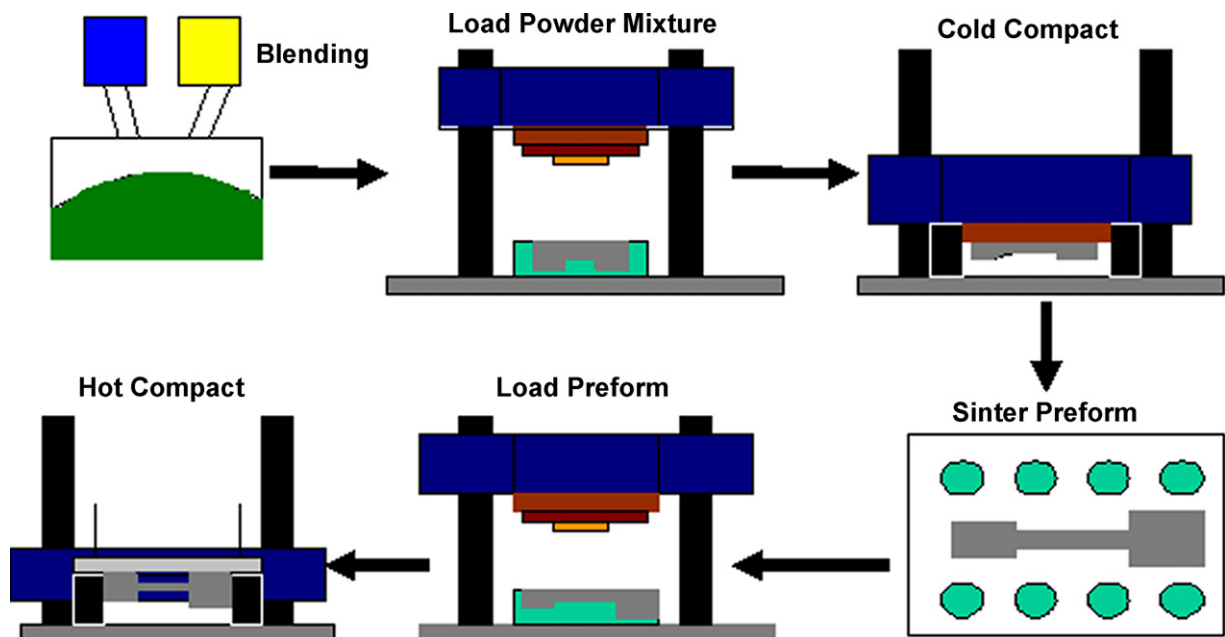


Fig. 71. Schematic of sinter forging process.

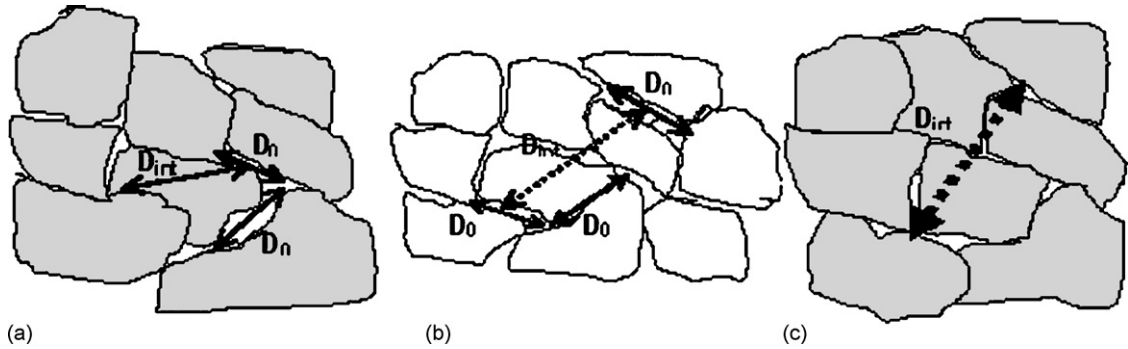


Fig. 72. Nanostructured grain/pore: (a) without agglomeration ( $D_{int} \sim D_0$ ), (b) with agglomeration ( $D_{int} > D_0$ ), and (c) without agglomeration (near fully sintered,  $D_{int} > D_0$ ).

Moreover, rapid strain hardening induces brittleness due to dynamic grain growth of the ceramic. Hence, sinter forging of alumina, with dispersion of zirconia, can result in reduction of defects will enhanced strength ( $>1$  GPa) [219].

Sinter forging of alumina–15 wt.% zirconia was sinter-forged at 1400–1450 °C for 15 min at 40 MPa to yield grain size of 200 nm. Densification behavior when compared to free sintering depicts quicker densification times for sinter-forged samples (Fig. 76) [214]. Applied compressive stress assists lower temperature transformation  $\theta$ - to  $\alpha$ -alumina owing to high density of  $\alpha$ -alumina [198,214]. Improved fracture toughness of sinter-forged samples is achieved when compared to free sintered samples [198]. Strong textures are also reported by sinter forging of alumina–zirconia nanocomposites (Fig. 77) [214].

Sinter forging of nanosized 2.5 mol.% yttria-stabilized zirconia was done at 1200 °C at stresses between 4 and 60 MPa for 2–60 min. Grain growth rate was observed to increase with increase in the applied pressure with higher stresses resulting rapid consolidation density [220].

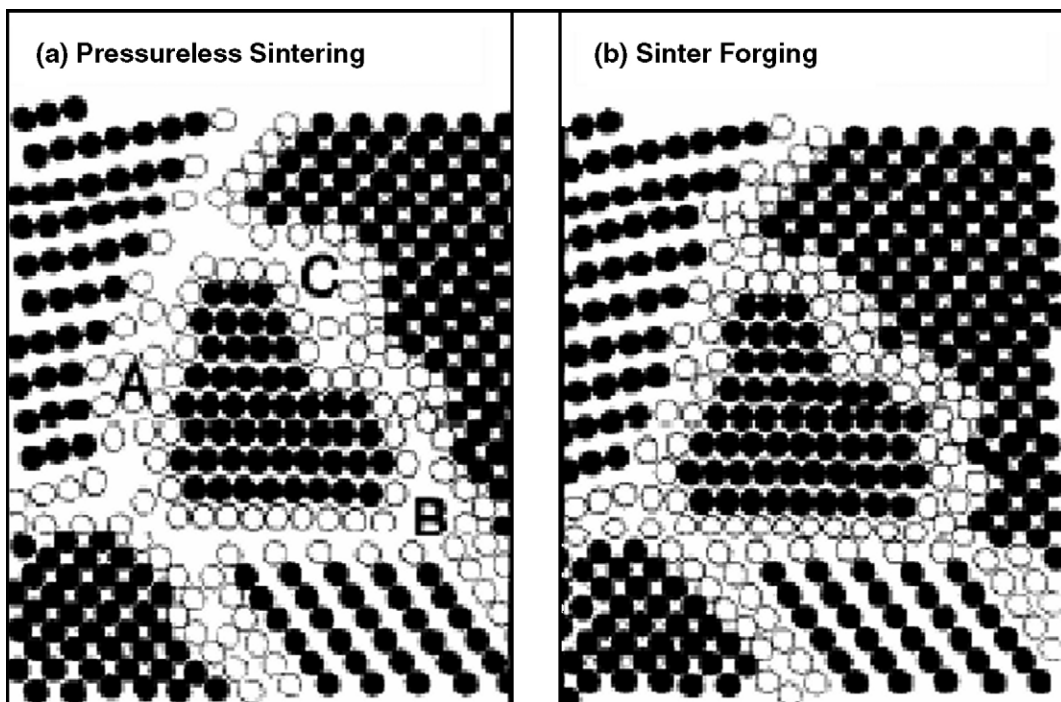


Fig. 73. Atomic arrangement in grains (solid circles) and grain boundary (open circles) during pressureless sintering (a) and sinter forging (b). (Reprinted from [215] with permission from Elsevier.)

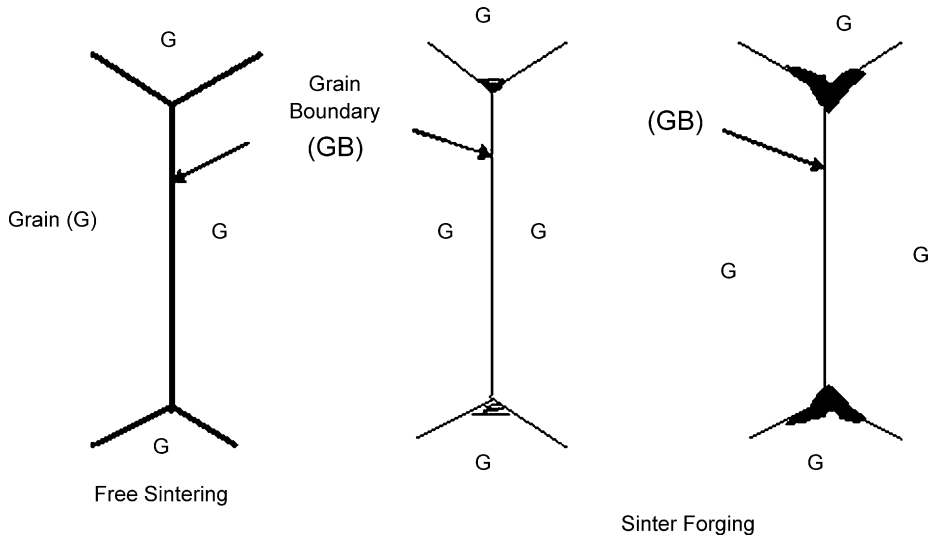


Fig. 74. Physical–chemical state of ceramic grain boundary after pressureless sintering or sinter forging.

Grain boundary reinforcement and elimination of flaws can help restricting intergranular fracture in sinter-forged fine-grained tetragonal zirconia polycrystal (TZP) ceramics [215]. Sinter-forged zirconia–hematite nanopowders depicted finer grains when compared to pressureless sintered compacts [221]. Grain growth during sintering is rather unavoidable, but can be restricted by rapid consolidation of nanocomposite. Alumina grain inhibitors can be added to zirconia pellets for restricting grain growth. Grain growth as a function of relative density is presented in Fig. 78 [211]. Grain size during sinter forging as a function of relative density is also compared with that of free sintering for 3 mol.% yttria-stabilized zirconia (Fig. 79) [222].

TZP green compacts with 46% density were presintered to 1000 °C for 15 min at the rate of 2 °C min<sup>-1</sup>, followed by sinter forging at 1150 °C under 90 MPa with a dwell time of 25 min. Two samples TZP–5 mol.% YO<sub>1.5</sub> and

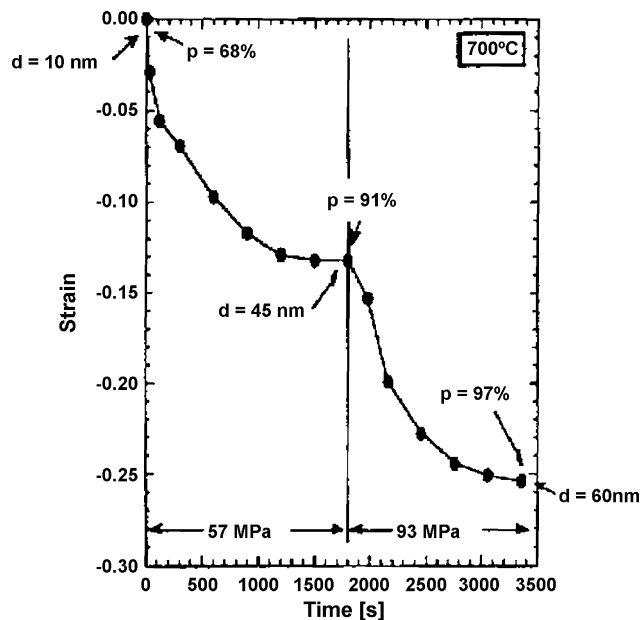


Fig. 75. Strain vs. time of a cylindrical sample under tension. (Reprinted from [218] with permission from MRS.)

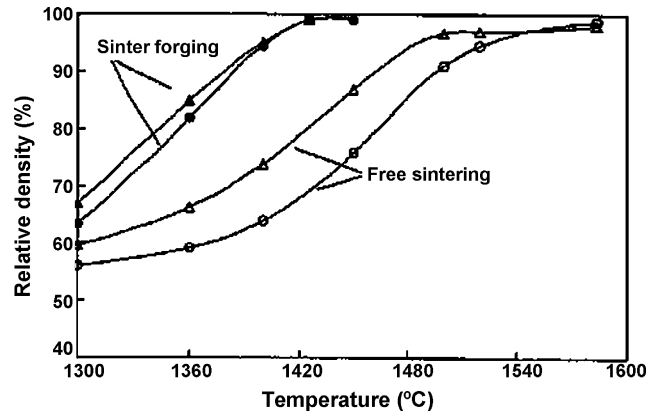


Fig. 76. Pressureless sintering and sinter forging densification behavior of zirconia toughened alumina (circles: calcined at 900 °C; triangles: calcined at 1100 °C). (Reprinted from [214] with permission from Springer.)

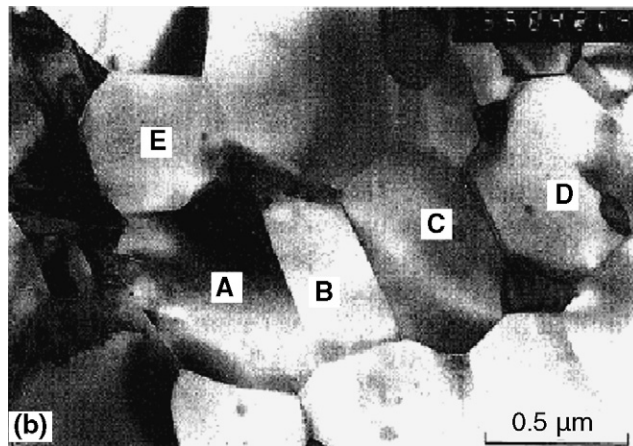


Fig. 77. TEM image of ZTA ceramic sintered at 1450 °C (15 min) followed by calcination at 1100 °C. (A–C) Grain elongation and (D and E) no grain elongation. (Reprinted from [214] with permission from Springer.)

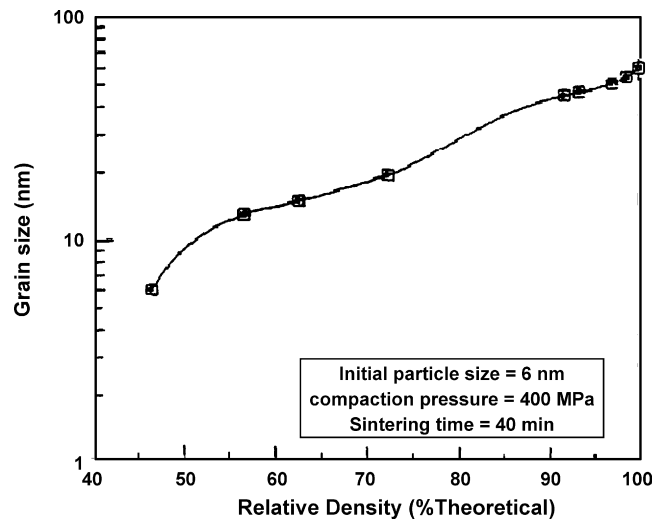


Fig. 78. Grain size as a function of percent theoretical density. (Reprinted from [211] with permission from Elsevier.)

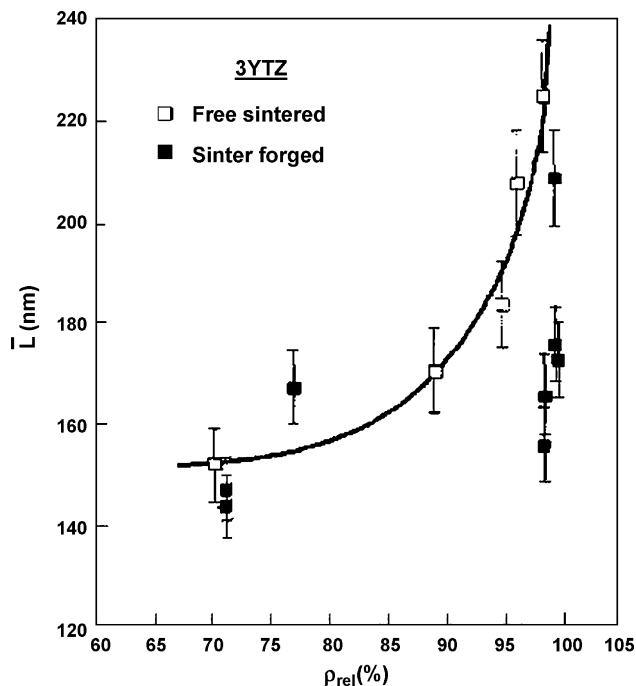


Fig. 79. Average grain size vs. relative density of free sintered (open symbols) and sinter-forged (filled symbols) 3YTZ. (Reprinted from [222] with permission from Elsevier.)

TZP-4 mol.%  $\text{YO}_{1.5}$ -4 mol.%  $\text{CeO}_2$  were sinter-forged and compared with properties obtained via pressureless sintering [215]. Finer grain size ( $\sim 0.18 \mu\text{m}$ ) and absence of large flaws in sinter-forged samples endorse superior mechanical properties (Fig. 80) as presented in Table 24 [215]. Grain boundaries and porosity at grain interface affect hardness values to a great extent when compared to that of pressureless sintering. Retention of finer grains after sinter forging succinctly depicted the difference from densification via pressureless sintering. Fracture energy improvement is attributed to grain boundary strengthening by various researchers (Table 25) [215].

Rapidly quenched  $\text{Al}_2\text{O}_3$ - $\text{ZrO}_2$  composite can be sinter-forged to utilize its excellent high temperature creep resistance. Absence of glassy grain boundary aptly distributes to form zircon without agglomerating and deteriorating intergrain cohesion and strength [223]. Uniform SiC distribution in  $\text{Al}_2\text{O}_3$  matrix resulted improved tensile strength than extruded samples owing to restricted flaw induction from processing [224]. Poor interparticle bonding was observed in sinter-forged SiC dispersed  $\text{Al}_2\text{O}_3$  composite when compared to that of hot-forged sample [224]. Moreover, sinter-forged SiC incorporated alumina composites displayed inferior fatigue performance owing to poor SiC distribution serving as stress-raisers for fatigue crack initiation as seen in Fig. 81.

**3.5.5.2. SiN.** Instead of introducing second phase particles such as BN and C to decrease Young's modulus of Si-N composite, these composites depict low sinterability and poor oxidation resistance. Hence, introduction of porosity can offer advantages of good damage tolerance, lightweight structure and lower cost [212,225]. Controlled sintering of Si-N composite is therefore required to obtain very fine and distributed porosity in the consolidated structure. Moreover, grain boundary composition, grain size, and final porosity also hold importance in deciding the final properties of the fabricated nanocomposite [204]. Silicon nitride is sinter-forged with high temperature lutetia-silica additives for improving strength at elevated temperature. Glass free grain boundary is attained due to sinter forging, exhibiting good oxidation resistance, higher glass transition temperatures, thereby exhibited improved high temperature strength [226–228].

$\text{Si}_3\text{N}_4$  ceramics with 5 wt.% additive of  $\text{Y}_2\text{O}_3$  have been investigated by researchers [212]. The powder was wet-mixed in methanol for 24 h, then dry sieved through -100 mesh. Powder was compacted at 2.5 MPa uniaxial pressure to form 45 mm  $\times$  45 mm green compact. Green compact was then sinter-forged at 1850  $^\circ\text{C}$ , ramped at rate of 10  $^\circ\text{C min}^{-1}$ , soaked for 30 min. Pressure of 30 MPa was applied with soaking time of 150 min to consolidate the nanocomposite

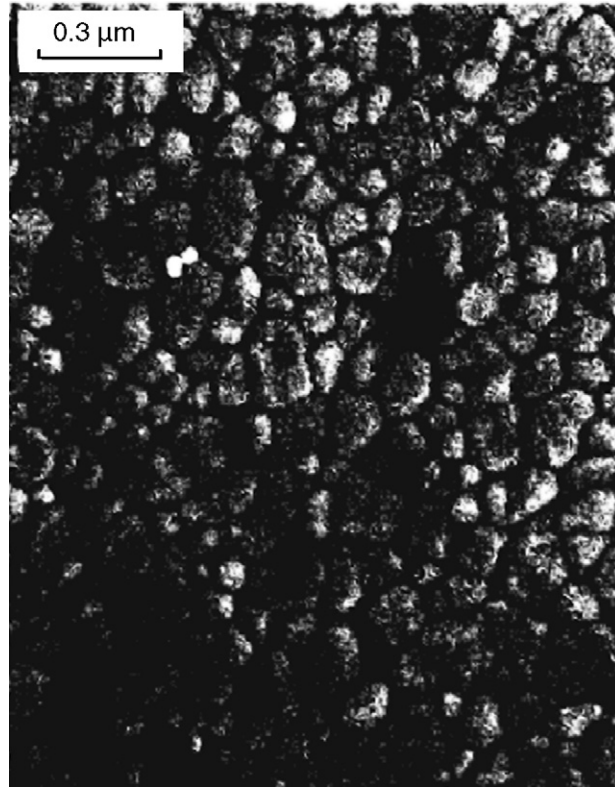


Fig. 80. YO<sub>1.5</sub>-TZP (5 mol.%) sample sinter-forged at 1150 °C for 25 min. (Reprinted from [215] with permission from Elsevier.)

[229]. Full density is not desirable in the nanocomposite, and the final density was obtained as 76% of theoretical density, containing 2.2 and 21.8% of closed and open pores, respectively. Porous microstructure with 2D alignment of fibrous  $\beta$ -Si<sub>3</sub>N<sub>4</sub> grains introduced excellent fracture toughness and strength. Crack bridging through aligned Si–N fibers and presence of fine and distributed pores provide the improved toughness to the consolidated nanocomposite. Where porous Si–N possesses higher fracture energy ( $\sim 500 \text{ J m}^{-2}$ ) compared to dense Si–N ( $\sim 180 \text{ J m}^{-2}$ ) [230,231].

In another study, Si<sub>3</sub>N<sub>4</sub>–Si<sub>2</sub>N<sub>2</sub>O was sinter-forged at 1600 °C at pressure of 20 MPa and 30 min to produce gears with improved mechanical properties [232]. Ytterbia additives also have been tried in Si–N matrix to result improved

Table 24

Microstructural and mechanical properties of tetragonal zirconia polycrystal (TZP) sinter-forged at 1150 °C at 25 min

Sample	Density (%)	Grain size ( $\mu\text{m}$ )	HV (GPa)	Reference
5 mol.% YO <sub>1.5</sub> -TZP	98.5	0.18	14.2 $\pm$ 0.5	[215]
4 mol.% YO <sub>1.5</sub> -4 mol.% CeO <sub>2</sub> -TZP	98.5	0.19	13.62 $\pm$ 0.3	[215]

Table 25

Fracture energy and toughness of tetragonal zirconia polycrystal (TZP) sinter-forged at 1150 °C at 25 min

Sample	$T_{\text{fract}}$ (°C)	Fracture energy ( $\text{J m}^{-2}$ )	$K_{\text{IC}}$ ( $\text{MPa m}^{1/2}$ )	Reference
5 mol.% YO <sub>1.5</sub> -TZP	20	297	9.8 $\pm$ 0.6	[215]
	320	160	7.2 $\pm$ 0.5	[215]
	760	81	5.1 $\pm$ 0.6	[215]
4 mol.% YO <sub>1.5</sub> + 4 mol.% CeO <sub>2</sub> -TZP	20	325	10.0 $\pm$ 0.5	[215]
	320	133	6.4 $\pm$ 0.7	[215]
	760	55	4.1 $\pm$ 0.2	[215]

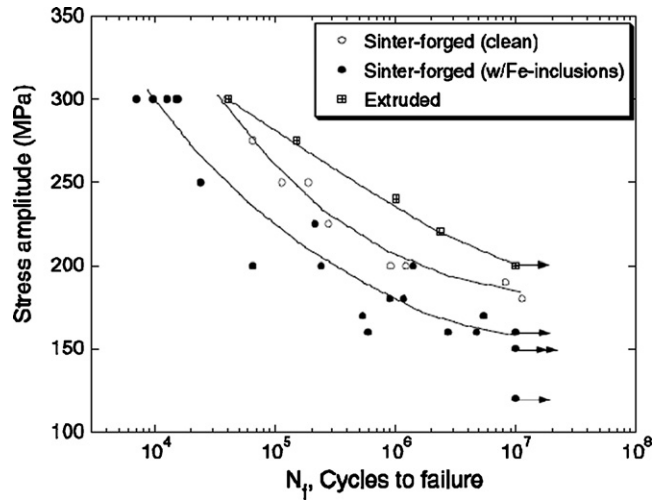


Fig. 81. S–N behavior of sinter-forged composites compared to extruded materials. (Reprinted from [224] with permission from TMS.)

strength and fracture energy over hot pressed composites (Fig. 82) [206]. Lutetia ( $\text{Lu}_2\text{O}_3$ ) additives upto 10 wt.% in Si–N matrix also have been used for nanoconsolidation of composite via sinter forging, which show elongated rod-like silicon nitride grains [204]. Anisotropic elongation of silicon nitride grains elongate inside the pores is also observed due to sinter forging [203]. Anisotropy of silicon nitride is depicted by the X-ray diffraction spectrum with strong (2 1 0) peaks (Fig. 83) [204].

**3.5.5.3. Cu–Fe.** Grain size control can be achieved with addition of Cu as second element in Fe matrix [213]. Elemental Fe and mechanically alloyed Fe–Cu or  $\text{Fe}_{85}\text{Cu}_{15}$  or  $\text{Fe}_{60}\text{Cu}_{40}$  powders were mixed with hardened stainless steel balls for mechanical milling in an argon atmosphere. Milling was done down to liquid nitrogen temperature to reduce agglomeration. After screening them through –100 mesh, perform was compacted in WC die at pressure of 1 GPa from few to 24 h. Resultant density of 70–80% of theoretical density compact was heated to 100 °C and pressed in range of 380–410 °C at applied pressure of 320–870 MPa. This process helped retain nanophases at 99.2% of theoretical density.

Nanophase Fe with grains ranging from 5 to 15 nm have been observed in this reported work [213]. Dark field TEM micrograph depicted fully dense Fe sample consolidated at 400 °C at pressure of 750 MPa with dwell time of 30 min [213]. Diffraction pattern of the corresponding image shows only Fe rings. Grain size ranging from a few nanometers to 80 nm is observed in the TEM image [213].

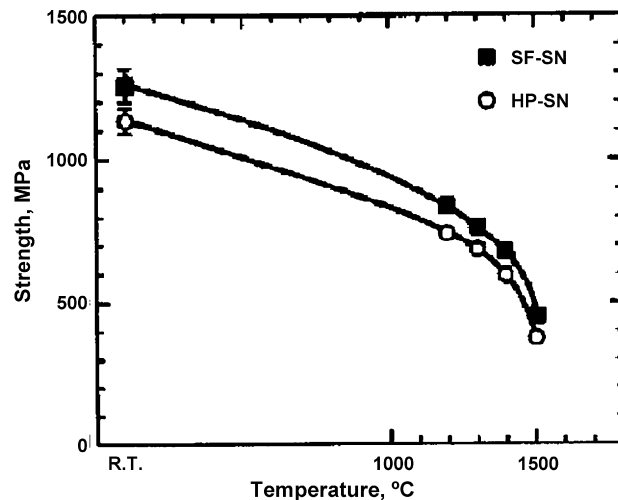


Fig. 82. High temperature strength of HP–SN and SF–SN specimen. (Reprinted from [206] with permission from Elsevier.)

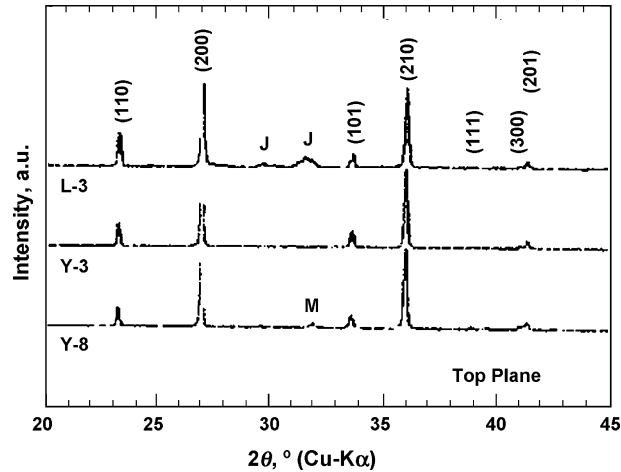


Fig. 83. XRD spectrum of various samples. Deflections from  $\beta\text{-Si}_3\text{N}_4$  are indexed. J and M are  $\text{Lu}_4\text{Si}_2\text{O}_7\text{N}_2$  and  $\text{Y}_2\text{Si}_3\text{N}_4\text{O}_3$  crystalline phases, respectively. (Reprinted from [204] with permission from Elsevier.)

Grain size distribution of  $\text{Fe}_{60}\text{Cu}_{40}$  sample also displayed inhomogeneous nanograins with finer grain size as compared to that in elemental Fe [213]. Histogram of grain size is presented in Fig. 84 [213].

**3.5.5.4. Steel.** 316L stainless steel was compacted in cemented carbide die under 300 MPa, presintered in argon for 30 min at  $1300^\circ\text{C}$ , and sinter-forged at  $1125^\circ\text{C}$  in argon at 5 and 8 MPa axial stress for 90 min. Density distributions were obtained through finite element modeling and compared with experimental data [233]. Besson and Abouaf models have been widely utilized by researchers for finite element modeling of forged sintering [234,235].

Tool steel powder were cold compacted at 300 MPa, calcined and sintered at  $1000^\circ\text{C}$  for 20 min in hydrogen and finally sinter-forged at  $1000^\circ\text{C}$  under axial pressure of  $\sim 20$  MPa. Grain size contours and density contours were predicted and presented by researchers (Fig. 85) showing a similar trend as in experimental data [235]. But, finite element calculations overestimated the relative density as observed experimentally by researchers [235].

**3.5.5.5. Superconductor materials.** Hot stacking and sinter forging of superconductors to maintain texture is reported by researchers [236]. Cohesion between particles is one of the critical parameters often neglected for modeling compaction of nanopowders. Dynamically relevant torque and point contacts have been modeled in two-dimension to

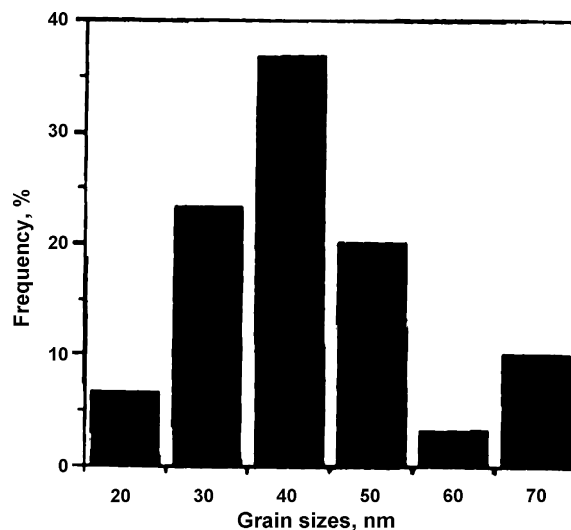


Fig. 84. Grain size distribution of the consolidated  $\text{Fe}_{60}\text{Cu}_{40}$  sample. (Reprinted from [213] with permission from JMR.)

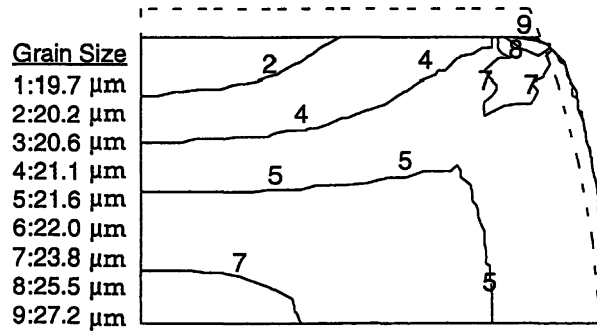


Fig. 85. Comparison of Abouaf and the grain size contour plot of tool steel powder after 20 min sinter forging at 1000 °C at 19.4 MPa. (Reprinted from [235] with permission from Elsevier.)

estimate contact properties [237]. Force chains, dependence of porosity on piston force and piston size has also been studied by researchers [237]. Model of sinter forging predicting density with respect to stress–strain–time profiles has been presented by researchers considering diffusion and plastic deformation for pore closure and densification of nanocomposite [238]. Grain growth behavior is investigated with variation in applied stress during sinter forging [239]. Higher strain rates restrict grain growth due to rapid plastic deformation and densification (Fig. 86) as modeled and compared by Hague and Mayo with experimental results [199,238]. Density of green compact, forging temperature, lubrication conditions at die–workpiece interface, flow stress experienced during consolidation, deformation speed, and contact time are critical factors in deciding deformation pattern of sinter-forged nanocomposite. Appropriate interfriction law, yield criterion and interaction of processing parameters in sinter forging are presented in reference [240].

Sinter forging retain nanocrystallinity, without introducing exaggerated grain growth. This technique is suitable to achieve full density of the nanocomposites rapidly. Anisotropy and porosity can also be modeled through sinter forging to achieve excellent fracture toughness. Improved high temperature and chemical properties are achieved by emanating glass free grain boundary in the resulting nanocomposite.

## 4. Non-equilibrium processing

### 4.1. Microwave sintering

#### 4.1.1. Introduction

Processing of nanostructured nanocomposites via microwave sintering is highlighted also since the consolidation can be achieved at much lower temperatures as shown in Fig. 87. This clearly encompasses the potential display by nanostructured materials whether it is biomedical, optoelectronic, pharmaceutical, magnetic, structural or energy

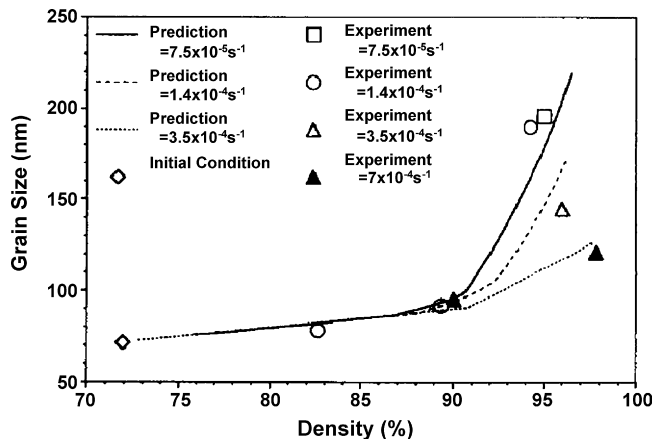


Fig. 86. Prediction of grain size as a function of density for sinter forging at 1100 °C. (Reprinted from [199] with permission from Elsevier.)

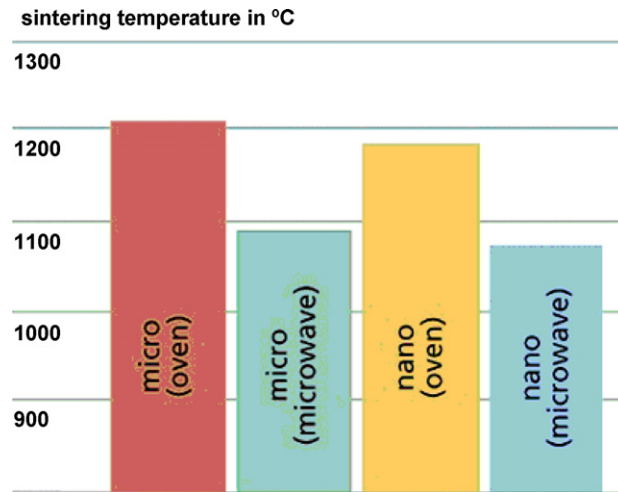


Fig. 87. Microwave consolidation temperatures for micro- and nanocomposite sintered samples [241].

related application [241]. Considering the particle agglomeration tendency of nanoparticles, high reactivity surface, inherent contamination tendency and grain coarsening impetus retain the challenge of consolidating nanopowders via microwave sintering while retaining grain sizes in nanometer range [242,243]. Microwave sintering provides improved mechanical properties by retaining fine grain microstructure via rapid volumetric heating, and in addition, hybrid heating attachments could also be coupled for successful sintering of various ceramics, composites, and glasses [244].

#### 4.1.2. Fundamental principles

Microwave sintering significantly differs from conventional processing technique for sintering ceramic nanocomposites. Microwave field generates oscillations of free electrons and ions at high frequency (~2.45–28 GHz) resulting rapid volumetric heating of material through thermal agitations [245–247]. High frequency magnetic field develops heat source within the specimen resulting preferential heating of porous regions with assisted material flow along interfaces to result consolidated nanocomposite [248]. Microwave frequencies of several GHz couple with internal polarized species such as molecule, lattice, charged ions, and space charge, but still heating and coupling mechanism are not clearly understood.

Nanopowder synthesis also holds the key to understanding and densification of powder controlling the grain size [249–251]. Grain growth can be suppressed by rapid heating and cooling rates and short hold times [252]. Thermal conduction transfers the radiation energy from surface to core by producing extreme thermal gradients, whereas microwave heating excites every crystal lattice resulting uniform distribution (or volumetric heating) of composite/ceramic body [244]. Hence, rapid heating with reduced thermal stresses becomes possible by microwave sintering.

Microwave absorption in dielectric material is dependent on the maximum frequency or temperature where loss factor ( $\tan \delta$ ) is maximum:

$$\tan \delta = \frac{\epsilon'_{\text{eff}}}{\epsilon'_f} = \frac{\sigma}{2\pi f \epsilon_0 \epsilon'_f}$$

where  $\epsilon'_{\text{eff}}$  is the dielectric loss factor,  $\epsilon'_f$  the dielectric constant,  $\epsilon_0$  the permittivity of free space,  $\sigma$  the conductivity of material, and  $f$  is the frequency of incident wave (GHz) [253]. Calculation of actual energy absorbed by dielectric material helps in controlled sintering of material via microwave processing. The average power absorbed by material is presented as [253,254]:

$$P = 2\pi f \epsilon_0 \epsilon'_f$$

Dielectric insulator absorbed energy when supplied with high frequency microwave radiation. Magnetrons, waveguides and resonant (or non-resonant) microwave cavities describe microwave system (Fig. 88) [248,253,255].

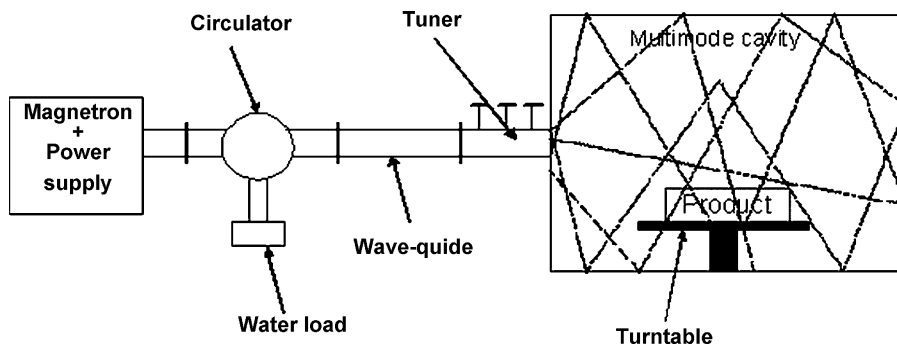


Fig. 88. Typical microwave sintering system.

#### 4.1.3. Advantages

Advantages of microwave sintering can be ascribed into following [245,256–258]:

- Materials can reflect, absorb or be transparent to microwaves, hence the properties can be altered depending on material properties, i.e. materials that absorb microwaves can be selectively heated.
- Efficient and rapid heating of material reduces the thermal shock observed from surface to core of the consolidated material.
- Sintering at lower temperatures and in shorter times is easily achievable through microwave sintering.
- Finer microstructure with improved material properties and product performance.
- Enhanced energy efficiency.
- Reduced contamination from container walls.
- Easy coating of adhesive thin film over hard particles because of higher energy absorption of soft material when compared to that of hard material.

However, microwave sintering has a few disadvantages when compared to conventional sintering routes [253]:

- Heat retention in materials with low loss tangents requires increased power for increasing the temperature of body, since the radiation losses vary with  $T^4$  term (Stefan–Boltzmann law).
- Additives may be required to improve absorption tending to add cost and impurities in the consolidated structure.
- Higher frequency germinates greater power absorption in material, but reduce the penetration depth during processing.
- The capital cost of microwave equipment is invariably higher than conventional plants, with invariably high energy costs associated with microwave energy generation.

#### 4.1.4. Equipment—process and mechanism

Microwave sintering furnace has usual rating of 1.0–1.5 kW, and 2.45–5.8 GHz to 28 GHz feed (with Gyrotron source). A microwave sintering apparatus is shown in Fig. 89. Few of the microwave sintering equipments are produced by Fuji Dempa Kogyo Ltd., Japan, MMT 101, Knoxville, TN, USA, MPC 941, Australia, Sharp, Singapore, Panasonic NN 6371 WM, USA, BPL BMC-900T, India [244,256,259,260].

A typical absorption, reflectance, and temperature profile with time during microwave sintering cycle is shown in Fig. 90 [248]. Factors such as electrical conductivity, dielectric constant, loss factor, moisture, density, crystal defects, interphases, thermal conductivity, and thermal capacity of material affect heating efficiency of microwave.

#### 4.1.5. Nanoconsolidation

4.1.5.1. *Si–N/SiC/MoSi<sub>2</sub>*. Si–N performs were prepared by uniaxial pressing followed by hydrostatic repressing at 4.5 kbar to generate performs with density of  $1.6 \text{ g cm}^{-3}$  (46% theoretical density). Microwave sintering at  $1750^\circ\text{C}$  displayed maximum densification rate within 5 min with density reaching 92–93% of theoretical density [261].

Sintering additives such as  $\text{Y}_2\text{O}_3$ ,  $\text{Al}_2\text{O}_3$ , and MgO have been used to refine the grain size during microwave sintering. Sintering was performed within  $1450\text{--}1850^\circ\text{C}$  with 1 h hold time using 28 GHz gyrotron source for microwave consolidation. Samples were densified to 98% of theoretical density with  $\alpha \rightarrow \beta$  transformation occurring



Fig. 89. Microwave sintering system with attached press. (Source: [www.ifs.tohoku.ac.jp/divisions/en/ifsd\\_isl.html](http://www.ifs.tohoku.ac.jp/divisions/en/ifsd_isl.html).)

in the microwave sintered  $\text{Si}_3\text{N}_4$  samples [248]. Resulting microstructure of microwave sintered Si–N evidenced transgranular propagation of fracture with little crack deflection.

Microwave sintering of  $\text{SiC}/3\text{Y}_2\text{O}_3\cdot 5\text{Al}_2\text{O}_3$  (YAG) powders at 2.45 GHz has been performed by researchers depicting that microwave sintering might not be potentially advantageous over conventional consolidation process. High resolution TEM and TEM images depicted SiC/YAG interface and their spatial distribution, respectively (Figs. 91 and 92) [248].

Despite the limited solid solubility of TiC and ZrC in each other below 2200 °C, synthesis of (Ti,Zr)C solid solution was achieved via microwave heating to 1800 °C followed by rapid cooling to room temperature. Phase identification was performed using XRD analysis, evincing  $(\text{Ti}_{0.5}\text{Zr}_{0.5})\text{C}$  phase retention [257]. Post-annealing treatment of the sintered structure indicated phase separation, confirming the better efficacy of microwave process in generating spinodal decomposition when compared to that of conventional annealing. Microwave annealing, therefore, in turn evinces nanosized particles due to spinodal decomposition and refines the microstructure [257].

$\text{MoSi}_2$ –SiC composites with improved fracture toughness and higher consolidated density have been prepared by microwave sintering for 10 min hold time at 800 W and 2.45 GHz [262]. Faster, cleaner and energy efficient fabrication of dense high temperature  $\text{MoSi}_2$ –SiC nanocomposite well captures the high temperature oxidation resistance, and high electrical conductivity with improved fracture toughness.

**4.1.5.2. Ceramic oxides.** Ce–Y–ZrO<sub>2</sub> ceramic oxide has been microwave sintered using 2.45 GHz microwave furnace at 0.5–5.0 kW for various temperatures [263–266]. Consolidation was achieved at shorter time for microwave sintered samples along with improved toughness ( $13.7 \text{ MPa m}^{1/2}$ ) when compared to that of conventionally sintered samples ( $11.2 \text{ MPa m}^{1/2}$ ; Fig. 93) [266]. Higher flexural strength was attributed to finer grain size ( $0.65 \mu\text{m}$ ) and higher

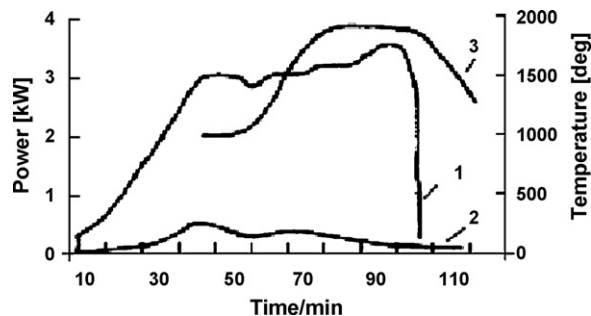


Fig. 90. Microwave sintering power and temperature–time profile resulted in the densification of small specimen. (Reprinted from [248] with permission from Elsevier.)

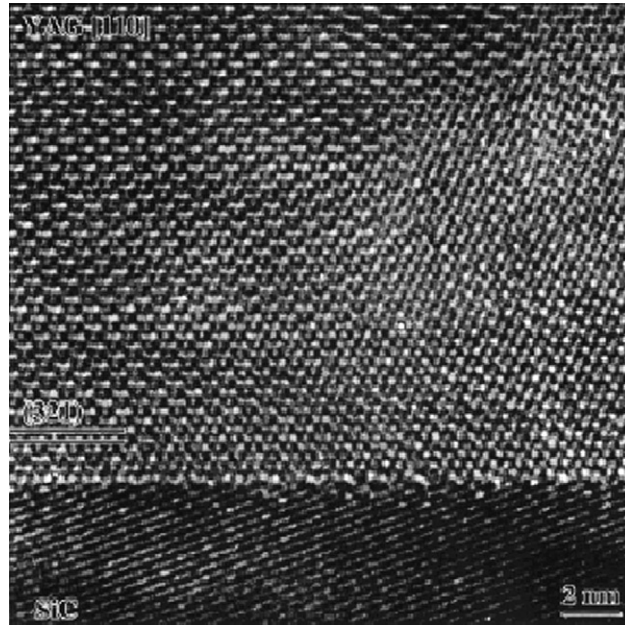


Fig. 91. High resolution TEM of SiC–YAG interface. (Reprinted from [248] with permission from Elsevier.)

tetragonal zirconia fraction in microwave sintered samples when compared to that of conventionally sintered samples (Fig. 94) [266].

Pellets of submicron  $\text{Al}_2\text{O}_3$  powder were microwave sintered to 97.8% theoretical density at 1000–1500 °C/1.2 h at 2.45 GHz microwave furnace. Low activation energy in microwave sintering ( $160 \text{ kJ mol}^{-1}$ ) when compared to

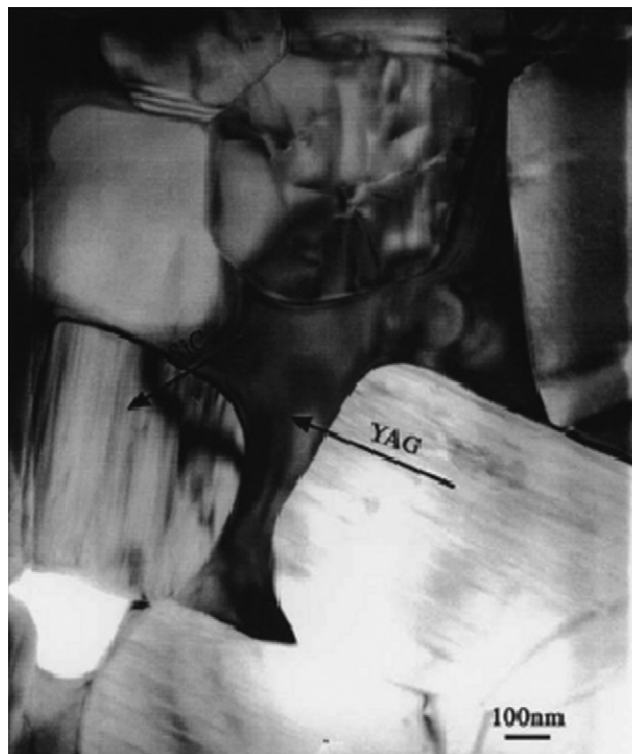


Fig. 92. Bright field TEM of YAG crystal seen between  $\alpha$ -SiC grains. (Reprinted from [248] with permission from Elsevier.)

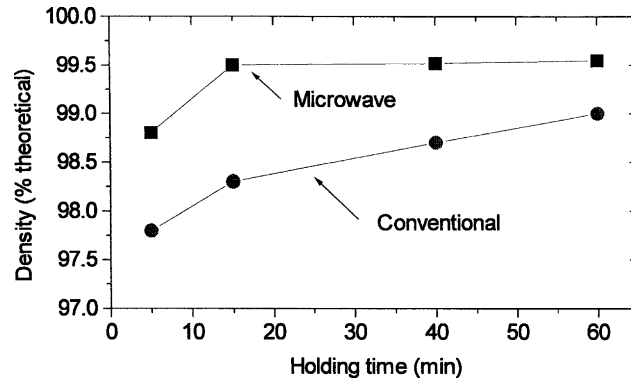


Fig. 93. Density vs. holding time at 1500 °C. (Reprinted from [266] with permission from Elsevier.)

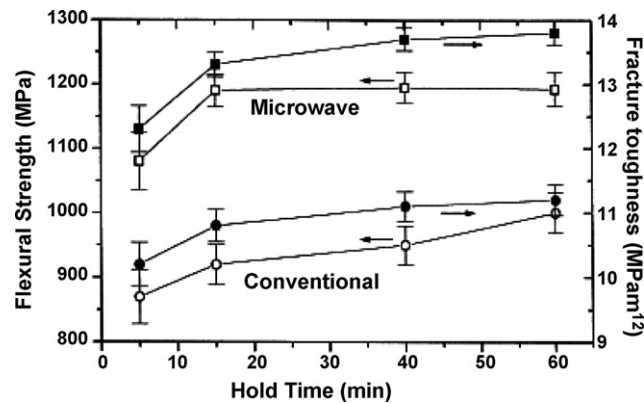


Fig. 94. Flexural strength and fracture toughness vs. holding time at 1500 °C. (Reprinted from [266] with permission from Elsevier.)

conventional sintering process ( $575 \text{ kJ mol}^{-1}$ ) leads to rapid grain growth. But fast sintering cycles and quicker consolidation time restricts the grain growth resulting finer grain growth of consolidated nanostructured composite. Variation of grain size with density for microwave and conventional sintering produced comparable grain sizes at same densification (Fig. 95) [267].

Transparent conducting oxides might find application in solar cells, electrochemical window, aesthetic applications, etc. [268–271]. Selective heating of TCO was done at 450 °C, which did not seem sufficient to form a

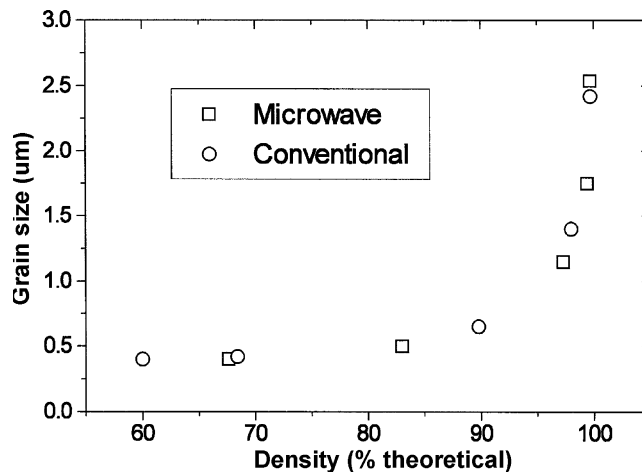


Fig. 95. Grain sizes vs. density for two sintering methods. (Reprinted from [267] with permission from Elsevier.)

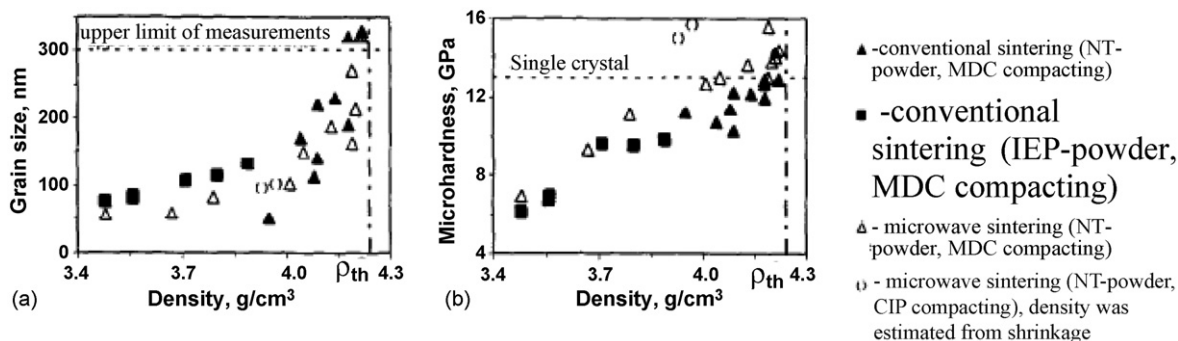


Fig. 96. (a) Grain size and (b) microhardness vs. density for samples prepared by microwave and conventional sintering. (Reprinted from [246] with permission from Elsevier.)

good semiconductor core-shell nanostructure [256]. Millimeter wave at 84 GHz frequency has also been used by researchers to consolidate nano-titania at 540 °C with hold times of 15 min to result 99% dense structures [246]. Conditions of sintering showed dependence on the density of samples rather than the temperature of the samples. Fig. 96a shows that average grain size increased with increasing temperature and time, such as the grain size of 100 nm at density of 3.9 g cm<sup>-3</sup> increased to 300 nm at density of 4.15–4.2 g cm<sup>-3</sup> [246]. Microhardness of nanoconsolidated samples showed 10% higher values than that of conventionally sintered samples at the same density (Fig. 96b) [246].

Microstructural evolution of alumina–10 wt.% zirconia powder at 1450 °C via microwave sintering yielded higher density when compared to that of conventional sintering. Increase in the grain size has been observed, Table 26, after microwave sintering, insinuating poor grain size retention capability of microwave sintering. This might arise due to high sintering hold time during processing [272]. Higher elastic modulus and higher fracture strength have been observed for microwave sintered Al<sub>2</sub>O<sub>3</sub>/ZrO<sub>2</sub> composites [273].

High purity alumina with particle size of 150 nm was cold-isostatically pressed at 280 MPa to result green density of 52–54%, which were then preheated to 1100 °C for 2 h to burn the binder. Microwave sintering was done at 1.5–6.0 kW generator at 2.45 GHz under hydrogen atmosphere. Fully dense fine-grained transparent alumina was successfully fabricated via microwave sintering at 1750 °C for 45 min with resulting density of 3.83 g cm<sup>-3</sup> (96.5% theoretical density; Fig. 97a and b) [245]. Polycrystalline structure transformation to single crystal is required for transparency via microwave sintering.

Grains and grain boundaries in nanocrystalline titania ceramic were prepared via conventional and microwave sintering technique [274]. Denser ceramic consolidation is obtained by microwave sintering. Table 27 presents crystallite sizes of microwave sintered TiO<sub>2</sub> [274].

Lead titanate ceramics sintered at 1100 °C for 30 min at 2.45 GHz and 1.2 kW depicted improved densification with low lead loss during processing. Uniform and fine grains were observed with improved dielectric and piezoelectric properties for microwave sintered samples (Fig. 98) [275].

**4.1.5.3. Inert matrix fuel.** Oxygen storage capability of ceria rich CeO<sub>2</sub>–ZrO<sub>2</sub> solid solution has attracted microwave sintering of this inert matrix fuel with additions of β-alumina. Decomposed powder and resulting microwave sintered structure (1100 °C, 2.45 GHz, 0.8 kW, 30 min) is presented in Fig. 99a and b [276]. Reduced porosity and around 92% of theoretically dense microstructure displayed controlled temperature to manipulate onset of calcination.

Table 26  
Microwave sintering of microwave sintered alumina/zirconia composites

Mode	Specimen	Sintering temperature (°C)	Sintering time (min)	Heating rate (°C min <sup>-1</sup> )	Grain size (μm)	Density (%)	Reference
Microwave	Al/Zr-1	1550	20	10	4.55	96	[272]
	Al/Zr-2	1450	20	22	2.42	95	[272]
Conventional	CAI/Zr-1	1450	20	10	0.77	87.4	[272]

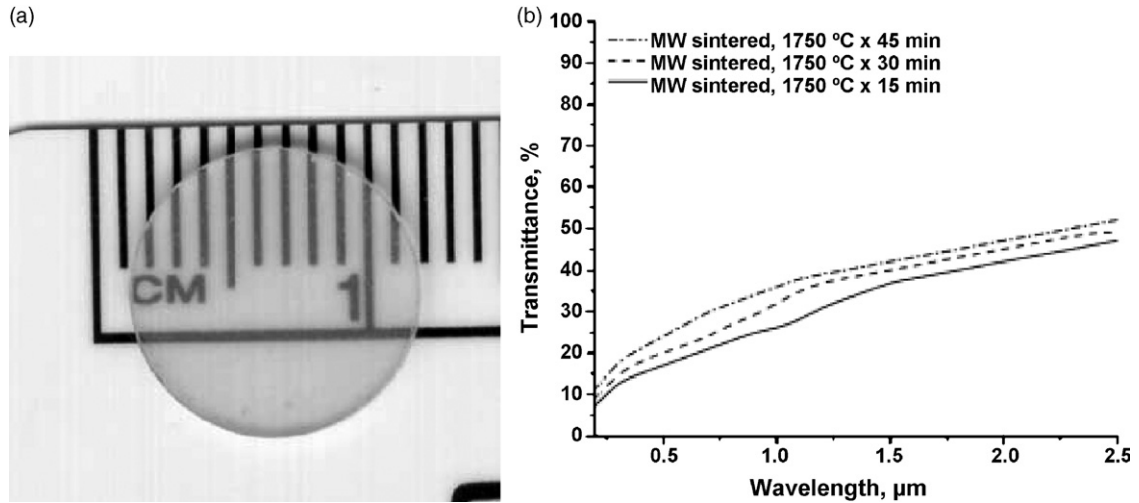


Fig. 97. (a) Highly transparent  $\text{Al}_2\text{O}_3$  sample microwave sintered at  $1750\text{ }^\circ\text{C}$  for 45 min and (b) transmittance of fabricated sample. (Reprinted from [245] with permission from Elsevier.)

Table 27

Characteristic of microwave sintered  $\text{TiO}_2$  ceramic

Sintering condition	$\rho$ ( $\text{g cm}^{-3}$ )	Porosity (%)	HV (GPa)	% R/A	Grain size (nm)	Crystallite size (nm)	GB state	$D_{\text{eff}}$ ( $\text{cm}^2 \text{s}^{-1}$ )	Reference
$30\text{ }^\circ\text{C min}^{-1}$ , $850\text{ }^\circ\text{C}$ , 13 min	4.18	1.3	13.4	R, 100	$>300$	300–500	Sharp	36–40	[274]
$50\text{ }^\circ\text{C min}^{-1}$ , $850\text{ }^\circ\text{C}$ , 13 min	4.20	0.8	13.4	R, 100; A, trace	213	200–1000	Sharp	35	[274]
$75\text{ }^\circ\text{C min}^{-1}$ , $850\text{ }^\circ\text{C}$ , 13 min	4.21	0.5	13.4	R, 100	$>300$	200–500	Sharp	40	[274]
$50\text{ }^\circ\text{C min}^{-1}$ , $800\text{ }^\circ\text{C}$ , 5 min	4.19	0.95	13.7	R, 98; A, 2	162	100–250	Incomplete	30	[274]
$50\text{ }^\circ\text{C min}^{-1}$ , $600\text{ }^\circ\text{C}$ , 0 min	3.48	14.8	13.7	R, 19; A, 81	56, 52	40–80	Round	–	[274]
$50\text{ }^\circ\text{C min}^{-1}$ , $685\text{ }^\circ\text{C}$ , $1\text{ }^\circ\text{C min}^{-1}$ to $700\text{ }^\circ\text{C}$ , 0 min	4.01	4.7	12.7	R, 88; A, 12	103, 66	100	–	20	[274]

R: rutile; A: anatase.

$\text{Zr}_{0.70}\text{Y}_{0.10}\text{Er}_{0.05}\text{Ce}_{0.10}\text{O}_{1.925}$  and  $\text{Zr}_{0.70}\text{Y}_{0.10}\text{Er}_{0.05}\text{Ce}_{0.15}\text{O}_{1.925}$  inert matrix fuels were precompacted at 300 MPa and microwave sintered at  $1200\text{ }^\circ\text{C}$  for hold times of 15, 30, and 60 min [277].  $\beta$ -Alumina assists absorption of microwave in heating ceramics which do not directly couple with microwave absorption. Densities around 90% of theoretical density were achieved using microwave sintering.

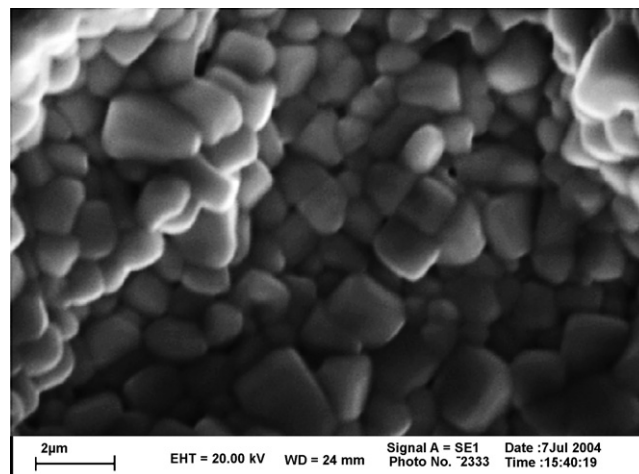


Fig. 98. SEM image of MS PCT ceramic. (Reprinted from [275] with permission from Elsevier.)

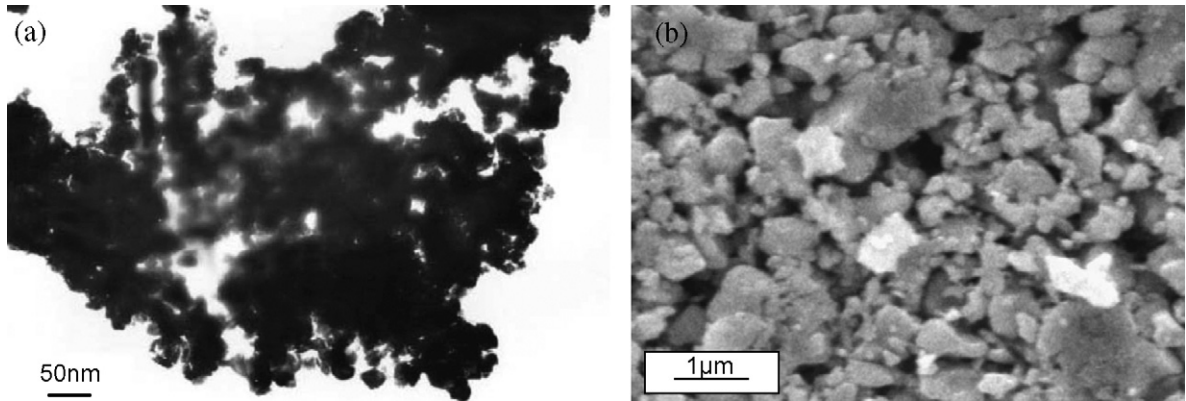


Fig. 99. (a) HRTEM of decomposed  $Zr_{0.9}Ce_{0.1}O_2$  gel and (b) ceramograph of microwave sintered  $Zr_{0.9}Ce_{0.1}O_2$  gel. (Reprinted from [276] with permission from Elsevier.)

**4.1.5.4. Bioceramic hydroxyapatite.** Hydroxyapatite is being widely used as clinical bio-compatible material for bone and dental implant/repair material. Hydroxyapatite samples were microwave heated at 1050–1100 °C with hold time of 5–10 min at 2.45 GHz [278]. Apatite phase prevailed after microwave sintering as observed through IR spectroscopy (Fig. 100) [278]. Grain sizes (0.3–0.5 μm) were 10 times smaller than those observed by conventional heating (3–5 μm; Fig. 101) [278]. Moreover, comparatively higher densities were obtained for microwave sintered samples, 3.02–3.12 g cm<sup>-3</sup> (96–99% theoretical density) when compared to conventional sintered samples, 2.96–3.09 g cm<sup>-3</sup> (94–98% theoretical density). Density of consolidated HAP reached 95% of theoretical density within 5 min [254]. TEM micrographs of microwave sintered HAP showed crystallite size in the range of 35 nm (Fig. 102) [254].

**4.1.5.5. Yttria-stabilized zirconia.** Conventional and microwave sintering was performed on nanocrystalline yttria partially stabilized zirconia, at 1250 °C for 120 and 30 min, respectively. Nanopowder densification via microwave sintering adopted 200 °C lower temperature (1250 °C) than that required for micron-sized powders. Near zero porosity was obtained for samples with refined grain size averaging ~140 nm [279].  $Y_2O_3$ - $ZrO_2$  (9 mol.%) microwave sintering yielded bimodal grain sizes (Fig. 103) [279].

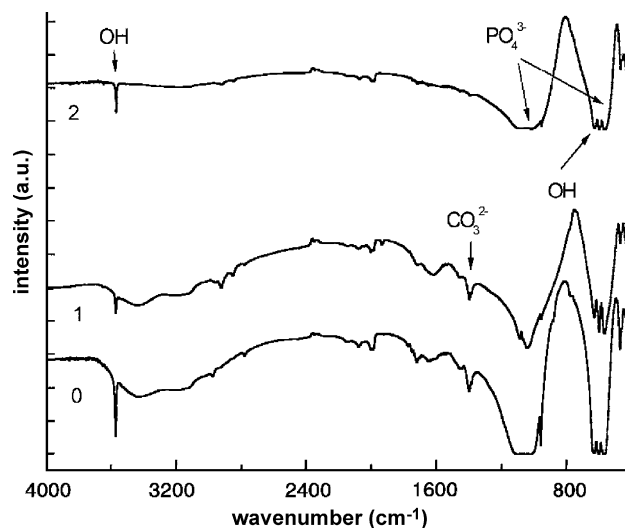


Fig. 100. IR spectrum of HA: (0) powder; (1) conventional sintering; and (2) microwave sintering. (Reprinted from [278] with permission from Springer.)

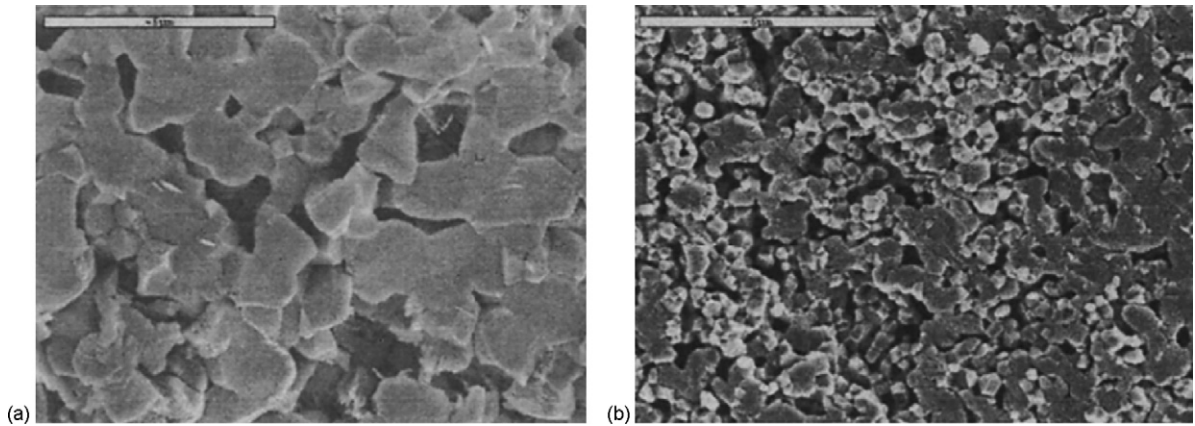


Fig. 101. SEM image of Fractured MA at 1000 $\times$  of: (a) conventional sintering and (b) microwave sintering. (Reprinted from [278] with permission from Springer.)

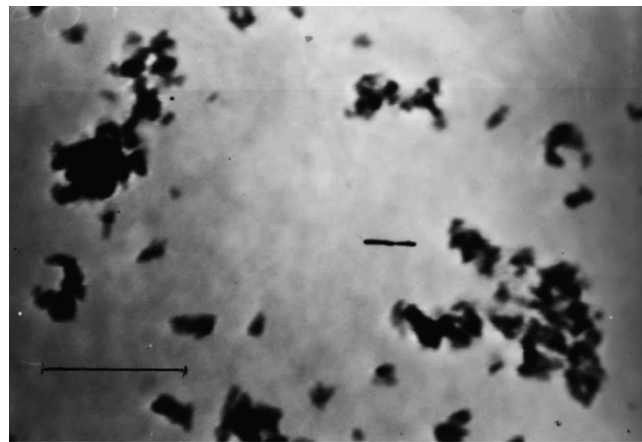


Fig. 102. TEM image of HAP prepared at 0  $^{\circ}$ C (bar: 100 nm). (Reprinted from [254] with permission from Elsevier.)

4.1.5.6. *WC/Co tool material.* Cementing properties of Co to facilitate liquid phase sintering of WC grains, distribution uniformity of binding phase is of great concern. The cutting and drilling tool WC/Co requires unique mechanical properties such as high hardness, high toughness, moderate modulus of elasticity and fine-grained matrix with distributed binder. Reprecipitation of Co via dissolution and migration is observed via conventional

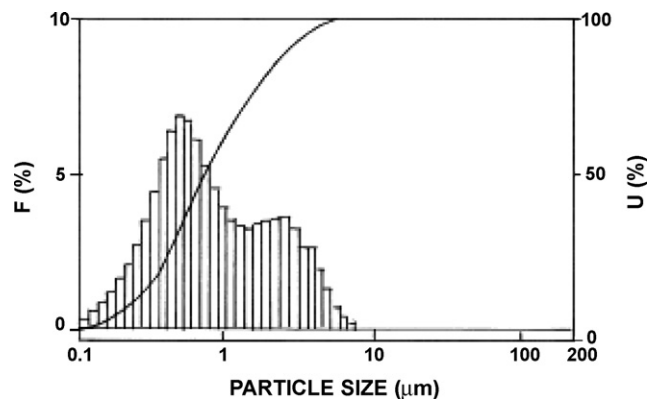


Fig. 103. Particle size spectrum of 9Y-CSZ powder calcined at 600  $^{\circ}$ C for 3 h. (Reprinted from [279] with permission from Elsevier.)

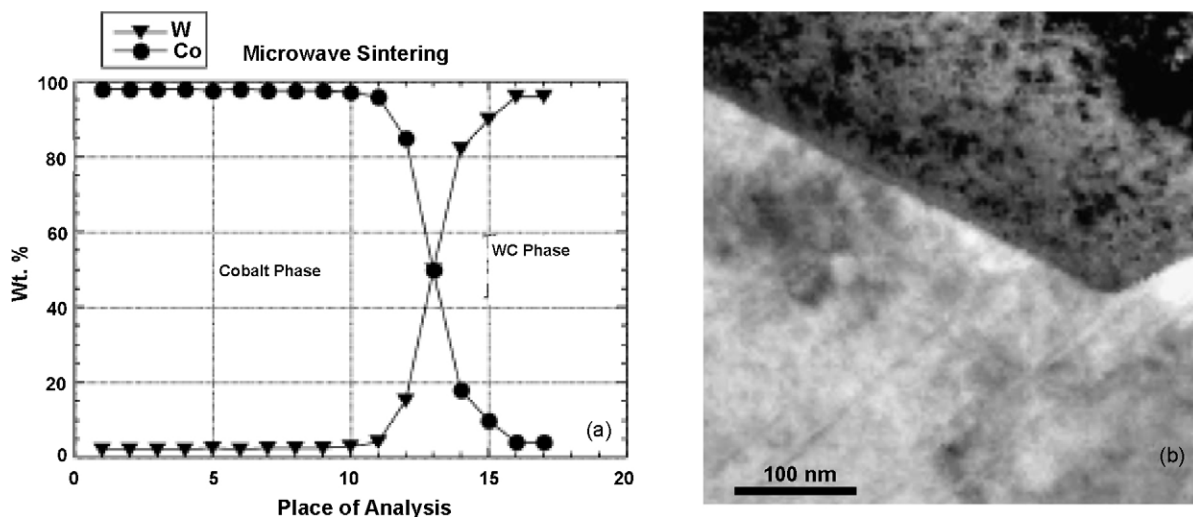


Fig. 104. (a) Concentration of Co and W in microwave sintered WC/Co and (b) bright field TEM image. (Reprinted from [247] with permission from Elsevier.)

nanoconsolidation technique containing 3D structure of WC with Co binder [247,280]. The near thermal conductivities of Co ( $69.2 \text{ W m}^{-1} \text{ K}^{-1}$ ) and WC ( $63 \text{ W m}^{-1} \text{ K}^{-1}$ ) aid to thermal conduction inside the sample. Small hysteresis loss in Co does not significantly contribute heat from magnetic domain oscillations. Rapid volumetric heating of WC/Co nanocomposite restrict the grain growth with resulting superior properties [247].

Higher amounts of dissolved W (up to 14–24 wt.%) have been observed in Co lattice [247]. Diffusion coefficients for migration of C, and W in Co matrix were investigated to relate dependence of temperature on the mobility of species [247]. Microwave sintering was used to raise temperature of samples to 1300–1450 °C for 10 min at 2.45 GHz frequency. Microwave sintered samples depicted that nearly no tungsten was dissolved in Co phase contrasting to the conventionally sintered WC/Co nanocomposite (Fig. 104) [247]. Fine-grained resulting microstructure via microwave sintering depicted sharp edges between WC and Co phases indicating the restricted dissolution of WC in Co phase [247]. Corrosion properties of microwave sintered samples were superior to those of conventionally sintered WC/Co nanocomposite (Table 28) [247].

Conventional sintering technique results poor core properties (since heat directs from surface to core of material), whereas microwave sintering shows poor surface properties (since material is heated from core to surface). Though the concept of two-directional microwave assisted rapid sintering is introduced by explorers for metallic materials, the process can be extended to fabricate nanocomposites (Table 29) [259]. Increase ductility was attributed to microstructural refinement and cleaner grain boundaries [259].

A new approach of hybrid microwave-laser synthesis have resulted average grain sizes of 20 nm in 3Y–ZrO<sub>2</sub> nanocomposite. This process maintains the reproducibility of fabricating nanocomposites with refined grain sizes and improved physical, chemical, and mechanical properties [280].

Sintering models with various sintering stages have been proposed by various researchers, with models capturing only a specific stage of sintering. These models can be used to estimate densification during microwave sintering. In

Table 28  
Comparative corrosion (in HNO<sub>3</sub>), erosion, and magnetic properties of WC/Co specimen

No.	Co (wt.%)	WC grain size	Method	Loss HNO <sub>3</sub> 48 h (wt.%)	Erosion wt. loss/area (kg m <sup>-1</sup> )	Magnetic saturation (g m <sup>3</sup> kg <sup>-1</sup> )	Magnetic coercivity	Reference
1	6	0.1–1	A	1.16	60.6	0.1517	197	[247]
2	6	0.1–1	B	0.20	37.1	0.1522	249.5	[247]

A: conventional method; B: microwave method.

Table 29  
Properties of microwave sintered samples

Material	Density ( $\text{g cm}^{-3}$ )	Porosity (%)	Microhardness	0.2% YS (MPa)	Work fracture ( $\text{J m}^{-3}$ )	Reference
Magnesium	$1.74 \pm 0.01$	0.03	$36.6 \pm 1.2$	$105 \pm 0$	$7.4 \pm 1.1$	[259]
Aluminum	$2.70 \pm 0.01$	0.31	$44.4 \pm 0.7$	$133 \pm 43$	$21.6 \pm 6.4$	[259]
Viromet	$7.39 \pm 0.006$	0.2	$16.2 \pm 0.2$	50.9	NA	[259]

addition, diffusion coefficient as a temporal function of temperature, grain size, shrinkage, and density assist in better representation of microwave sintering [281].

Rapid grain growth results for higher holding times and transformation to single crystals improves the transparency of polycrystalline structure. Near zero porosity can be achieved with refined grains for microwave-sintered nanocomposites resulting higher densities and enhanced ductility. Enhanced physical, chemical, and mechanical properties have been evinced in contamination free nanocomposites processed via microwave sintering.

## 4.2. Thermal spray processing

### 4.2.1. Introduction

Thermal spraying is a group of processing techniques, which are being employed in deposition of a wide range of material coatings (thickness  $> 50 \mu\text{m}$ ) in the fields of automobile, aerospace, gas turbine technology, electronics, telecommunications, air and space navigation, medical equipments in order to achieve high strength, toughness, better wear and corrosion resistance or to minimize thermal mismatch [282–287]. Although thermal spray process emerged more than 40 years back, considerable improvement of the process technology has been achieved mainly in last 10 years with better control of spray process parameters via advanced and automated equipments, modern production techniques for imperative feedstock materials and state-of-the-art methods of quality assurance [282–284]. The recent development of thermal spray techniques raised the utility of these techniques to a high level platform, where *fabrication of freestanding structures* and synthesis of spherical and composite powders has become possible [288–291].

### 4.2.2. Fundamental principles

The principle behind the thermal spray techniques is to spray metallic or non-metallic materials or mixture of them in molten or partially molten state at a high speed on a surface-prepared substrate where deposit build-up takes place with rapid solidification of individual molten droplets or splat [282–285,292–294]. The feedstock could be either powder particles or wires, whereas combustion flame, plasma jet or arc struck between two consumable wires could be used as heat source. A wide range of materials from metals, ceramics, polymers or mixture of them in any required proportion can be sprayed in the processes.

### 4.2.3. Types of thermal spray techniques

Depending on the variety of feed stock materials and heat sources, there are various thermal spray processes, viz. (i) plasma spray process, where the heat source is a plasma flame produced by passing some inert gas in between two electrodes, (ii) high velocity oxyfuel spraying (HVOF), where combustion of fuel gas produces the required heat energy, and (iii) wire arc spraying, where the arc is being produced between two consumable electrodes (Table 30) [282–285]. Plasma spraying and HVOF are the two most promising techniques in synthesizing coatings and structural components of improved properties and are being largely exercised both in research laboratories and in industry. The extremely high solidification rate in plasma spraying and high velocity oxyfuel spraying makes it feasible to achieve *excellent grain refinement and possibly nanostructured materials* by posing restriction to grain growth during resolidification of splats [295–298]. Recently, one more spraying technique, *cold spraying* has evolved tremendous expectation where no heat source is used to melt powder particles. In this process, powder is sprayed at an extremely high speed towards the substrate and gets consolidated due to the heavy plastic deformation [299–303]. Achievement of nanostructure is likely in cold-sprayed deposit as the particles experience a large amount of mechanical deformation. In this present study, synthesis of nanostructured composite materials via plasma spraying, high velocity oxyfuel spraying and cold spraying has been depicted elaborately.

Table 30  
Comparison of various thermal spraying techniques

Processes	Heat source	Feedstock	Feedstock velocity (m s <sup>-1</sup> )	Maximum temperature attained (°C)	Mode of achieving nanostructure
Plasma spraying	Plasma arc	Powder	350–1000	15000–20000	Rapid solidification
High velocity oxyfuel spraying	Combustion of fuel gas	Powder	700–1400	3000–6000	Rapid solidification and high impact
Wire arc spraying	Electric arc	Electrically conductive wires	–	5000–20000	Rapid solidification
Cold spraying	No heating		500–1200	No heating	Using nanosized or nanostructured powder

#### 4.2.4. Advantages

- Coatings/free standing structures of wide varieties of metals or non-metals can be deposited/fabricated by adopting thermal spray technique optimizing the spray parameters. The techniques are very much advantageous in case of higher melting point ceramics, which are difficult to process by conventional casting methods. In fact, coatings of any material can be deposited on any kind of substrate by controlling the spray parameters (i.e. heat input, feed rate, spray gun movement, etc.) and installing proper cooling arrangement in well-prepared substrates.
- Metals, ceramics and polymers of any composition can be mixed and sprayed by thermal spray methods to synthesize composite materials with optimized strength, minimized thermal mismatching, wear and corrosion resistance.
- Damaged or wear out engineering and structural components can easily be reinstated by applying coatings without replacing the whole component.
- The spray techniques are economically advantageous and time saving with respect to other conventional processing methods like casting or powder metallurgy.
- Grain growth during solidification can be restricted in plasma spraying and high velocity oxyfuel spraying by virtue of extremely rapid solidification rate in the processes and thus nanostructure can be achieved toward improving mechanical properties in the sprayed material.
- It is likely to incorporate metastable and amorphous phases in sprayed material attributed to rapid solidification rate in plasma and high velocity oxyfuel spraying and thus a bunch of novel and advanced material systems with unique properties can be originated.
- Oxide free deposit can be obtained by practicing vacuum plasma spraying and cold spraying, which have been discussed later in this review paper.

### 4.3. Plasma spraying

#### 4.3.1. Introduction

The earliest plasma spraying was introduced in 1957 by Thermal Dynamic Corporation at Lebanon in New Hampshire and instantly found its application in the aeronautics industry, particularly in NASA [282]. Later in 1970s, Pratt and Whitney along with Gator Gard induced high gas velocity direct current arc torches, which was followed by development of high energy, high velocity Plazet in late 1980s and commercialized by TAFA [282]. Later on, synthesis of denser coating with minimized oxidation became possible with the introduction of controlled atmosphere or vacuum plasma spraying (VPS) [282,283,304].

#### 4.3.2. Fundamental principles

In plasma spraying, metallic or non-metallic powder or their mixture is fed along with a high pressure carrier gas through a spray gun into a heat source of plasma arc (10,000–15,000 K) where the powders are melted or partially melted and deposited on a substrate (Fig. 105) [282,283,304–309]. A primary gas is employed to create the plasma plume produced by a direct current (DC) or radio-frequency (RF) high voltage discharge between two electrodes. The resistance heating from the arc causes the primary gas to reach extreme temperatures, dissociate and ionize to form plasma. Mostly, almost in about 95% cases, the plasma spraying is carried out in air at atmospheric pressure and the

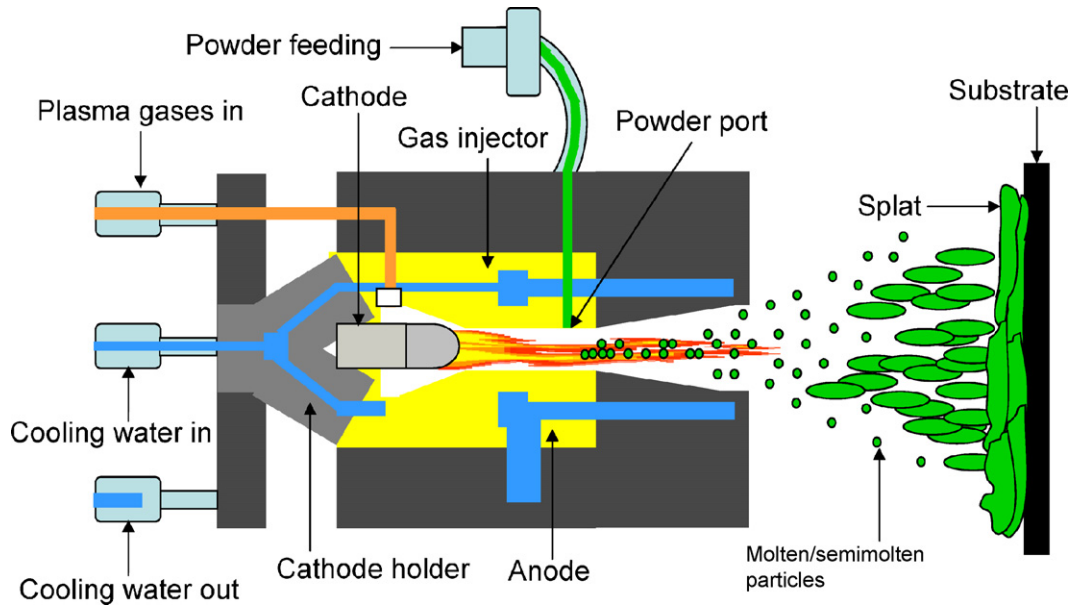


Fig. 105. Schematic of plasma spraying operation.

process is called atmospheric plasma spraying (APS). It is very much likely to cause oxidation of metal powders at molten/semi-molten state during APS, which will cause degradation of deposit. To avoid the oxidation, plasma spraying has been developed to perform controlled atmosphere chamber filled with a neutral gas (mostly argon) either at atmospheric pressure or nearly at a soft vacuum (20–50 kPa).

The plasma spray gun comprises a copper anode and thoriated tungsten cathode, both of which are water-cooled. Plasma gas (argon, nitrogen, hydrogen, helium) flows around the cathode and through the anode, which is shaped as a constricting nozzle. The plasma exits the anode nozzle as a free or neutral plasma flame (plasma which does not carry electric current), which is quite different to the plasma transferred arc coating process where the arc extends to the surface to be coated. When the plasma is stabilized and ready for spraying the electric arc extends down the nozzle, instead of shorting out to the nearest edge of the anode nozzle. This stretching of the arc is due to a thermal pinch effect. Cold gas around the surface of the water-cooled anode nozzle being electrically non-conductive constricts the plasma arc, raising its temperature and velocity. Powder is fed into the plasma flame most commonly via an external powder port mounted near the anode nozzle exit. The powder is so rapidly heated and accelerated that spray distances can be in the order of 25–150 mm [282,283,304–309].

The solid particles introduced in the plasma jets are accelerated and melted or partially melted. There is no limitation in the melting temperature of the sprayed material provided the material melts, i.e. the difference between melting temperature and decomposition or evaporation temperatures is higher than 300 K. Upon impact on the substrate, the droplets form splats which solidify in a few microseconds. Therefore, the next droplet causes impact on already solidified splats. The coating, resulting from the layering of splats which thickness is between 0.8 and a few micrometers, has a lamellar structure and its properties are different from those of the same bulk material. Plasma spraying has the advantage that it can spray very high melting point materials such as refractory metals like tungsten and ceramics like zirconia unlike combustion processes. Plasma-sprayed coatings are generally much denser, stronger and cleaner than the other thermal spray processes with the exception of HVOF and detonation processes.

Even after the practical use of DC-plasma spraying for many years the process remains highly empirical. The production of coatings is still based on trial and error approaches, depending on the experience and the instinctive feeling of the staff. The irreproducibility of a high quality plasma coating therefore continues to be a major problem for the rapid expansion of this technology. The main reason for this is the lack of understanding of the underlying physical processes during plasma spraying. There are more than 50 macroscopic parameters that influence the quality of a coating (Table 31) [310].

Table 31  
Processing parameters in plasma spraying

---

Burner chamber and nozzle
Power supply
Plasma gas
Mass flow rate plasma gas
Cooling
Mass flow rate cooling gas
Nozzle geometry
Powder feed
Powder fraction and shape
Thermal properties of powder material
Carrier gas
Mass flow rate of carrier gas
Injection geometry
Plasma jet
Jet velocity and temperature
Particle velocity and temperature
Particle trajectories
Particle impact
Particle impact distribution
Particle velocity at impact
Particle impact angle
Molten state of particle at impact
Substrate type
Substrate temperature

---

Reproduced from [310] with permission from Elsevier.

#### 4.3.3. Equipment—process and mechanism

A complete plasma spray system comprised of plasma console, powder feeder, plasma gun and high frequency power supply unit. The spraying is generally carried out in an enclosed plasma booth, which should be placed inside a sound proof chamber with the facility of vacuum dust collection. Primary, secondary and career gases are required to create the plasma plume, shroud the plume from the direct contact of atmosphere and carry out the powder through the plasma gun nozzle, respectively. A six-axis automatic robot can be employed to control the movement of the plasma gun. The temperature of electrodes is kept normal through proper channeling of coolant (water) by using a water pump.

There are various companies, viz. Sulzer Metco, Praxair Inc., Tekna Plasma System Incorporation, etc., which supply plasma spray system, plasma gun and powder feeder of different models in the market. ValuPlaz<sup>TM</sup>, Metco A-2000 and Plasma-Technik A2000 Plasma Spray System from Sulzer Metco and PlazJet from TAFE, Praxair Inc. are few examples of plasma spray systems. There are various models of plasma and HVOF guns available in market, e.g. Twin-System gun from Sulzer Metco, SG series and Jet Coat from Praxair Inc. and PL series from Tekna Plasma System Incorporation, etc. A cross-sectional image of SG-100 plasma gun from Praxair Inc. has been demonstrated in Fig. 106, showing the position and shape of electrodes, inlets for powder and plasma gases and power supply.

Processing of fiber reinforced composite materials by plasma spray technique was first patented by United Technologies Corp., West Germany (Patent no. 01941491/DS) in 1968, where Al alloy matrix was reinforced by boron, silicon carbide or silicon carbide coated boron. Technical reports on consolidation of composite materials by plasma spraying has started appearing since early 1970s, and till then an appreciable amount of research has been conducted on plasma spray synthesized metal matrix and ceramic matrix composite [311,312].

Aluminum (Al)-based composite materials with ceramic reinforcement ( $\text{TiB}_2$  or  $3\text{Al}_2\text{O}_3 \cdot 2\text{SiO}_2$ ), which were produced by vacuum plasma spraying technique, showed exceptionally high values of elongation, especially after thermo-mechanical treatment [313]. High volume fraction alumina-reinforced copper composite plates were produced by plasma spray, which exhibited appreciable amount of electrical conductivity even after reinforcing with ceramic materials [314]. Plasma-sprayed Ni-based composite coatings reinforced with WC has been reported to possess improved abrasive wear resistance [315].

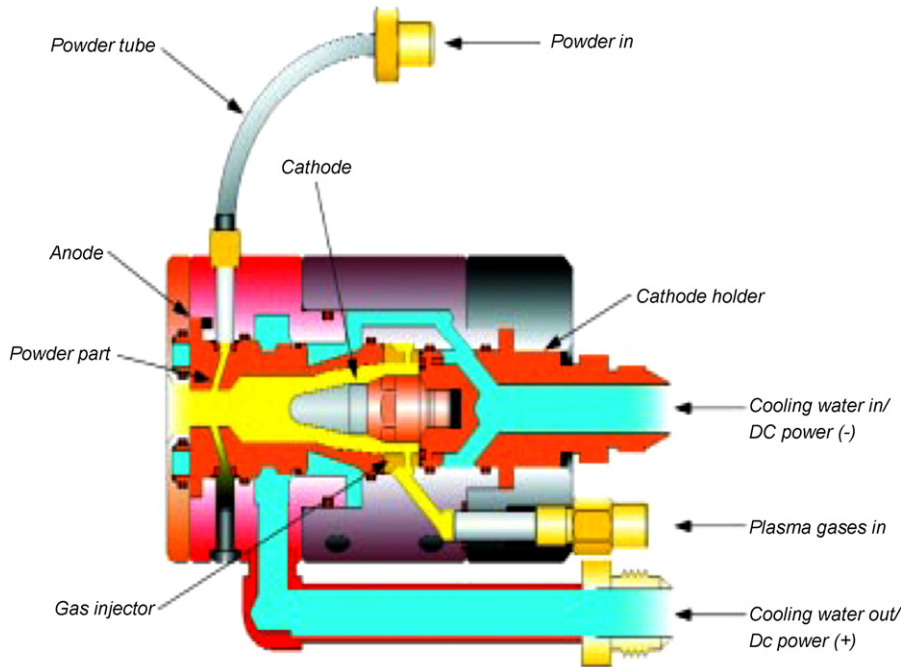


Fig. 106. Cross-sectional view of SG-100 plasma gun from Praxair Surface Technologies. (Source: [www.praxair.com](http://www.praxair.com).)

Al-based composite coating with Al–Mo–Ni reinforcement exhibited increased hardness attributed to Al–Mo–Ni strengthening [316]. Synthesis of plasma-sprayed W–Cu composite has been studied by Pintsuk et al. [317] and Döring et al. [318], where with increase in Cu amount to 60 vol.%, the coating exhibits a well-solidified structure with almost no porosity, which is attributed to better melting of the powder mixture due to higher amount of Cu. Cu–Mo composite coatings, which can be used as heat spreader material for electronic power module applications attributed to their high thermal conductivity and suitable thermal expansion coefficients, has been successfully prepared by vacuum thermal spraying process [319].

In situ composites are also being synthesized by plasma spray method. For example, aluminum-based composites with other metals like Fe, Cr, or Ni have been plasma-sprayed, where intermetallics formed by the reaction of aluminum and second metal provides the reinforcement strengthening [320,321]. Synthesis of  $\text{Fe}_2\text{O}_3$ –Al composite has been reported by Dong et al. [322]. The microstructure shows formation of hard  $\text{Al}_2\text{O}_3$  ceramic and  $\text{FeAl}_2\text{O}_4$  spinel along with Fe and Al matrix due to the reactive synthesis process. The composite structure provides better wear resistance than single-phase  $\text{Al}_2\text{O}_3$  coating. Synthesis of in situ TiC–Fe and TiN–Ti composite using reactive plasma spray technique has also been practiced by various researchers, where methane and nitrogen has been used as reactive gases, respectively [323–325].

#### 4.3.4. Nanoconsolidation

Significant improvement in mechanical properties, viz. tensile strength, hardness, fracture toughness, and wear resistance in the presence of nanosized grains or particles has been confirmed by scientific community [326,327]. The high cooling rate ( $10^6$ – $10^8$   $\text{K s}^{-1}$ ) during rapid solidification of molten powder in plasma spraying provides a high grain nucleation rate, however the time for grain growth is not allowed, which results in extensive grain refinement. There exist a plethora of literatures documenting achievement of nanostructure in metal, alloy, and ceramic systems by practicing plasma spraying attributed to the extremely high solidification rate of the process, which is not the focus of the present review. The current trend is mainly directed in synthesizing nanostructured composite materials by plasma spray technique, which has been reported in the subsequent sections of this review.

Thermal spray techniques are also being exercised to fabricate near-net shape nanocomposite structures besides the traditional coating synthesis. There are various near-net shape fabrication techniques such as laser additive manufacturing (LAM), laser-engineered net shaping (LENS<sup>TM</sup>), Osprey forming, and three-dimensional printing

Table 32

Vacuum plasma spray parameters for deposition of hypereutectic Al–Si alloy nanocomposite [297]

Parameter	Value
Primary gas	Argon 35 psi
Secondary gas	Helium 110 psi
Powder carrier gas	Argon 70 psi
Arc current	400 A
Arc voltage	35.4 V
Standoff distance	10 cm
Chamber pressure	650 Torr

3DP<sup>TM</sup>, where components are fabricated by layer by layer deposition of material in the form of powder wire or atomized droplet on computer aided designed (CAD) solid prototypes [328,329]. However, fabrication of materials with low laser absorption coefficient is not feasible by laser assisted techniques, whereas, consolidation of refractory metals and high temperature ceramics are limited in Osprey technique [330–332]. Plasma spray forming is a modified plasma spray technique for near-net shape fabrication and consolidation of wide range of materials, particularly, which are hard to fabricate by conventional techniques. The plasma-sprayed material is deposited on a specially designed substrate with suitable surface-finish, which is removed after the completion of deposition and thus the near-net shape free standing structure can be obtained.

**4.3.4.1. Hypereutectic Al–Si with primary silicon reinforcement.** Vacuum plasma spray (VPS) forming technique was adopted by Agarwal's research group in fabricating free-standing bulk nanocrystalline structure of hypereutectic aluminum alloy (Al–21 wt.% Si) using *micron-size* (15–45  $\mu\text{m}$ ) gas atomized, spherical hypereutectic Al–Si prealloyed powder feedstock [297]. The processing parameters are tabulated in Table 32.

The cross-sectional microstructure of the Al–Si deposit exhibits a dense splat structure containing fine eutectic Al–Si grains with homogeneously distributed ultrafine primary Si ( $\sim 1 \mu\text{m}$ ) particles throughout the eutectic Al–Si matrix (Fig. 107). The ultrafine primary Si particles precipitated from the Al–Si alloy due to the rapid solidification in VPS process. Further decrease in size of Si particle caused due to fragmentation attributed to high velocity impact of the molten powder. The Si particles act as second phase reinforcement in the Al–Si matrix and improve the mechanical properties of the composite, which has been discussed later in this section. The high magnification TEM image of the composite shows light-shaded Si-rich and dark-shaded Al-rich equiaxed nanosized grains (25–100 nm) with bimodal size distribution (Fig. 108) [297].

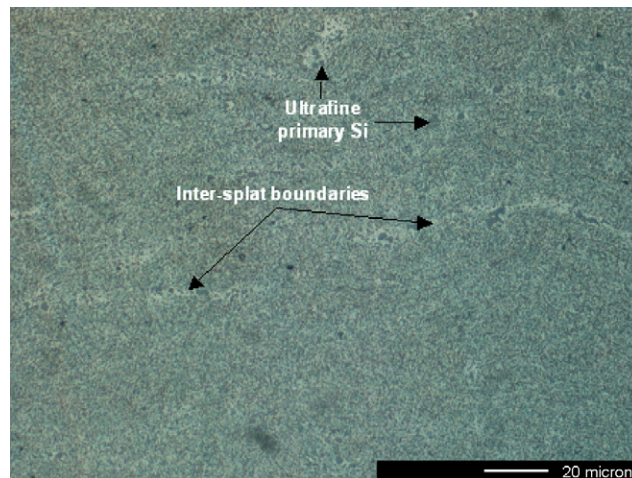


Fig. 107. Cross-sectional optical micrograph of the VPS formed Al–Si nanocomposite showing the presence of eutectic Al–Si grains and ultrafine primary silicon particles [297].

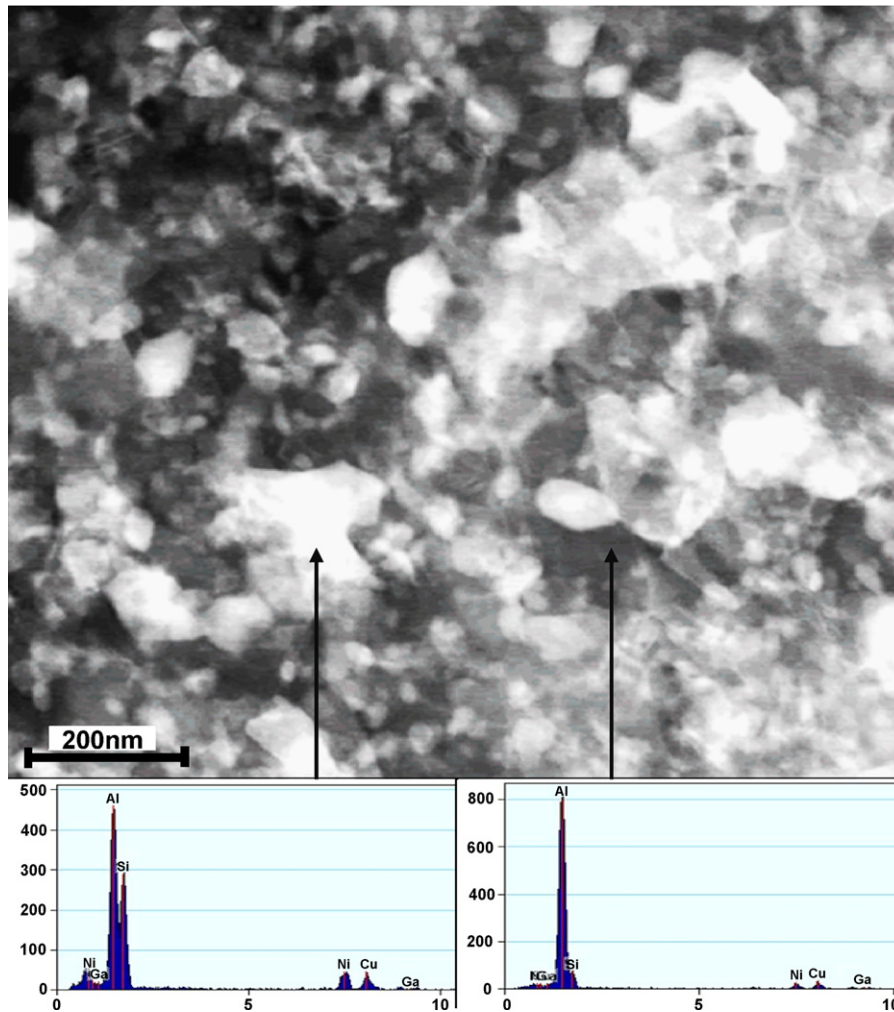


Fig. 108. Homogeneous distribution of nanosized ultrafine primary silicon and Al-Si matrix grains with EDX spectra [297].

The mechanical properties of VPS formed Al-Si alloy has been compared with similar material system processed by conventional casting (Al-17 wt.% Si) [333,334] and spray atomization followed by hot extrusion (A390 alloy: Al-17Si-4.5Cu-0.6Mg) [334] in Table 33. The VPS deposit exhibits higher hardness ( $151 \pm 14 \text{ kg mm}^{-2}$ ) than that of conventionally cast alloy ( $\sim 100 \text{ kg mm}^{-2}$ ), which is due to the presence of nanostructured grains with ultrafine hard primary silicon particles in sprayed structure. The elastic modulus, tensile strength and strain of the vacuum plasma-sprayed structure were measured as 82 GPa, 345 MPa and 0.43%, respectively. Improvement in UTS of the VPS formed Al-Si composite compared to the conventionally cast alloys is attributed to the presence of nanostructured grains with bimodal size distribution and composite strengthening by primary Si particles with (110 GPa) high elastic modulus. The solid solution strengthening by ultrafine Si in the Al-Si alloy and high dislocation density due to the

Table 33

Comparison in mechanical properties of hypereutectic Al-Si alloys synthesized by different techniques [297]

Differently processed hypereutectic Al-Si alloy	Microhardness ( $\text{kg mm}^{-2}$ )	Elastic modulus (GPa)	Ultimate tensile strength (MPa)	Strain (%)
VPS formed alloy	$151 \pm 14$	82	345	0.43
Conventionally cast alloy	$\sim 100$	$\sim 75$	$\sim 180$	$< 1$
Spray atomized deposit with hot extrusion	No data	80	448	7.0

mismatch of thermal expansion coefficient of Al matrix and Si particles also contribute to the high UTS of the composite [297].

**4.3.4.2. Al–CNT nanocomposite.** Successful fabrication and detailed characterization of CNT reinforced hypereutectic Al–Si composite freestanding cylindrical structure by plasma spray forming (PSF) has been carried out by Agarwal and co-workers [335]. In recent times, carbon nanotubes are being employed as a potential reinforcement in fabricating high strength composites due to their extremely high elastic modulus ( $\sim 1$  TPa) and superior tensile strength ( $\sim 200$  GPa) [336,337]. However, the research on CNT reinforced metal matrix and ceramic matrix composites has been rather limited, compared with polymer matrix composite [338–340].

Gas atomized, prealloyed, spherical hypereutectic Al–21 wt.% Si alloy powder of 15–45  $\mu\text{m}$  size was used as the matrix. Multiwalled carbon nanotube (10 wt.%) were added as the reinforcement. Al–Si powder and carbon nanotube were blended and mixed in a ball mill for 48 h to achieve homogeneous mixing. The blended powder was plasma-sprayed on well-polished 6061Al rotating mandrel of predefined dimensions. Plasma spray formed hollow and tapered cone-shaped Al–CNT composite structure (34 mm larger outer diameter, 45 mm length and wall thickness 1 mm) is shown in Fig. 109.

Metallographically polished cross-sectional view (Fig. 110a) of composite shows resolidified structure in presence of certain amount of porosity (2–5  $\mu\text{m}$ ). Retention of carbon nanotubes in the composites is affirmed from the SEM micrograph (Fig. 110b) of the fractured surfaces. The entangled nanotubes are present at the edges of successive fractured splats. The microhardness values of the nanocomposite ( $157 \pm 6 \text{ kg mm}^{-2}$ ) and is higher than that of



Fig. 109. Plasma spray formed hollow cone-shaped Al–CNT composite structure [335].

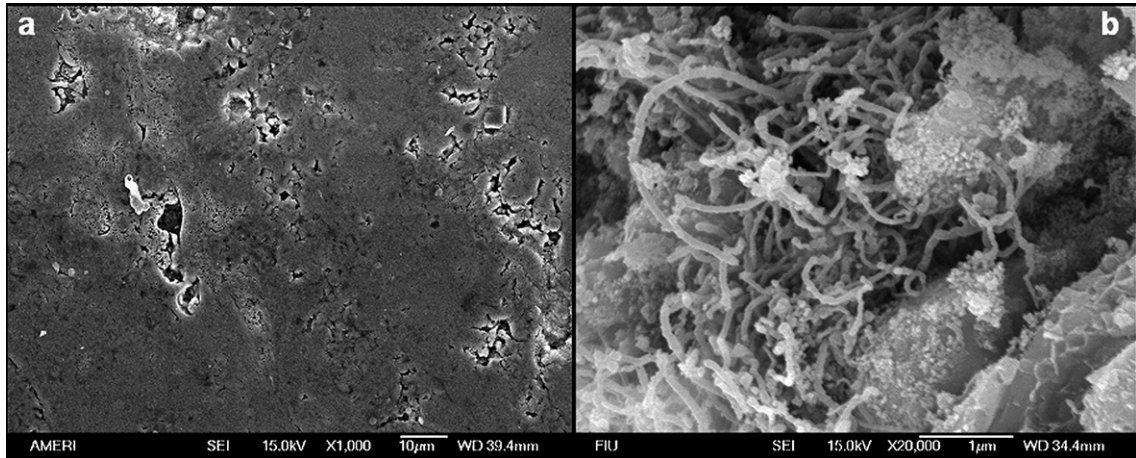


Fig. 110. (a) Polished cross-sectional SEM image of plasma spray formed Al–CNT composite showing well-solidified structure with some porosities and (b) fractured surface showing the presence of carbon nanotubes [335].

conventionally cast Al–20 wt.% Si alloys ( $\sim 100 \text{ kg mm}^{-2}$ ). This could be attributed to the dispersion strengthening of the composites by extremely hard carbon nanotubes (62–150 GPa) and nanocrystalline structure of the composites.

**4.3.4.3. Al–alumina nanocomposite.** The mechanical properties of plasma-sprayed hypereutectic aluminum-based nanostructured composite coatings with nanosized aluminum oxide reinforcement on 6061Al substrate were investigated by Agarwal et al. [341]. Mixtures of hypereutectic Al alloy powder (50–100  $\mu\text{m}$ ) and nanosized alumina powder (30–60 nm) with 20 and 30 wt.% were used as feedstock material. Blending of nanosize alumina powders with micron size Al–Si powders facilitated the spraying of nanopowders as the larger powders act as a carrier.

The cross-sectional view of composite coatings on 6061Al substrate exhibit crack-free microstructure with some porosity and good coating–substrate adherence (Fig. 111). The microstructural features and tribological behavior of the composite coatings are compared in Table 34. The coating with 30 wt.% nano-alumina shows lower coating thickness due to poor powder flow behavior caused by higher nanosized particle content. The poor powder flow also resulted in low alumina volume fraction and higher porosity level in Al–30 wt.% alumina coating. Retention of nanostructured aluminum oxide domains (20–50 nm size) in the coating can be observed in Fig. 112. The composite coatings showed better microhardness in comparison with 6061Al substrate due to presence of hard nanosized alumina particles. The presence of hard and brittle alumina also resulted in better tribological behavior of the coatings (Table 34) [341].

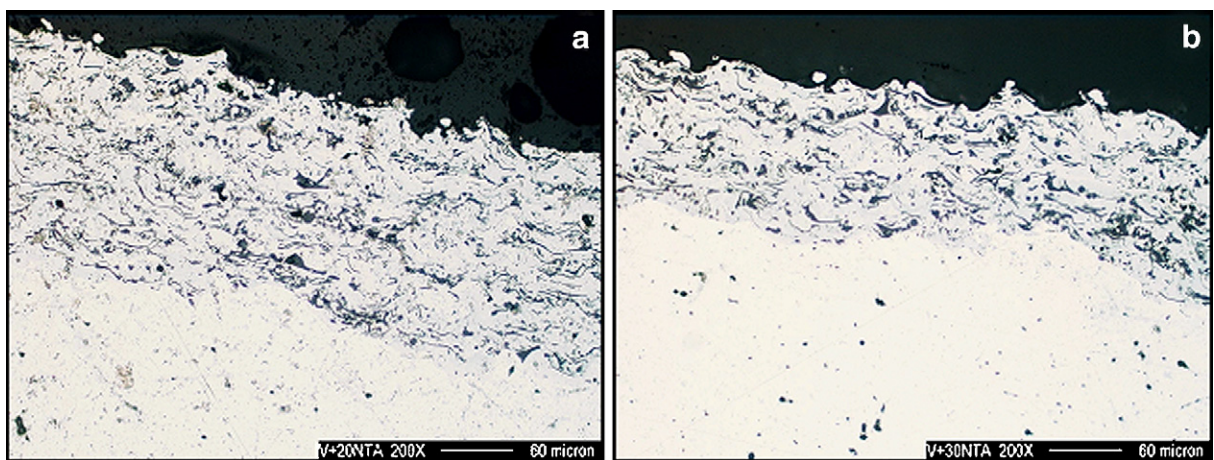


Fig. 111. Optical micrographs of the plasma-sprayed Al-based nanostructured coatings on 6061 aluminum substrate: (a) with 20 wt.% and (b) 30 wt.% alumina [341].

Table 34

Summary of microstructural and tribological features of Al–alumina composite coatings and substrate [341]

Coating features	Al + 20 wt.% alumina	Al + 30 wt.% alumina	6061Al substrate
Coating thickness	180 ± 20 μm	120 ± 20 μm	N/A
Density (theoretical, g cm <sup>-3</sup> )	2.77	2.88	2.7
Density (water immersion, g cm <sup>-3</sup> )	2.67	2.70	N/A
Volume percent (reinforcement)	16.5 (black phase)	17.1 (black phase)	N/A
Microhardness (VHN)	233 ± 12	241 ± 15	85 ± 10
Wear (weight loss in 10 min, g)	0.011	0.010	0.015
Coefficient of friction	0.36	0.36	0.50

**4.3.4.4. In situ Mo–MoO<sub>2</sub> nanocomposite.** Plasma-sprayed Mo deposits are used mostly for automotive, aerospace and pulp and paper industries due to their exceptional wear-resistance properties [342]. A coating of ~2 mm thickness was deposited by spraying Mo powder (10–40 μm) on steel substrates, which were kept at 190 and 440 °C for 10 min. The spraying was carried out using a plasma torch (Model PT-F4) at an operating voltage and current of 70 V and 500 A, respectively, where a mixture of Ar and H<sub>2</sub> was used as carrier gas.

Atmospheric plasma spraying of Mo powder resulted in formation of Mo/Mo oxide nanocomposite due to some oxidation of Mo. The plasma-sprayed deposit exhibited typical splat morphology with some amount of porosity in between the successive splats. The XRD spectra (Fig. 113) of the Mo-deposit show presence of Mo with very minute amount of Mo oxides (primarily MoO<sub>2</sub> and minor presence of Mo<sub>4</sub>O<sub>11</sub>). Fine particles of MoO<sub>2</sub> (5–10 nm) can be observed embedded randomly in the columnar grains of Mo (Fig. 114). The oxides (MoO<sub>2</sub>, Mo<sub>4</sub>O<sub>11</sub>, and Mo<sub>8</sub>O<sub>23</sub>Mo) were formed as the Mo droplets picked up oxygen primarily in flight and solidified with various oxide stoichiometries. The MoO<sub>2</sub> particles formed maintaining a definite orientation relation with the matrix.

**4.3.4.5. Zirconia–alumina nanocomposite.** Deposition of nanostructured zirconia–alumina (30 vol.%) composite coatings was carried out by Liang's research group via atmospheric plasma spraying [343]. Commercial yttria-stabilized zirconia powders (~50 nm) and alumina powders (~20 nm) were used as the starting particles. The ball milled (20 h) powder mixture reconstituted into spherical or ellipsoidal granules (~60 μm) by spray drying process, where the two oxide powders exhibited homogenous distribution. The spray-dried powder was sprayed through a

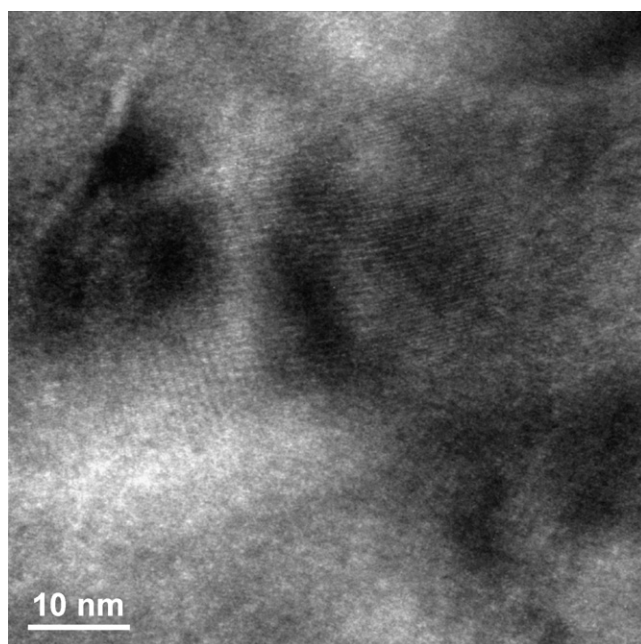


Fig. 112. HRTEM micrograph showing nanosize domains (black regions) of aluminum oxide in Al–Al<sub>2</sub>O<sub>3</sub> composite coating [341].

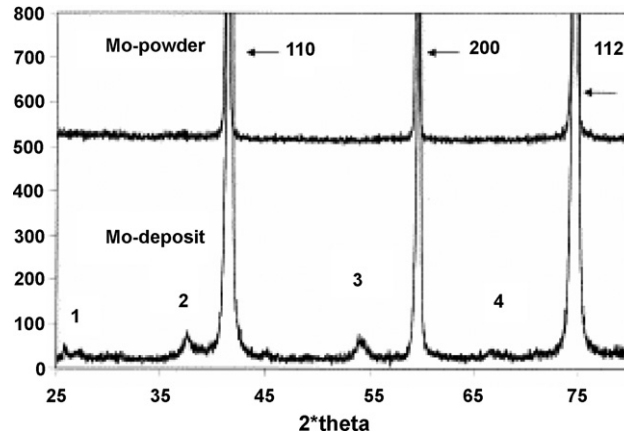


Fig. 113. XRD of the Mo powder and the plasma-sprayed deposit. The  $\text{MoO}_2$  reflections observed in the deposits are broadened, indicating that the oxide particles are quite small. (Reprinted from [342] with permission from Elsevier.)

Twin-System gun (Plasma-Technick AG, Switzerland) using a Metco A-2000 atmospheric plasma spraying system (Sulzer Metco AG, Switzerland). Table 35 lists the plasma spray parameters. The spraying was carried out on degreased and grit blasted stainless steel coupons cooled by compressed air.

The coating ( $\sim 450 \mu\text{m}$  thickness) exhibited smooth surface and dense structure with  $\sim 6\%$  porosity and showed excellent adherence to the substrate. The fractured coating surface (Fig. 115) shows a bimodal grain structure, where (i) both typical lamellar splat structure ( $1 \mu\text{m}$  thickness), comprised of columnar grains of  $150 \text{ nm}$  size (Fig. 115a) and (ii) equiaxed grains (size less than  $100 \text{ nm}$ ), formed due to extremely high cooling rate during the solidification process. Attribute to its dense composite structure, the coating exhibited microhardness of  $8.4 \text{ GPa}$ , which was about 1.5 times that of the nanostructured zirconia coating deposited using same nanostructured zirconia powder.

**4.3.4.6.  $\text{MoSi}_2\text{-Si}_3\text{N}_4$  composite.** Consolidation of near-net shape bulk  $\text{MoSi}_2\text{-Si}_3\text{N}_4\text{-SiC}$  nanocomposite using vacuum plasma spray forming has been practiced by Seal's research group [344].  $\text{MoSi}_2$  ( $20 \mu\text{m}$ ) 50 wt.%, 50 wt.%  $\text{Si}_3\text{N}_4$  +  $\text{MoSi}_2$  ( $50\text{--}100 \text{ nm}$ ) with 4 wt.% SiC powder particle, mixed by ball milling, was vacuum plasma-sprayed

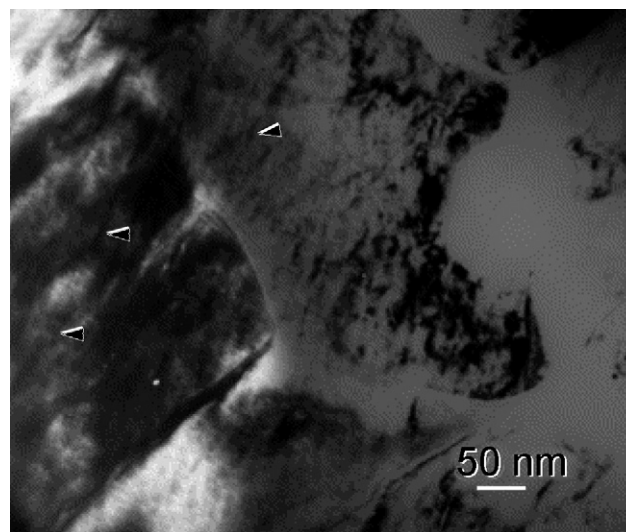


Fig. 114. A bright field TEM micrograph showing the dispersion of nanocrystalline  $\text{MoO}_2$  as shown by arrow in plasma-sprayed Mo- $\text{MoO}_2$  nanocomposite. (Reprinted from [342] with permission from Elsevier.)

Table 35  
Plasma spraying parameters for nanostructured ZrO<sub>2</sub>–30 vol.% Al<sub>2</sub>O<sub>3</sub> coating

	Parameter						
	Current (A)	Voltage (V)	Primary gas (Ar, slpm)	Secondary gas (H <sub>2</sub> , slpm)	Carrier gas (Ar, slpm)	Spray distance (mm)	Feeding distance (mm)
Value	620	68	40	12	4	100	6

Reprinted from [343] with permission from Elsevier.

using a SG-100 gun (Praxair Surface Technologies). The plasma parameters are presented in Table 36. The spraying was carried out on a rotating well-polished mandrel and spray-formed cylindrical bulk nanocomposite (Fig. 116) was released taking the advantage of CTE mismatch between the mandrel and the deposit.

Polished cross-section views of the plasma-sprayed nanocomposite as a function of the wall thickness shows overall compact structure with relative density value of about 90% (Fig. 117). A homogenous microstructure with Si<sub>3</sub>N<sub>4</sub> particles (dark gray color), MoSi<sub>2</sub> matrix (light gray), and the pores (black) are visible. The middle region of the cylinder showed relatively higher fracture toughness than the other regions of the composites. The higher fracture toughness is attributed to the crack deflection by homogeneous distribution and the retention of nanostructures.

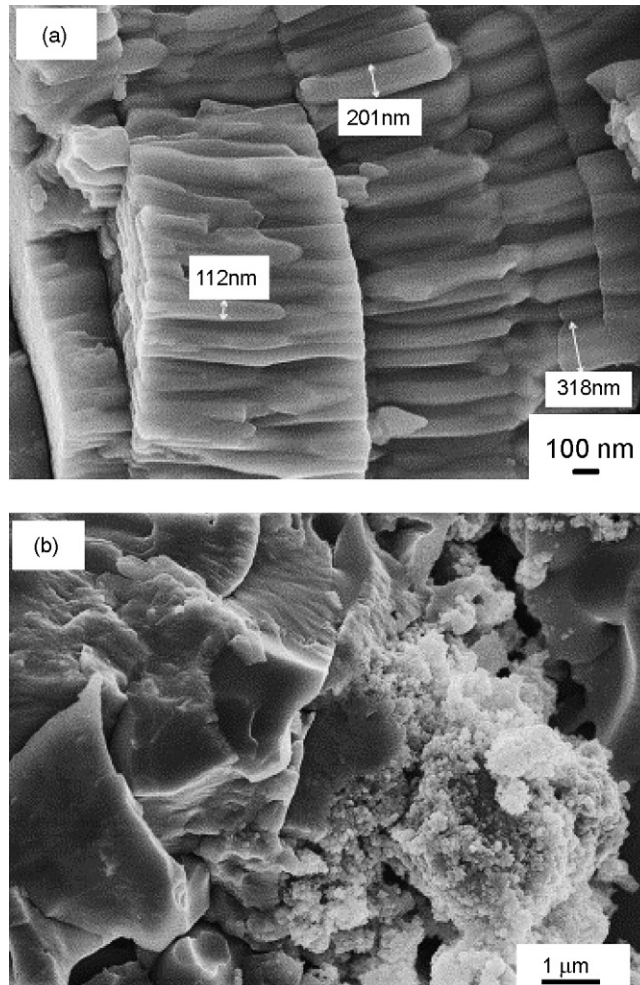


Fig. 115. SEM micrographs of: (a) fracture surface morphology of lamellar structure and (b) fracture surface of bimodal structure in plasma-sprayed ZrO<sub>2</sub>–Al<sub>2</sub>O<sub>3</sub> composite coating. (Reprinted from [110] with permission from Elsevier.)

Table 36

Processing parameters of vacuum plasma-sprayed bulk  $\text{MoSi}_2\text{-Si}_3\text{N}_4\text{-SiC}$  nanocomposite [344]

Plasma gases	Argon–helium
Torch power	29 kW
Argon gas flow rate	170 SCFH
Helium gas flow rate	38 SCFH
Vacuum level	400 Torr
Motion parameters	Torch at 200 in. $\text{min}^{-1}$ , part at 40 rpm

**4.3.4.7. Alumina–Ni nanocomposite.** Fabrication of freestanding bulk alumina nanocomposite with nanosized Ni reinforcement by air plasma spraying has been practiced by Seal and co-workers using Ni coated  $\text{Al}_2\text{O}_3$  powder as feedstock [345]. The Ni coated  $\text{Al}_2\text{O}_3$  powder was procured by electroless coating technique, where high purity (99.95%) alumina particles were coated with a 30 nm thick nickel layer with 3–4 wt.% of Ni loading in the alumina matrix. The composite powder was air plasma-sprayed on a surface-finished cylindrical mandrel made of 6061Al to fabricate a cylindrical-shaped nanocomposite structure of 1.2 in. outer diameter, 1 in. inner diameter, and 1.5 in. length (Fig. 118).

The cross-sectional microstructure of the nanocomposite coating exhibits a 96–98% dense structure with no significant cracks or porosity (Fig. 119). The hardness (1025 HV) of the Ni–alumina composite was measured to be better than that achieved for the monolithic alumina developed using plasma spray ( $940 \pm 20$  HV). The composite also showed improved fracture toughness ( $\sim 5 \text{ MPa m}^{1/2}$ ) compared to hot press sintered Ni–alumina composite ( $\sim 3.5 \text{ MPa m}^{1/2}$ ), which is attributed to the crack blunting capability of ductile nickel.

**4.3.4.8. Alumina–CNT nanocomposite.** Alumina–CNT nanocomposite coating was deposited by Agarwal’s research group adopting air plasma spraying a mixture of spray-dried nanosized alumina (5–60  $\mu\text{m}$ ) powder and 4 wt.% multiwalled carbon nanotube (95% purity, o.d. 40–70 nm) [346]. The cross-sectional view of the coating (Fig. 120) confirms retention of CNTs in between partially resolidified splats of spray-dried alumina agglomerates. The grain size measurement from XRD spectra of the composite coating revealed evolution of a bimodal size grain structure with larger grains (0.134  $\mu\text{m}$ ) of parent  $\alpha\text{-Al}_2\text{O}_3$  phase and smaller grains (14 nm) of  $\gamma\text{-Al}_2\text{O}_3$  phase. The microhardness value of plasma-sprayed  $\text{Al}_2\text{O}_3\text{-MWCNT}$  (563.4–575.7 VHN) did not differ much with that of plasma-sprayed  $\text{Al}_2\text{O}_3$  coating (578.2–584.2 VHN). However, the CNT reinforced coating (2.62–4.73  $\text{MPa m}^{1/2}$ ) exhibited almost 44% improvement in fracture toughness, compared with plasma-sprayed alumina coating without any reinforcement (2.53–3.29  $\text{MPa m}^{1/2}$ ). This is attributed to bimodal grain size distribution and crack bridging effect of retained CNTs.

**4.3.4.9. Nanostructured hydroxyapatite–zirconia composites powders.** Spherical nanostructured powder from irregular micron-size powders can be produced by employing plasma spray technique by virtue of the rapid

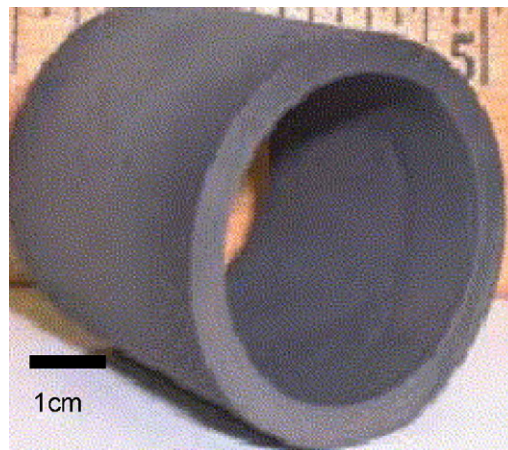


Fig. 116. Plasma-sprayed ring type  $\text{MoSi}_2\text{-Si}_3\text{N}_4\text{-SiC}$  nanocomposite with a diameter of 3.5 cm, a wall thickness of 0.5 cm, and a height of 2.4 cm [344].

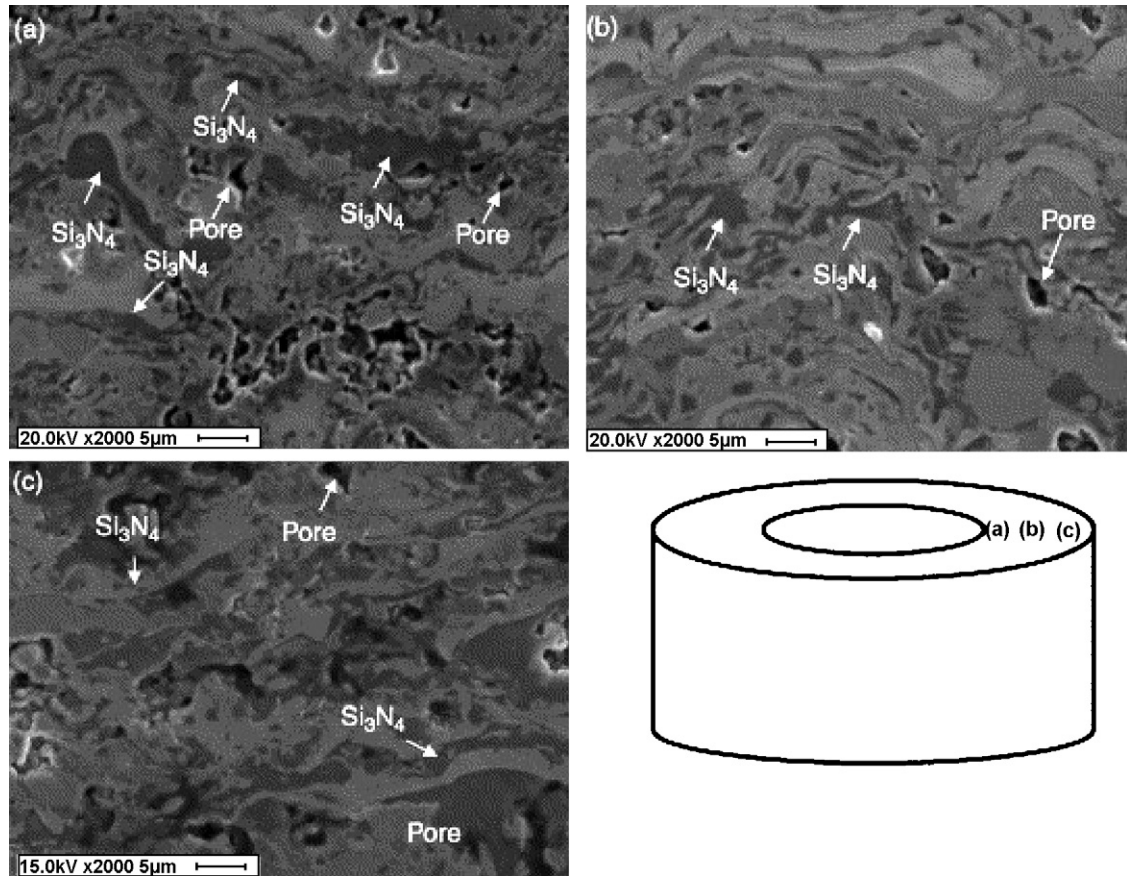


Fig. 117. SEM micrographs of the cross-section of the plasma-sprayed cylindrical bulk nanocomposite with thickness: (a) inside, (b) middle, and (c) outside of cylinder [344].



Fig. 118. Cylindrical-shaped alumina-Ni nanocomposite structure with 1.2 in. outer diameter, 1 in. inner diameter, and 1.5 in. length [345].

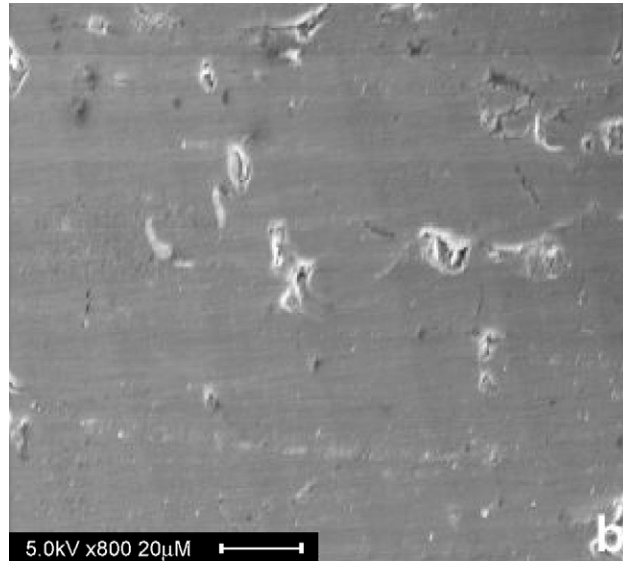


Fig. 119. Cross-sectional micrograph of air plasma-sprayed alumina–Ni nanocomposite bulk structure showing dense structure [345].

solidification [291]. Ultrafine hydroxyapatite (HA)/ZrO<sub>2</sub> composite powders was synthesized using 35 kW Tekna Plasma System Inc., where wet suspension of HA/ZrO<sub>2</sub> was axially sprayed through an RF plasma torch (PL-35) and the powders were subsequently collected in cyclone collectors [347]. The plasma-sprayed powders composed of mixture of HA/CaP particles and HA/CaP/ZrO<sub>2</sub> composite particles. The various morphologies of the powders indicated that nanosized ZrO<sub>2</sub> particles existed both within and as fine scale surface-attachments on HA/calcium phosphate particles. It was also observed that medium and larger composite powders contained larger amounts of embedded nano-ZrO<sub>2</sub> and only minute traces of CaZrO<sub>3</sub>, which was formed by the reaction of HA and ZrO<sub>2</sub>.

#### 4.4. High velocity oxyfuel spraying

##### 4.4.1. Introduction

High velocity oxyfuel spraying is based on high pressure combustion process, has been widely used in the automotive and aerospace industry to deposit coatings of metals and ceramics. Jet Kote™ system was the first HVOF

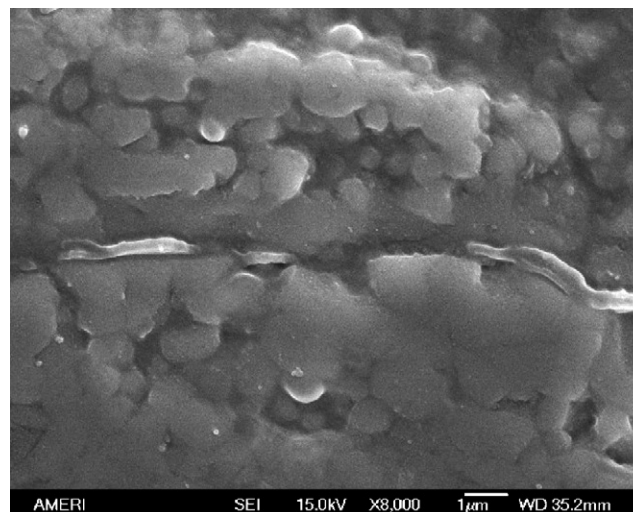


Fig. 120. Plasma-sprayed Al<sub>2</sub>O<sub>3</sub>–4 wt.% MWCNT nanocomposite coating [346].

torch of its kind, manufactured by Stellite Coatings, started operating at a pressure of 0.41 MPa [282]. Afterwards, different advanced models and designs of HVOF system invented with a present operating pressure up to 1.35 MPa (Terojet, Eutectic Castolin, CH).

#### 4.4.2. Fundamental principles

Like plasma spray technique, in HVOF spraying also, powder particles ejected from a nozzle experiences heating and after partial/complete melting deposit on a substrate. However, a combustion flame as the heat source and extremely high particle velocity are the characteristic of this spray method. A combustion flame of highly compressed fuel gas with required oxygen content, undergoes free expansion attributed to the specific torch design and thereby powder particles, expelled out with the oxyfuel mixtures experience a very high gas acceleration and deposit on a substrate after encountering the combustion flame (Fig. 121) [282,283]. Therefore, the adhesion or bonding of particles in the deposits is result of two factors, viz. (i) the partial/complete melting and resolidification of particles and (ii) mechanical interlocking of particles attributed to heavy plastic deformation upon impact.

The HVOF unit uses an oxygen–fuel mixture consisting of propylene, propane, or hydrogen, depending on users coating requirements. Fuel gases are mixed in a proprietary siphon system in the front portion of the HVOF gun. The thoroughly mixed gases are ejected from the nozzle and ignited externally to the gun. Ignited gases form a circular flame configuration, which surrounds the powdered material as it, flow through the gun. Combustion temperature is between 3000 and 6000 °C depending on fuel. The circular flame shapes the powder stream to provide uniform heating, melting, and acceleration. Pre-selected oxygen, fuel and air values are specified for each material to optimize dwell time in the flame.

#### 4.4.3. Nanoconsolidation

The rapid cooling is the main driving force in procuring nanosized grains in HVOF sprayed deposit, alike plasma spraying. However, there are two primary differences between plasma spraying and HVOF spraying in the event of nanostructure achievement in the sprayed deposit.

- (i) Firstly, depending on the selection of fuel gas and proportion of the fuel gas to oxygen, the sprayed powder particles experience much lower temperature in HVOF process (3000–6000 °C) compared to plasma spraying (15,000–20,000 °C) (Table 30). Thus, both the degree of melting and solidification rate is lesser in case of HVOF spraying, considering the material system and substrate condition as identical. Therefore, the driving force for nucleation of grains and restriction to grain growth is comparatively lesser in HVOF sprayed deposit.
- (ii) Secondly, the spray velocity in HVOF spraying ( $700\text{--}1400\text{ m s}^{-1}$ ) is much higher than in plasma spraying ( $350\text{--}1000\text{ m s}^{-1}$ ), which causes a higher degree of particle impact in HVOF process. This heavy impact leads to fragmentation of resolidifying particles and thus formation of large number of nucleation sites, which causes higher extent of grain refinement in the deposit structure. Consolidation of nanostructured composite has been discussed in the later section with example.

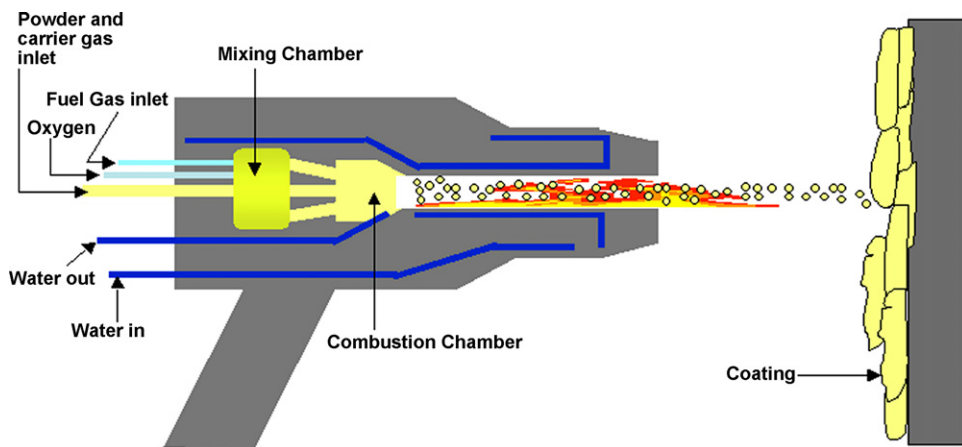


Fig. 121. Schematic of high velocity oxyfuel spraying.



Fig. 122. HVOF spray formed hypereutectic Al-Si nanocomposite ring structures (3.85 cm inner diameter with a thickness of 2.5 mm) [348].

**4.4.3.1. Hypereutectic Al-Si alloy nanocomposite.** Free standing ring-shaped Al-21Si nanocomposite structures (3.85 cm inner diameter with a thickness of 2.5 mm) (Fig. 122) were fabricated by HVOF spraying, where gas atomized, spherical hypereutectic Al-21 wt.% Si alloy powders (15–45  $\mu\text{m}$ ) were used as feedstock powder [348].

Fig. 123 shows a cross-sectional micrograph of the spray deposited composite structure showing a homogenous and highly dense splat structure, consisting of ultrafine primary (2–4  $\mu\text{m}$ ) Si and network of eutectic Si in the eutectic Al-Si matrix. Formation of a thin oxide layer of uneven thickness can also be observed on the splat surfaces as a common characteristic of HVOF process. High magnification SEM micrograph of cross-section of the deposit (Fig. 124) exhibits nanosized (25–50 nm) dissolved eutectic Si particles in Al-Si matrix. Few microscopic pores are also visible

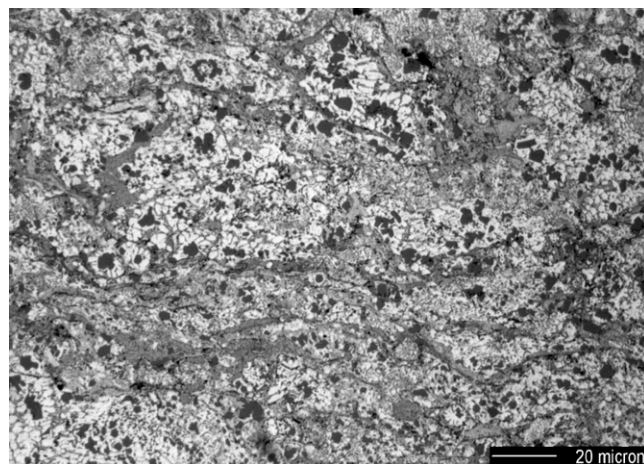


Fig. 123. Optical micrograph of the cross-section of HVOF sprayed Al-Si composite structure showing ultrafine primary (2–4  $\mu\text{m}$ ) Si and network of eutectic Si in the eutectic Al-Si matrix [348].

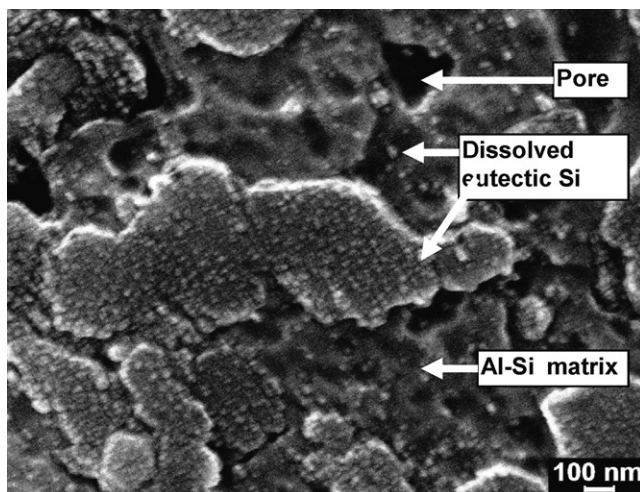


Fig. 124. SEM micrograph of the HVOF formed ring structure showing dissolved fine eutectic Si in the eutectic Al–Si matrix [348].

due to the high velocity and the turbulence of the impinging powder melts, which will potentially help in blunting the crack tip by forming bigger plastic zone at the tip.

The modulus of elasticity ( $138 \pm 17$  GPa) of the nanocomposite structure was measured by nanoindentation technique shows an intermediate value of elastic modulus for pure Al (71.9 GPa) and Si (162.9 GPa), which insinuates the ‘composite’ behavior of hypereutectic Al alloy with Si as the second phase reinforcement. The composite also showed better microhardness value ( $441 \pm 34$  VHN) than conventionally cast (cooling rate of  $\sim 10^2$  K s<sup>-1</sup>) eutectic Al–20 wt.% Si alloys (100–150 VHN). The improvement in mechanical properties of the HVOF sprayed Al–Si nanocomposite is attributed to several factors, viz. the presence of nanostructured matrix, composite strengthening by primary silicon particles, solid solution strengthening by dissolved eutectic Si and generation of immobile dislocation due to the thermal mismatching of Al–Si matrix and primary Si particles [348].

**4.4.3.2. Alumina–Ni composite.** Development of Al<sub>2</sub>O<sub>3</sub>–Ni HVOF sprayed nanocomposite coating towards improving fracture toughness of bulk component has been reported by Turunen et al. [349]. Spray-dried agglomerates prepared from nanosized powder mixtures of Ni and Al<sub>2</sub>O<sub>3</sub> with varying percentage of Ni (2 and 5 vol.%) was obtained by carrying out calcination followed by a H<sub>2</sub> reduction treatment to a solution mixture of Ni(NO<sub>3</sub>)<sub>2</sub> and AlO(OH). A Praxair HV-2000 spray gun fitted with 22-mm combustion chambers was employed for coating deposition on grit blasted carbon steel plates. Nitrogen was selected for a carrier gas along with hydrogen as a fuel gas. The diagnostic data for spray condition has been reported in Table 37.

The cross-sectional SEM image of the coating with an average thickness of 0.48 μm shows dense and distinct splat structure (Fig. 125) with relative content of α and γ-phases as measured by XRD were 4 and 96%. Alumina grains are found to be in nanometer dimension. The fine structure was retained in spite of melting of the powder in the HVOF process and only a small amount of α-Al<sub>2</sub>O<sub>3</sub> evolved from the γ-phase. Introduction of nickel alloying decreases hardness and wear resistance of the coatings, but increases toughness of the coatings.

**4.4.3.3. TiC–Ni cermet composite.** Deposition of TiC–Ni composite was carried out by Eigen et al., where ball milled commercially available (Ti, Mo)(C,N) with a particle size 1.5 μm and Ni and Co powders with a particle size of 2.5 was HVOF sprayed using a Diamond Jet 2700 torch (Sulzer-Metco) with ethylene as fuel gas was used [350].

Table 37  
Diagnostic data for HVOF spray condition of alumina–Ni nanocomposite [350]

Ratio H <sub>2</sub> /O <sub>2</sub>	Total flow (l min <sup>-1</sup> )	Stand-off (mm)	T (°C)	Spray velocity (m s <sup>-1</sup> )
2.00	1050	150	1990 ± 4	1014 ± 7

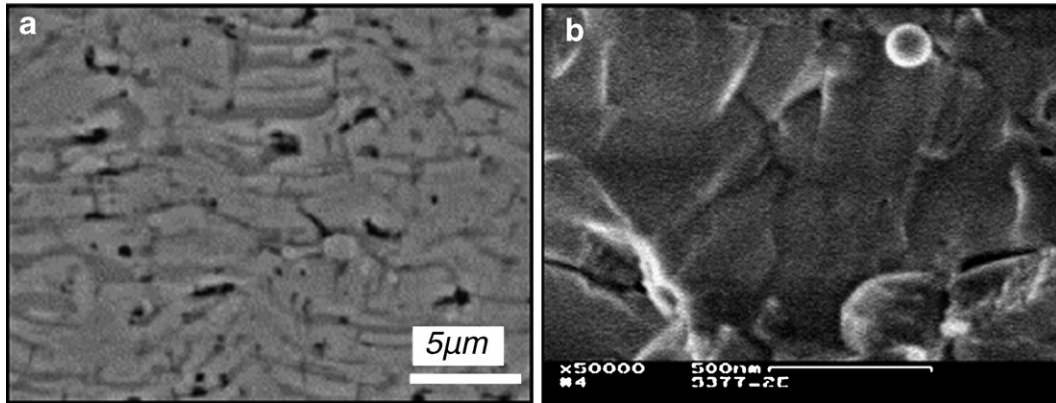


Fig. 125. Cross-sectional SEM images of HVOF sprayed alumina–Ni composite showing: (a) dense splat structure and (b) retained nanosized grains in the coating. (Reprinted from [341] with permission from Elsevier.)

The cross-sectional SEM image shows flat, plate-like splats, indicating the high degree of deformation of the particles, without breaking (Fig. 126). XRD study of the coatings revealed highly reduced peak intensities of the carbide compared to the metallic phase, which reflects the loss of hard phases during the spray process. Carbides partially decomposed due to the presence of oxygen in the flame gas and the ambient atmosphere and resulted in formation of  $\text{TiO}_2$ , CO, and  $\text{CO}_2$ . HVOF coatings show slightly less hardness, as a consequence of the lack in hard phases.

**4.4.3.4. Hydroxyapatite–zirconia composite.** Successful deposition of hydroxyapatite/nano-zirconia composite coating through HVOF spraying was reported by Khor and co-workers, where plasma spheroidized HA/nano-zirconia composite powders of composition 90 wt.% HA + 10 wt.% zirconia of  $\sim 40 \mu\text{m}$  size was used as feedstock [351]. The deposition was carried out on grit-blasted Ti–6Al–4V substrates, using a fully computerized HV2000 HVOF system (Praxair, USA) with a nozzle diameter of 19 mm. Hydrogen and argon was used as fuel gas and carrier gas, respectively. The flow rates of oxygen, hydrogen, and argon were 283, 566, and  $19 \text{ l min}^{-1}$ , respectively. The spray distance was 250 mm and powder feed rate was  $6 \text{ g min}^{-1}$ .

A comparative depiction of cross-sectional SEM images with (Fig. 127b) and without (Fig. 127a) zirconia reinforcement in hydroxyapatite has been provided. The coating of hydroxyapatite with zirconia shows a layered and dense composite structure with evenly distributed zirconia particles (Fig. 127b). The porosity level of the coating decreased to a great extent with the incorporation of zirconia particles which are located at the HA splats interface.

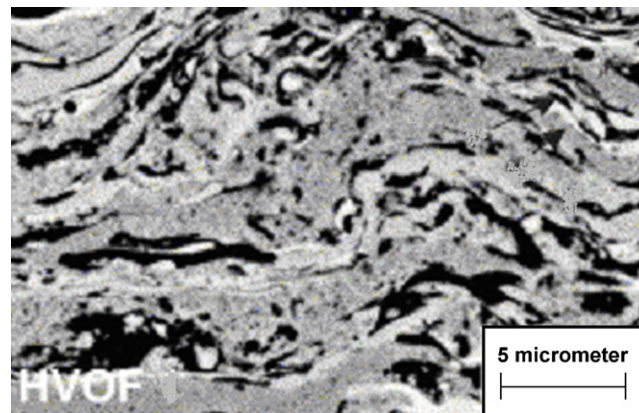


Fig. 126. Splat morphology in HVOF sprayed TiC–Ni cermet nanocomposite coating. (Reprinted from [351] with permission from Elsevier.)

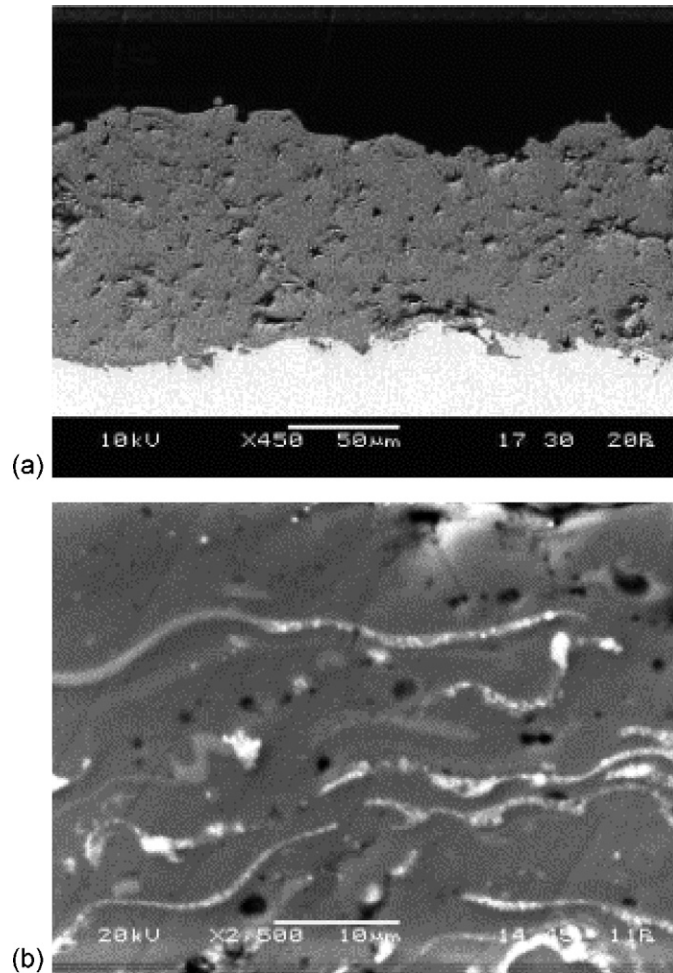


Fig. 127. Typical cross-sectional microstructure of the HVOF sprayed: (a) pure HA coating and (b) HA/nano-zirconia coating showing an improved structure brought about by the incorporation of zirconia. (Reprinted from [353] with permission from Elsevier.)

**4.4.3.5. Nylon 11–silica/carbon black nanocomposite.** The use polymer coatings is still not very popular due to the coating's few limitations, viz. low scratch resistance, poor adhesion to metal substrates, or high coating permeability. However, recently the practice of polymer-based nanocomposite synthesis has become more frequent as the composites exhibit considerable improvement in physical properties compared to pure polymers or conventional composites [352,353].

Fabrication of polymer nanocomposite by HVOF spraying has been exercised by Knight's group, where nylon 11 was chosen as matrix material due to its high chemical resistance, higher melting ( $\sim 183^\circ\text{C}$ ) and degradation ( $\sim 360\text{--}550^\circ\text{C}$ ) point with two most commonly used polymer fillers silica and carbon black were selected as reinforcements [354,355]. A ball-milled mixture of nylon 11 powders ( $30\text{--}60\ \mu\text{m}$ ) and silica ( $7\text{--}12\ \text{nm}$ ) or carbon black ( $6\ \text{nm}$ ) was sprayed using a Stellite Coatings Jet Kote II HVOF combustion spray gun with internal powder injection and a  $76\ \text{mm}$  long by  $8\ \text{mm}$  diameter nozzle, was used to spray the polymers. The processing parameters are summarized in Table 38. It has been confirmed by FTIR analysis that, HVOF spraying parameters did not result in significant degradation of the starting polymers. Both the composites with different reinforcements exhibited distinct splat structure with fine or no-cell structure, corresponding to better spatial filler distribution in the polymer matrix (Fig. 128). Higher crystallinity was also observed for the reinforced contents nylon 11 coatings, which is attributed to the fillers acting as nucleation sites, promoting crystallization.

Table 38

Processing parameters of HVOF sprayed nylon 11 nanocomposites

Powder feed rate	$0.25 \text{ g s}^{-1}$ ( $151 \text{ g min}^{-1}$ )
Powder carrier gas	Nitrogen
Powder carrier gas flow	$0.5 \times 10^{-4} \text{ m}^3 \text{ s}^{-1}$ (60 SCFH)
Powder carrier gas pressure	0.97 MPa (140 psi)
Sample velocity	Stationary
Gun surface speed	$0.23 \text{ g m s}^{-1}$ (45 ft min <sup>-1</sup> )
Step size per pass	$3.2 \times 10^{-3} \text{ m}$ (0.125 in.)
Spray distance	0.2 m (8 in.)

Reprinted from [354] with permission from *Journal of Applied Polymer Science*.

## 4.5. Cold spraying

### 4.5.1. Introduction

The potential significance of cold spraying process was recognized first in the mid-1980s during high velocity wind tunnel tests at the Institute of Theoretical and Applied Mechanics (ITAM) of the Russian Academy of Sciences (RAS) in Siberia. Later in 1990s, scientists and researchers in North America initiated detailed practice of this no-melting spray process [299,300].

### 4.5.2. Fundamental principles

Cold spraying is a high kinetic energy coating process, where fine powder particles are propelled by a high pressure ( $\sim 3.5 \times 10^6 \text{ N m}^{-2}$ ) supersonic gas jet at above a critical velocity (500–1200  $\text{m s}^{-1}$ ) towards a well-prepared substrate and forms a deposit there (Fig. 129) [299–301,356–360]. The bonding and deposition of the powder particles occur step by step, where first the surface oxide of the particles are ruptured and fresh surfaces are exposed attributed to

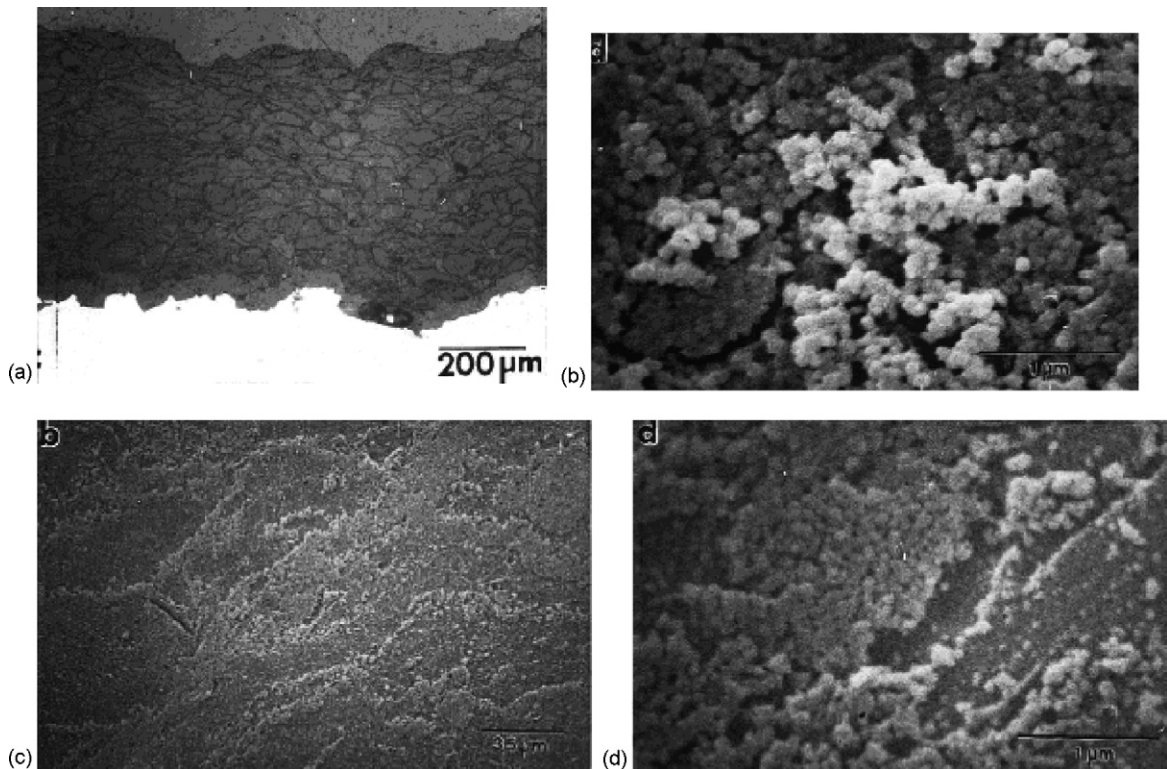


Fig. 128. HVOF sprayed nylon 11 nanocomposites with (a and b) silica and (c and d) carbon black reinforcement. (Reprinted from [354] with permission from *Journal of Applied Polymer Science*.)

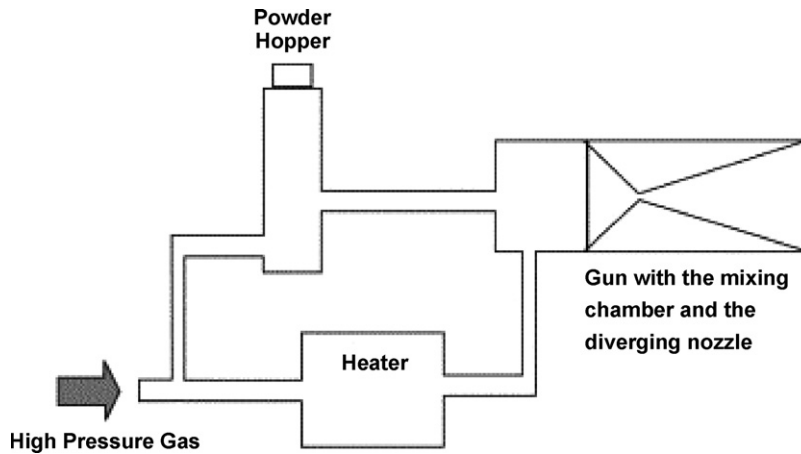


Fig. 129. Schematic of the cold-spray process.

the extremely high kinetic energy during the impact of the powder particle with the substrate. The particles then are plastically deformed and are bonded with the substrate as well as with each other by mechanical interlocking [361,362]. No microstructural evidence has been reported indicating the melting of the spray particles [358]. The bonding in particles in this process is attributed to the adiabatic shear instabilities at the particle–substrate or particle–particle interfaces, caused due to the heavy particle impact [356].

A converging–diverging DeLaval type of nozzle is employed to attain the high velocity by compressed gas flow (usually helium, nitrogen, or their mixture) through high inlet pressure [358,360]. A critical velocity is required for generating sufficient kinetic energy to cause plastic deformation of the surfaces, thereby leading to deposition of spray material on substrate with a strong bonding [357,358]. Therefore, coatings at present are limited to ductile materials like aluminum, stainless steel, copper, titanium, and alloys. Hard and brittle materials like ceramics cannot be sprayed in the pure form, but can be applied as composites with a ductile matrix phase. Substrate materials are also limited to those that can withstand the aggressive action of the spray particles. Soft or friable substrates will erode rather than be coated.

The particles remain in the solid-state and are relatively cold, so the bulk reaction on impact is solid-state only. The process imparts little to no oxidation to the spray material, so surfaces stay clean which aids bonding. No melting and relatively low temperatures result in very low shrinkage on cooling, in addition with the high strain induced on impact, the coatings tend to be stressed in compression and not in tension like liquid/solid-state reactions of most of the other thermal spray processes. Low temperatures also aid in retaining the original powder chemistry and phases in the coating, with only changes due deformation and cold working.

#### 4.5.3. Nanoconsolidation

Cold spray process is moderately new consolidation process and currently is going through major modification in processing parameters towards improving the mechanical properties of materials considering the economic aspects. As plasma spraying is a rapid solidification process, where the cooling rate is in the range of  $10^6$ – $10^8$  K s<sup>-1</sup>, it is quite feasible to retain the nanostructure of the feedstock material or to achieve nanostructure by massive grain refinement. This is also true in case of high velocity oxyfuel spraying, although the cooling rate is not as high as plasma spraying. The high velocity (2–4 Mach) impact in HVOF process results in fragmentation of resolidifying grain structure, which induces more number of nucleation sites. This results in achieving higher order grain refinement. However, as cold-sprayed material does not go through the process of melting and resolidification, there is no possibility of procuring nanostructure by virtue of grain refinement. It may be feasible to attain nanostructure in cold-sprayed material attributed to the heavy plastic deformation of the sprayed powders caused by the supersonic jet impact. However, technical literature in support of this theory is yet to be published. The only reasonable approach to achieve nanostructured material by cold spraying is to spray nanosized powders or micrometer size powders with nanosized grains or to spray composite agglomerates of micron and nanosize powders, which have been discussed below with case study.

Table 39  
 Characteristics of the WC–Co composite coating produced by the cold spray

Specimen description	Thickness ( $\mu\text{m}$ )	Hardness (HV = 500 g)	Co hardness (HV = 1 g) <sup>a</sup>	Hardness by HVOF
Powder	–	–	176 (101–239)	–
Coating	~900	2053 (1926–2127)	192 (120–262)	~1200

Reprinted from [358] with permission from Elsevier.

<sup>a</sup> Measured by dynamic ultra-micro hardness tester.

**4.5.3.1. WC–Co nanocomposite.** WC–Co coatings are well-known for their use in wear-resistance applications. However, cold spraying of cermets such as WC–Co and ceramics depositions by the cold spray process are rather limited due to the lack of ductile phase. Kim's research group in South Korea has conducted cold spraying of cermet system, where spherical and compact agglomeration of 12 wt.% Co (5–45  $\mu\text{m}$ ) and WC (100–200 nm) were cold-sprayed on stainless steel substrate [358]. The cold spray system was developed in RIST, South Korea, which includes powder carrying gas preheater as well as main gas preheater, gas pressure regulators, powder feeder, and spray gun. The spray processing parameters are provided in Table 39.

The cross-sectional microstructure shows (Fig. 130a) a very dense and uniform coating structure. The coating does not show any large crack, but some tiny pores are visible due to brittleness of the WC particles. High magnification dark field image of the coating distinctly shows bright WC particles and dark Co phase with a few tiny pores as indicated by an arrow (Fig. 130b). It is observed that the average size of WC particles for the as-sprayed coating is around 200 nm, which is almost the same size of the WC particles exhibited by the feedstock powder. The average hardness of the coating is above 2000 HV, which is approaching the intrinsic hardness of WC (2000–2400 HV). A comparison of hardness values is given in Table 39.

The nanostructured WC–Co cold-sprayed coating has also been studied by Lima et al. [358]. The coating showed higher density and better microhardness compared to those of the nanostructured feedstock. The coating microhardness enhancement is dependent on the impact velocity than the nanostructured particle microhardness itself. The impact of the particles against the substrate at supersonic velocities, promotes a densification in each nanostructured particle. There is no significant difference between the average grain size of the nanostructured feedstock and coating.

Thermal spray science and technology has flourished and experienced major modification in the last 10 years in both industries and research laboratories. Different forms of this techniques, viz. thermal spraying and high velocity oxyfuel spraying are being exercised and guaranteed successful synthesis of metal, ceramic, and polymer-based nanostructured composite materials, which has been delineated throughout this section. However, it must be mentioned that fabrication of near-net shape nanostructured materials with improved mechanical properties by thermal spray techniques is still in infancy and there is immense scope for modification and innovation.

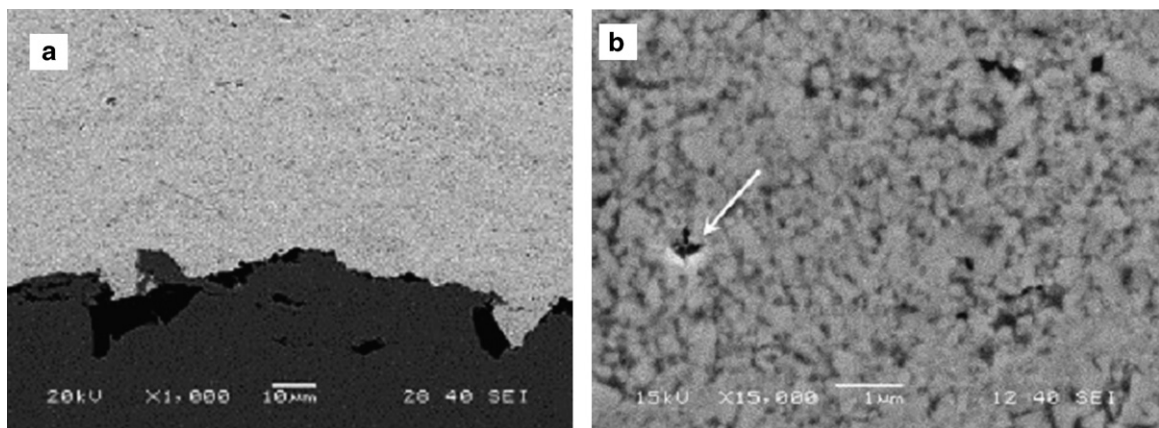


Fig. 130. (a) Cross-sectional SEM picture of showing dense and adhered cold-sprayed WC–Co coating and (b) high magnification dark field image showing gray WC and dark Co phase with distributed pores (arrow mark). (Reprinted from [358] with permission from Elsevier.)

## 4.6. Spark plasma sintering

### 4.6.1. Introduction

With the growing need for processing and consolidating nanopowders, retaining the initial microstructure in the fabricated component is still a challenge. Though manufacturing of novel materials are limited on laboratory scale, vigorous demand in market persist in driving serious attention to new consolidation techniques apart from hot pressing, high temperature extrusion, and hot isostatic pressing. Since longer processing times at high temperatures ( $\sim 1800^\circ\text{C}$ ) often result in extraneous grain growth, hence the new nanopowder processing technique, namely spark plasma sintering (SPS), has evolved in the recent decade, which overcomes these obstacles using rapid heating to sintering temperatures leading to rapid sintering of nanocomposites [363–370]. Attractive properties of initial nanopowders are well conserved by fabrication of bulk material through SPS. Consolidation of metals, composites, ceramics, intermetallics, cermets, nanocomposites, and carbon nanotube reinforced ceramics has been accomplished by spark plasma sintering [371–385].

### 4.6.2. Fundamental principles

Spark plasma sintering, also referred to as electric field assisted sintering (EFAS), field assisted sintering technique (FAST), plasma assisted sintering (PAS), and plasma pressure consolidation (PPC) is a pressure assisted rapid sintering technique which momentarily generates high temperature plasma (spark plasma) between the gaps of compacted powder via electrical DC pulsing discharge [378,381–384].

Sintering can be done at wide range of temperatures and pressures, with controls of temperatures or current during processing [386]. SPS has evolved as sinter consolidation method to fabricate exotic and novel materials, which are difficult to fabricate by conventional processing techniques. This pressure assisted sintering method allows much shorter sintering temperatures and times, serving as an effective technique for obtaining fully dense nanocrystalline composites [371].

The DC pulse discharge could generate: spark plasma, spark impact pressure, Joule heating, and an electrical field diffusion effect [382,383]. Fig. 131 shows aforesaid mechanisms during SPS consolidation. Formation of plasma during SPS has direct effect on sintering of particles, with role of current and its pulsing still under controversy [374]. Rapid heating, pressure application, and powder surface activation allow rapid consolidation of nanocomposites retaining the initial grain structure.

### 4.6.3. Advantages

SPS is a rapid solidification technique where high quality and uniform compacts can be sintered rapidly at comparatively lower temperatures when compared to conventional sintering methods [365]. Tamed advantages of SPS process include [364]:

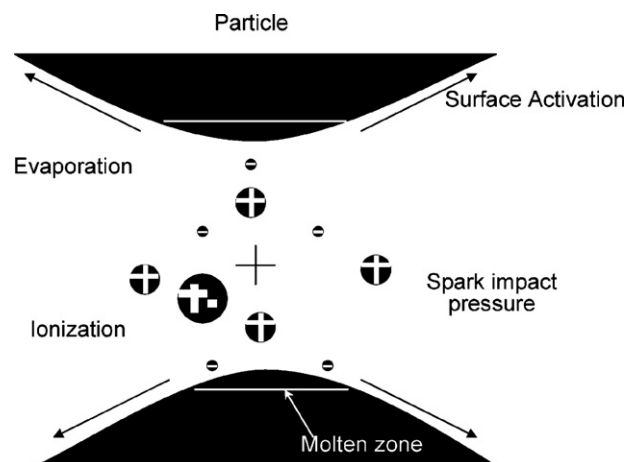


Fig. 131. Schematic of dominant sintering mechanism during SPS.

- Initial internal structure of powder particles is preserved by restricting high temperature exposure during sintering. Pulsed resistance heating by generation of localized plasma between powder particles maintains the integrity of starting microstructure without grain coarsening.
- Synergetic combination of electrical energy and mechanical pressure drastically reduces the consolidation time. Resistance pulse heating generating high localized temperature and assisted consolidation pressure contribute in rapid consolidation of nanopowders without affecting starting grain size.
- Pulse discharge plasma generated between powder particles aids in removing surface oxide layer. This increase in surface activity adjoining clean surfaces thereby leads to enhanced particle sintering.

Hence, advantages of SPS include in situ cleaning of oxide surfaces, generating cleaner materials with high consolidated densities. Rapid densification of powders retains the novel properties of initial powder promoting the cost-effective fabrication of bulk nanocomposites.

#### 4.6.4. Equipment—process and mechanism

Schematic of typical SPS apparatus is shown in Fig. 132 (SPS 23), consisting of a graphite die where powder is loaded and is heated by passing electric current. Dr. Sinter (1020 SPS-1050 T) apparatus, pioneered by Sumitomo Coal Mining Co. Ltd., Japan, is widely used by most researchers [364–368,371,379–384]. Hold time, ramp rate, pulse duration, and pulse current and voltage can be set for controlling the temperature of the sintering cycle. Change in temperature, pulse power (voltage and/or current), sintering displacement, and sintering rate are recorded in situ during spark plasma sintering [371,379–384].

Powder mixtures are initially cold pressed ( $\sim 200$  MPa) into a compact disc (with diameter ranging around 2 cm and thickness around 5 mm) followed by SPS processing to produce nanoconsolidated nanocrystalline composites. Typical SPS processing parameters include: (a) applied pressure between 50 and 100 MPa, (b) pulse duration of  $\sim 10$  ms with on–off cycle of 2–2.5 ms, and (c) maximum pulse parameter of 10,000 A and 10 V. After applying given pressure, samples are heated to preset temperature (for few minutes) and are ramped rapidly ( $\sim 150$ – $500$  K  $\text{min}^{-1}$ ) to sintering temperatures ( $\sim 900$ – $1300$  °C) with hold time of 3–5 min to complete the sintering [382]. Samples are usually cooled to below 100 °C within 5 min after the completion of sintering [387,388].

Densification of green compact occurs in four stages namely, vacuum creation, pressure application, resistance heating and cooling down as shown schematically in Fig. 133 [386]. Process of SPS is carried out in vacuum to account for removal of gases and result a densely consolidated composite. Heating is accomplished by spark discharge between particles, which activates the surface by removing surface oxide. This helps in heat and mass transfer between the purified particles to carry heat and sinter them to full density. Initially, samples show increase in volume due to thermal

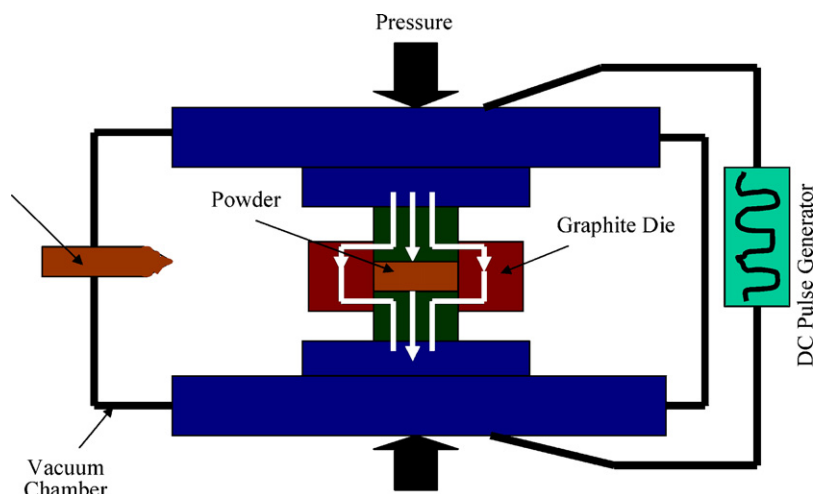


Fig. 132. Schematic of SPS setup.

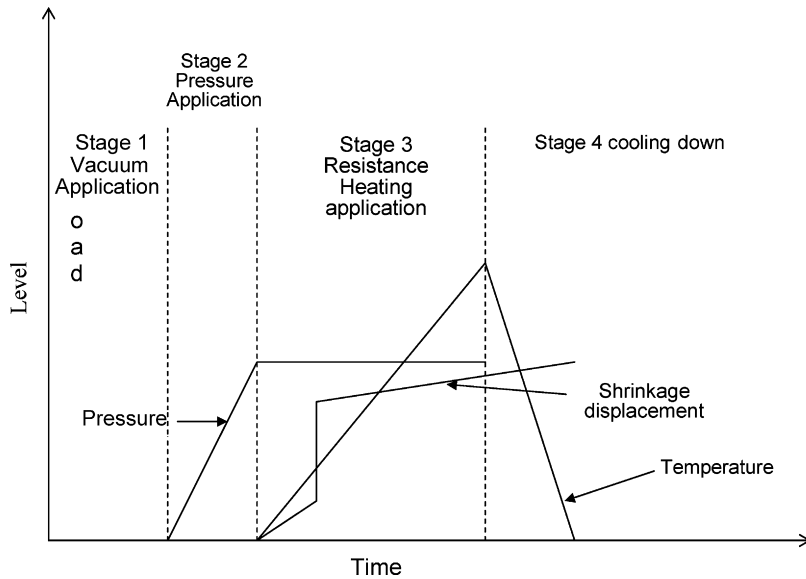
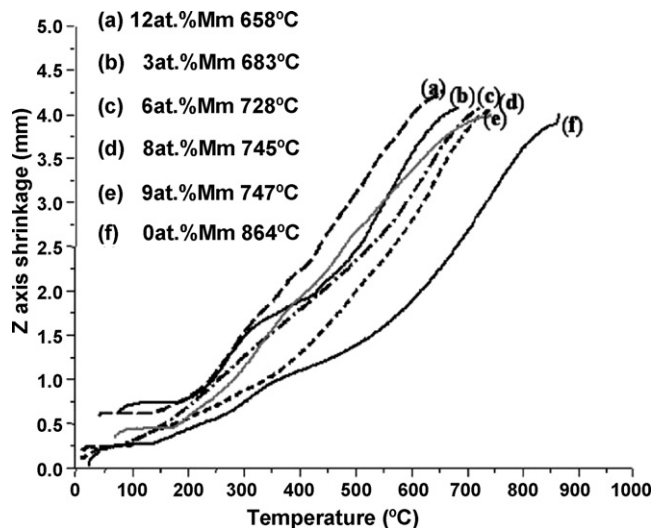


Fig. 133. Schematic of SPS sintering stages.

expansion followed by shrinkage occurring primarily during the resistance heating when the green discs are held at high temperatures and pressures [386]. Onset of sintering is dependent on the initial particle size, which decides the onset of shrinkage. It is generally difficult to determine when sintering process goes to completion, however, shrinkage of specimen could help deducing the completion of SPS sintering [389,390].

#### 4.6.5. Nanoconsolidation

Activation energy for nanosize grain metal powder particles is higher than that of conventional micron-sized powder and exhibit lower melting and sintering temperatures [391,392]. Hence, nanograin consolidation can be achieved in shorter durations without much problem of grain coarsening. Shrinkage as a function of temperature is shown in Fig. 134 [389]. Hence, sintering temperature can be optimized by predeciding shrinkage of consolidated structure. Addition of alloying element can also aid in formation of amorphous phase along grain

Fig. 134. Shrinkage as a function of temperature for  $(\text{Al} + x\% \text{Mn})_2 \text{Ti}$  during SPS. (Reprinted from [389] with permission from Elsevier.)

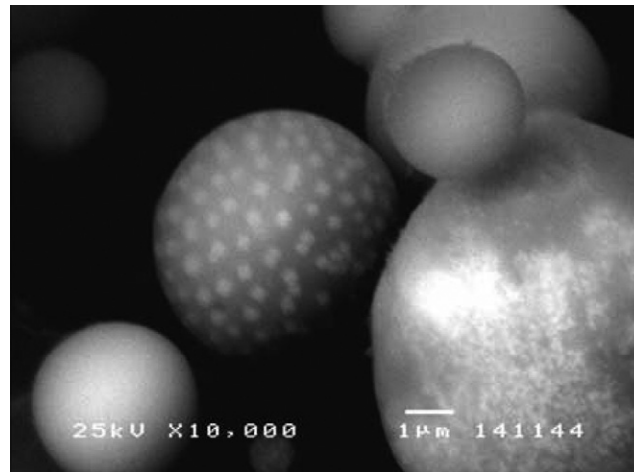


Fig. 135. As-sprayed calcium phosphate particle showing embedded nano-ZrO<sub>2</sub> particles. (Reprinted from [395] with permission from Elsevier.)

boundary and help determining the sintering temperatures to result dense consolidation of nanocrystalline nanocomposites [389].

**4.6.5.1. Nano-ZrO<sub>2</sub>-HA.** SPS has been used to sinter nano-zirconia and investigate effect of various parameters such as temperature, heating rate and cyclic pulsing on sinter processing [393]. Nanocrystallites depicted high hardness as obtained through mechanical property evaluation of SPS nanoconsolidated zirconia [394].

HA is an important bioceramic material with its properties much similar to that of mineral phase of bone. Limitation of its application is due to extreme brittleness making it unusable for load-bearing impact applications. Hence, the challenges such as improving fracture toughness and manipulating physical and chemical properties to reduce complications arising due to thermal mismatches and solid solubility differences can be well handled by SPS [395].

Initial powders of HA–20 wt.% ZrO<sub>2</sub> were RF induction plasma fed through atomizing probe to result 2–10 µm particles. ZrO<sub>2</sub> particles were uniformly distributed (bright spots in calcium phosphate matrix) as seen in Fig. 135 [395]. This composite powder was SPSed at pressure of 4.5–17.3 MPa and temperature of 1075 ± 25 °C. Post-sintering single pores and multiple pores within a particle can also be seen (Fig. 136) [395]. Embedded ZrO<sub>2</sub> particles resemble the initial microstructure of fine ZrO<sub>2</sub> dispersed in calcium phosphate matrix. Porosity

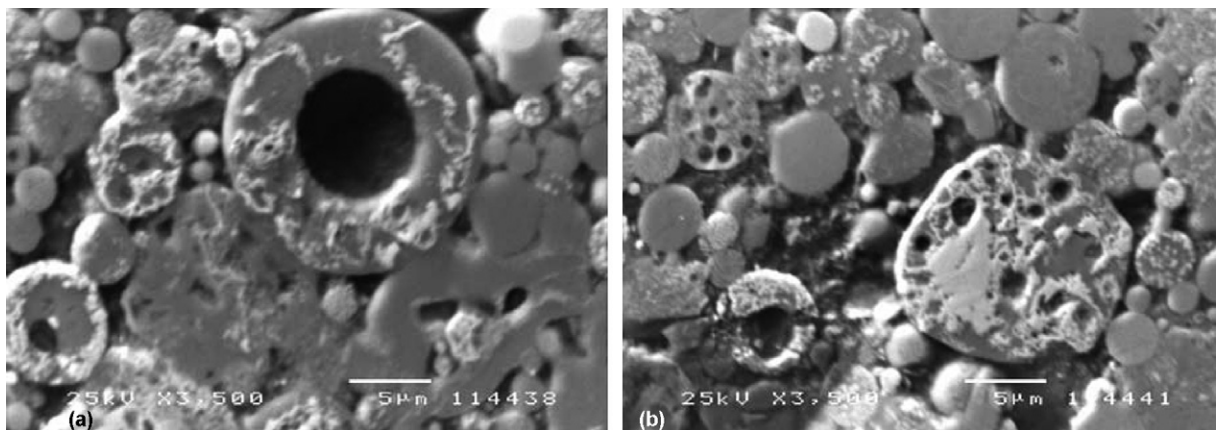


Fig. 136. Back scattered SEM image depicting: (a) single and (b) multiple intra-particle pores embedded with ZrO<sub>2</sub> particles. (Reprinted from [395] with permission from Elsevier.)

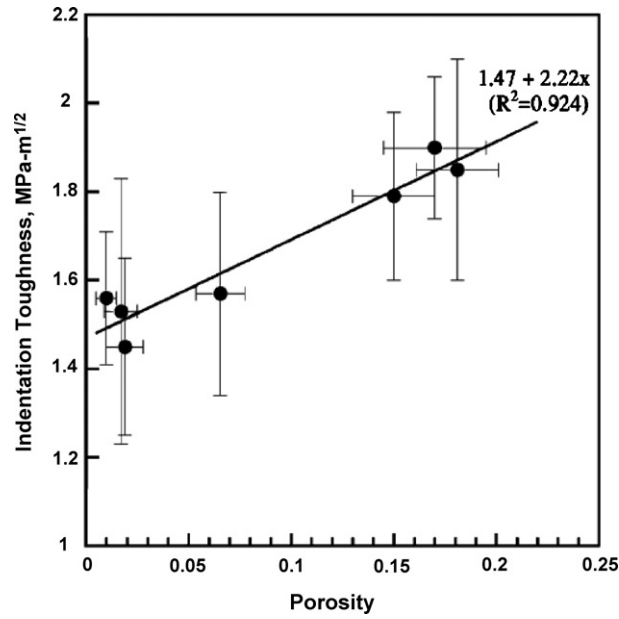


Fig. 137. Indentation toughness shown as a function of porosity for ZrO<sub>2</sub>-HA nanocomposite. (Reprinted from [395] with permission from Elsevier.)

measurement from optical micrograph correlated increased with decreasing sintering temperature. Fracture toughness from Palmqvist was used for fracture toughness calculations showing increasing toughness with increasing porosity (Fig. 137) [395,396]. For higher porosity levels (>25 vol.%), indentations did not always produce cracks.

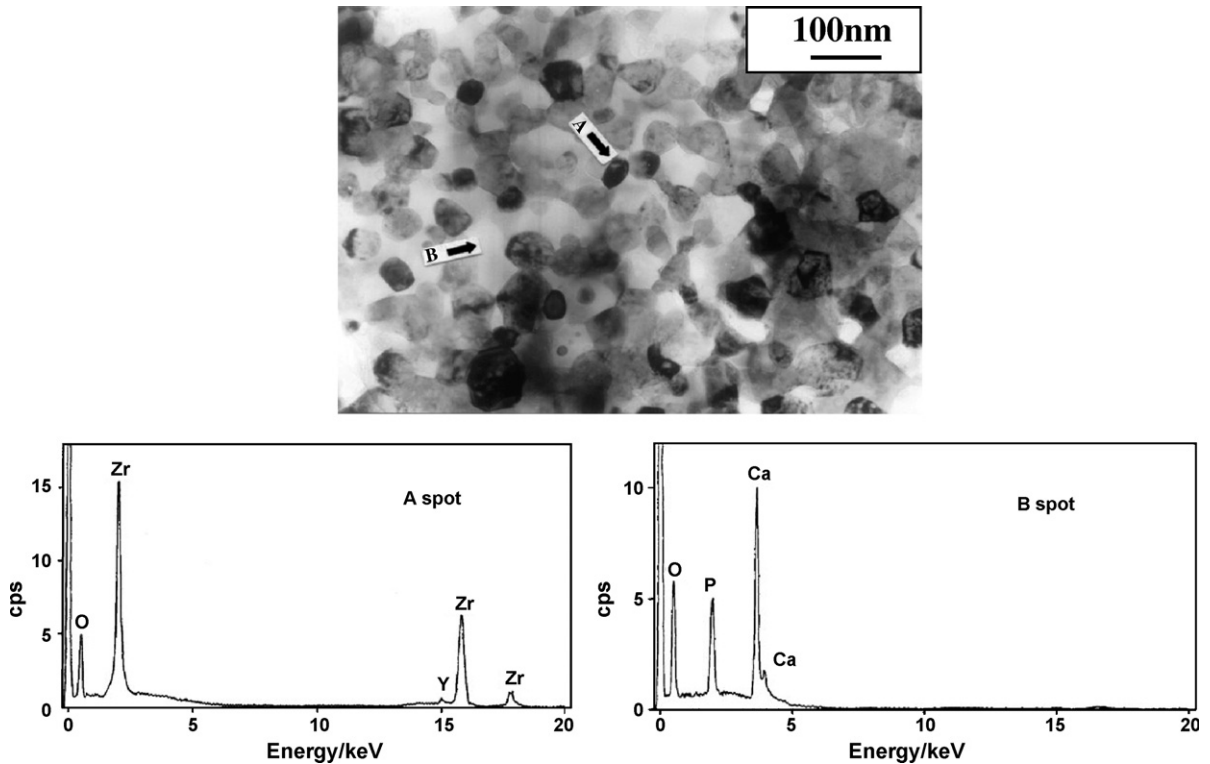


Fig. 138. TEM and EDS of Y-TZP and HA nanocomposite consolidated via SPS. (Reprinted from [397] with permission from Elsevier.)

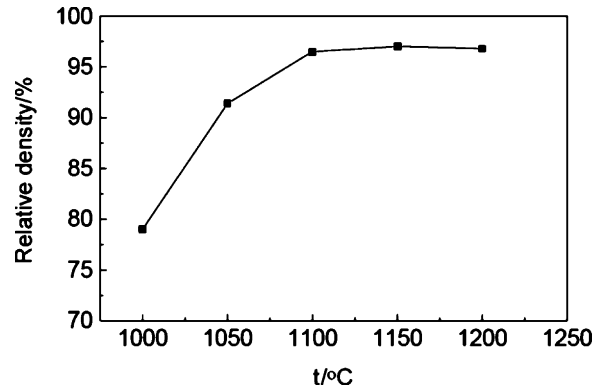


Fig. 139. Sintering density variation with temperature. (Reprinted from [397] with permission from Elsevier.)

Conventional sintering of HA–TZP(3Y) cannot avoid deleterious formation of TCP and fully stabilized  $ZrO_2$  (since TCP formation leads to reduction in biocompatibility whereas strength and toughness impairment is observed with presence of stabilized  $ZrO_2$ ). SPS processing of HA–TZP(3Y) nanocomposite yielded uniform distribution of  $\sim 50$  nm Y–TZP and  $\sim 100$  nm HA grains (Fig. 138) [397]. Densities up to 97.3% were obtained at 1150 °C leading to high density compacts of ceramic nanocomposite (Fig. 139) [397].

**4.6.5.2. Nano-Ti–Ni shape memory alloys.** Novel properties such as shape memory effect, super elasticity, biocompatibility and high damping capacity of Ti–Ni alloys make them potential biomedical and microelectromechanical system (MEMS) engineering materials. Near-net consolidation of these alloys can be achieved using powder metallurgy, hot isostatic pressing, metal injection molding, and combustion synthesis with self-propagating wave. But, these conventional processes do not retain the nanostructure of the initial powder owing to elongated duration of high temperature sintering consolidation. Localized temperature generation via low voltage pulsed current momentarily raises temperatures up to tens of thousands of degrees between powder particles sintering them to high density compacts. This shorter sintering time restricts exaggerated grain coarsening during processing.

Nanoparticle size of the nano-Ti–Ni shape memory alloy was retained as observed through TEM images (Fig. 140a and b) [391]. Crystallinity of nanosize powder was verified using XRD analysis comprising both austenitic and martensitic phase (Fig. 141) [391]. The sintering temperature used by researchers was 800 °C, which was much lower than that used by others used for micron size powder consolidation [398]. Though the sintering time is 5 min,

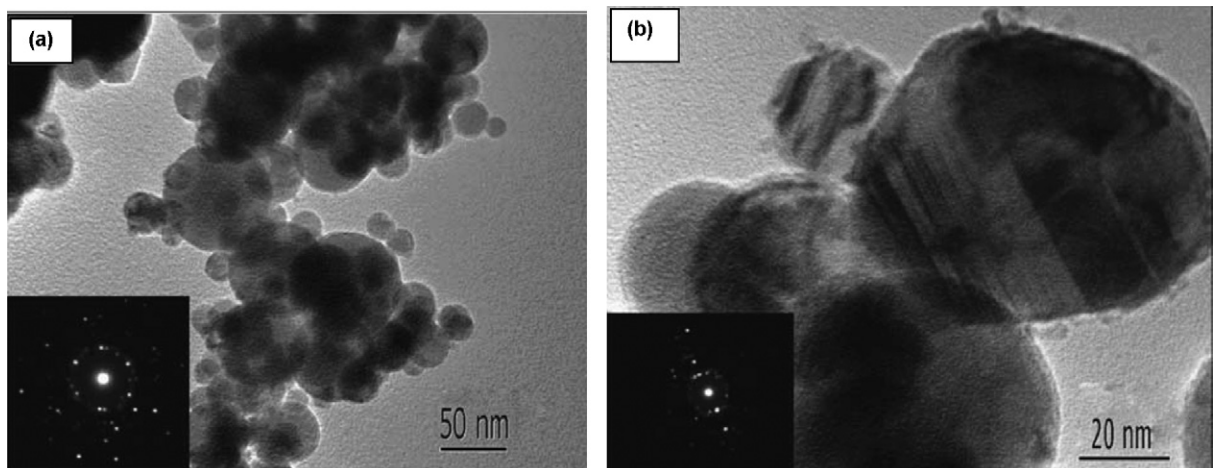


Fig. 140. (a) Nanosize Ti–Ni powder with inset showing its diffraction pattern and (b) martensitic structure. (Reprinted from [391] with permission from Elsevier.)

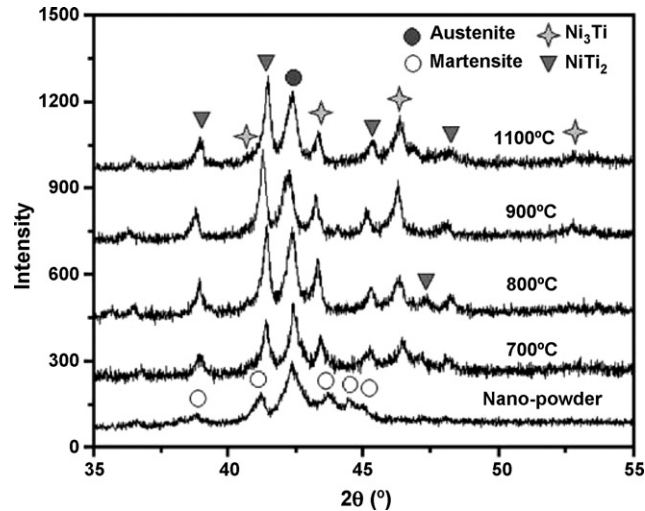


Fig. 141. XRD spectrum of nanosize powders and TiNi sintered samples. (Reprinted from [391] with permission from Elsevier.)

formation of intermetallic phases occur by solid-state interdiffusion of atoms. These additional phases affect the transformation temperatures without exhibiting shape memory behavior or martensitic transformation.

**4.6.5.3. Ceramic nanocomposites.** Amorphous Si–C–N has been consolidated by SPS with reduced amount of glassy phase additives (liquid phase sintering) to reach full density [378]. Solid-state sintering of Si<sub>3</sub>N<sub>4</sub>–SiC nanocomposite therefore dominates in resulting higher creep resistance of bulk ceramic nanocomposite. Solid-state sintering was not enough to reach full density, hence increasing additive level of yttria could be sintered within 10 min at 1600 °C. Microstructure was composed of submicron-sized matrix of Si<sub>3</sub>N<sub>4</sub> and SiC with nanosized silicon carbide particles enclosed in Si<sub>3</sub>N<sub>4</sub> grains (Fig. 142) [378].

Refinement of grain structure and addition of second phase particles help in improving the fracture toughness of composites. Improvements up to 75% increase in fracture toughness were observed by Krakhmalev [399] in Mo(Si,Al)<sub>2</sub>/SiC composites fabricated by SPS of mechanically alloyed powders.

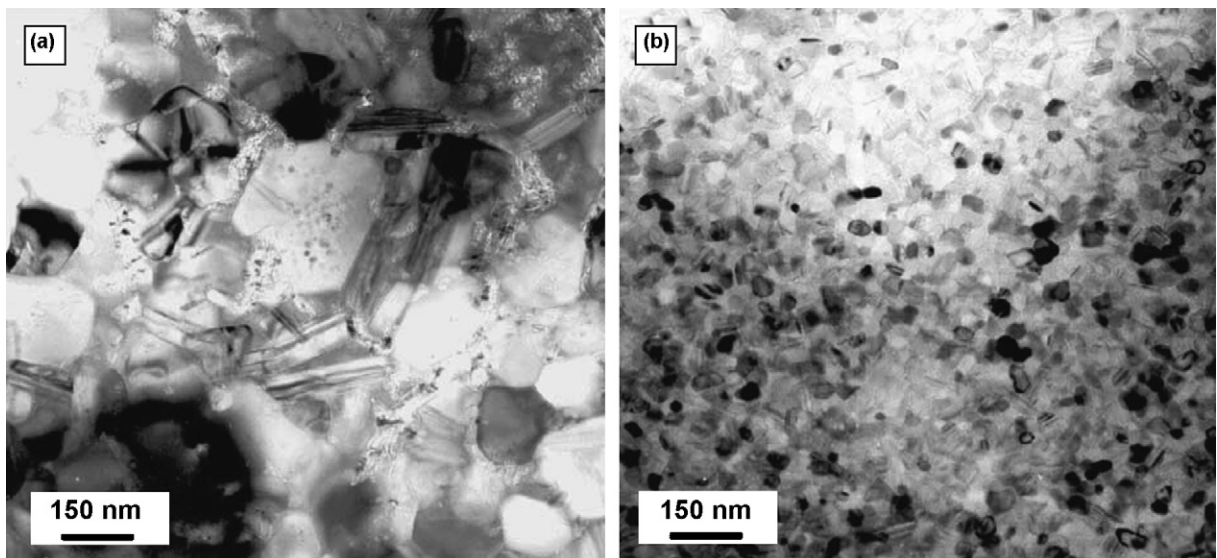


Fig. 142. Grain size of Si–C–N powder when sintered at 1600 °C with addition of: (a) 8 wt.% Y<sub>2</sub>O<sub>3</sub> and (b) 1 wt.% Y<sub>2</sub>O<sub>3</sub>. (Reprinted from [378] with permission from Elsevier.)

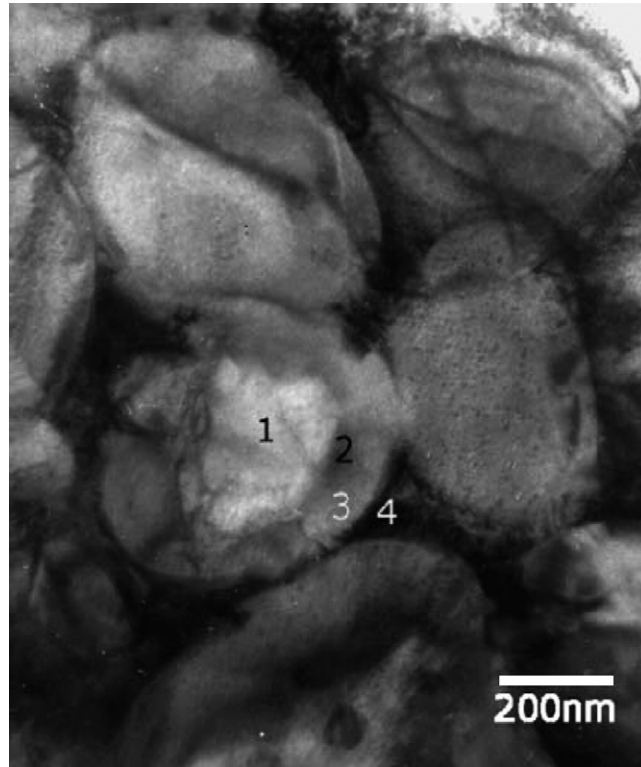


Fig. 143. TEM micrograph showing core and rim structure in a Ti(C,N) cermet. (Reprinted from [366] with permission from Elsevier.)

Owing to high mechanical strength and hardness, high temperature ceramics such as  $\text{Si}_3\text{N}_4$  and  $\text{SiAlON}$  ( $\text{Si}_{3-x}\text{Al}_x\text{O}_x\text{N}_{4-x}$ ) are difficult to be mechanically fabricated. TiN nanocoating over  $\text{Si}_3\text{N}_4$  surfaces resulted lower electrical resistivity ( $\sim 10^{-4} \Omega \text{ cm}$ ).

**4.6.5.4. Ti(C,N) cermet.** Nano-TiC and TiN nanocomposite ceramics SPS sintered showed Ostwald ripening with typical core–rim structure (Fig. 143) [366]. Dissolution and reprecipitation of rim phases (Ti,Mo)(C,N) occurs on Ti(C,N) grains during SPS. Core and inner rim contained higher Ti and Mo, with nanostructure forming seen in the microstructure. Smaller grains pin the dislocations and it also hinder crack-extension by crack-deflection. This consolidation technique reduced the average grain sizes of the cermet with increasing nanoindentation under SPS. This nanoaddition also improved the fracture toughness of the nanocomposite.

**4.6.5.5. Intermetallic consolidation.**  $\text{L1}_2$ -based intermetallic structure  $(\text{Al} + 12.5 \text{ at.}\% \text{ M})_3\text{Zr}$  ( $\text{M} = \text{Cu}, \text{Mn}$ ) synthesized by mechanical alloying were consolidated to fully dense compacts using SPS. Microstructure showing grains ranging from 80 to 100 nm,  $\text{L1}_2$  structure was maintained even after sintering via SPS. Fracture toughness of  $5.35 \text{ MPa m}^{1/2}$  was obtained, which is almost three times that of bulk specimen (Fig. 144) [387]. Low temperature ductility is influenced by intergrain impurity segregation along with intrinsic crystal symmetry and cleavage strength, hence grain refinement vitally enhances the ductility of intermetallics [389]. Homogeneous dispersion of  $\text{Al}_8\text{Mn}_5$  secondary phases was observed in  $(\text{Al} + x \text{ at.}\% \text{ Mn})_3\text{Ti}$  matrix, with grain sizes ranging between 45 and 60 nm (Fig. 145) [389].

Zirconium–tri-aluminide prepared by SPS for 0 min at  $600^\circ\text{C}$  portrayed grain sizes in the range 20–30 nm, as calculated by Scherrer formula and endorsed by TEM pictures, was the smallest grain sizes ever reported for nanocrystalline powders (Fig. 146) [400].

**4.6.5.6. Cemented tungsten carbide.** Cemented carbides with ultrafine grains help improving its strength and hardness. Variation of shrinkage and temperature with SPS processing time for WC powders depicted that lower grain

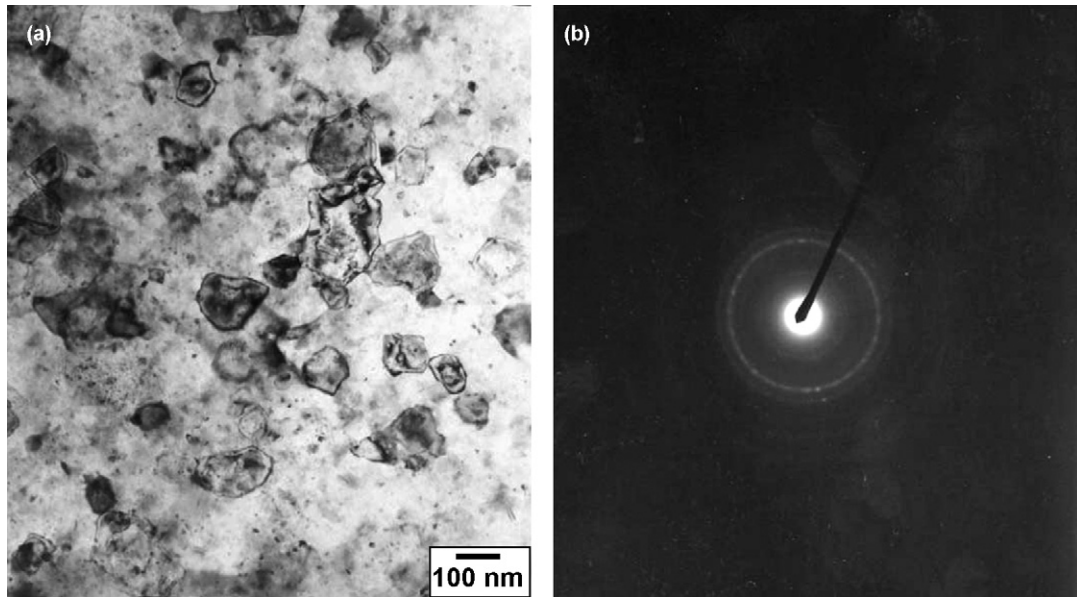


Fig. 144. TEM micrograph of  $(\text{Al}-12.5 \text{ at.}\% \text{ Cu})_3 \text{ Zr}$  specimen: (a) bright field image and (b) diffraction pattern. (Reprinted from [387] with permission from Elsevier.)

sizes require lower temperatures for consolidation. Shrinkage onstart was also at lower end of temperature for ultrafine powers (Figs. 147 and 148) [386]. Excellent grain growth constrain is imposed by high heating rates and short high temperature exposure. Fig. 149 [365]. Doping with second phase material has also shown reduction in grain growth and improvement in fracture toughness of WC–Co cermets [401]. Optimum CNT incorporation is needed to avoid

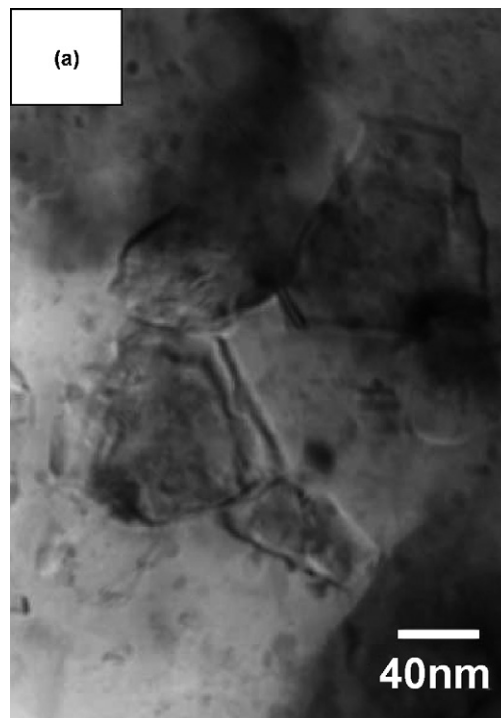


Fig. 145. TEM micrograph of  $(\text{Al}-8 \text{ at.}\% \text{ Mn})_3 \text{ Ti}$  after heat treatment at  $900^\circ \text{C}$  with 1 h holding. (Reprinted from [389] with permission from Elsevier.)

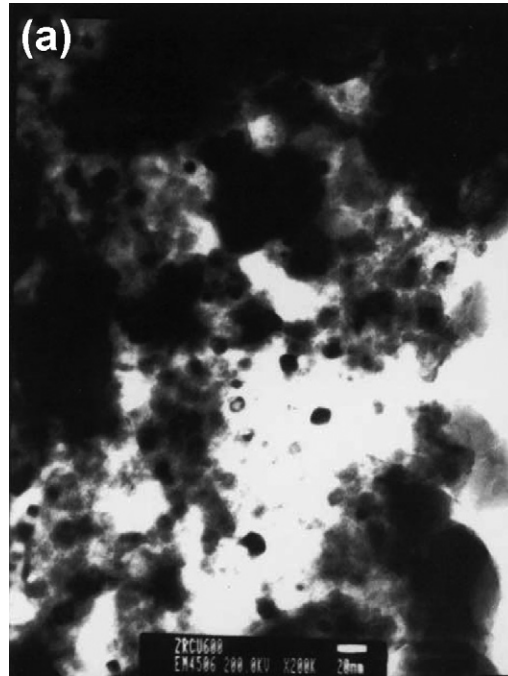


Fig. 146. TEM dark field image of (Al–12.5 at.% Cu)<sub>3</sub>Zr intermetallic prepared by SPS for 0 min at 600 °C specimen. (Reprinted from [400] with permission from Elsevier.)

deterioration of the mechanical properties of WC–Co nanocomposite due to excessive carbonization of sintered hard metals (Fig. 150) [402].

4.6.5.7. *SiC–ZrO<sub>2</sub>(3Y)–Al<sub>2</sub>O<sub>3</sub>*. Ceramic matrix nanocomposites have been fabricated by SPS sintering to fully dense structures with sintering temperature at least 200 °C lower than those produced by hot pressing [403]. Heterogeneous precipitation of nano-SiC particles dispersion in the Al<sub>2</sub>O<sub>3</sub> matrix was obtained by SPS for various sintering temperatures. Fracture toughness can be well influenced by the sintering temperatures by rapid SPS

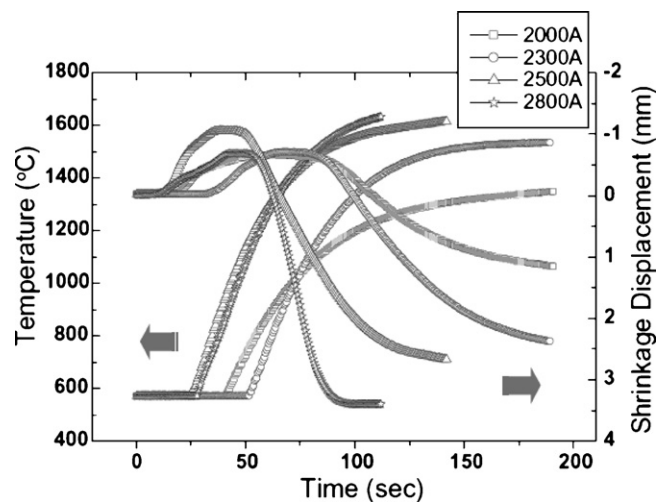


Fig. 147. Heating time dependence on attained temperature and shrinkage for different particle sizes during sintering at 60 MPa (and current of 2800 A) of WC. (Reprinted from [386] with permission from Elsevier.)

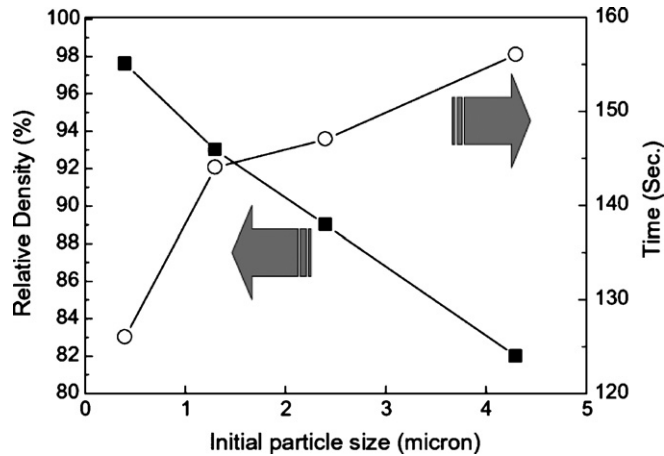


Fig. 148. Sintering time and consolidation density of sintered WC as a function of initial particle size. (Reprinted from [386] with permission from Elsevier.)

sintering process (Figs. 151 and 152) [404]. Apart from reducing the  $\text{Al}_2\text{O}_3$  grain size, intragranular nanocomposites synthesis via SPS induced compressive stresses at the grain boundary and thereby increases its fracture toughness.

**4.6.5.8. CNT  $\text{Al}_2\text{O}_3$  nanocomposite consolidation.** SPS has been used to incorporate CNTs in improving strength of consolidated nanocomposites. Versatility of SPS includes converting multiwall carbon nanotubes to well crystallized diamond grains ranging between 300 nm and 10  $\mu\text{m}$  [405]. With many publications in processing nanocrystalline  $\text{Al}_2\text{O}_3$ , Amiya's group staggered the astonishing results of improved fracture toughness, of upto three times than that of alumina, using SPS consolidation of CNT–alumina composite [381,382,384]. The primary interest was diverted to

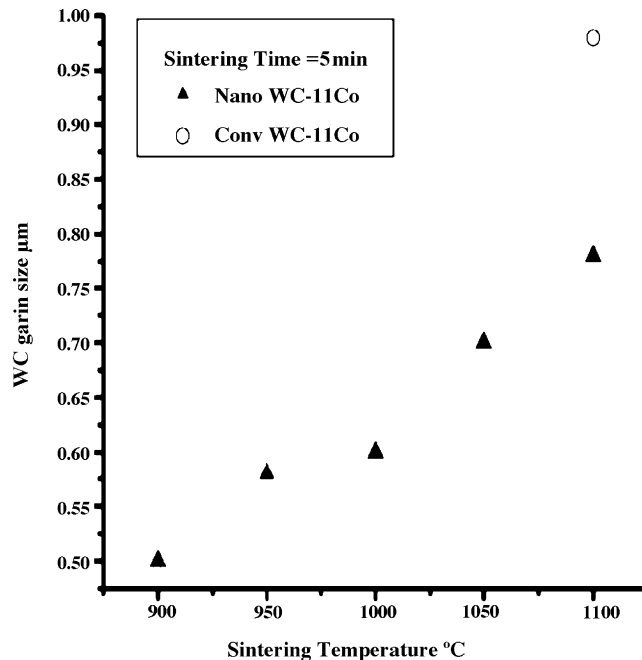


Fig. 149. Sintering temperature dependence of conventional and nano-WC–11Co cemented carbide powders on grain size of WC. (Reprinted from [365] with permission from Elsevier.)

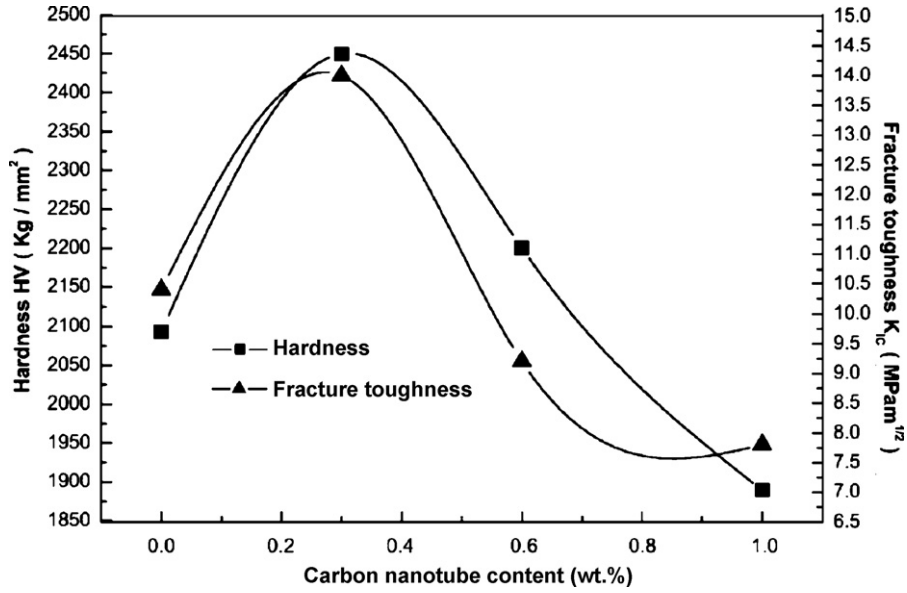


Fig. 150. Effect of carbon nanotube variation on the hardness and toughness of WC-Co CNT nanocomposite. (Reprinted from [402] with permission from Elsevier.)

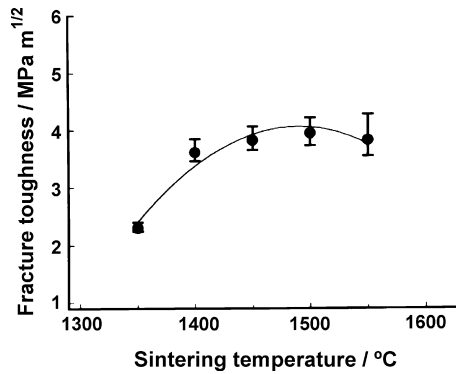


Fig. 151. Effect of sintering temperature on the fracture toughness of 5 vol.% SiC-Al<sub>2</sub>O<sub>3</sub> nanocomposite. (Reprinted from [404] with permission from Elsevier.)

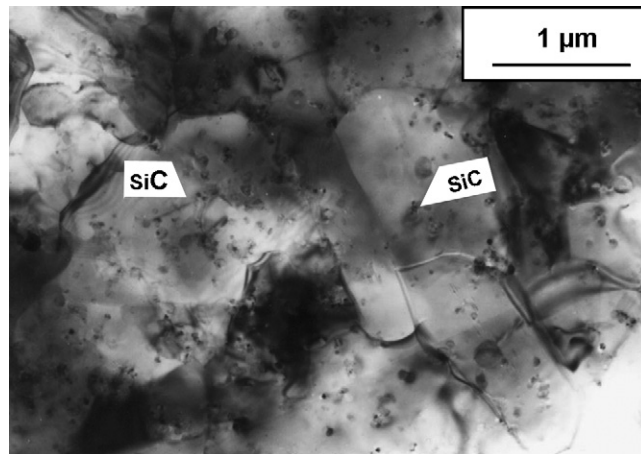


Fig. 152. TEM micrograph of 5 vol.% SiC-Al<sub>2</sub>O<sub>3</sub> composite. (Reprinted from [404] with permission from Elsevier.)

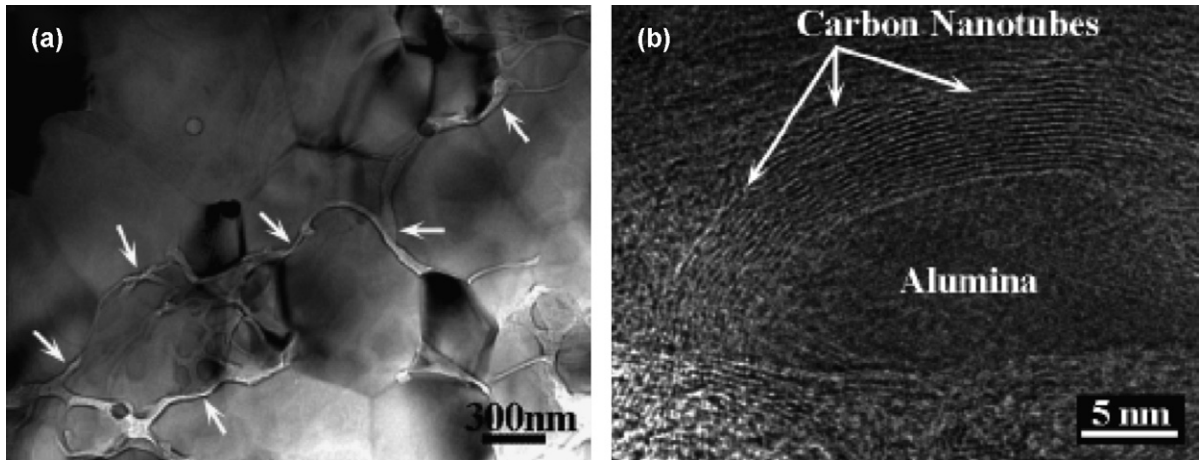


Fig. 153. (a) Bright field and (b) high resolution TEM micrograph of SPS consolidated SWCN/ $\text{Al}_2\text{O}_3$  nanocomposite. (Reprinted from [384] with permission from MRS.)

Table 40

Processing, physical properties, electrical conductivity, and mechanical properties of CNT-nanocomposite consolidated via SPS processing

Material	Process condition	Density (% TD)	Grain size (nm)	$K_{IC}$ ( $\text{MPa m}^{1/2}$ )	Electrical conductivity ( $\text{S m}^{-1}$ )	Reference
Pure $\text{Al}_2\text{O}_3$	1150 °C/3 min	100	350	3.3	$10^{-12}$	[381,382]
5.7 vol.% carbon black/ $\text{Al}_2\text{O}_3$	1150 °C/3 min	100	200	7.9	15	[381,382]
5.7 vol.% SWNT/ $\text{Al}_2\text{O}_3$	1200 °C/3 min	100	200	6.4	1050	[381,382]
10 vol.% SWNT/ $\text{Al}_2\text{O}_3$	1200 °C/3 min	99	100	8.1	1510	[381,382]
15 vol.% SWNT/ $\text{Al}_2\text{O}_3$	1150 °C/3 min	99	100	9.7	3345	[381,382]

enhance electrical properties incorporating CNTs in the alumina matrix [382]. The entrapment of SWNT along grain boundaries during SPS consolidation of CNT- $\text{Al}_2\text{O}_3$  nanocomposite can be seen in Fig. 153. Comprehensive results from are presented in Table 40. Later, retention of CNTs in Padture's group was indirectly depicted by presence of carbonaceous material along grain boundary (Fig. 154) during SPS consolidation of CNT- $\text{Al}_2\text{O}_3$  nanocomposite

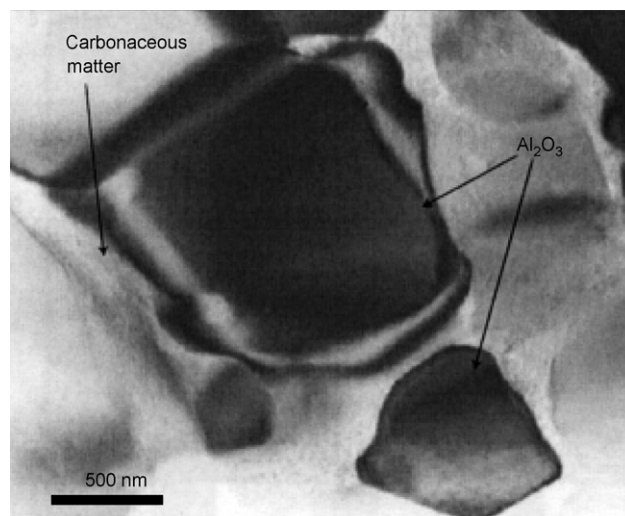


Fig. 154. Carbonaceous material seen along grain boundary of SPS consolidated alumina-CNT nanocomposite. (Reprinted by permission from Macmillan Publishers Ltd. [406].)

[406]. Padture's group repeated the SPS methodology of the Amiya's group and showed that toughness of CNT–alumina matrix was not improved [406]. The discrepancy in data was because Amiya's group had used indentation methods to calculate fracture toughness, and the alumina–CNT composite showing contact-damage resistance, which was tracked through Hertzian indentation [406,407].

Analytical densification map calculations were carried without considering particle coarsening, grain growth, surface diffusion, and evaporation–condensation. Though latter two contribute towards sintering by neck growth, they have no contribution to densification during pressureless sintering [370]. Analytical models have been studied for optimized SPS parameters in deciding the comparison of sintering temperatures when compared to that of conventional processing [408].

Near-net consolidation and sintering of exotic nanocomposites can be processed via pressure assisted spark plasma sintering without recurrence of grain growth. Retention of nanocrystallinity of the starting powder thereby producing fully dense and cleaner nanocomposites form the common feature of fabricated nanocomposites. Improved fracture toughness, ductility, and electrical properties have been commonly depicted by spark plasma sintered nanocomposites.

#### 4.7. Laser-based techniques

##### 4.7.1. Introduction

Civilized world now enjoys the new era of expectations laser had opened up since discovery of ruby-laser in 1960 by Maiman [409]. From fabricating nanocomposite powders for subsequent consolidation, laser is used to fabricate polymer/metal/ceramic nanocomposites [410]. Since nanocomposites display enhanced magnetic, optical, physical, mechanical, and chemical properties, hence advanced synthesis techniques such as laser ablation/processing are required for the development of nanocomposite materials [411]. Significant hardness improvement is observed in Ni when its particle size is decreased from 10  $\mu\text{m}$  to 10 nm [412]. Nanoparticle size, shape and morphology also depict a strong influence on performance of nanocomposite [413]. Along with interfacial parameters, layer thickness, epitaxial stresses, layer volume, etc., also throw a significant effect on the performance of the nanocomposite [414].

##### 4.7.2. Fundamental principles

Einstein predicted stimulated emission phenomenon in 1917 using a mathematical argument [415]. The idea was considered absurd since the event of creating laser was perceived next to impossible in occurrence. Various energy states of a molecule are quantized and exist only at particular energy levels of not at all. Electric discharge cause low pressure gas ( $\sim 35\text{--}50$  Torr) to generate plasma, which take up Boltzmann distribution excited states ( $n_i = A e^{-E_i/KT}$ , where  $n$  is number of molecules in energy state  $i$ ,  $E$  the energy of state  $i$ ,  $k$  the Boltzmann constant,  $T$  the absolute temperature, and  $A$  is the constant). By chance this molecule loses its total energy by collision or spontaneous emission, and photon of particular wavelength is emitted travelling in any direction. Process schematic is represented

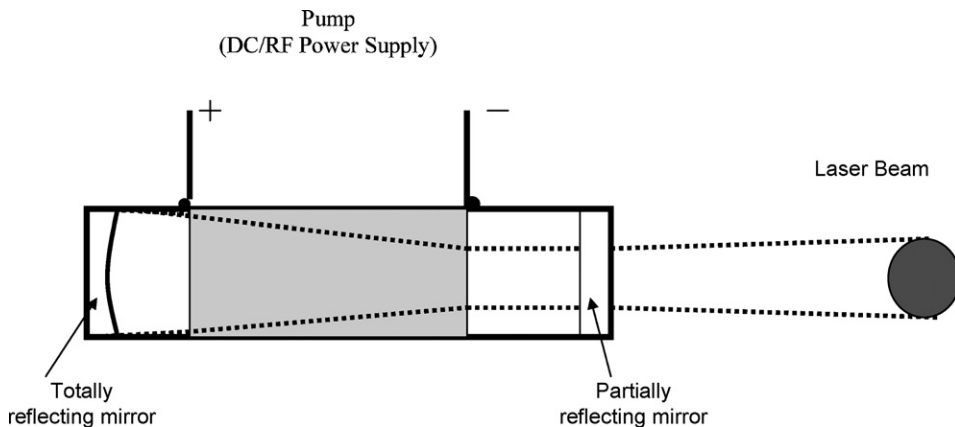


Fig. 155. Basic construction of stable laser cavity.

for carbon dioxide molecule in Fig. 155 [415]. One of these photons, again by chance, will oscillate between the mirrors. It can again strike another excited molecule and stimulate emission of another photon of identical wavelength, travelling in same direction and with same phase. These now sweep back and forth to generate cavity of other similar photons from other excited molecules allowing inversion of population of excited species available for stimulated emission (amplification) than for absorption.

Monochromaticity, beam divergence, coherence and brightness influence the practical application of laser determining its focusing and direction to remote locations for laser processing [416]. Laser linewidth, i.e. spread of wavelength from laser source is also of prime importance in spectroscopic and photochemical applications of laser. Beam divergence can be changed using suitable optical system. Shape profile of laser is represented by transverse electromagnetic modes described by waveguide theory labeled as TEM<sub>mn</sub>, where *m* and *n* are number of nodes in two orthogonal directions [416]. Both cylindrical and rectangular modes have TEM<sub>00</sub> as transverse mode of highest symmetry. Some mode patterns of resonator cavities are shown in Fig. 156 [415].

Spectral radiance is defined as  $B_\nu = B/\Delta\nu$ , where *B* is the brightness ( $=P/(\pi R^2\theta^2)$ , where *P* is the total power, *R* the beam radius, and  $\theta$  is the beam divergence) and  $\Delta\nu$  is the laser linewidth (Hz). Laser intensity vary along optical path, increasing in regions of beam convergence. While beam intensity varies, beam power stays constant in absence of absorption or other losses. Hence, distribution of laser intensity at or near focal point is usually required. Simple calculations consider propagating beam with Gaussian profile operating at TEM<sub>00</sub> mode. Gaussian beam radius (*w'*) can be calculated as [416]:

$$w' = \frac{2\lambda f}{\pi D}$$

where  $\lambda$  is the wavelength, *f* the focal length, and *D* is the lens diameter.

#### 4.7.3. Advantages

A few of unlimited advantages of laser processing can be summarized as follows:

- Ability to focus to a fine spot.
- Source can be tailored according to substrate (variable laser wavelength).
- Power and pulse can be adjusted to provide close control over key hole geometry.
- Small heat affected zone.
- Can be remotely operated.
- Contactless machining.
- Excellent spatial control.
- Can be focused through transparent objects.
- No X-ray shielding required.

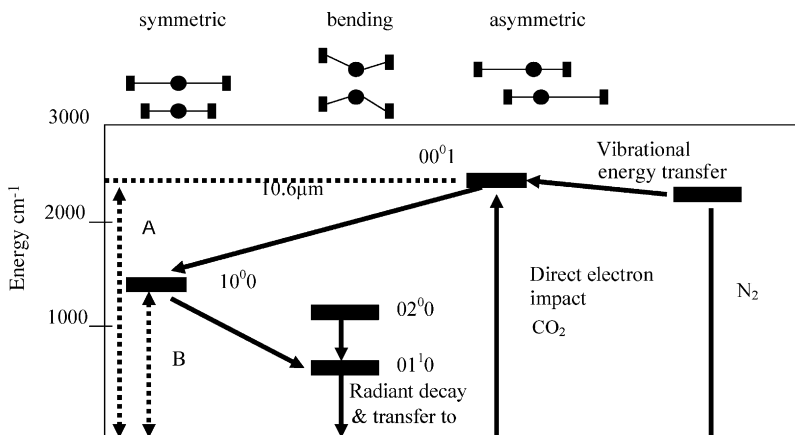


Fig. 156. Energy levels of CO<sub>2</sub> molecule.

#### 4.7.4. Disadvantages

A few disadvantages of laser processing are as follows:

- Laser equipment is expensive and bulky.
- Strict safety precautions must be observed in the operating room.
- Capital intensive (minimum capitalization of \$150k).
- Requires specially trained operators.
- Perceived as laboratory process.

#### 4.7.5. Equipment—process and mechanism

HL2006D Nd:YAG laser, Lambda Physik LPX 200/LPX 300 KrF laser, Concerto BMI/TCL femtosecond excimer laser, Hobart HLP 3000 Nd:YAG laser, etc., have been used by researchers for laser processing of nanocomposites. Commercial laser processing equipment is shown in Fig. 157.

Basic construction of laser includes two parallel mirrors forming an optical oscillator capable of amplifying light by stimulated emission (hence LASER: light amplification by stimulated emission of radiation). Usually, DC or RF power or focused pulse of light is used as pumping the active medium to activate energy state. Schematic of basic laser cavity is presented in Fig. 158 [415].

Electromagnetic radiation striking surface experiences reflection, absorption, and transmission [415]. Higher intensities cause Rayleigh, Brillouin, and Raman scattering as it interacts with matter. Apart from power, laser properties include wavelength, coherence, mode/diameter and polarization.

The laser medium can be a solid, gas, liquid, or semiconductor. Lasers are commonly designated by the type of lasing material employed [417]: *solid-state lasers* have lasing material distributed in a solid matrix (e.g. Nd:YAG), *gas lasers* (helium and helium–neon), *excimer lasers* (the name is derived from the terms excited and dimers) use reactive gases, such as chlorine and fluorine, mixed with inert gases such as argon, krypton, or xenon, *dye lasers* use complex organic dyes, such as rhodamine 6 G, in liquid solution or suspension as lasing media (tunable lasers), *semiconductor lasers*, sometimes called diode lasers are generally very small and use low power. Typical wavelength for lasers processing are given as follows: He–Ne (red: 632.8 nm; green: 543 nm), Ar (514.5 nm), ruby (694.3 nm), Nd:YAG (1064 nm), CO<sub>2</sub> (10,600 nm), ArF (UV: 193 nm), KrF (UV: 248 nm) [417]. Laser processing can be classified as direct (for laser sintering, laser surface engineering, laser surface alloying, etc.), or indirect (such as laser ablation) with concept of heating, melting, boiling, or plasma formation. Laser can be applied either as pulsed or continuous wave. Pulsed wave geometry can be altered depending on laser processing application. Focused laser intensity development with time can be visualized in Fig. 159.



Fig. 157. The 790 Beam Director laser machine. (Source: <http://www.raymax.com.au/a/73.html>.)

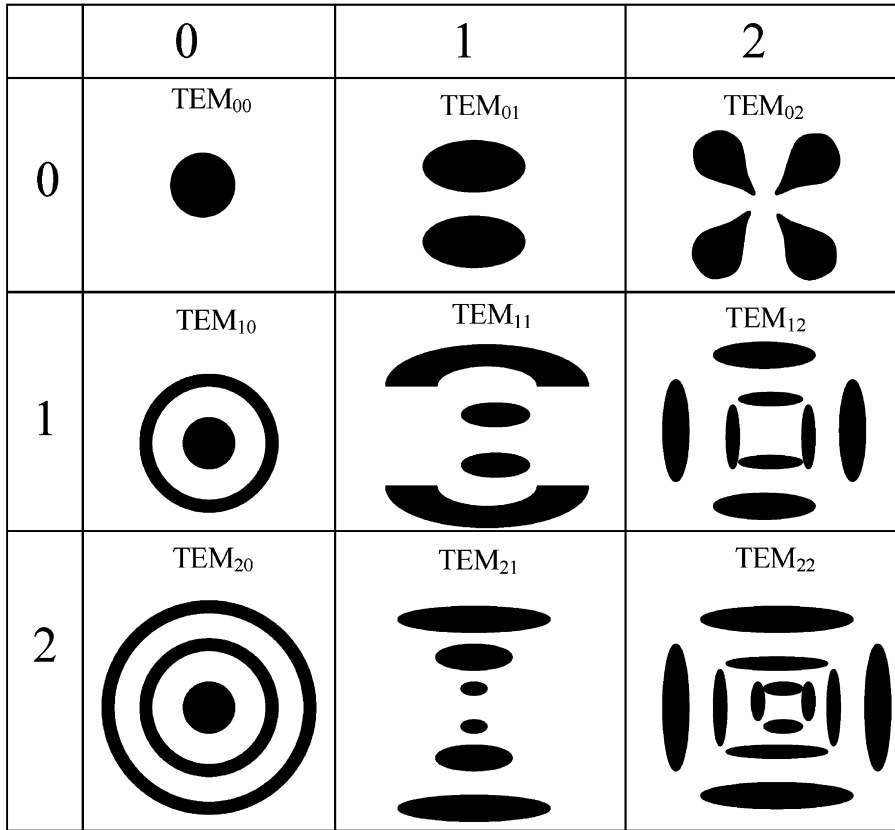


Fig. 158. Various laser mode patterns.

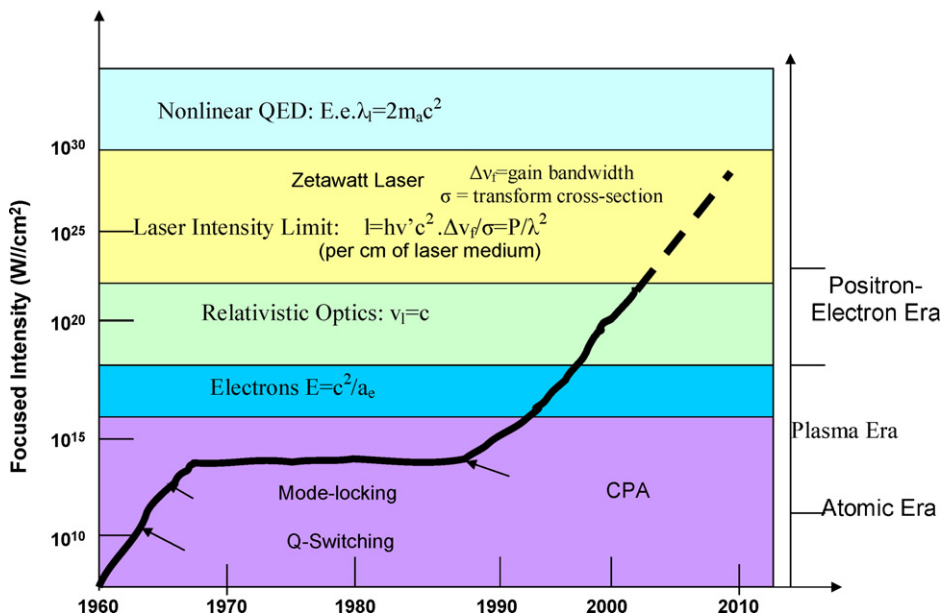


Fig. 159. History of laser development. (Source: <http://www.nationmaster.com>.)

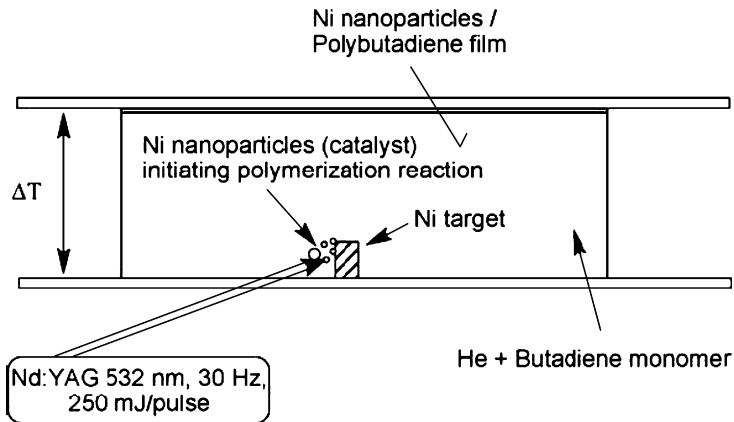


Fig. 160. LVCC chamber for polymerization of metal/polymer nanocomposite. (Reprinted from [418] with permission from Elsevier.)

#### 4.7.6. Nanoconsolidation

4.7.6.1. *Metal–polymer nanocomposites via laser ablation.* Laser ablation of metallic targets catalyze reactions such as polymerization of organic molecules due to formation of metallic atoms, ions, electrons and neutral or charged clusters, leading to formation of metal/polymer nanocomposites [418]. Gas phase polymerization can be efficiently processed using laser vaporization controlled condensation (LVCC) for producing metallic/intermetallic nanoparticles–polymer nanocomposite. Pulsed laser (532 nm Nd:YAG laser) with intensity flux of  $10^6$ – $10^7$   $\text{W cm}^{-2}$  is focused on target resulting vaporization with yields of  $10^{14}$ – $10^{15}$  atoms from surface area of  $0.01 \text{ cm}^2$  in a  $10^{-8}$  pulse. Fig. 160 shows LVCC chamber used for gas phase polymerization of butadiene using Ni nanoparticles [418].

Resulting microstructure depicted strong influence of gas phase reaction of metallic/intermetallic with polymer to encapsulate tuning of metal–polymer nanocomposite. FeAl and Ni nanoparticles were deposited in the polymer matrix (Fig. 161a and b). FeAl polymer nanocomposite are shown in Fig. 162a and b, prepared from 1 to 15% 1,3-butadiene in He, respectively [418]. FeAl nanoparticles are seen well dispersed and randomly distributed in polymer matrix. One percent butadiene inset displayed crystalline rings whereas 15% butadiene sample depicted diffused rings indicating amorphous matrix resin.

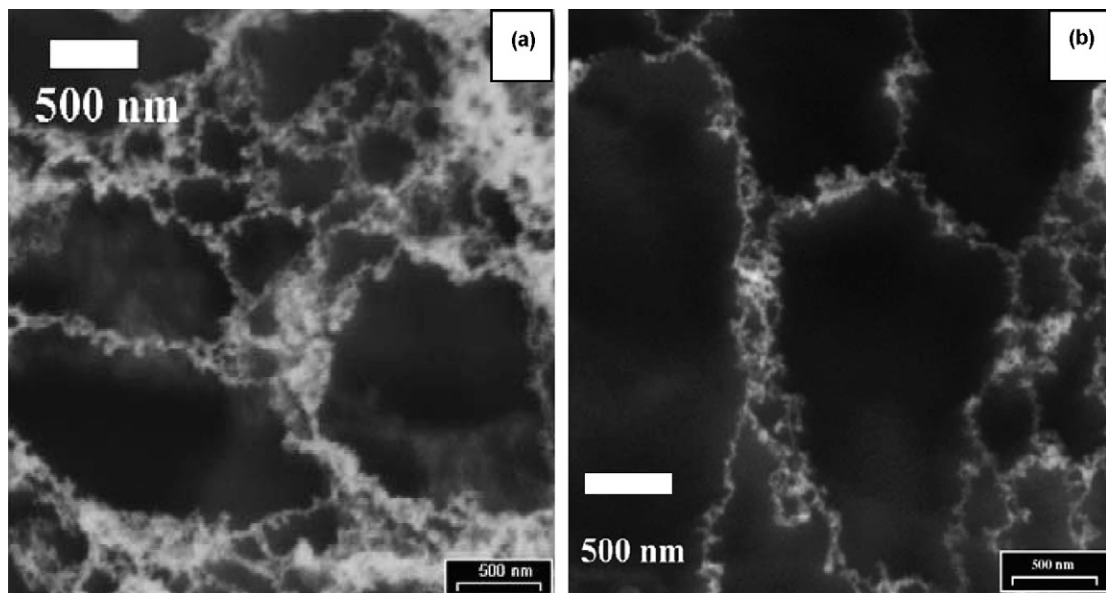


Fig. 161. SEM of: (a) FeAl/polybutadiene nanocomposite and (b) Ni–butadiene nanocomposite prepared by LVCC. (Reprinted from [418] with permission from Elsevier.)

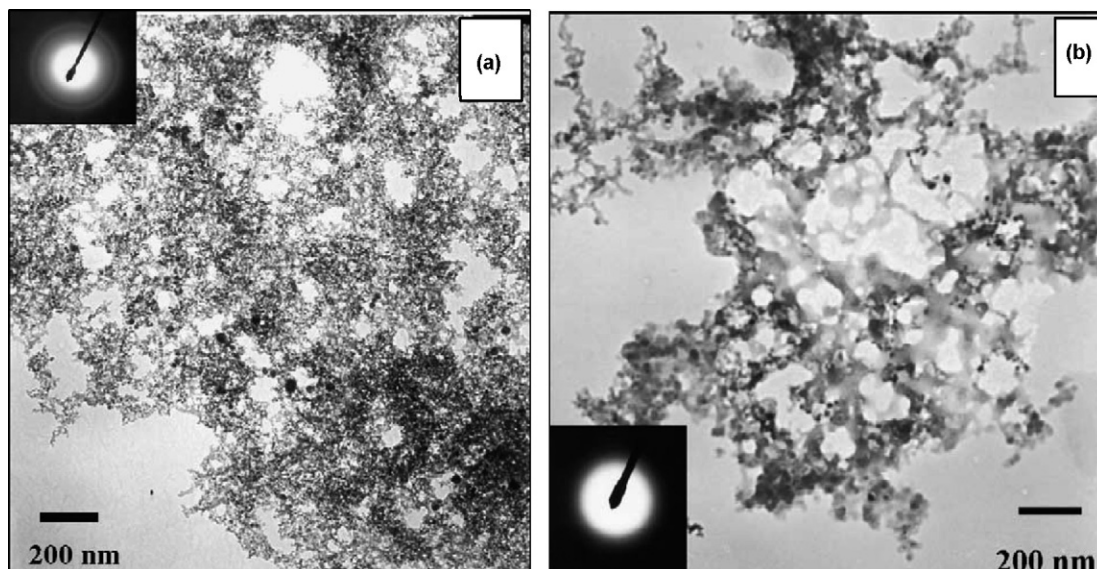


Fig. 162. TEM and selected electron diffraction pattern (inset) of FeAl in: (a) 1% and (b) 15% 1,3-butadiene in He. (Reprinted from [418] with permission from Elsevier.)

**4.7.6.2. Metal–ceramic nanocomposite.** ArF laser (12 ns, 193 nm) operating at 5 Hz is focused alternately high purity  $\text{Al}_2\text{O}_3$  ceramic target and high purity metal target (Bi, Cu, or Fe) to grow film over silicon or carbon coated mica substrates [419]. Energy density of  $2 \text{ J cm}^{-2}$  is used, which is enough to ablate the metal. These nanocrystal embedded matrices exhibit special mechanical, catalytical, electrical, and optical properties, which can be engineered [419]. Nanocrystals are evinced in reflectivity curves as sharp peaks at constant thickness intervals of the U-shaped host reflectivity curve. Attenuation is affected by laser pulses and absorption increases since metal content also increases. The growth of nanocrystals from 1.5 to 4.0 nm is evinced with increasing pulse (Fig. 163) [419]. This was reasoned to the coalescence of nanocrystals to result elongated grains by nucleation and growth of crystals at substrate sites.

Cu nanocrystals embedded in amorphous  $\text{Al}_2\text{O}_3$  have also been developed by researchers for development of ultrafast optical switching devices [420]. ArF excimer laser beam ( $\lambda = 193 \text{ nm}$ ,  $\tau = 20 \text{ ns}$ , FWHM, 10 Hz repetition rate) was used to fabricate Cu: $\text{Al}_2\text{O}_3$  thin films grown at room temperatures at different laser fluences ( $1.4\text{--}2.1 \text{ J cm}^{-2}$ ) and Ar pressures ( $1 \times 10^{-6}$  to  $1 \times 10^{-1}$  Torr) on Si and glass substrates. Fluence plays a role in nucleation of nanocrystal as shown in Fig. 164, showing dominance of lateral growth over vertical growth of nanocomposites [420].

Presence of Ni nanoparticles improves the ferromagnetic and toughness of Ni–alumina nanocomposites [1]. 2.5 kW Hobart HLP 3000 Nd:YAG laser-based thermal processing of Ni coated alumina particles transformed the metallic layer into nanoparticulates in situ [421]. Processing was done at continuous mode in localized nitrogen atmosphere at pressure of 137.8 kPa. Presence of small ( $\sim 5 \text{ nm}$ ) Ni particles was revealed in HRTEM analysis of laser processed Ni–alumina nanocomposite and EDS spectrum of the selected area confirmed the presence of Ni, Al, and O (Fig. 165) [421].

Diamond-like carbon (DLC)–silver and functionally gradient DLC–titanium films are developed using single target PLD process [422]. DLC coated films have shown improvement in albumin/fibrinogen adhesion when compared to those for many polymer surfaces [423]. DLC–silver provides anti-microbial functionality since they are toxic to many species of bacteria. Lambda Physik LPX 200 excimer laser (KrF 248 nm) has been used for laser ablation with pulse of 25 ns, pulse frequency of 10 Hz, energy density of  $5 \text{ J cm}^{-2}$  with target to substrate distance of 4.5 cm. Silver nanodots were observed with Z-contrast image of DLC–silver nanocomposite film, Fig. 166 demonstrating self-organized silver into 2–5 nm nanoparticles array with high fraction of  $\text{sp}^3$  hybridized carbon atoms [422]. Also, these DLC nanocomposites film exhibited better adhesion with substrate because of chemical bonding with substrate and reduced internal compressive stress [422].

Laser ablation of Pt/ $\text{TiO}_2$  nanocomposite thin films is pulsed laser deposited by two-beam PLD technique (ArF excimer laser for ionization after Nd:YAG laser ablation) [424]. Ablation fluence of  $1.4 \text{ J cm}^{-2}$  was followed by ionization at time delay of 1–1.5 ms with fluence of  $0.2 \text{ J cm}^{-2}$ . Pt/ $\text{TiO}_2$  nanocomposite thin films depict unique

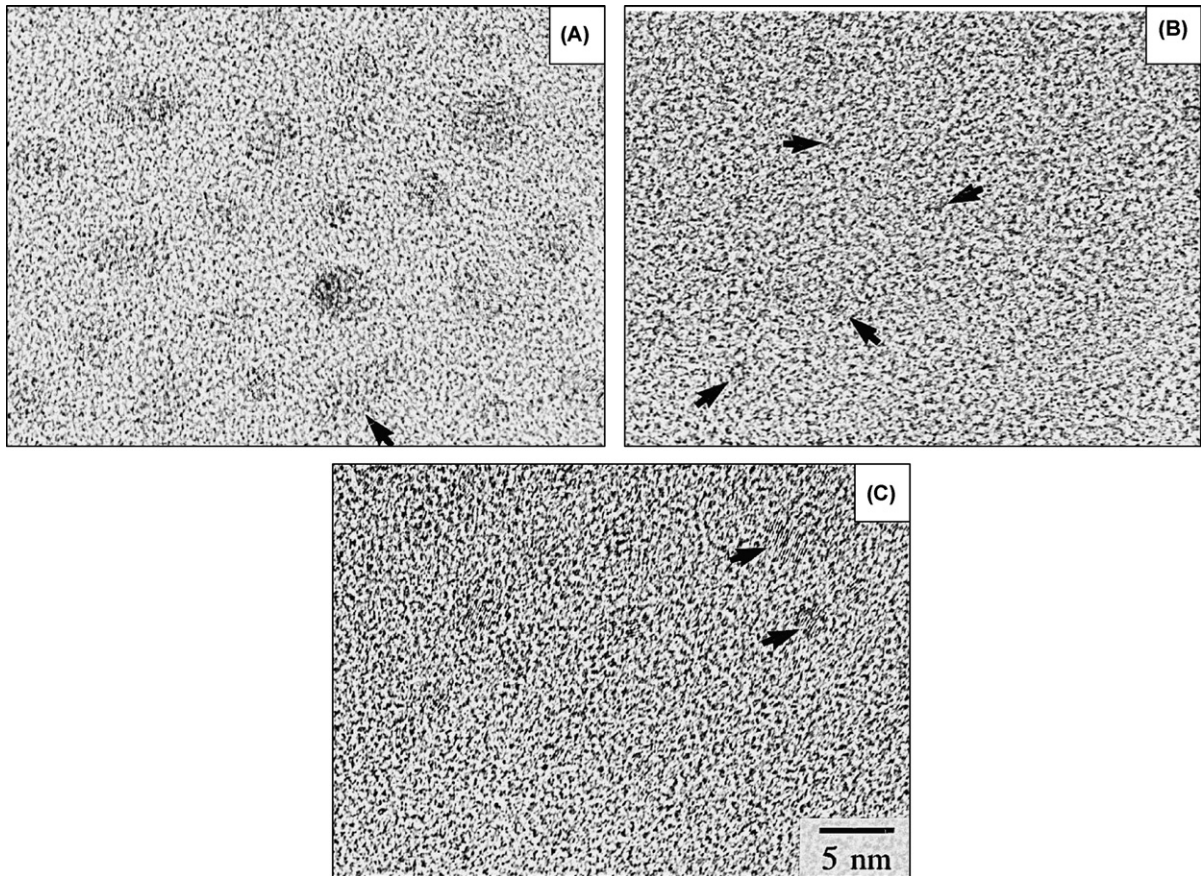


Fig. 163. HRTEM images of Cu:Al<sub>2</sub>O<sub>3</sub> films grown in vacuum by: (A) 160 pulses and (B) 80 pulses on the Cu target and (C) in an Ar pressure of  $1.4 \times 10^{-4}$  Torr by 80 pulses on the Cu target. (Reprinted from [419] with permission from Elsevier.)

optical and chemical properties with bandgap less than that of pure TiO<sub>2</sub> [425,426]. Pt nanoparticles 30 nm in diameter were observed by TEM microscopy.

Yttria-stabilized zirconia/Au nanocomposite film has been fabricated using hybrid PLD and magnetron sputtering (called MSPLD) [427]. Magnetron sputtering of gold (99.99% pure) was used to produce plasma, and YSZ (ZrO<sub>2</sub>–

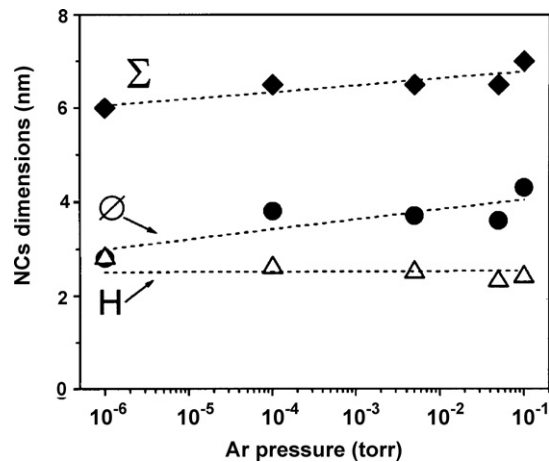


Fig. 164. Mean diameter  $\emptyset$  in the film plane, mean separation  $\Sigma$ , center to center in the film plane and  $H$  mean height of the nanocrystals in the direction perpendicular to the film plane. (Reprinted from [420] with permission from Elsevier.)

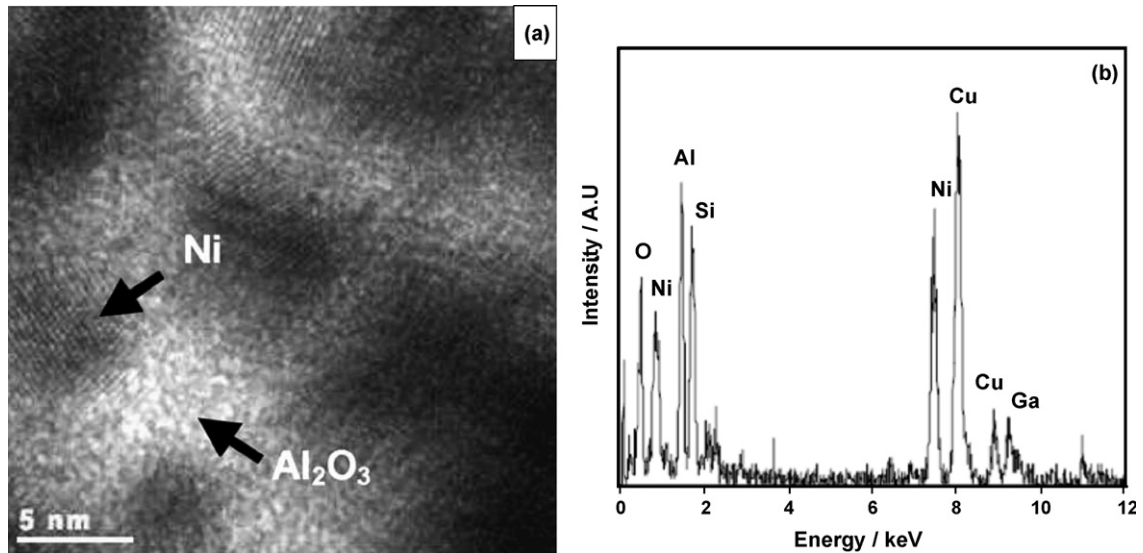


Fig. 165. (a) HRTEM bright field image of the Ni–alumina nanocomposite showing lattice fringes of Ni nanoparticles and (b) EDS spectrum of Ni–alumina nanocomposite. (Reprinted from [421] with permission from Elsevier.)

5 wt.% Y<sub>2</sub>O<sub>3</sub>) was laser ablated using KrF excimer laser (LPX300 Lambda Physik). UHV chamber at  $1 \times 10^{-6}$  Pa vacuum was later filled with 1.3 Pa Ar to facilitate magnetron sputtering, with laser pulse of 248 nm wavelength, 900 mJ energy and 25 ns in width. Three different gold concentrations were studied by researchers with 5 at.% Au showing small (1–2 nm) gold regions displaying amorphous films (Fig. 167) [427]. High magnification images of 8.5 at.% Au revealed crystalline regions of 5–10 nm in diameter, whereas 22 at.% Au films were crystalline with grain sizes as large as 10–20 nm. Improved ductility, because of absence of strong chemical bonding between YSZ and gold nanocrystals, is observed in YSZ/Au amorphous matrix. Variation on elastic modulus is also reflected in film structure

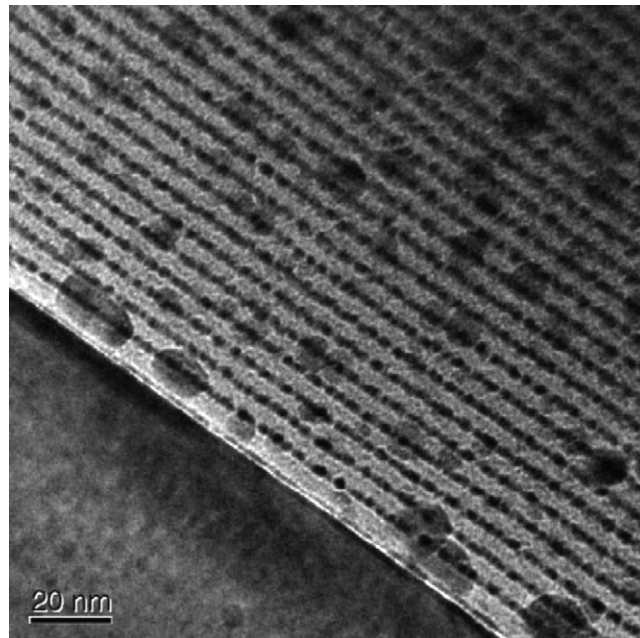


Fig. 166. Z-contrast bright field image of DLC–Ag nanocomposite film. DLC appears as the brighter region within this image. (Reprinted from [422] with permission from Elsevier.)

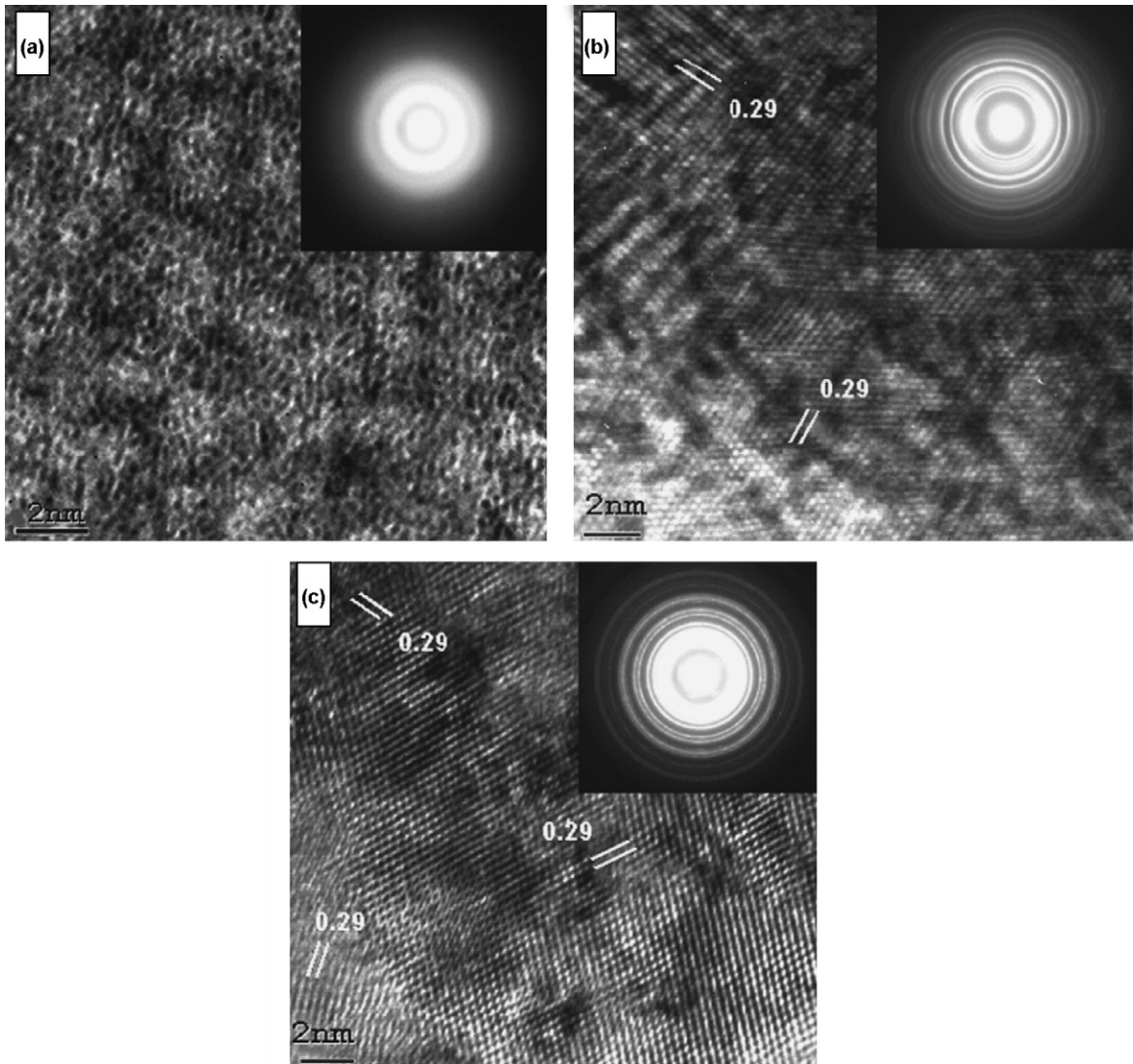


Fig. 167. TEM micrograph of YSZ/Au composite with varying gold contents: (a) 5 at.% Au, (b) 8.5 at.% Au, and (c) 22 at.% Au, with insets showing SAD pattern. (Reprinted from [427] with permission from Elsevier.)

transitions (Fig. 168) [427]. High elastic hardness of 15–20 GPa and high elastic modulus of 250 GPa was achieved for nanocrystalline/amorphous nanocomposite coatings.

**4.7.6.3. Ceramic films.** Pulsed laser deposition (PLD) allows low temperature deposition and precise deposition concentration of elements during fabrication effectively allowing controlled reproduction of nanocomposites via laser synthesis. Femtosecond laser (Concerto, BMI/TCL,  $\lambda = 800$  nm, pulse duration 150 fs, 1 kHz, energy per pulse = 1.5 mJ) is focused for 9 s onto graphite target and 1 s onto tantalum target. SEM evinced nanostructured film with size distribution between 15 and 175 nm [428]. Average grain size of 82 nm was observed for dispersed nanoparticles with a standard deviation of 49 nm (Fig. 169) [428]. High resolution TEM (HRTEM) depicted crystalline structure in the dark particles (up to 100 nm in size), whereas dark gray particles (about 10 nm in size) appear completely amorphous (Fig. 170) [428]. Full width half maximum (FWHM) of crystalline phases was consistent with crystallite nodule size of 100 nm via grazing angle X-ray diffraction spectra of a-C:Ta film (Fig. 171) [428].

Si/C/N nanopowders have been synthesized using  $\text{CO}_2$  (10.6  $\mu\text{m}$ ) laser pyrolysis via its interaction with liquid/gaseous precursor [429]. TEM micrographs depicted similar round grains with an average diameter of 15 nm, but specific surface areas vary with a factor of 3. IR spectra of as-formed nanopowders depicted wide band without any

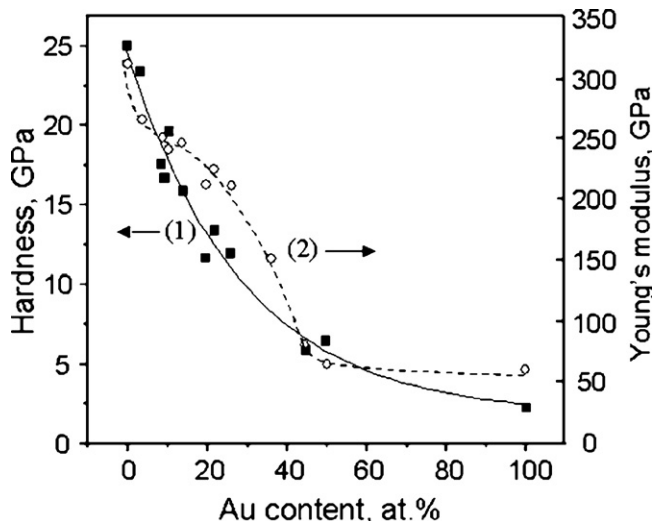


Fig. 168. (1) Nanoindentation hardness and (2) Young's modulus of YSZ/Au composite films as a function of Au content. (Reprinted from [427] with permission from Elsevier.)

structure in  $1200\text{--}800\text{ cm}^{-1}$  (attributed to Si–N–Si, Si–C, and Si–O bonds) in amorphous SiCNO structure. Hence, SiCN-based powders are not a simple mixture of  $\text{Si}_3\text{N}_4\text{--SiC}$  powders (Fig. 172) [429].

PLD of DLC coatings has been prepared using ultraviolet 248 nm lasers for graphite ablation. Coatings exhibited high contact toughness withstanding 70 N load without brittle failure [430]. TiC crystallites of about 10–20 nm were encapsulated in DLC matrix as seen in Fig. 173 [430].

**4.7.6.4. Carbon nanotube–hydroxyapatite nanocomposite.** Laser surface alloying of CNT–HA is carried out using HL2006D Nd:YAG laser with laser power of 400 W, beam diameter 4 mm, and beam scanning speed of  $4\text{ mm s}^{-1}$  [431,432]. HA is a potential bone implant material which bonds chemically with living bone tissues because of similar chemical composition and crystal structure as of apatite in human skeleton system [433]. SEM micrographs show rough coating surface with little interlinking of pores. TEM studies depicted existence of undamaged CNTs in laser surface alloyed nanocomposite coating (Fig. 174) [432]. Since laser surface alloying is a non-equilibrium process, amorphous region is also seen along with crystalline regions in HRTEM images (Fig. 175) [432]. Hardness variation was observed between 9 and 13 GPa and the Young's modulus increased from 149 to 180 GPa with increasing CNT content (Table 41) [431].

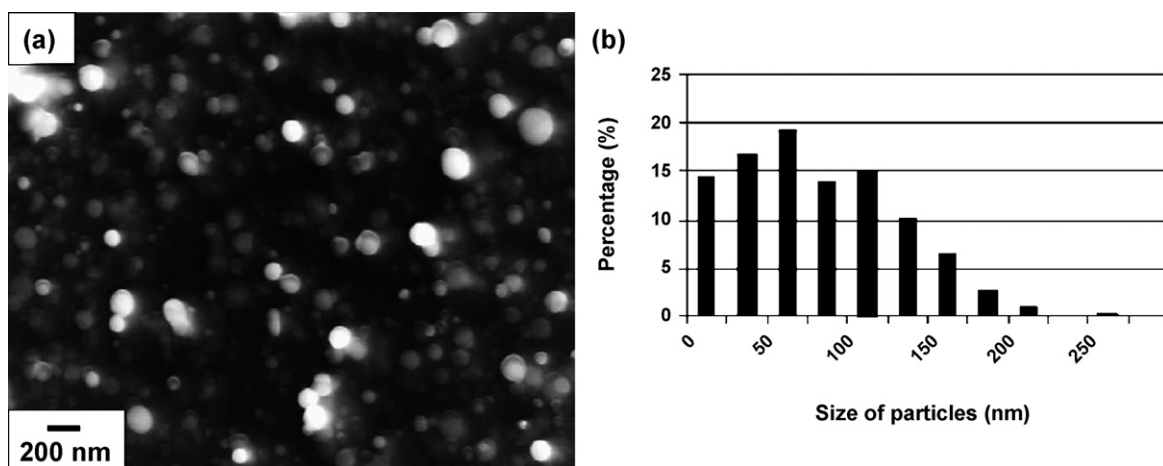


Fig. 169. (a) FESEM image of C:Ta film and (b) size distribution of the clusters embedded in the film. (Reprinted from [428] with permission from Elsevier.)

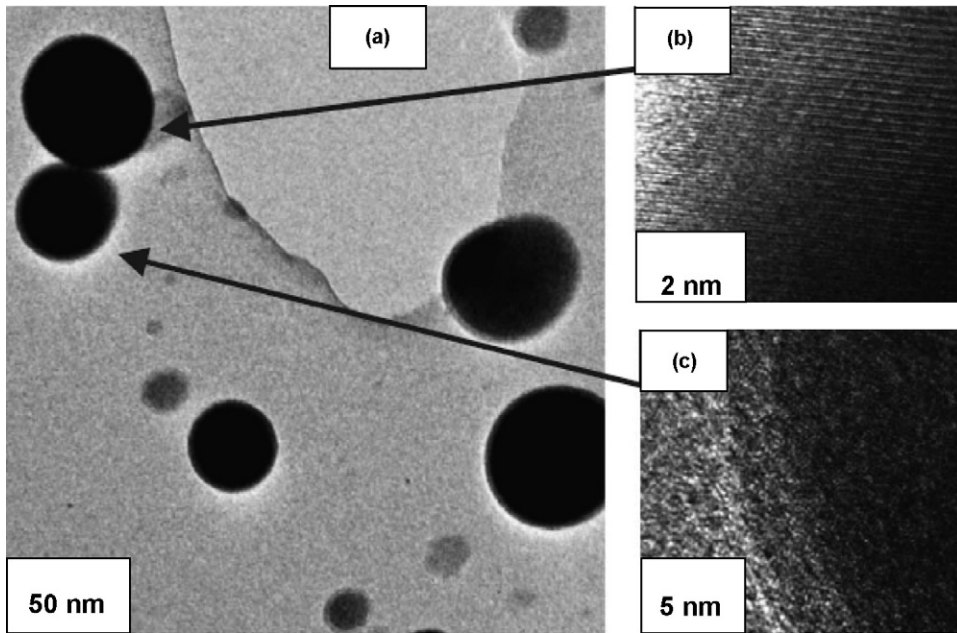


Fig. 170. TEM image of: (a) the a-C:Ta film. High resolution images of: (b) black nodules and (c) light black nodules. (Reprinted from [428] with permission from Elsevier.)

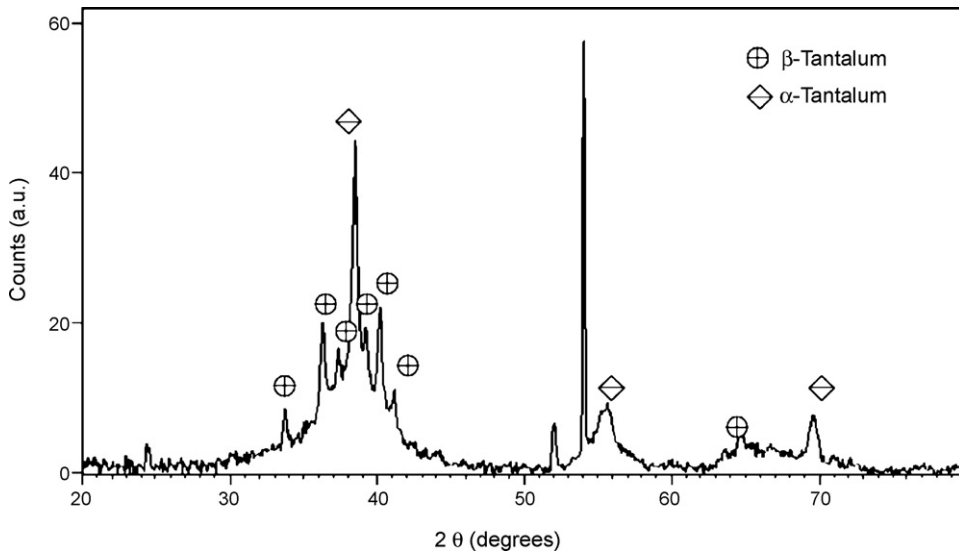


Fig. 171. Grazing angle X-ray diffraction spectra of the a-C:Ta film, observed with an incident X-ray beam angle of  $0.7^\circ$ . The un-indexed peaks correspond to the doped-Si substrate. (Reprinted from [428] with permission from Elsevier.)

Table 41  
Hardness and modulus of different laser surface alloyed coatings

Property	CNT-free coating	HA-5% CNT coating	HA-10% CNT coating	HA-20% CNT coating	Reference
$H$ (GPa)	9.047	9.743	11.026	12.811	[431]
$E$ (GPa)	149.435	152.186	164.265	180.604	[431]

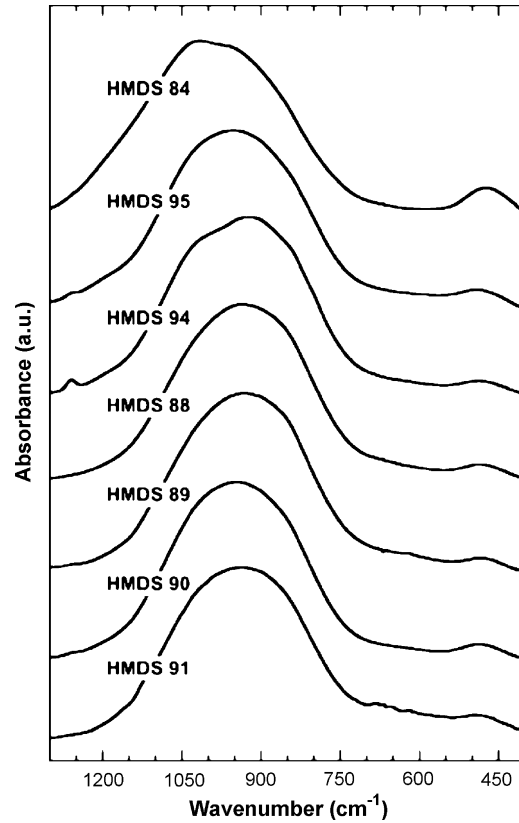


Fig. 172. IR spectra of as-formed nanopowders. (Reprinted from [430] with permission from Elsevier.)

**4.7.6.5. Nanoelectronics.** Quantum dots or semiconductor nanoparticles are acquiring much attention in the electronic, optical, and chemical industry owing to their ‘quantum size effect’ [434]. The 2.0 kW Nd:YAG laser (1.06  $\mu\text{m}$ ) with defocused spot diameter of 4 mm is irradiated onto 300  $\mu\text{m}$  thick polystyrene foil (1  $\text{cm}^2$ ) with 10–50 ms pulse time [435]. TEM images depict formation of CdS nanocrystals in the polymer matrix (Fig. 176) [434].

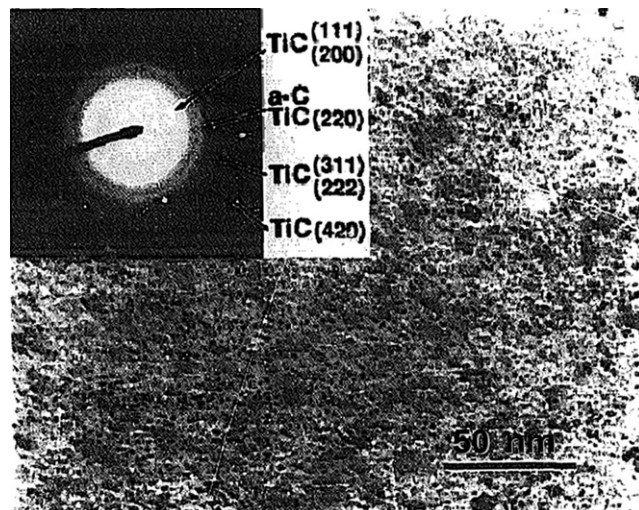


Fig. 173. Bright field TEM image of TiC-DLC nanocomposite with insert showing SAD pattern. (Reprinted from [430] with permission from Elsevier.)

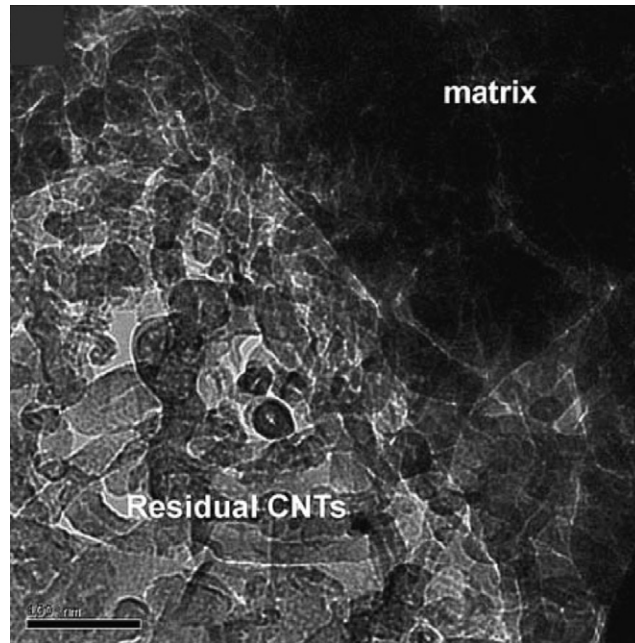


Fig. 174. TEM image showing residual CNTs in laser surface alloyed nanocomposite coating. (Reprinted from [432] with permission from Elsevier.)

Nanoparticle formation by laser synthesis is reported as a function of energy absorbed and temperature experienced by photon pumping in the solution. Temperature can be functioned to laser and foil properties as [416,436]:

$$T = \frac{\varepsilon P \ln[1 + (4kt/d^2)]}{4\pi KL}$$

where  $\varepsilon$  is the emissivity of the surface,  $P$  the total laser pulse power (W),  $k$  the thermal conductivity ( $\text{W m}^{-1} \text{ }^\circ\text{C}^{-1}$ ),  $t$  the pulse time (s),  $d$  the radius of laser spot (m),  $K$  the thermal diffusivity ( $\text{m}^2 \text{ s}^{-1}$ ), and  $L$  is the thickness of polymer

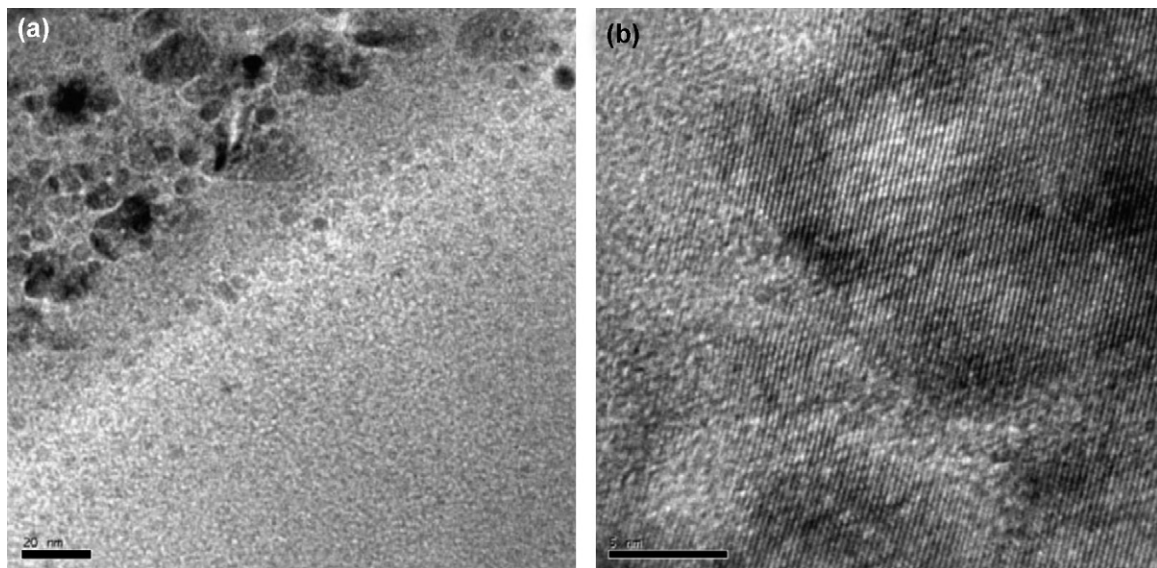


Fig. 175. TEM image showing (a) amorphous regions in conjunction with crystalline HA in the as-alloyed coating and (b) corresponding (30–31) HRTEM of crystalline HA. (Reprinted from [432] with permission from Elsevier.)

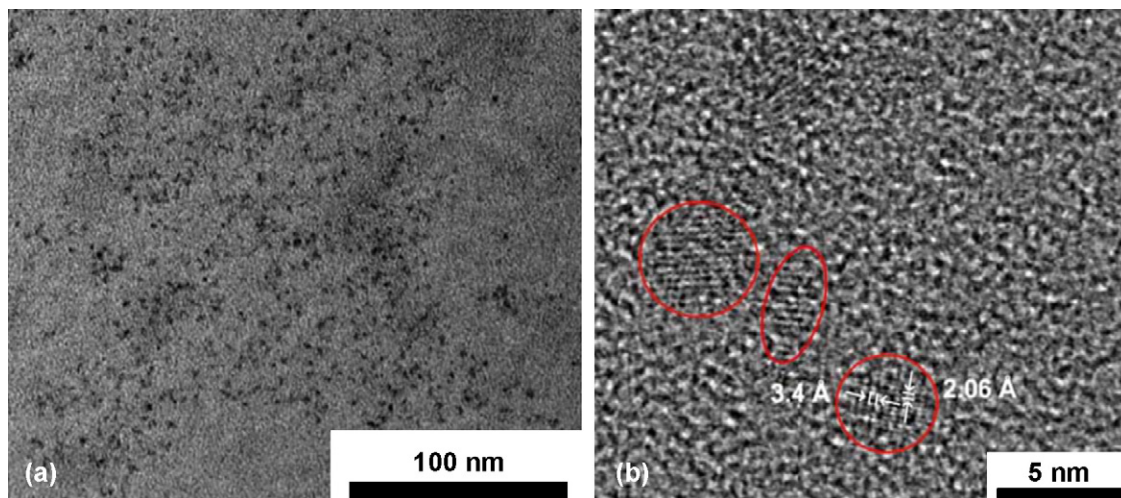


Fig. 176. (a) Low resolution TEM images of nanocomposite after thermal treatment and its dissolution in chloroform and (b) HRTEM of the same sample of CdS. (Reprinted from [434] with permission from Elsevier.)

foil (m). Temperature consideration becomes important for nanowires embedded in insulating matrices and is especially useful for manufacturing nanoelectronics devices or conductive plastics for realization of advanced applications.

Polymerization of metallo-organic polymer nanocomposites is achieved through laser ablation by gas phase reaction. In situ nanoparticulate transformation or nucleation of nanocrystals via laser processing result improved mechanical, catalytical, electrical, and optical properties of fabricated nanocomposite. Low temperature and precision processing are striking features allowing reproducibility in laser consolidation of nanocomposites. However, laser consolidation of nanocomposite is relatively restricted to synthesis of nanocomposite coatings.

## 5. Room temperature processing

### 5.1. Electrodeposition

#### 5.1.1. Introduction

The art of deposition of gold and silver for jewellery emerged later on, as a key materials processing tool for pure metals to composites. The past decade witnessed Electrodeposition as a technique which is versatile in making coatings, bulk products in micro to nanodimensions. The chronological evolution of this technique to its present status is presented in Fig. 177. The precursor (electrolyte) for the material to be developed using electroplating is used as an electrolyte and the material on which the material is to be deposited is termed as a cathode. If coating is the objective of the processing, then the substrate material itself is used as a cathode. Over the past decade, the potential of

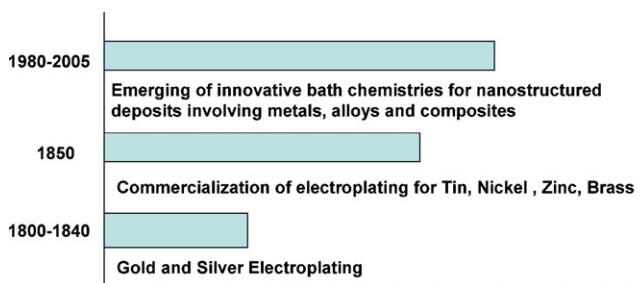


Fig. 177. Chronological events that led to nanostructured electrodeposits.

electroplating, especially for nanomaterials processing has been appreciated in terms of its highly dense structure, no post-treatments, ease of formation of bulk nanostructures for a wide range of material systems with a high production rate.

### 5.1.2. Fundamental principles

Electrodeposition or electroplating has been termed as the process in which the deposit of a (usually) thin layer (of metal) is formed ‘electrolytically’ on a substrate (that is usually a metal). The purpose of such process may be to enhance or change the substrate’s appearance and/or attributes such as corrosion resistance. Examples include the deposition of gold or silver on jewelry and utensils, and the deposition of chrome on automobile parts. The object that is to be plated is submerged into the electrolyte (plating bath). Placed usually at the center of the bath, the object that is to be deposited acts as a negatively charged cathode. The positively charged anode completes the electric circuit; those may be at opposite edges of the plating tank, thus making the deposition possible both sides of the cathode. Material systems with nanostructures are developed with ease because of the processing being carried out at relatively low temperatures and some of the processing is carried out with a surfactant that retains the nanostructures.

Materials processed via electrodeposition are: pure Ni [437], Ni-based nanocomposites [438], copper [439], layered Cu–Ni nanocomposites [440], pure cobalt [441], Co–Ni alloys [442], WC-based coatings [443], TiO<sub>2</sub>–Ni nanocomposite coatings [444] to name a few. The electrodeposited material finds applications in mechanical devices, such as, Electrosleeves<sup>TM</sup> [445], energy storage [446], and electrical utilities [447].

### 5.1.3. Advantages

- A room temperature processing technique that can be used both as a coating and free-form manufacturing technique.
- Process parameters can be controlled at will to achieve the end properties.

### 5.1.4. Equipment—process and mechanism

The laboratory setup for electrodeposition has an electrolytic bath maintained at a particular composition with cathode and anode immersed in the bath. The anode is made out of a noble material such as Pt and the cathode is a well-polished material where the deposition will be done. The key variables of the electrodeposition include temperature of the bath, current density complexing agents, agents to improve the bath conductivity and pH. These can be manipulated in achieving the required grain size in nanocrystalline range. Table 42 depicts the material systems that have been electrodeposited and the property amelioration that resulted as a consequence.

A power source in the form of a battery or rectifier which converts AC electricity to regulated low voltage DC current is providing the necessary current. This type of circuit arrangement directs electrons from the power supply (rectifier) to the cathode (the object to be plated). In the bath, the electric current is carried largely by the positively charged ions from the anode(s) toward the negatively charged cathode. This movement makes the metal ions in the bath to migrate toward extra electrons that are located at or near the cathode’s surface outer layer. Finally, the metal ions are removed from the solution and are deposited on the surface of the object as a thin layer.

In its rudimentary stage, batteries have been used to carry out the process, which later on got augmented to the DC current. Table 43 puts together a list of materials systems that have been processed using the variants, DC and pulse DC. Varying the current density, temperature of the bath changes the chemistry of the electrodeposit altogether.

Table 42  
Electrodeposition parameters of the materials systems along with the properties achieved

Material	Property amelioration	Reference
Ni-based alloys	High solid solubility, negligible localized corrosion, coefficient of friction, wear resistance, strength, hardness, electrical conductivity	[437]
WC/Co Ni, WC/Co Ni P	Wear resistance	[443]
Ni–ZrO <sub>2</sub>	Hardness improvement	[453]
Ni–TiO <sub>2</sub>	Improved hardness and corrosion resistance	[444]
Ni–alumina	Low coercivity	[466]
Ni–Co/Si <sub>3</sub> N <sub>4</sub>	High hardness, wear resistance	[470]

Table 43  
Different variants of electrodeposition with examples

DC electrodeposition	Pulse electrodeposition	Pulse reverse electroplating
Ni–ZrO <sub>2</sub> [453], Ni–Al <sub>2</sub> O <sub>3</sub> [466]	Ni–Mo [446], Ni/SiC [471], Ni [437], Ni–ZrO <sub>2</sub> [454], Zn [473]	Ni [437], Ni–ZrO <sub>2</sub> [437]

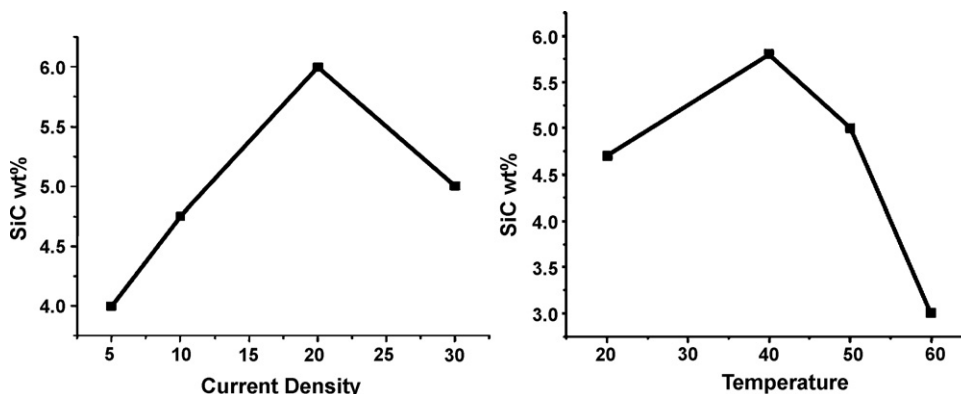


Fig. 178. Effect of electrolytic bath conditions on the amount of SiC particulates in Ni–Co alloy [471].

Notable example [34] is the variation in the amount of SiC particulates in Ni–Co alloy due to the variation in current density from 5 to 30 mA cm<sup>-2</sup>. Variation in bath temperature from 20 to 60 °C also has an effect on the SiC content in the composite (Fig. 178).

A typical electrodeposition schematic is shown in Fig. 179. Almost all the electrodeposition bath conditions maintain a pH less than 7, which means that the bath is acidic. Most of the precursors are chlorides or sulfates of the metal to be deposited. Temperatures usually maintained less than 100 °C, it is safe to have a corrosion resistant metallic tank preferably made of high quality stainless steels such as 3XX series (Austenitic Stainless steels). Electrodeposition of nanocomposites requires the reinforcements such as silicon nitride, alumina to be suspended uniformly in the bath which necessitates the entire tank to be ultrasonically vibrated. Hielscher USA Inc. [448] specializes in ultrasound technologies and provides custom made solutions for ultrasonification. Since the ingredients for the electrodeposit are obtained from the electrodeposit are available from the bath, the anode needs to be essentially stable and inert towards the bath. Usually, Pt is used as anode. Another inexpensive option is having the same material to be electrodeposited as an anode. Controlling the composition of the element in the electrodeposit might get complicated in the latter case, as there is a significant contribution of the element from the anode. Cathode material is usually the substrate on to which the deposition is desired. The power setup depends on what kind of electrodeposition is preferred. For instance, if DC electrodeposition is planned to be conducted, the rectifiers for those kind of deposition

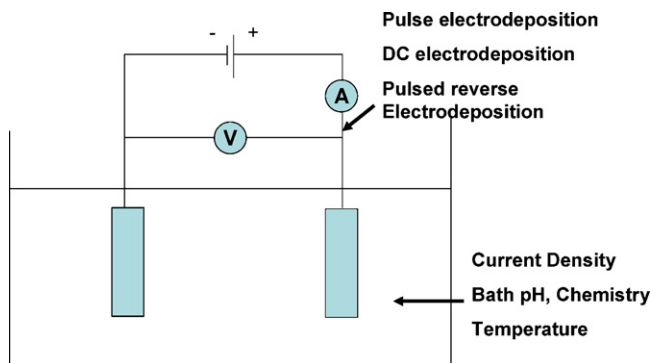


Fig. 179. Laboratory setup of electrodeposition with key variables that make electrodeposition a suitable tool for development of nanocrystalline materials in bulk form.

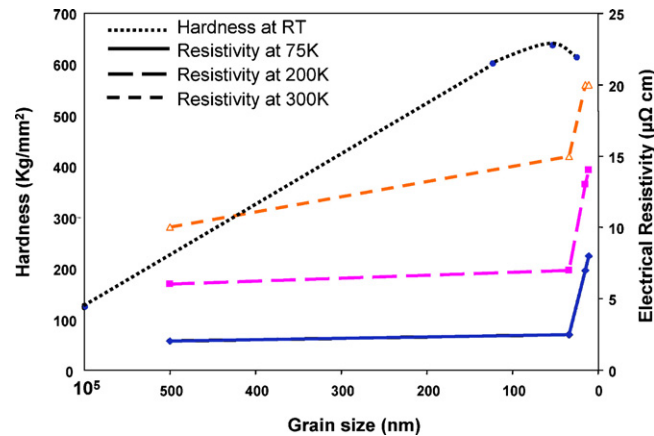


Fig. 180. Hardness and resistivity values as a function of grain size for nickel [437].

are available in the market. Separate rectifiers are available for pulsed DC, or pulsed reverse current electrodeposition as well. Rectifiers have also been made available to easily toggle between DC, pulsed DC or pulsed reverse DC (Dynatronix Company [449]). Microsoft Windows™ based software is available to monitor and change the electrodeposition parameters even from a remote location. Microlink engineering solutions [450] provide both hardware and software for security monitoring that can shut down the electrodeposition process instantaneously, if there is any break down in the system. All the ingredients for making electrolytic bath are supplied by Sigma–Aldrich or Fisher Scientific. All the nanoparticles to be dispersed in the solution can be obtained from companies like Nanophase Technologies Corporation, Inframat Corporation.

#### 5.1.5. Nanoconsolidation

Metals, alloys, composites with nanostructures have been processed successfully using the technique and has been shown to exhibit property amelioration compared to its micron grain size counterparts.

**5.1.5.1. Nickel-based alloys and nanocomposites.** Nickel alloy systems and nanocomposites have been studied extensively using electrodeposition. Initially, pure nanocrystalline nickel in bulk form [451] have been developed and proved to have high hardness and resistivities compared to their conventional micron grain nickel (Fig. 180). Some important properties of micron and nano-nickel are compared in Table 44. Nanocrystalline nickel has been successfully deposited in nuclear steam generator tubes [445]. It seems to have improved a host of structural properties such as hardness, yield strength, ultimate tensile strength, modulus of elasticity (see Table 45). Furthermore, nanoparticles have arrested the intergranular crack propagating due to stress corrosion cracking (SCC) in the alloy 600 tubing.

Bath composition plays an important role in producing amorphous and nanocrystalline materials. One such example is the electrodeposition of Ni–W alloy [452]. Citric acid, sodium tungstate, ammonium chloride in the bath composition remained crucial in determining the alloy composition. Keeping the citric acid content constant, if the ammonium chloride content is increased, the amount of tungsten and the deposition rate of the alloy are enhanced.

Table 44  
Mechanical properties of 10 μm Ni with 10 nm electrodeposited Ni [445]

Property	Ni 10 μm	Ni 10 nm
Yield strength (MPa)	103	~900
Ultimate tensile strength (MPa)	403	~2000
Tensile elongation (MPa)	50	1
Modulus of elasticity (GPa)	207	204
Vickers hardness (kg mm <sup>-2</sup> )	140	650
Work hardening coefficient	0.4	0.0
Wear rate (dry air pin on disk, μm <sup>3</sup> μm <sup>-1</sup> )	1330	7.9
Coefficient of friction (dry air pin on disk)	0.9	0.5

Table 45  
Mechanical properties of micron Ni compared with Electrosleeve™ material [445]

Property	Micron Ni	Electrosleeve™
Yield strength (MPa) (RT)	103	690
Ultimate tensile strength (MPa) (RT)	403	1100
Elongation (%) (RT)	50	~15
Modulus of elasticity (GPa) (RT)	207	214

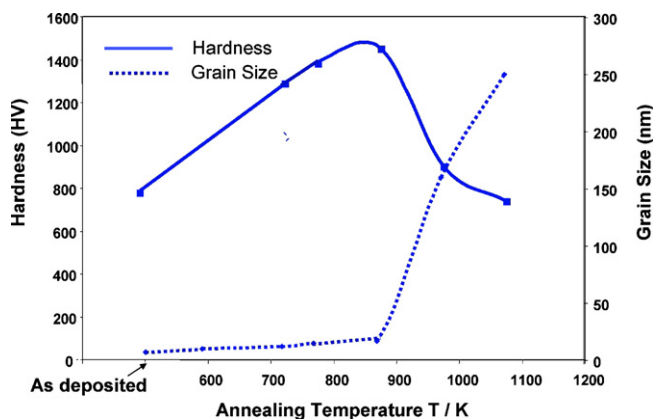


Fig. 181. Hardness and grain size variation as a function of annealing temperature for Ni–W [452].

However, the increase in tungsten content led to the cracking in the deposits. However, it has been observed that there is a decrease in cracking, if the citric acid content is varied, instead of ammonium chloride. Through X-ray diffraction, the amorphous structure of the alloy is ascertained in the as deposited condition. Ni–25 at.% W alloy, upon annealing at 723 K led to crystallization with fcc Ni phase. Such ultrafine grains (12 nm) led to a large increase in hardness compared to the as-deposited amorphous Ni–W alloy. The as deposited Ni–25 at.% W alloy with an amorphous structure exhibited high hardness of about 770 HV and after annealing the hardness was largely increased to about 1100 HV (Fig. 181).

Ni–ZrO<sub>2</sub> is a nanocomposite produced by codeposition of ZrO<sub>2</sub> particles during electroplating of nickel [453]. Nanocrystalline ZrO<sub>2</sub> powders were suspended in the plating solution of composition mentioned in Table 46. DC plating was carried out at 333 K on polished Ti substrates with nominal current densities of 0.01–0.1 A cm<sup>-2</sup>. Vickers hardness measurements correlated with the amount of ZrO<sub>2</sub> particles embedded in the matrix. The maximum hardness achieved was 600 HV at 4 vol.% of ZrO<sub>2</sub>. Another study on Ni–ZrO<sub>2</sub> by Wang et al. [454] had some variants in the bath composition and used DC, pulsed current and pulsed reverse current electrodeposition to compare the hardness values. One possible explanation is the difference in the bath pH and the difference in the volume fraction of ZrO<sub>2</sub> in the composite. Bath pH is a primary factor of controlling the grain size of the composite. There is an optimal level of pH up to which the grain size is reduced after which there is reversal in the trend. This might be the reason for the different hardness levels achieved for the same material systems. It is worth mentioning, that the hardness values of the nanomaterial are much higher than that for a pure Ni deposit (Fig. 182). However, the hardness values of Ni–ZrO<sub>2</sub> nanocomposites seems to be much higher than that of a conventional Ni of 10 μm grain size [455].

Table 46  
Effect of bath composition on the hardness values of Ni–ZrO<sub>2</sub> nanocomposites

Electrodeposition type	Bath composition (g l <sup>-1</sup> )				Bath pH	Hardness (HV)	Reference
	NiSO <sub>4</sub>	NiCl <sub>2</sub>	H <sub>3</sub> BO <sub>3</sub>	ZrO <sub>2</sub>			
Pulsed	26	3	3	1	3	42	[45]
Pulse reverse	26	3	3	1	3	46	[45]
DC	30	4	4	1–5	2	60	[45]

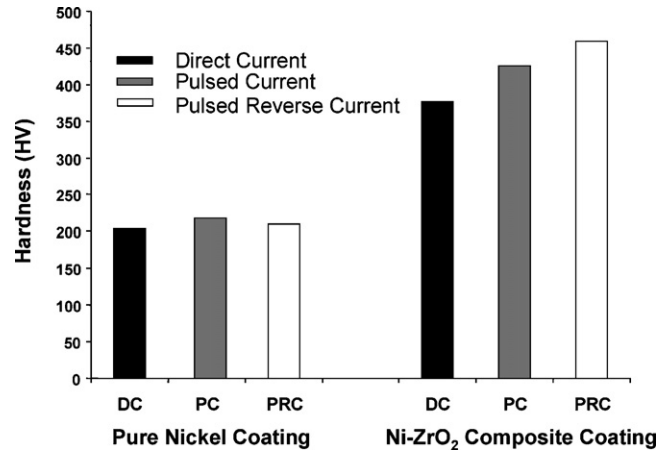


Fig. 182. Hardness graph of Ni-ZrO<sub>2</sub> compared with that of pure nanocrystalline nickel [454].

Layered nanocomposites can also be developed using electrodeposition. Notable examples are Cu/Co [456], Cu/Ni multilayers [457–460,440]. Coherency between the lattices of the bi-layers plays an important role in the interfacial strength of the nanocomposite. The composition of the electrolyte and the deposition time contribute to the strength of the nanocomposite. Oberle and Cammarata showed that the strength levels increase rapidly at about 40 nm and attains maximum values at 20 nm layer thickness and drops thereafter. It is interesting to note that dog bone-shaped tensile samples were made out of these bulk deposits with a gauge length of 12 mm and pneumatic grips were employed to carry out tensile testing at a strain rate of  $1.8 \times 10^{-4} \text{ s}^{-1}$  [440]. Table 47 summarizes the parameters being used to achieve high strength bi-layered Cu/Ni nanocomposites.

**5.1.5.2. Electrodeposition for magnetic and electrical applications.** Co base alloys, Ni base alloys developed using electrodeposition have quite desirable soft magnetic properties such as low coercivity, increased electrical resistivity, and high saturation magnetization [447,461]. Magnetic nanostructures are normally manufactured through techniques like ion implantation [462], sputtering [463], and metal evaporation [464,465]. Electrodeposition can be thought of as an economical alternative to these methods. Moreover, among these techniques, electrodeposition is capable of producing dense nanostructures which makes them impart grain size independent saturation magnetization to the material.

The saturation magnetization values achieved during the magnetization studies of the bulk nanostructure of cobalt have been given in Table 48. As mentioned in Table 43, different material systems are tried with the variants in electrodeposition such as pulse DC, DC, and pulse reverse DC. It has been found that these variants change the coercivity values in accordance with the microstructure. Ni–alumina processed with DC and pulsed DC electrodeposition [466] has shown different coercivity values as compared with that of pure cobalt in Table 48. The explanation for these values can be gathered from the TEM picture shown in Fig. 183 [466]. Fig. 183a and b shows pictures from samples plated under DC conditions with different current densities and alumina powder concentration in the bath. Grain size of 30 and 60 nm, respectively, are achieved for higher and lower current densities. The amount of alumina powder concentration was higher in the former and lower in the latter. Fig. 183c is from the sample developed using PDC technique and it is observed that the average matrix grain size is around 20 nm. Aus et al. [447] produced Co nanostructure with 15 nm grain size (Fig. 184). Hibbard et al. [441] showed cobalt nanostructures with a mean size of 20 nm (Fig. 185).

Table 47

Electrodeposition parameters for layered nanocomposites with the strength data

No.	Power ratings	$T$ (°C)	$\lambda_{\text{Ni}}/\lambda_{\text{Cu}}$	pH	Deposit thickness	Cathode rotation ( $\mu\text{m}$ )	Strength (MPa)	Reference
1	Ni $90 \text{ mA cm}^{-2}$ , Cu $1.5 \text{ mA cm}^{-2}$	–	9	3.8	25–50	Ni: 60, Cu: 600	1900	[457]
2	Ni $105 \text{ mA cm}^{-2}$ , Cu 0.14 V	45	9	3.5	50	Ni: 0, Cu: 750	1100	[458]
3	Not available	RT	1	–	10	–	1700	[459]
4	Cu 0.12 V	40	3	–	10–17	–	1254	[460]

Table 48  
Magnetic properties of nanocrystalline cobalt

Microstructure	$M_s$ ( $A\ m^{-1}$ )	$H_c$ ( $kA\ m^{-1}$ )
Polycrystalline	$1.34 \times 10^6$	6.1
Nanocrystalline	$1.38 \times 10^6$	0.48
Fine powder	$1.12 \times 10^6$	5.8

Reprinted from [461] with permission from Kluwer Academic Publishers.

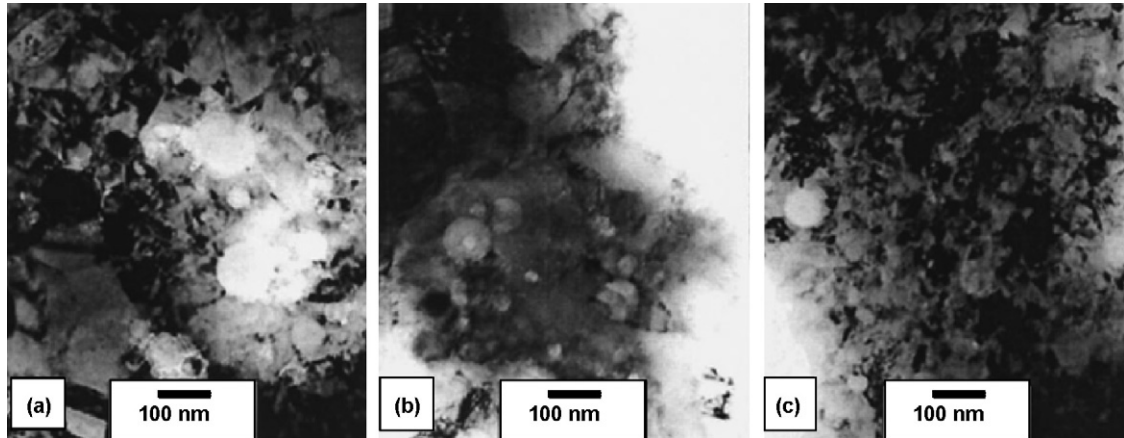


Fig. 183. TEM pictures of Ni–alumina samples processed with different conditions: (a) DC electrodeposition with  $j = 770\ A\ m^{-2}$ , (b) DC electrodeposition with  $j = 150\ A\ m^{-2}$ ,  $C_p = 10\ g\ l^{-1}$ , and (c) pulse DC electrodeposition with  $j_p = 1000\ A\ m^{-2}$  and  $C_p = 10\ g\ l^{-1}$ . (Reproduced with permission from Elsevier from [466].)

The PDC plated Ni/ $Al_2O_3$  [466] shows about half the  $H_c$  value of the Ni/alumina film plated under DC conditions. This can be due to the less pinning of nickel grain boundaries by small dispersoids. High coercivity is desirable for hard magnetic materials while low coercivity is favored for soft magnetic materials.

The latest development in improving the deposition rate during the process has been the evolution of high speed jet electrodeposition. Bulk Co–Ni alloys by high current density jet electrodeposition has been developed by Qiao et al.



Fig. 184. TEM microstructure of nanocrystalline Ni with an average grain size of 11 nm. (Reproduced with permission from Elsevier from [447].)

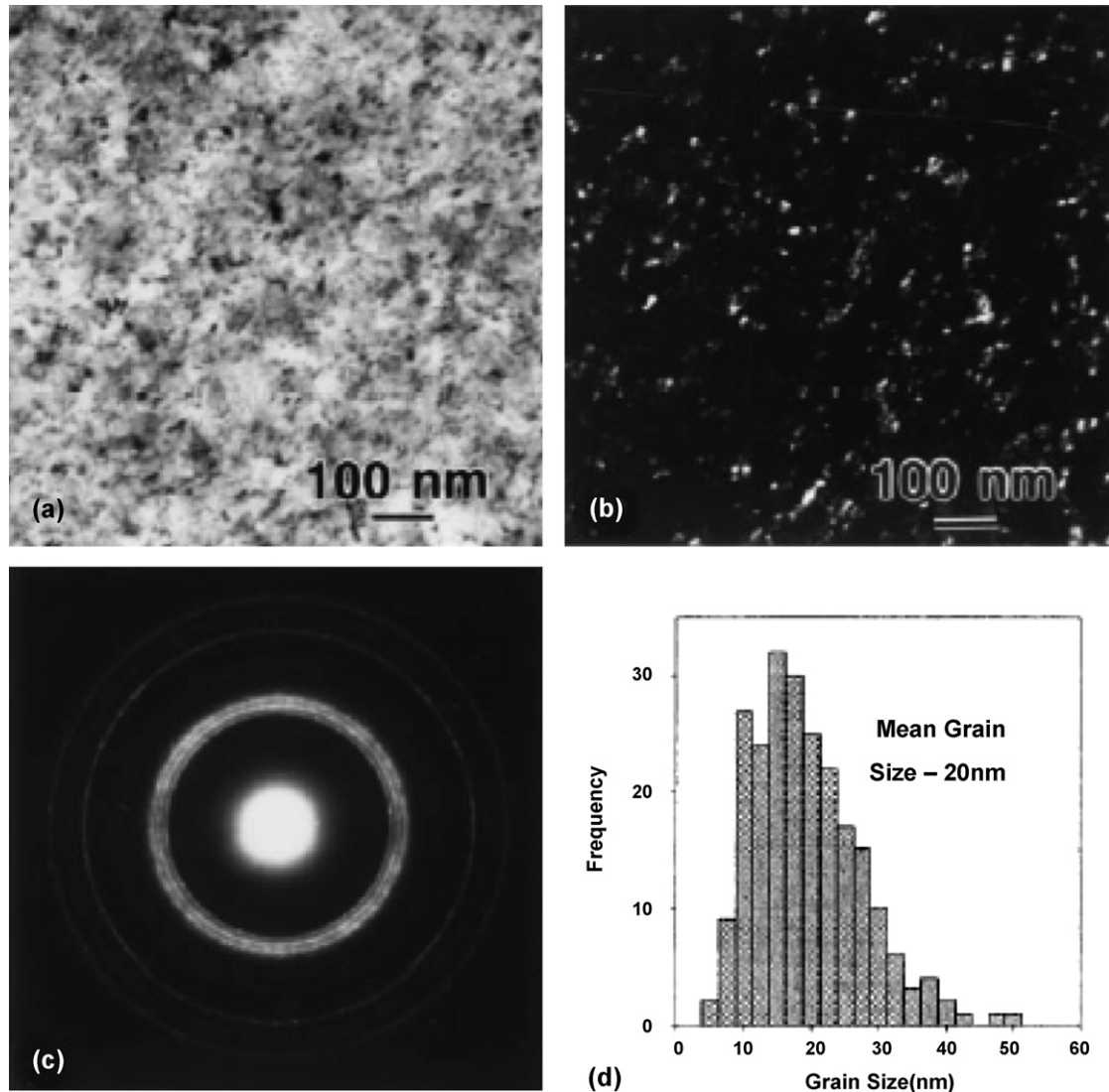


Fig. 185. Bright field (a) and dark field (b) images of nanocrystalline cobalt and (c) corroboration of nanostructures with SAD pattern and (d) the grain size distribution of the as electrodeposited nanostructure. (Reproduced with permission from Elsevier from [441].)

[467]. The jet speed has been found to have a profound influence on the grain size of the alloy and the Co composition. Various factors such as, Co to Ni ionic ratio in electrolyte, the cathodic current density also plays a role in shaping the structural features. The effect of various parameters on Co content and the grain size of the alloy have been revealed in Figs. 186 and 187. There seems to be a phase transformation from fcc structure for low Co content to a mixture of fcc and hcp structures at Co content higher than 60.39%. Fig. 188 depicts the TEM micrograph of Co–Ni alloys deposited at difference current densities and is found that with increasing current densities, the grain size decreased from 100 to 10 nm.

**5.1.5.3. Electrodeposited nanocomposites for wear applications.** Electrodeposition has also been used to make coatings with improved tribological properties. Improvement in the wear resistance has been observed in WC–Co nanocomposites [443], pure nanocrystalline Ni [468], Ni matrix nanocomposites [469–471]. Pulse current or DC electrodeposition has been predominantly used to carry out the coating on substrates. While the electrolytic bath composition seems to be simple for deposition of pure nickel coatings, preparation of electrolytic bath for WC–CoNiP coatings is rather complicated. Surfactants need to be used for uniform dispersion of WC within the bath having known

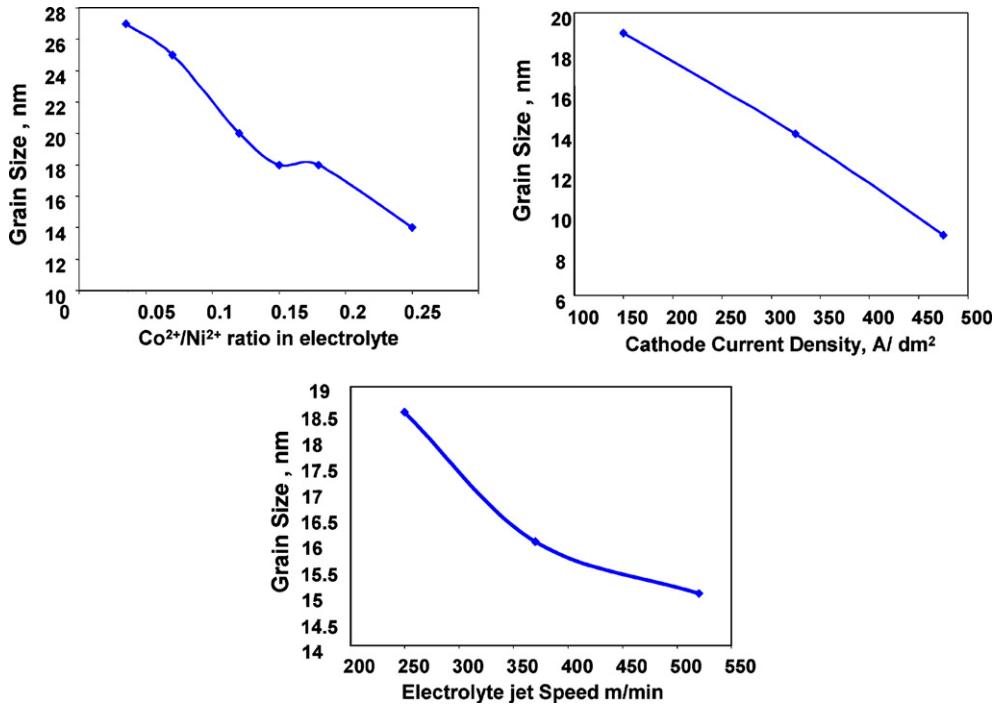


Fig. 186. Electrodeposition parameters affect the grain size of the electrodeposit. (Reproduced with permission from Elsevier from [467].)

the density of WC and its propensity to get settled. pH of the bath can also be varied to optimize the properties such as hardness, wear rate, friction coefficient (is it a function of the grain size). TEM micrographs of pure nanocrystalline Ni with evidence of retained nanostructures using SAD pattern has been shown in Fig. 189. The average grain size is found to be 13 nm. The hardness and wear rate values for a pure nanocrystalline coating is compared to different grain

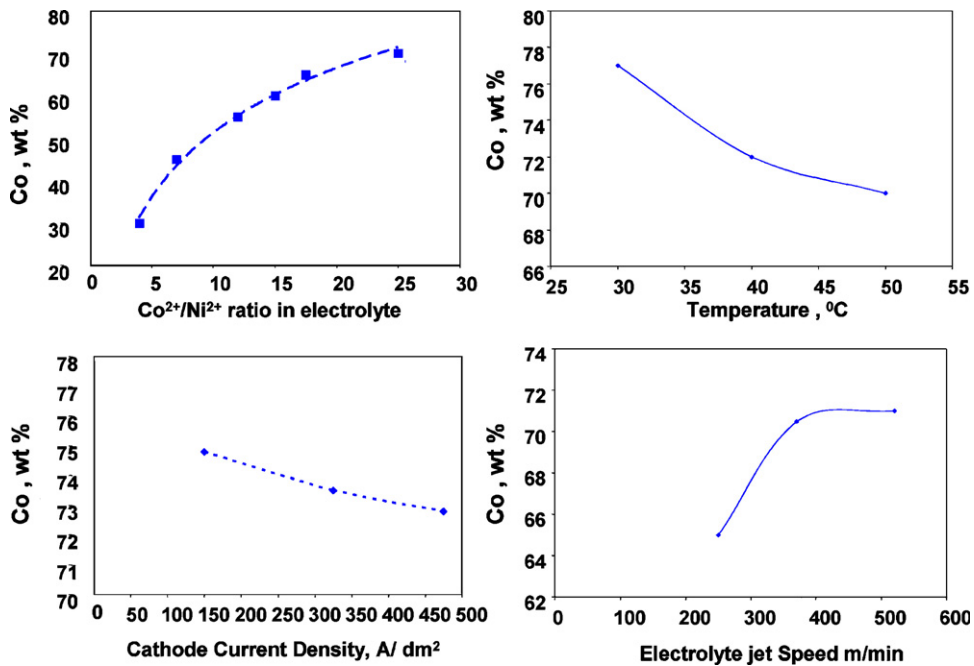


Fig. 187. Data depicting the variation of cobalt content in the alloy with different electrodeposition parameters [467].

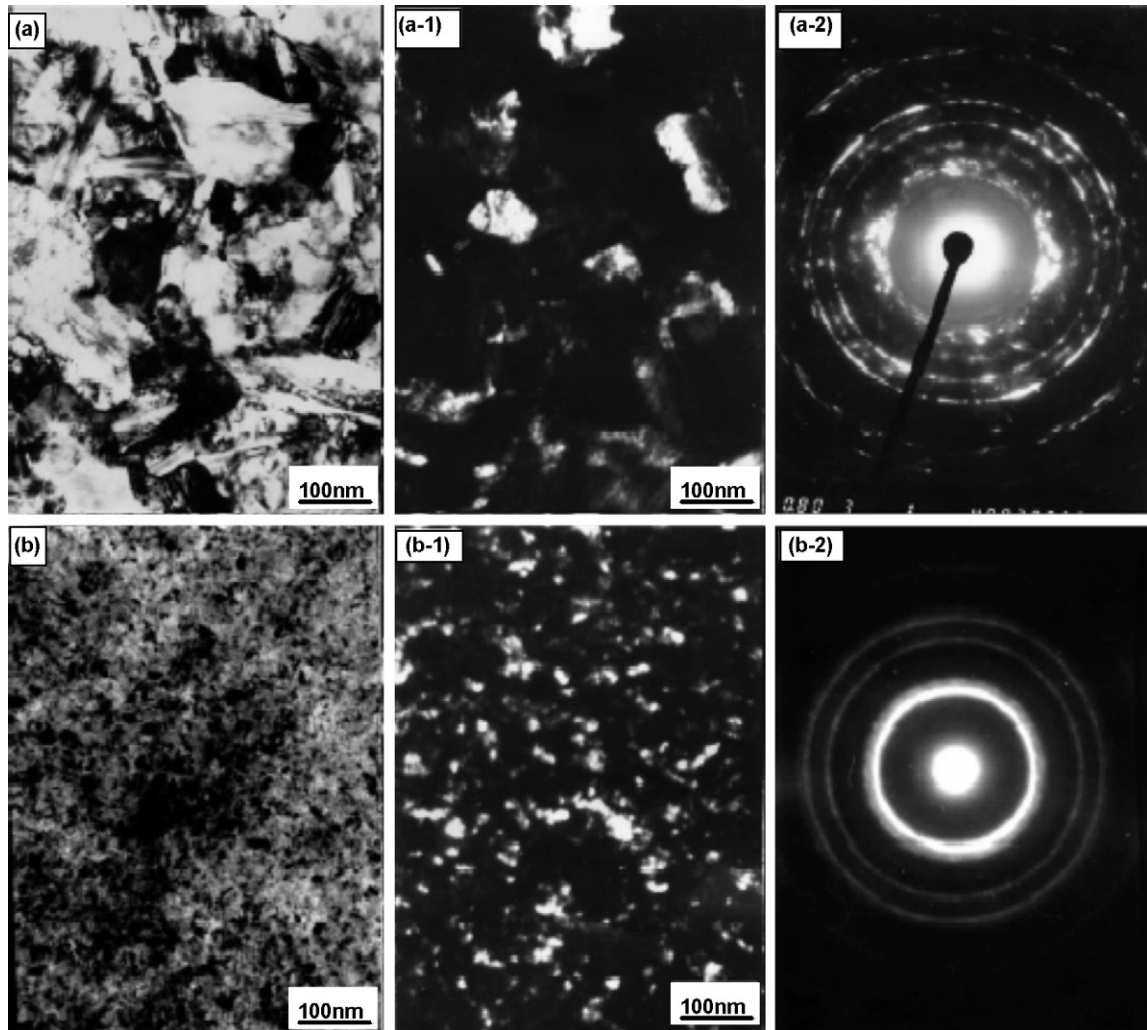


Fig. 188. TEM micrographs and diffraction patterns for Co–Ni alloys deposited at  $0.21 \text{ mol l}^{-1} \text{ CoSO}_4 \cdot 7\text{H}_2\text{O}$ ,  $T = 40^\circ \text{C}$ : (a)  $159 \text{ A dm}^{-2}$  and (b)  $477 \text{ A dm}^{-2}$ . (Reproduced with permission from Elsevier from [467].)

sizes of Ni in Fig. 190. Fig. 191 gives the tribological data for a Ni–CO alloy with  $\text{Si}_3\text{N}_4$  particulates dispersed in various vol.%. Processing cost for making the material varies with the cost for making a composite shoots up to a lot higher value compared to developing a coating for pure nanocrystalline Ni (Fig. 192). The wear rates for nanocrystalline Ni are recorded after 10,000 cycles while the values for the Ni–Co nanocomposite are unknown. The reduction in the wear rates for increasing silicon nitride content has been attributed to the formation of hydroxylated silicon oxide formed by the tribological chemical reaction between nano- $\text{Si}_3\text{N}_4$  and water vapor. It is being mentioned that the hydroxylated silicon oxide layer act as solid lubricant thereby bringing down the wear rate. Experimental evidence for nanostructures has been corroborated using the WC–Co NiP micrographs indicated in Fig. 193.

**5.1.5.4. Nanocrystalline Ni–Fe.** Ni–Fe nanocrystalline alloys with different compositions and grain sizes were fabricated by electrodeposition [472]. Iron composition is varied by changing the ionic ratio of Ni to Fe in the electrolyte. The bath composition for electrodeposition include 1.2 M nickel sulfamate, 0.5 M boric acid,  $2 \text{ g l}^{-1}$  L-ascorbic acid, and  $0.5 \text{ g l}^{-1}$  sulfamate nickel anti-pit (SNAP). Iron chloride or iron sulfate can be added to the bath to get to the specified Ni/Fe ion ratio. The substrate has been rotated at an rpm of 500 and the pH of the electrolyte is maintained at 2 during the process. The alloy has been found to be strengthened due to the decrease in

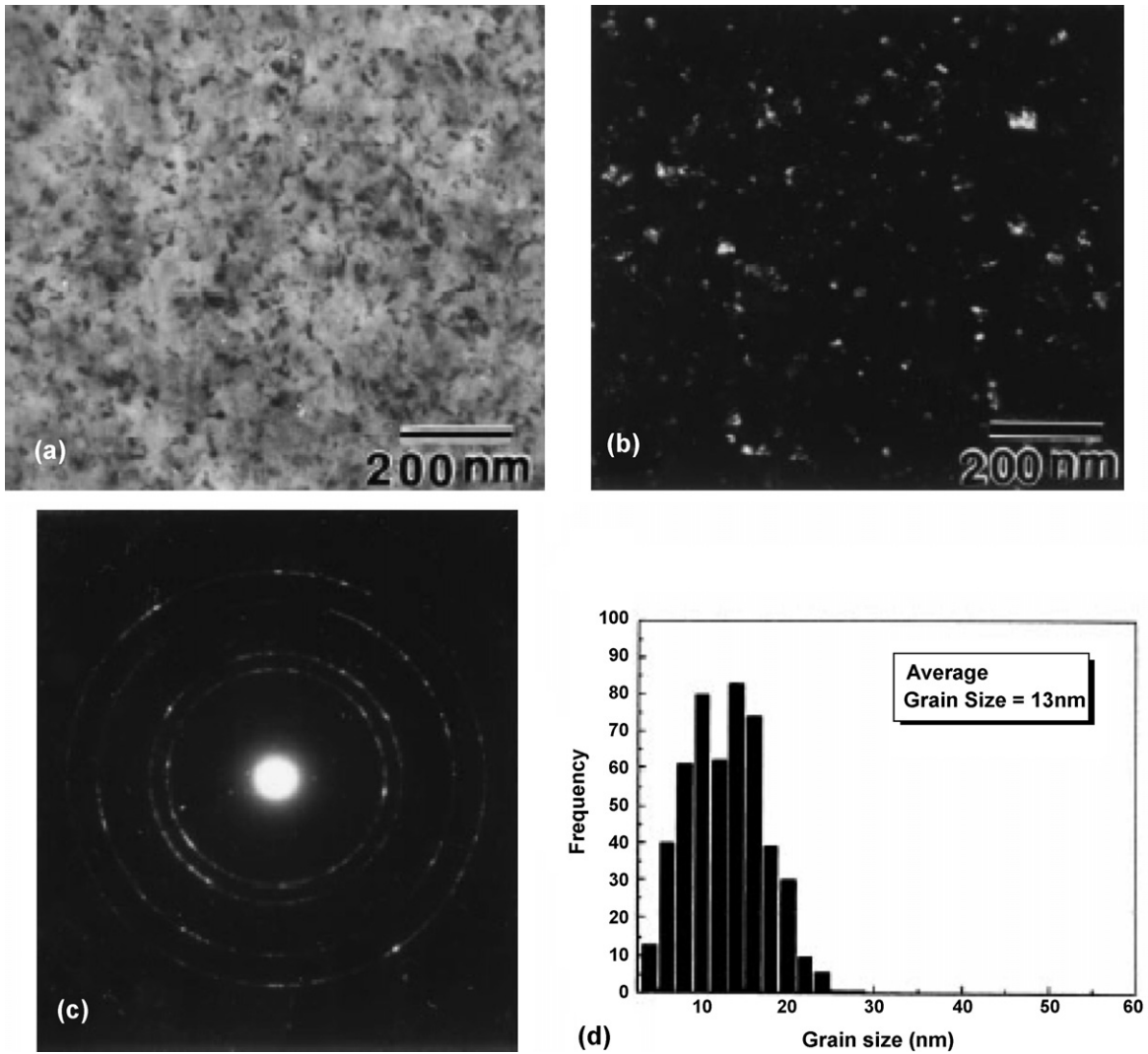


Fig. 189. (a) Bright field and (b) dark field TEM micrographs with (c) electron diffraction pattern and (d) grain size distribution of pure nanocrystalline Ni intended for wear application. (Reproduced with permission from Elsevier from [468].)

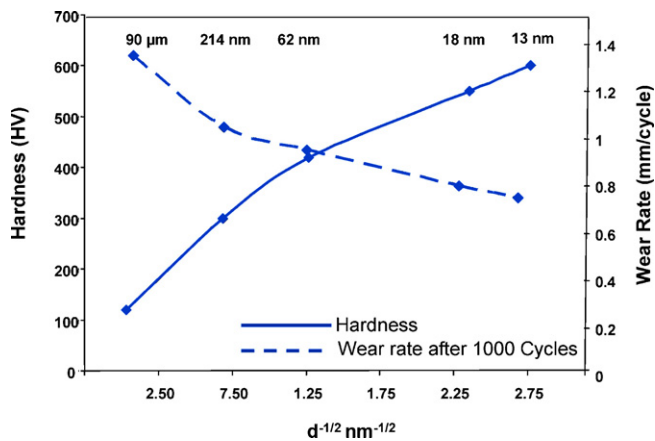


Fig. 190. Hardness and wear rate of pure electrodeposited Ni as a function of grain size [468].

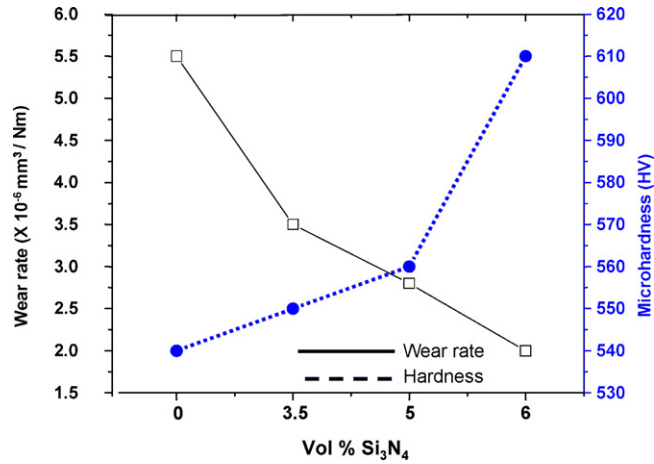


Fig. 191. Hardness and wear rates of Ni–Co/Si<sub>3</sub>N<sub>4</sub> nanocomposite with Si<sub>3</sub>N<sub>4</sub> composition [470].

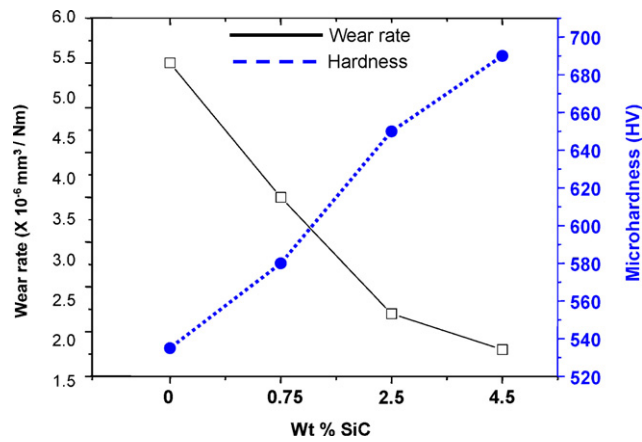


Fig. 192. Hardness and wear rates of Ni–Co/SiC nanocomposite with SiC composition [471].

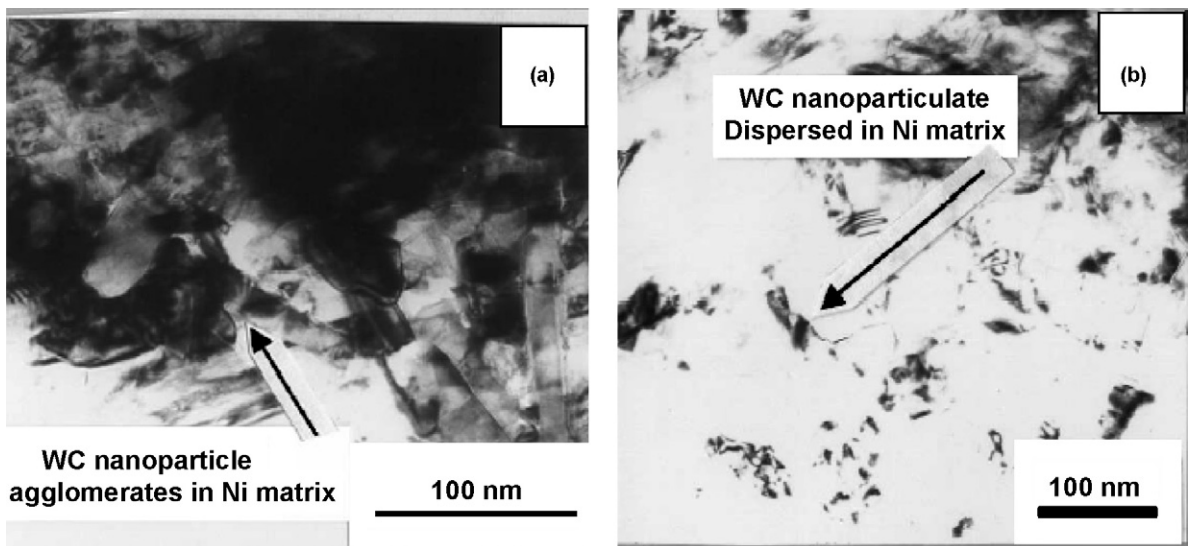


Fig. 193. TEM micrograph of the electroplated coatings showing (a) areas of agglomerated WC nanoparticles in Co–Ni matrix and (b) dispersion of 20 nm WC particulates in Co–Ni matrix. (Reproduced with permission from Elsevier from [443].)

Table 49  
Flow stress values of Ni–Fe compared with Ni at different grain size ranges

	Grain size (nm)				
	60–70	35	25	20	15
$\sigma_{\text{flow}}$ Ni (MPa)	900	900–1000	1200	1200	1400
$\sigma_{\text{flow}}$ Ni–Fe (MPa)	1800	1900	1800	2000	2200

Reproduced from [472] with permission from Elsevier.

the grain size achieved by this process. Flow stress of Ni–4–6% Fe is compared with that of pure Ni at various grain sizes in Table 49.

**5.1.5.5. Nanocrystalline Zn.** Electrodeposited Zn [473] and TiO<sub>2</sub>–Ni nanocomposite coatings [444] has been increasingly being used to provide corrosion resistance to substrates that are prone to corrode otherwise. The electrolytic bath for depositing TiO<sub>2</sub>–Ni nanocomposite coatings has a composition of 250 g l<sup>-1</sup> NiSO<sub>4</sub>·6H<sub>2</sub>O, 25 g l<sup>-1</sup> H<sub>3</sub>BO<sub>3</sub>, 5 g l<sup>-1</sup> saccharin. Twelve-nanometer anatase or 1 μm rutile particles were suspended by mechanical stirring at a pH of 3 and a temperature of 30 °C. DC current is used to carry out electrodeposition. SEM picture as shown in Fig. 194 is from the electrodeposit developed using anatase particles. Corrosion resistance test is performed using immersion test in an acidic corrosive water solution containing 5% NaCl and 1 g l<sup>-1</sup> CuCl<sub>2</sub>·2H<sub>2</sub>O at 50 °C for a week. The corrosion rate as a function of amount of anatase and rutile nanoparticles has been mentioned in Table 50. The grain boundaries and triple junctions of Ni matrix were considered potential sites for the corrosion to occur. The dispersion of fine titania particles along these sites inhibits the preferential corrosion sites and prevents the chemical attack on the coating. As it can be seen, the corrosion rate for nanocomposite with anatase phase has been much lower than the one with coarse rutile phase. By virtue of its smaller size, it is able to fill all the potential corrosion prone sites which the coarse rutile particles are unable to fill.

Zn [473] has been electrodeposited on a cold rolled low carbon steel disk and zinc as a soluble anode. The bath chemistry comprised of 0.4 M zinc chloride, 2.2 M ammonium chloride, 0.35 M boric acid, 0.2–1.5 g l<sup>-1</sup>

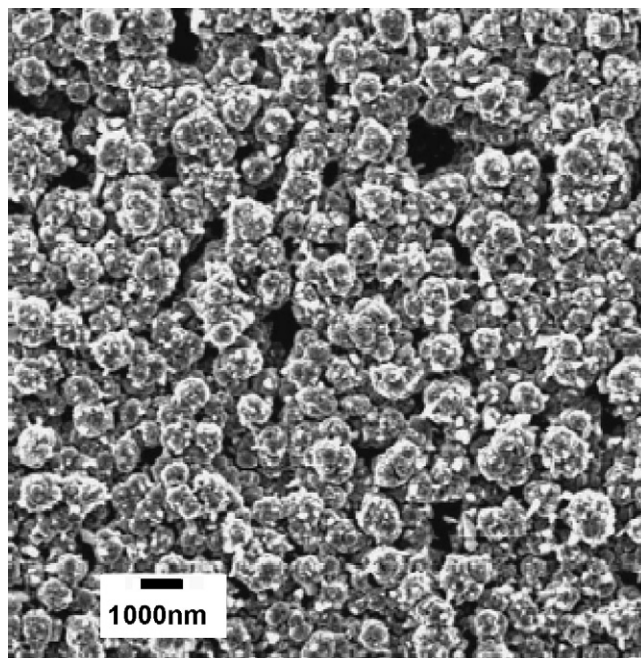


Fig. 194. SEM micrograph of the nanocomposite coating obtained from an electrolyte containing 100 g l<sup>-1</sup> anatase titania nanoparticles (12 nm). (Reproduced with permission from Elsevier from [444].)

Table 50

Variation of corrosion rate ( $\nu$ ) as a function of composition of anatase and rutile in the electrodeposit

Anatase		Rutile	
wt.% TiO <sub>2</sub>	$\nu$ (g m <sup>-2</sup> h <sup>-1</sup> )	wt.% TiO <sub>2</sub>	$\nu$ (g m <sup>-2</sup> h <sup>-1</sup> )
4.0	16.0	5.0	12.0
4.5	15.5	6.0	10.0
4.7	15.0	7.0	8.0
5.0	14.5	8.3	7.0
8.0	10.0	11.0	6.0

Reproduced from [444] with permission from Elsevier.

polyacrylamide, 0.02–0.5 g l<sup>-1</sup> thiourea maintained at a pH of 4.7. Current density has been manipulated to get to nanostructured Zn. It was found that with increase in current density, the microstructure gets refined and form nanostructures at around 2 A cm<sup>-2</sup> as shown in Fig. 195. The average grain size is estimated to be 56 nm.

Electrodeposition is a versatile technique to process metals, ceramics or nanocomposites both as coatings and bulk free form structures. Composition of the electrodeposits can be precisely controlled by controlling the bath composition, current, voltage and hence the resulting physico-chemical properties.

## 5.2. Nanoconsolidation for self-assembling structures

### 5.2.1. Introduction

Molecular self-assembly is ubiquitous in nature and has recently emerged as a new approach in chemical synthesis, nanotechnology, polymer science, materials engineering. Molecular self-assembly systems lie at the interface between molecular biology, chemistry, polymer science, materials science, and engineering. Many self-assembling systems have been developed. Molecular self-assembly systems represent a significant advance in the molecular engineering of simple molecular building blocks useful for a wide range of applications. Self-assembly is an emerging technology for development of nanostructured materials [474–481]. Development of new materials and technologies often broadens the questions we can address therefore deepen our understanding of seemingly intractable phenomena. Molecular self-assembly systems will create a new class of materials at the molecular level. It is believed that application of these simple and versatile molecular self-assembly systems will provide us with new opportunities to study some complex and previously intractable biological phenomena. Molecular engineering through molecular design and self-assembly of biological building blocks is an enabling technology that will likely play an increasingly important role in the future technology and will change our lives in the coming decades.

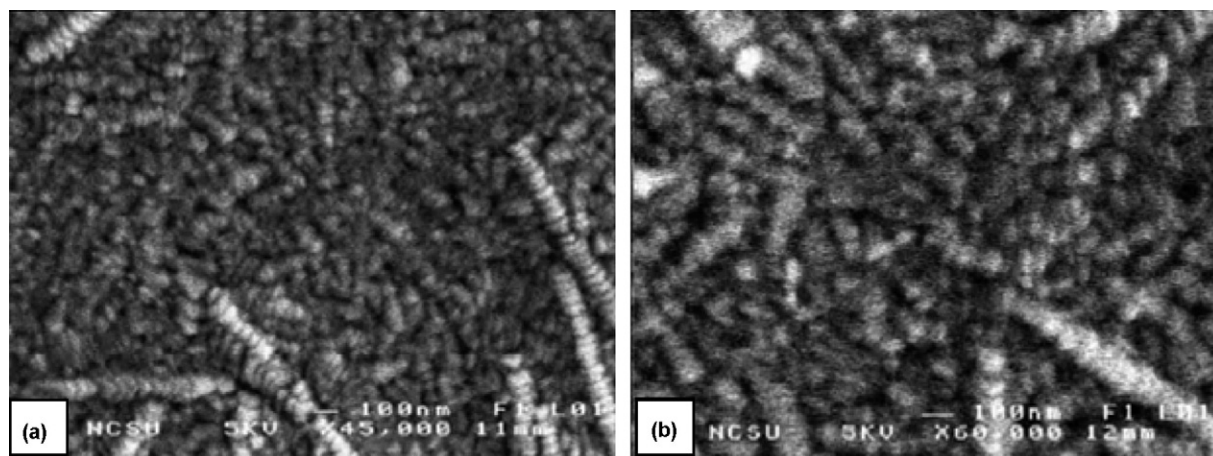


Fig. 195. FESEM images for zinc electrodeposited at  $j_p = 2$  A cm<sup>-2</sup>: (a) surface view and (b) cross-sectional view. (Reproduced with permission from Elsevier from [473].)

Materials that are capable of self-assembly can be categorized in to synthetic and biological variants. Polymers, colloids, liquid crystals, proteins, DNA, biopolymers are some of the examples that fall in to either one of this category. Polymers are repetitive units of monomers which can be also termed as long chain molecules. Various polymeric materials self-assemble in to nanostructures. Crystalline lamellae self-assembling in to crystalline polymers is a classic examples. Lipids, colloids, liquid crystals are some of the synthetic materials that can be self-assembled. Structural proteins present such as keratin, collagen that are normally found in bone, hair also can be self-assembled and categorized as biological self-assembling structures. Although, synthetic and biological could be self-assembled, it should be mentioned that structural proteins present in biological entities such as silk in the silk worm have unmatched strength, stiffness compared to the synthetic ones. Having said that, the self-assembly of these biological types are quite complex.

The building block is a structural protein called ‘fibroin’ present in silk. The structure is an anti-parallel  $\beta$ -sheets of fibroin. It is formed by an intermolecular hydrogen bonding between peptide chains. Polypeptide chains consist of sequence of amino acids abbreviated in the form Gly-Ser-Gly-Ala-Gly-Ala. Gly chains start from the end of the  $\beta$ -sheets opposite to the end from the end from which the Ser and Ala chains start. It is the orientation of these chains that dictates the tensile strength of the silk which is used in fabrics. Likewise, there are many biological proteins like collagen, keratin that assume importance by the way they are structured inside hair, wool, nails, horn, feathers, etc. Deoxyribonucleic acid (DNA) is a nucleic acid, usually in the form of double helix that contains genetic instructions specifying the biological development of all cellular forms of life. DNA is a long polymer of nucleotides and encloses the sequence of the amino acids residues in proteins using the genetic code, a genetic code of nucleotides. DNA has cholesteric phases that are also termed as chiral nematic phases which have a helical orientation. More information on the structure of these proteins can be found in reference [482].

### 5.2.2. Fundamental principles

Self-assembly from the point of view of molecular materials can be described as the reversible and co-operative assembly of predefined components in to an ordered superstructure. Self-assembly can also be categorized in to two different categories namely, static self-assembly and dynamic self-assembly. Static self-assembly occurs with the systems at equilibrium that do not dissipate energy while dynamic self-assembly occurs on systems that dissipate energy. Due to the fluctuations in the molecular position and particle position, self-assembly could occur in soft



Fig. 196. Nanoparticles and nanowire arrays templated by a stripe pattern formed at the surface of a polystyrene–PMMA di-block copolymer by vapor deposition of gold. (Source: <http://magazine.uchicago.edu/0212/features.>)

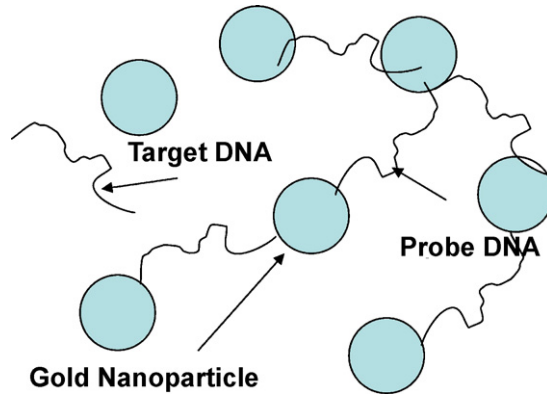


Fig. 197. Schematic of gold nanoparticles in gene sequence detection system.

materials. By virtue of thermal energy, materials with nanodimensions could get their slender non-covalent bonds broken or rejoin again. Even small variations in the pH, a structural transition could be triggered that could lead to a host of applications involving nanomechanical systems. Intermolecular forces such as hydrogen bonding, van der Waals forces, hydrophobic interactions, etc., should be weaker than the covalent bonds that hold molecules together for self-assembly to occur.

DNA plays a crucial role in many of the structures and devices in nanobiotechnology. Instead of using silicon as the platform for tiny circuits, as is done in the current manufacturing technique of photolithography, DNA strands have been used to create grids less than one 10-millionth of a meter square. The smallest features on these square DNA lattices are approximately 5–10 billionths of a meter (nanometers) compared to 65 nm in silicon circuits created using photolithography. This is step towards mass-producing electronic or optical circuits at a scale 10 times smaller than the smallest circuits now being manufactured. DNA is also being exploited to make nanowires that could be used in gene sequence detection. Vesicles (a relatively small and enclosed compartment within a cell) formed by lipids represent model systems for the cell membrane. The incorporation of channel-forming proteins in to lipid bi-layers has been studied exhaustively and synthetic structural and functional mimics have been devised. Block copolymers from vesicles could be polymerized could be used in encapsulation applications. Proteins that could form channels inside cells could be used in delivery and nanoreactor capabilities.

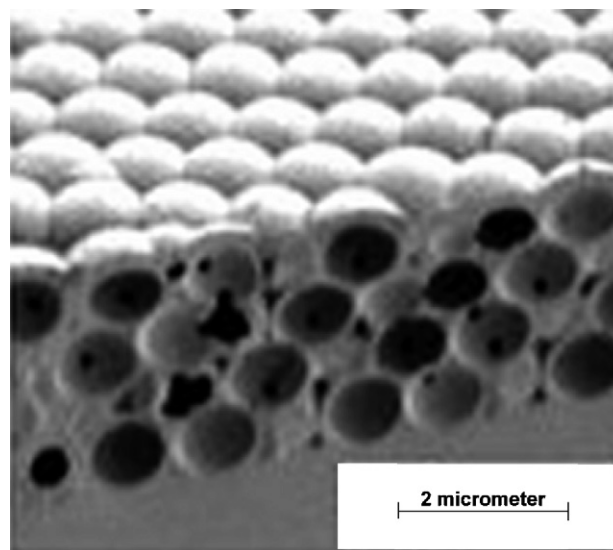


Fig. 198. SEM cross-section image of thin film inverse opal structure of polycrystalline templated by 855 nm silica spheres. (Reproduced from [487] with permission from Macmillan.)

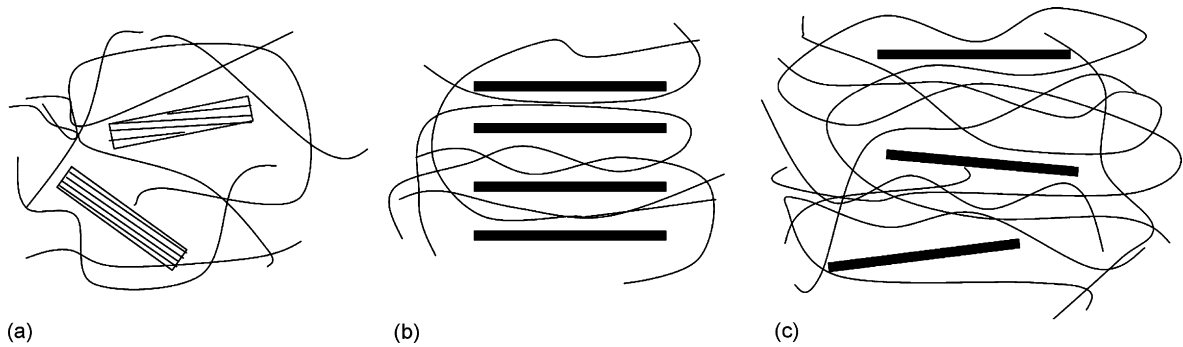


Fig. 199. Polymer clay nanocomposites—hybrid structures. (a) Phase separated nanocomposite, (b) intercalated nanocomposite, and (c) exfoliated nanocomposite.

### 5.2.3. Nanoconsolidation

Nanoparticles with controlled size, shape and functionality is a prerequisite for an effective self-assembly to occur. Metal nanoparticles are used in patterning the surface of the substrate say, a di-block copolymer either by formation of nanoparticles within micelles in solution or direct patterning at the surface using selective wetting. Spherical nanoparticles are preferred for such patterning. Fine spherical particles can be attained using fine milling. This method is more common in making sunscreen lotions. Fig. 196 reveals the arrays of nanoparticle and nanowire templated by a stripe pattern formed at the surface of a polystyrene–poly(methyl methacrylate) di-block copolymer by vapor deposition of gold [483]. The gold exhibits selective wetting behavior on polystyrene domains.

**5.2.3.1. Functionalized nanoparticles.** One classic example of how nanoparticles could be consolidated for using it in gene detection is noteworthy. These are termed as functionalized nanoparticles and could be used in many biotechnological applications. Gold nanoparticles have been functionalized with proteins to detect biological molecules. Nanoparticle arrays could also be used in magnetic storage devices where they can be patterned. For genetic screening purposes, Fig. 197 reveals a schematic by which gold nanoparticles could be able to attach itself to

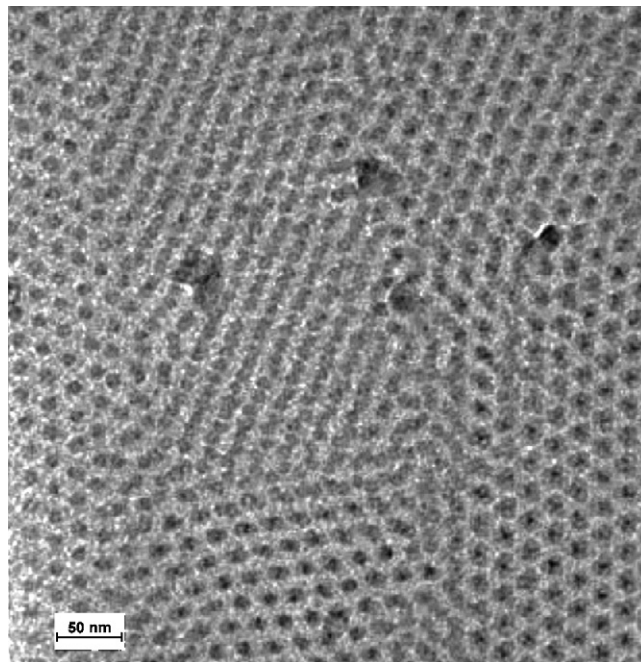


Fig. 200. TEM micrograph of polystyrene oxide and (b) polyethylene oxide block copolymer micelles containing the liquid crystal solubilized in the poly(styrene oxide) core. (Reprinted from [489] with permission from Springer Verlag–GmbH.)

the target DNA. Two sets of gold particles are prepared. The first set of nanoparticles attaches itself to DNA that binds to one end of target DNA and the second set carries DNA that binds to the other end of the target DNA. That way, agglomeration occurs by binding of gold nanoparticles together. Aggregates cause the light scattering spectrum shift that could lead to the detection in the gene sequences. Of late, this method is being further scaled up to enable electrical detection of DNA. Here, one end of the target DNA binds itself to a surface of a microelectrode through an oligonucleotide and the other end binds to an oligonucleotide attached to gold nanoparticles. This binding causes gold nanoparticles to fill the gap between the electrodes which changes the capacitance or conductivity of the system. This could help primarily in gene detection.

**5.2.3.2. Colloidal nanoparticles crystals.** There is an immense interest in photonic band gap crystals because they can be used to confine photons or to modulate or control simulated light emission or to construct lossless wave-guides. 3D crystals have the capability to have a complete bandgap due to which photon propagation is prevented in all spatial directions. For crystals with fcc lattice, there could be a complete band gap due to the fact that the Brillouin zone in these crystals is almost spherical. The inverse structure of an fcc that is spheres of air in continuous solid medium is a promising thought that will lead to a complete band gap. The potential application for this thought is to apply electric field to orient molecules in a particular direction with respect to the pore lattice. This could be used in light wave localization or wave guiding applications. Porous nanoparticles enable this thought to become a reality. Porous gold nanostructures within the interstices of a latex colloidal crystal have been prepared to make inverse opal structures. Similarly, inverse opal structures of titania could also be prepared and nanoporous polycrystalline silica. Fig. 198 reveals a cross-sectional SEM image of thin film inverse opal structure of polycrystalline silicon templated by 855 nm silica spheres [484].

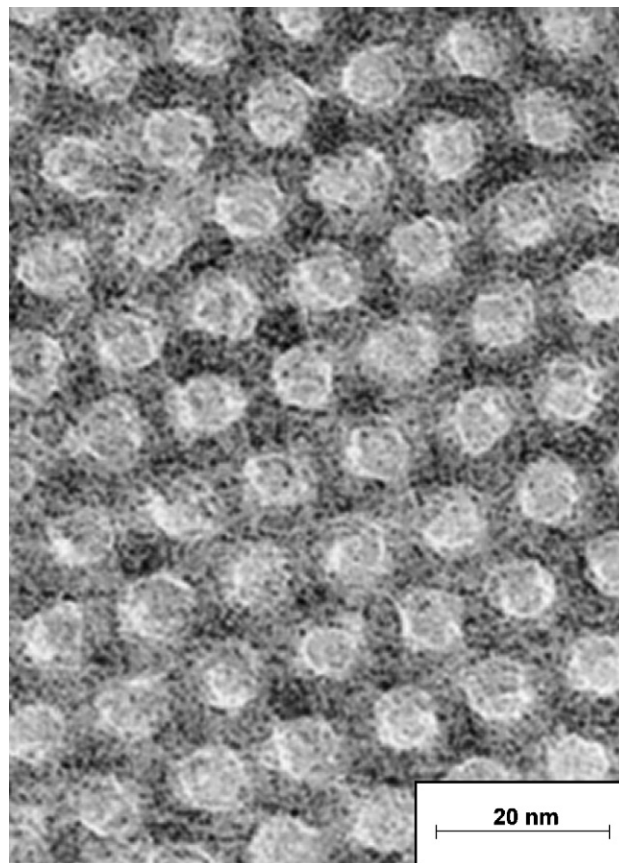


Fig. 201. Hexagonal structure showing calcined mesoporous silica. Templates are done using an amphiphilic tri-block copolymer. (Reprinted from [490] with permission from AAAS.)

**5.2.3.3. Polymer clay nanocomposites.** Polymer nanocomposites could be fabricated by intercalating polymers in layered inorganic hosts [485]. Polymers mixed with clay particles are effective in modifying the properties of polymers, and significant increases in the thermal and mechanical properties have been realized. The possible structures for polymer–clay nanocomposites is shown in Fig. 199 [486]. Clays are colloidal suspension of plate-like mineral particles, with a large aspect ratio. They could form silicate layers when combined with octahedrally coordinated aluminum or magnesium atoms. The layers lead to a lamellar phase for the clay in water. Out of all the possible configurations listed in the figure, intercalated structure leads to enhanced barrier properties, due to the tortuous path for gas diffusion around the clay platelets.

**5.2.3.4. Liquid crystal nanodroplets.** Phased array optics is another application where the ability to pattern liquid crystal nanodroplets at the nanoscale is a requirement for liquid crystal displays. This is a method to reconstruct a three-dimensional image on a two-dimensional surface [487]. Optics allows this to be done if the phase and amplitude of the light waves from the virtual image are controlled. An array of switchable light sources 200 nm apart is sufficient to reconstruct any desired light wave pattern. Fig. 200 reveals a TEM image of an array of block copolymer micelles containing liquid crystal solubilized in the micellar core [488].

**5.2.3.5. Bionanoparticles.** Viruses can be considered as natural nanoparticles with various shapes. From the point of view of nanotech applications, they can be made to play the role of delivery agents. With the acidic nature of the medium in which the virus operates, the virus adopts a compact spherical structure. The moment solution

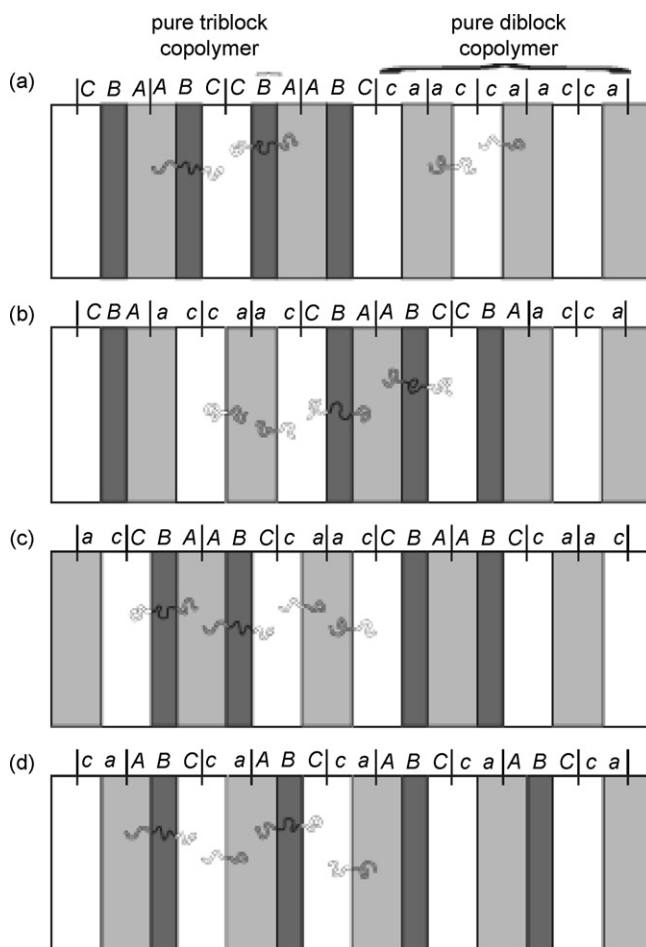


Fig. 202. Schematic of a non-centrosymmetric lamellar structure observed in a blend of ABC tri-block and AC di-block copolymers. (a–d) Different stacking sequences, the most stable of them is the configuration (d). (Reproduced from [491] with permission from Macmillan.)

turns alkaline, the structure becomes porous thereby enabling a controlled release of the drug molecules. However, inflammatory and immunological responses induced by viruses may limit their utility for repeated administration. Synthetic polymers such as polylysine and poly(oxyethylene) are explored to carry out a non-viral gene delivery.

**5.2.3.6. Mesoporous silica as templated nanostructures.** Molecular sieves containing large pore sizes are quite useful for reactions involving large molecules [489]. Inorganic materials such as silica, alumina, and titania can be templated by tapping the potential of surfactants capable of self-assembly. Such templated materials turn out to be mesoporous (relatively large pores size (some tens of nanometers)) compared to zeolites and are potential materials to be used as catalysts and molecular sieves. Fig. 201 shows a hexagonal honeycomb pattern where the silica has been templated from a hexagonal packed cylinder phase using an amphiphilic tri-block copolymer [490].

**5.2.3.7. Lamellar phase in liquid crystal mesophases.** The lamellar phase is a ubiquitous phase present in diverse systems ranging from surfactants in solution to block copolymers. Non-centrosymmetric structures have been found to possess macroscopic electric polarization and hence can be tapped for their piezo and pyro electricity. A schematic of the stacking of these non-centrosymmetric structures observed in a blend of ABC tri-block and AC di-block copolymer has been sketched in Fig. 202 [491]. There are four configurations shown in the figure of which (d) is the minimum energy configuration that could be stable. The structure of Fig. 202d is a macrophase separated, random lamellar, centrosymmetric lamellar stack which is a stable structure that is energetically favored. Such lamellar block copolymer structures could be used to self-assemble all polymer solid-state batteries, by using a tri-block copolymer where the three blocks correspond to the anode, electrolyte, and the cathode. Due to this arrangement, leakage of the toxic liquid electrolyte could be avoided. The processing of such electrolytic setup just needs a spin coating setup. Application of these lamellar block copolymers for making nanocapacitors and nanotransistors are also on the cards.

**5.2.3.8. ABC tri-block structures.** ABC tri-block copolymers when arranged in a lamellar fashion have been found to have a different application as shown in the previous section compared to when it is arranged in an intricate fashion as shown in Fig. 203 [492]. The figures on the top are TEM micrographs of the arranged tri-block copolymers while the bottom ones are the schematic of the two different possible configurations. Another pattern of

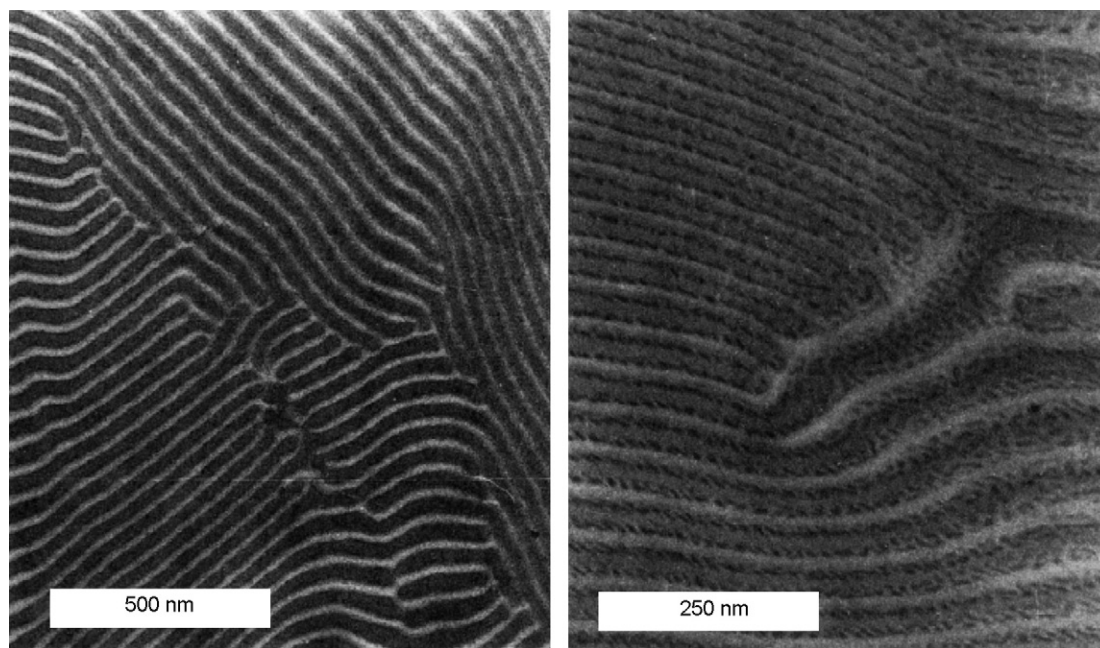


Fig. 203. Sample morphologies observed for polystyrene-*b*-polybutadiene-*b*-polymethyl methacrylate tri-block with a minority midblock component. (Reproduced from [492] with permission from ACS.)

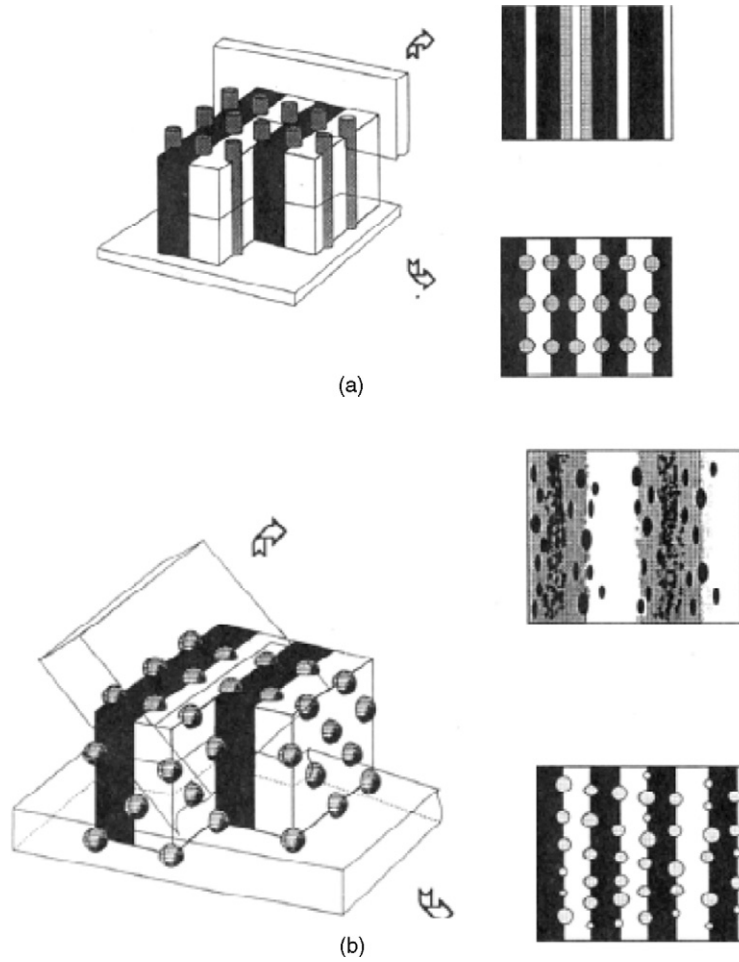


Fig. 204. Schematic diagrams depicting intricate morphologies of lamellar interfaces, (a) with cylinders at lamellar interfaces in (b) and spheres at lamellar interfaces. (Reproduced from [492] with permission from ACS.)

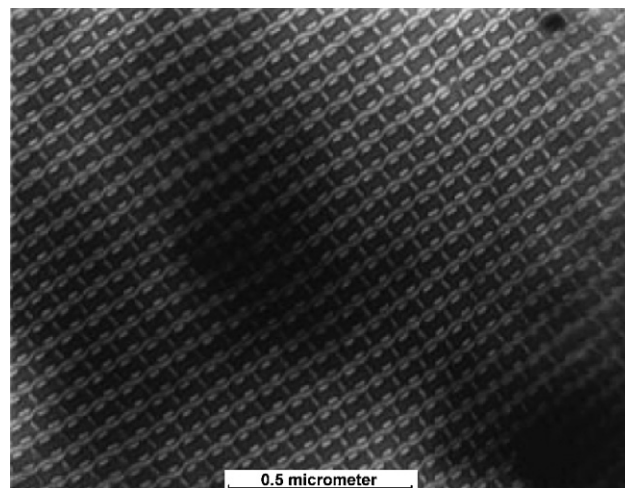


Fig. 205. Knitting pattern morphology observed by TEM on a polystyrene-*b*-poly(ethylene-*co*-butylene)-*b*-poly(methylmethacrylate) tri-block copolymer (stained with RuO<sub>4</sub>). (Reproduced from [493] with permission from ACS.)

organic structures is shown in Fig. 204 [493]. It is basically a knitting pattern morphology observed by TEM on polystyrene-*b*-poly(ethylene-*co*-butylene)-*b*-poly(methylmethacrylate) tri-block copolymer that is stained with RuO<sub>4</sub>. The potential applications include nanoscale electronic devices or three color arrays for high resolution displays (Fig. 205).

Self-assembly in soft materials (polymers, biological proteins, etc.) could be used to template nanostructures in inorganic matter, either in bulk or at the surface. The development of drug delivery systems using functionalized nanoparticles is also a much discussed subject. Use of self-assembly for gene tracking is also a much promising area of nanotechnology. Use of di-block and tri-block copolymers for piezoelectric applications, functionalized nanoparticles for encapsulation (drug delivery) applications, gene detections could be considered as a boon which would further help in utilizing self-assembly in a commercial way. Most likely, the first commercial nanostructures are going to be nanoparticles fabricated in micellar or vesicular nanoreactors and mesoporous templated materials for catalysts and separation media.

## 6. Future challenges

There are several challenges ahead on successful realization of the roadmap on the commercial applications of nanocomposites. Some of the key issues are listed below:

*Nanopowders synthesis:* Most of the nanocomposite fabrication techniques use nanopowders as the feedstock materials. Though synthesis and production of nanopowders have developed by leaps and bounds in the last decade, it is yet to attain the maturity to produce a large amount of nanopowders at an affordable cost for their successful consolidation into nanocomposite. There exists a need to develop techniques which are not only economical but also capable of producing high volume of nanoparticles.

*Handling of nanopowders:* The ultrafine powders have high surface area and hence these are susceptible to contamination due to their high surface activity. The presence of such surface contaminants would definitely compromise the physical, chemical, and mechanical properties of the final products. Therefore, nanopowders should be stored and handled in a novel manner to avoid any contamination so that the benefit of ‘nanosize effect’ can be harnessed to the fullest extent. Developing means of proper handling and storage of nanoparticles prior to their processing to make engineering components is another challenging aspect of nanocomposite manufacturing.

*Fabrication/consolidation techniques:* The promise of the nanotechnology is based upon the ability to create nanostructured materials that will produce novel properties in the ‘macroscale’. The traditional consolidation techniques have a strong limitation to preserve the nanostructure in the end product due to the problem of excessive grain growth. Hence, there is an immediate need not only to investigate the available powder consolidation techniques but also to dig out some new means for densification of nanopowders.

*Interdisciplinary effort:* The widespread application of nanotechnology for societal benefit strongly depends on the active participation all disciplines of science and technology at all levels. To understand this wonderful but poorly explained technology, development of a cross-functional scientific workforce that transcends the conventional limits of various disciplines is required. Academicians and administrators in the universities need to develop and implement new paradigms for training students and researchers of a new breed who do not afraid to cross-domains of various scientific disciplines.

## 7. Concluding remarks

Fabrication technology can strongly affect the morphology and materials properties in the nanometer domain, thus innovations for manufacturing of freestanding parts and composites with retained nanostructure remain a challenge. The nanocomposite materials are expected to have extensive applications in cars, ships, airplanes and even in space vehicles. Although substantial progress has been made in understanding the structure–property relationships in nanomaterials, but further progress is needed in the areas of nanocomposite manufacturing using suitable techniques. A number of techniques are reviewed in this article in order to provide a snapshot on the recent advances in consolidation of nanocomposite. The role that the consolidation technologies might play in the future development of novel and unique three-dimensional multifunctional structures, which cannot be realized using traditional manufacturing techniques, is also emphasized.

## Acknowledgments

Financial supports for Seal from DOD SBIR #DASG60-P-02-41, S. Seal's ONR Young Investigator Award (ONR-YIP), NSF EEC-0139614, 0136710, NSF DMR-9974129, FSGC, DURIP, NASA SBIR Phase II, DOE SBIR Phase I, Plasma Process Inc. are gratefully acknowledged. Authors would also like to thank Dr. A.K. Vasudevan for useful discussion. The authors (A. Agarwal's group) at Florida International University would like to thank financial support from Office of Naval Research (N000140510398), National Science Foundation CAREER award (NSF DMI 0547178), and Florida International University Foundation.

## References

- [1] T. Sekino, T. Nakajima, K. Niihara, *Mater. Lett.* 29 (1996) 165.
- [2] M. Sternitzke, *J. Eur. Ceram. Soc.* 17 (1997) 1061.
- [3] R. Roy, R.A. Roy, D.M. Roy, *Mater. Lett.* 4 (1986) 323.
- [4] H. Riedel, J. Kleebe, H. Schonfelder, F. Aldinger, *Nature* 374 (1995) 526.
- [5] K. Niihara, *J. Ceram. Soc. Jpn.* 99 (1991) 974.
- [6] D.N. Lambeth, E.M.T. Velu, G.H. Bellesis, L.L. Lee, D.E. Laughlin, *J. Appl. Phys.* 79 (1996) 4496.
- [7] S. Ozkar, G.A. Ozin, R.A. Prokopowicz, *Chem. Mater.* 4 (1992) 1380.
- [8] M.J. Mayo, *Int. Mater. Rev.* 41 (1996) 85.
- [9] C.C. Koch, *Nanostruct. Mater.* 2 (1993) 109.
- [10] W.D. Kingery, H.K. Bowen, D.R. Uhlmann, *Introduction to Ceramics*, John Wiley & Sons, New York, 1976.
- [11] R. Birringer, U. Herr, H. Gleiter, *Phys. Lett.* 102A (1984) 365.
- [12] F. Froes, C. Suryanarayana, *J. Min. Met. Mater. Soc.* 41 (1989) 12.
- [13] C. Lieber, *Solid State Commun.* (1998) 607.
- [14] C. Suryanarayana, *J. Min. Met. Mater. Soc.* (2002) 22.
- [15] R. Valiev, *Nature* (2002) 887.
- [16] G. Langford, M. Cohen, *Trans. Am. Soc. Met.* 82 (1969) 623.
- [17] J.G. Sevillano, P.V. Houtte, E. Aernoudt, *Prog. Mater. Sci.* 25 (1980) 69.
- [18] R. Valiev, A. Korznikov, R. Mulyukov, *Mater. Sci. Eng. A* (1993) 141.
- [19] M.D. Baró, Yu.R. Kolobov, I.A. Ovid'ko, H.-E. Schaefer, B.B. Straumal, R.Z. Valiev, I.V. Alexandrov, M. Ivanov, K. Reimann, A.B. Reizis, S. Suriñach, A.P. Zhilyaev, *Rev. Adv. Mater. Sci.* 2 (2001) 1.
- [20] S. Ferrasse, V. Segal, K. Hartwig, R. Goforth, *J. Mater. Res.* 12 (1997) 1253.
- [21] M. Furukawa, Z. Horita, M. Nemoto, T.G. Langdon, *Mater. Sci. Eng. A* 324 (2002) 82.
- [22] R.Z. Valiev, R.K. Islamgaliev, I.V. Alexandrov, *Prog. Mater. Sci.* 45 (2000) 103.
- [23] I. Saunders, J. Nutting, *Met. Sci.* 18 (1984) 571.
- [24] J.A. Wert, L.K. Austin, *Mater. Sci. Technol.* 8 (1992) 1104.
- [25] J.A. Wert, N.E. Patron, C.H. Hamilton, M.W. Mahoney, *Met. Trans.* 32 (1981) 1267.
- [26] H. Gleiter, *Prog. Mater. Sci.* (1989) 223.
- [27] C.C. Koch, Y.S. Cho, *Nanostruct. Mater.* 1 (1992) 207.
- [28] T.C. Lowe, R.Z. Valiev, *J. Min. Met. Mater. Soc.* 52 (2000) 27.
- [29] D.G. Morris, *Mechanical Behavior of Nanostructured Materials*, Uetikon-Zuerich, Enfield, 1998.
- [30] G. Salishchev, R. Zaripova, R. Galeev, O. Valiakhmetov, *Nanostruct. Mater.* 6 (1995) 913.
- [31] V.M. Segal, *Mater. Sci. Eng. A* 197 (1995) 157.
- [32] V.M. Segal, *Mater. Sci. Eng. A* 338 (2002) 331.
- [33] R.Z. Valiev, *Ann. Chim. Fr.* 21 (1996) 369.
- [34] Y.M. Wang, E. Ma, *Acta Mater.* 52 (2004) 1699.
- [35] J.R. Weertman, *Mater. Sci. Eng. A* 166 (1993) 161.
- [36] J. Gubicza, N.Q. Chinh, G. Kralics, I. Schiller, T. Ungar, *Curr. Appl. Phys.* 6 (2006) 194.
- [37] Y. Kolobov, B. Kieback, K.V. Ivanov, T. Weissgaerber, N.V. Girsova, Y. Pochivalov, G.P. Grabovetskaya, M.B. Ivanov, V.U. Kazyhanov, I.V. Alexandrov, *Int. J. Ref. Met. Hard Mater.* 21 (2003) 69.
- [38] N.K. Tsenev, I.R. Kuzeev, B.E. Selsky, *Mater. Sci. Forum* 207–209 (1996) 837.
- [39] C. Xu, M. Furukawa, Z. Horita, T.G. Langdon, *Mater. Sci. Eng. A* 398 (2005) 66.
- [40] R.Z. Valiev, N.A. Krasilnikov, N.K. Tsenev, *Mater. Sci. Eng. A* 137 (1991) 35.
- [41] N.H. Ahmadeev, R.Z. Valiev, V.I. Kopylov, R.R. Mulyukov, *Russ. Metall.* 5 (1992) 96.
- [42] V.M. Segal, V.I. Reznikov, A.E. Drobyshevskij, V.I. Kopylov, *Russ. Metall.* 1 (1981) 115.
- [43] V.M. Segal, V.I. Reznikov, V.I. Kopylov, D.A. Pavlik, V.F. Malyshev, *Processes of Plastic Transformation of Metals*, Naukai Teknika, Minsk, 1984.
- [44] M. Furukawa, Z. Horita, M. Nemoto, T.G. Langdon, *J. Mater. Sci.* 36 (2001) 2835.
- [45] Y. Iwahashi, Z. Horita, M. Nemoto, T.G. Langdon, *Acta Mater.* 46 (1998) 3317.
- [46] V.M. Segal, *Mater. Sci. Eng. A* 271 (1999) 322.

- [47] V.V. Stolyarov, Y.T. Zhu, I.V. Alexandrov, T.C. Lowe, R.Z. Valiev, *Mater. Sci. Eng. A* 199 (2001) 59.
- [48] Y. Iwahashi, M. Furukawa, Z. Horita, M. Nemoto, T.G. Langdon, *Met. Mater. Trans. A* 29 (1998) 2245.
- [49] Y. Iwahashi, J. Wang, Z. Horita, M. Nemoto, T.G. Langdon, *Scripta Mater.* 35 (1996) 143.
- [50] H.S. Kim, Y. Estrin, *Mater. Sci. Eng. A* 410–411 (2005) 285.
- [51] Y. Iwahashi, Z. Horita, M. Nemoto, T.G. Langdon, *Acta Mater.* 45 (1997) 4733.
- [52] K. Oh-ishi, Z. Horita, M. Furukawa, M. Nemoto, T.G. Langdon, *Met. Mater. Trans. A* 29 (1998) 2011.
- [53] G. Purcek, *J. Mater. Process. Technol.* 169 (2005) 242.
- [54] T.V. Clyne, P.J. Withers, *An Introduction to Metal Matrix Composites*, Cambridge University Press, Cambridge, 1995, pp. 176–177.
- [55] M.J. Tan, X. Zhang, *Mater. Sci. Eng. A* 244 (1998) 80.
- [56] M. Kawasaki, Y. Huang, C. Xu, M. Furukawa, Z. Horita, T.G. Langdon, *Mater. Sci. Eng. A* 410–411 (2005) 402.
- [57] I. Sabirov, O. Kolednik, R.Z. Valiev, R. Pippin, *Acta Mater.* 53 (2005) 4919.
- [58] M.A. Muñoz-Morris, I. Gutierrez-Urrutia, D.G. Morris, *Mater. Sci. Eng. A* 396 (2005) 3.
- [59] J. Bridgmen, *Processing of Metals Under High Pressure Conditions*, Techizdat M, Moscow, 1936.
- [60] R.I. Kuznetsov, I.V. Bykov, V.P. Chernyshov, V.P. Pilyugin, N.A. Yefremov, V.V. Posheyev, *Plastic Deformation of Solid Bodies Under Pressure*, IFM UNTS RAN, Sverdlovsk, 1985.
- [61] V.A. Zhorin, D.P. Shashkin, N.S. Enikolopyan, *Dokl. Akad. Nauk SSSR* 298 (1988) 135.
- [62] N.A. Smirnova, V.I. Levit, V.I. Pilyugin, R.I. Kuznetsov, M.V. Degtyarov, *Fiz. Met. Metalloved.* 62 (1989) 566.
- [63] O.V. Mishin, V.Y. Gertsman, R.Z. Valiev, G. Gottstein, *Scripta Mater.* 35 (1996) 873.
- [64] R.K. Islamgaliev, N.F. Yunusova, I.N. Sabirov, A.V. Sergueeva, R.Z. Valiev, *Mater. Sci. Eng. A* 319–321 (2001) 877.
- [65] H. Jiang, Y. Zhu, D.P. Butt, I.V. Alexandrov, T.C. Lowe, *Mater. Sci. Eng. A* 290 (2000) 128.
- [66] A.P. Zhilyaev, S. Lee, G.V. Nurislamova, R.Z. Valiev, T.G. Langdon, *Scripta Mater.* 44 (2001) 2753.
- [67] I. Sabirov, R. Pippin, *Scripta Mater.* 52 (2005) 1293.
- [68] X. Sauvage, F. Wetscher, P. Pareige, *Acta Mater.* 53 (2005) 2127.
- [69] R. Chau, M.B. Maple, W.J. Nellis, *J. Appl. Phys.* 79 (1996) 9236.
- [70] W.H. Gourdin, *J. Appl. Phys.* 55 (1984) 172.
- [71] N.N. Thadhani, R.A. Graham, T. Royal, E. Dunbar, M.U. Anderson, G.T. Holman, *J. Appl. Phys.* 82 (1997) 1113.
- [72] S. Ando, Y. Mine, K. Takashima, S. Itoh, H. Tonda, *J. Mater. Proc. Technol.* 85 (1999) 142.
- [73] J. Bystrzycki, J. Paszula, R.A. Varin, *Mater. Sci. Eng. A* 240 (1997) 546.
- [74] S.I. Shkuratov, E.F. Talantsev, J.C. Dickens, M. Kristiansen, J. Baird, *Appl. Phys. Lett.* 82 (2003) 1248.
- [75] W.H. Gourdin, *Prog. Mater. Sci.* 30 (1986) 39.
- [76] D. Raybould, D.G. Morris, G.A. Cooper, *J. Mater. Sci.* 14 (1979) 2523.
- [77] M. Jain, T. Christman, *Acta Metall. Mater.* 42 (1994) 1901.
- [78] P. Ruuskanen, A. Deribas, A. Shtertser, T. Korkala, *J. Mag. Mag. Mater.* 182 (1998) 185.
- [79] J.C. Rawers, G. Korth, *Nanostruct. Mater.* 7 (1996) 25.
- [80] R.A. Varin, L. Zbronec, T. Czujko, Y.K. Song, *Mater. Sci. Eng. A* 300 (2001) 1.
- [81] M. Ohkoshi, T. Akashi, K. Yamada, A.B. Sawaoka, *J. Mater. Proc. Technol.* 85 (1999) 131.
- [82] T.G. Nieh, P. Luo, W. Nellis, D. Lesuer, D. Benson, *Acta Mater.* 44 (1996) 3781.
- [83] Z.Q. Jin, K.H. Chen, J. Li, H. Zeng, S.F. Cheng, J.P. Liu, Z.L. Wang, N.N. Thadhani, *Acta Mater.* 52 (2004) 2147.
- [84] P.J. Coughlin, A. Crawford, N.N. Thadhani, *Mater. Sci. Eng. A* 267 (1999) 26.
- [85] T. Chen, J.M. Hampikian, N.N. Thadhani, *Acta Mater.* 47 (1999) 2567.
- [86] A. Hoganas, *Technical Report*, 1992.
- [87] R. Mccurrie, *Ferromagnetic Materials: Structure and Properties*, Academic Press, Burlington, 1994.
- [88] R.A. Andrievski, *J. Mater. Sci.* 29 (1994) 614.
- [89] H. Hahn, J. Logas, H.J. Hoffer, T. Bier, R.S. Averback, *Multicomponent Ultrafine Microstructures*, MRS Fall 1988 meeting, Boston, MA, Nov. 30–Dec. 1, 1988.
- [90] H. Hahn, J. Logas, R.S. Averback, *J. Mater. Res.* 15 (1990) 609.
- [91] S.-C. Liao, K.D. Pae, W.E. Mayo, *Nanostruct. Mater.* 8 (1997) 645.
- [92] S.C. Liao, Y.J. Chen, W.E. Mayo, B.H. Kear, *Nanostruct. Mater.* 11 (1999) 553.
- [93] S.C. Liao, K.D. Pae, W.E. Mayo, *Mater. Sci. Eng. A* 204 (1995) 152.
- [94] B.H. Kear, J. Colaizzi, W.E. Mayo, S.C. Liao, *Scripta Mater.* 44 (2001) 2065.
- [95] S.C. Liao, W.E. Mayo, K.D. Pae, *Acta Mater.* 45 (1997) 4027.
- [96] S.C. Liao, Y.J. Chen, B.H. Kear, W.E. Mayo, *Nanostruct. Mater.* 10 (1998) 1063.
- [97] R.A. Lefever, G.L. McVay, R.J. Baughman, *Mater. Res. Bull.* 9 (1974) 863.
- [98] C.J. Shih, J.M. Yang, A. Ezis, *Comp. Sci. Technol.* 43 (1992) 13.
- [99] F. Monteverde, V. Medri, A. Bellosi, *J. Eur. Ceram. Soc.* 22 (2002) 2587.
- [100] C.H. Jung, S.J. Lee, *Intl. J. Ref. Met. Hard Mater.* 23 (2005) 171.
- [101] D. Ehre, E.Y. Gutmanas, R. Chaim, *J. Eur. Ceram. Soc.* 25 (2005) 3579.
- [102] L. Gao, J.G. Li, T. Kusunose, K. Niihara, *J. Eur. Ceram. Soc.* 24 (2004) 381.
- [103] L. Carroll, M. Sternitzke, B. Derby, *Acta Mater.* 44 (1996) 4543.
- [104] C.E. Borsari, N.M.R. Jones, R.J. Brook, R.I. Todd, *J. Eur. Ceram. Soc.* 17 (1997) 865.
- [105] H.Z. Wang, L. Gao, J.K. Guo, *Ceram. Int.* 26 (2000) 391.
- [106] G.J. Li, X.X. Huang, J.K. Guo, *Mater. Sci. Eng. A* 352 (2003) 23.

- [107] N. Bamba, Y.H. Choa, T. Sekino, K. Niihara, J. Eur. Ceram. Soc. 18 (1998) 693.
- [108] S.T. Oh, M. Sando, T. Sekino, K. Niihara, Nanostruct. Mater. 10 (1998) 267.
- [109] D.S. Cheong, K.T. Hwang, C.S. Kim, Composite A 30 (1999) 425.
- [110] R. Zhou, Z. Feng, Y. Liang, F. Zheng, Q. Xian, Ceram. Int. 27 (2001) 571.
- [111] H.Z. Wang, L. Gao, J.K. Guo, J. Eur. Ceram. Soc. 19 (1999) 2125.
- [112] C.J. Lin, C.C. Yang, W.C.J. Wei, Nanostruct. Mater. 11 (1999) 1361.
- [113] J. Hu, T.W. Odom, C.M. Lieber, Acc. Chem. Res. 32 (1999) 435.
- [114] J.M. Wu, Z.Z. Li, J. Alloys Compd. 299 (2000) 9.
- [115] Z.L. Zhao, Y. Zhao, Y. Niu, C.L. Wang, W.T. Wu, J. Alloys Compd. 307 (2000) 254.
- [116] M.S. El-Eskandarany, A.A. Mahday, H.A. Ahmed, A.H. Amer, J. Alloys Compd. 312 (2000) 315.
- [117] J.C. Goldsby, Ceram. Int. 27 (2001) 701.
- [118] K. Il Moon, H. Sub Park, K. Sub Lee, J. Alloys Compd. 325 (2001) 236.
- [119] G.J. Zhang, J.F. Yang, T. Ohji, Mater. Sci. Eng. A 328 (2002) 201.
- [120] K.S. Mazdiyasi, R. Ruh, J. Am. Ceram. Soc. 64 (1981) 415.
- [121] Y.L. Li, G.J. Qiao, Z.H. Jin, Mater. Res. Bull. 37 (2002) 1401.
- [122] Y.L. Li, J.X. Zhang, G.J. Qiao, Z.H. Jin, Mater. Sci. Eng. A 397 (2005) 35.
- [123] H.Y. Jin, W. Wang, J.Q. Gao, G.J. Qiao, Z.H. Jin, Mater. Lett. 60 (2006) 190.
- [124] Y. Ji, J.A. Yeomans, J. Eur. Ceram. Soc. 22 (2002) 1927.
- [125] J.G. Li, L.A. Gao, J.K. Guo, J. Eur. Ceram. Soc. 23 (2003) 69.
- [126] A. Albitzer, M. Salazar, E. Bedolla, R.A.L. Drew, R. Perez, Mater. Sci. Eng. A 347 (2003) 154.
- [127] W.P. Tai, Y.S. Kim, J.G. Kim, Mater. Chem. Phys. 82 (2003) 396.
- [128] K.M. Lee, I.H. Moon, Mater. Sci. Eng. A 185 (1994) 165.
- [129] S.H. Wang, P.W. Kao, Acta Mater. 46 (1998) 2675.
- [130] H.V. Atkinson, S. Davies, Met. Mater. Trans. 31 (2000) 2981.
- [131] S. Billard, G.F. Dirras, J.P. Fondere, B. Bacroix, in: Proceedings of 2nd International Conference on Nanomaterials by Severe Plastic Deformation, Wien, Austria, 2002.
- [132] R. Vassen, D. Stover, Mater. Sci. Eng. A 301 (2001) 59.
- [133] R. Vassen, D. Stover, J. Am. Ceram. Soc. 82 (1999) 2585.
- [134] K. Upadhyay, W.P. Hoffmann, S.L. Rodgers, J. Mater. Syn. Proc. 5 (1997) 141.
- [135] A. Kaiser, R. Vassen, D. Stover, H.P. Buchkremer, Nanostruct. Mater. 8 (1997) 489.
- [136] A. Kaiser, Herstellung und Charakterisierung von Nanoverbundwerkstoffen, Ph.D. Thesis, Rheinisch-Westfälische Technische Hochschule Aachen, 1996.
- [137] R. Bohn, T. Klassen, R. Bormann, Intermetallics 9 (2001) 559.
- [138] R. Bohn, T. Klassen, R. Bormann, Acta Mater. 49 (2001) 299.
- [139] S. Bhaduri, S.B. Bhaduri, Ceram. Int. 28 (2002) 153.
- [140] X.Y. Qin, S.H. Cheong, J.S. Lee, Mater. Sci. Eng. A 363 (2003) 62.
- [141] C. Cayron, E. Rath, I. Chu, S. Launois, J. Nucl. Mater. 335 (2004) 83.
- [142] S. Billard, J.P. Fondere, B. Bacroix, G.F. Dirras, Acta Mater. 54 (2006) 411.
- [143] C. Balazsi, F. Weber, Z. Kover, Z. Shen, Z. Konya, Z. Kasztovszky, Z. Vertesy, L.P. Biro, I. Kiricsi, P. Arato, Curr. Appl. Phys. 6 (2006) 124.
- [144] Z. Livne, A. Munitz, J.C. Rawers, R.J. Fields, Nanostruct. Mater. 10 (1998) 503.
- [145] C.C. Anya, S.G. Roberts, J. Eur. Ceram. Soc. 17 (1997) 565.
- [146] L. Gao, W. Li, H.Z. Wang, J.X. Zhou, Z.J. Chao, Q.Z. Zai, J. Eur. Ceram. Soc. 21 (2001) 135.
- [147] J. Sun, L. Gao, Ceram. Int. 29 (2003) 971.
- [148] J. Markmann, A. Tschope, R. Birringer, Acta Mater. 50 (2002) 1433.
- [149] K.I. Moon, H.S. Hong, K.T. Hong, K.S. Lee, S.J. Kim, Mater. Sci. Eng. A 380 (2004) 46.
- [150] M. Oehring, F. Appel, T. Pfullmann, R. Bormann, Appl. Phys. Lett. 66 (1995) 941.
- [151] F. Appel, U. Lorenz, U. Sparka, R. Wagner, Strength of Materials 10th International Conference ICSMA, Sendai, (1994), p. 341.
- [152] R. Bohn, G. Fanta, T. Klassen, R. Bormann, J. Mater. Res. 16 (2001) 1850.
- [153] S. Revol, S. Launois, R. Baccino, G. Le Marois, R. Rigal, Fusion Eng. Des. 58–59 (2001) 761.
- [154] [www.ceramext.com](http://www.ceramext.com).
- [155] G.E. Dieter, Mechanical Metallurgy, McGraw-Hill, New York, 1996.
- [156] R. Cockcroft, Met. Mater. Trans. A 3 (1969) 351.
- [157] C. Wick, Source Book on Cold Forming, American Society of Metals, Metals Park, OH, 1976, p. 34.
- [158] M. Watkins, Int. Met. Rev. 18 (1973).
- [159] H. Pugh, International Conference on Hydrostatic Extrusion, London, UK, (1974), p. 45.
- [160] B.J. Kellett, C. Carry, A. Mocellin, J. Am. Ceram. Soc. 73 (1990) 1922.
- [161] A. Peigney, E. Flahaut, C. Laurent, F. Chastel, A. Rousset, Chem. Phys. Lett. 352 (2002) 20.
- [162] S.F. Hassan, M. Gupta, Compos. Struct. 72 (2006) 19.
- [163] W.L.E. Wong, S. Karthik, M. Gupta, J. Mater. Sci. 40 (2005) 3395.
- [164] L. Lu, M.O. Lai, C. Yan, L. Ye, Rev. Adv. Mater. Sci. 6 (2004) 28.
- [165] K.I. Moon, K.S. Lee, J. Alloys Compd. 291 (1999) 312.
- [166] G. Liang, Q. Meng, Z. Li, E. Wang, Nanostruct. Mater. 5 (1995) 673.

- [167] H. Ferkel, *Adv. Eng. Mater.* 5 (2003) 886.
- [168] B.C. Ko, Y.C. Yoo, *J. Mater. Sci. Lett.* 18 (1999) 1765.
- [169] L. Geng, T. Imai, J.F. Mao, M. Takagi, C.K. Yao, *Mater. Sci. Technol.* 17 (2001) 187.
- [170] A. Singh, M. Nakamura, M. Wantanabe, A. Kato, A.P. Tsai, *Scripta Mater.* 49 (2003) 417.
- [171] B.Q. Han, E.J. Lavernia, F.A. Mohamed, *Philos. Mag. Lett.* 83 (2003) 89.
- [172] B.Q. Han, E.J. Lavernia, *Adv. Eng. Mater.* 7 (2005) 247.
- [173] P.S. Prevey, K. Mills, *Metals Handbook*, vol. 2, American Society for Metals, Cleveland, OH, 1990, pp. 380–392.
- [174] D.J. Lloyd, *Int. Mater. Rev.* 39 (1994) 1.
- [175] M.R. Krishnadev, R. Angers, C.G.K. Nair, G. Huard, *J. Min. Met. Mater. Soc.* 45 (1993) 52.
- [176] A. Luo, *Met. Mater. Trans. A* 26 (1995) 2445.
- [177] M. Gupta, M.O. Lai, D. Saravanaranganathan, *J. Mater. Sci.* 35 (2000) 2155.
- [178] X.N. Zhang, R.J. Wu, *Damping Capacity of Pure Mg Metal Matrix Composites*, *Composite Materials III* 249 (2003) 217.
- [179] [www.ceramics.nist.gov/srd/summary/scdaos.htm](http://www.ceramics.nist.gov/srd/summary/scdaos.htm).
- [180] T. Imai, M. Mabuchi, Y. Tozawa, M. Yamada, *J. Mater. Sci. Lett.* 9 (1990) 255.
- [181] R.S. Mishra, R.Z. Valiev, S.X. McFadden, R.K. Islamgaliev, A.K. Mukherjee, *Scripta Mater.* 40 (1999) 1151.
- [182] T.G. Nieh, C.A. Henshall, J. Wadsworth, *Scripta Met.* 18 (1984) 1405.
- [183] T.G. Nieh, J. Wadsworth, *Mater. Sci. Eng. A* 147 (1991) 129.
- [184] T. Imai, M. Mabuchi, Y. Tozawa, Y. Nurase, J. Kusui, *Metal and Ceramic Matrix Composites: Process, Modelling and Mechanical Behavior*, ASME TSM, Warrendale, PA, 1990, p. 235.
- [185] R.S. Mishra, T.R. Bieler, A.K. Mukherjee, *Acta Met. Mater.* 43 (1995) 877.
- [186] Z. Shen, H. Peng, J. Liu, M. Nygren, *J. Eur. Ceram. Soc.* 24 (2004) 3447.
- [187] I.W. Chen, X.H. Wang, *Nature* 404 (2000) 168.
- [188] H.-D. Kim, Y.-J. Park, B.-D. Han, M.-W. Park, W.-T. Bae, Y.-W. Kim, H.-T. Lin, P.F. Becher, *Scripta Mater.* 54 (2006) 615.
- [189] N.G. Ma, G.Z. Wang, D.H.L. Ng, *Composite A* 36 (2005) 1222.
- [190] T. Iizuka, H. Kita, T. Hirai, K. Osumi, *Wear* 257 (2004) 953.
- [191] H.T. Kim, Y.H. Han, *Ceram. Int.* 30 (2004) 1719.
- [192] Y.-M. Miao, Q.-L. Zhang, H. Yang, H.-P. Wang, *Mater. Sci. Eng. B* 128 (2006) 103.
- [193] W. Li, L. Gao, *Scripta Mater.* 44 (2001) 2269.
- [194] R.K. Sadangi, O.A. Voronov, B.H. Kear, *Nanostruct. Mater.* 12 (1999) 1031.
- [195] H.Z. Wang, L. Gao, L.H. Gui, J.K. Guo, *Nanostruct. Mater.* 10 (1998) 947.
- [196] S.-T. Oh, T. Sekino, K. Niihara, *J. Eur. Ceram. Soc.* 18 (1998) 31.
- [197] R. Richards, W. Li, S. Decker, C. Davidson, O. Koper, V. Zaikovski, *J. Am. Chem. Soc.* 122 (2000) 4921.
- [198] A.J.A. Winnubst, M.M.R. Boutz, Y.J. He, A.J. Burggraaf, H. Verweij, *Ceram. Int.* 23 (1997) 215.
- [199] D.C. Hague, M.J. Mayo, *Mater. Sci. Eng. A* 204 (1995) 83.
- [200] A.J. Allena, S. Krueger, G.G. Long, H.M. Kerch, H. Hahn, G. Skandan, *Nanostruct. Mater.* 7 (1996) 113.
- [201] S. Kumar, A.K. Jha, in: F.D.S. Marquis (Ed.), *Powder Materials: Current Research and Industry Practices III*, The Mineral, Metals & Material Society (TMS), (2003), p. 93.
- [202] J.R. Vassen, *DKG* 76 (1999) 19.
- [203] N. Kondo, Y. Inagaki, Y. Suzuki, T. Ohji, *Mater. Sci. Eng. A* 335 (2002) 26.
- [204] N. Kondo, Y. Suzuki, T. Ohji, *Key Eng. Mater.* 247 (2003) 219.
- [205] E. Ma, D. Jia, K.T. Ramesh, *Powder Materials: Current Research and Industry Practices*, TMS Fall Meeting, Indianapolis, IN, November 4–8, 2001.
- [206] N. Kondo, Y. Suzuki, T. Miyajima, T. Ohji, *J. Eur. Ceram. Soc.* 23 (2003) 809.
- [207] A.S. Helle, K.E. Easterling, M.F. Ashby, *Acta Metall.* 33 (1985) 2163.
- [208] R.L. Coble, *J. Appl. Phys.* 41 (1970) 4798.
- [209] H.A. Kuhn, B.L. Ferguson, *Powder Forging*, Metal Powder Industries Federation, Princeton, 1990, p. 59.
- [210] B. Budiansky, J.W. Hutchinson, S. Slutsky, *Mechanics of Solids—The Rodney Hill 60th Anniversary Volume*, Pergamon, New York, 1982, p. 13.
- [211] G. Skandan, *Nanostruct. Mater.* 5 (1995) 111.
- [212] J.F. Yang, N. Kondo, T. Ohji, *Ceram. Trans.* 142 (2003) 177.
- [213] L. He, L.F. Allard, K. Breder, E. Ma, *J. Mater. Res.* 15 (2000) 904.
- [214] A.J.A. Winnubst, Y.J. He, H. Verweij, A.J. Burggraaf, *J. Mater. Sci.* 29 (1994) 6505.
- [215] Y.J. He, A.J.A. Winnubst, C.D. Sagel-Ransijn, A.J. Burggraaf, H. Verweij, *J. Eur. Ceram. Soc.* 16 (1996) 601.
- [216] H. Gleiter, *Deformation of Polycrystals: Mechanisms and Microstructures*, Riso National Laboratory, Roskilde, 1981, p. 15.
- [217] X. Xhu, R. Birringer, U. Herr, H. Gleiter, *Phys. Rev. B* 35 (1987) 9805.
- [218] H.J. Holler, R.S. Averback, H. Hahn, H. Gleiter, *J. Appl. Phys.* 74 (1993) 3832.
- [219] M.M.R. Boutz, C.V. Minden, R. Janssen, N. Claussen, *Mater. Sci. Eng. A* 233 (1997) 155.
- [220] C. Auechalanukul, M.J. Roddy, W.R. Cannon, *Ceram. Trans.* 18–21 (2004) 137.
- [221] T.P. Raming, A.J.A. Winnubst, W.E.V. Zyl, H. Verweij, *J. Eur. Ceram. Soc.* 23 (2003) 1053.
- [222] D.M. Owen, A.H. Chokshi, *Acta. Mater.* 46 (1998) 719.
- [223] S. Balasubramanian, H. Keshavan, W.R. Cannon, *J. Eur. Ceram. Soc.* 23 (2005) 1359.
- [224] N. Chawla, J.J. Williams, R. Saha, *J. Light Met.* 2 (2002) 215.

- [225] Y. Inagaki, N. Kondo, T. Ohji, *J. Eur. Ceram. Soc.* 22 (2002) 2489.
- [226] N. Kondo, M. Asayama, Y. Suzuki, T. Ohji, *J. Am. Ceram. Soc.* 86 (2003) 1430.
- [227] C.M. Wang, M. Mitomo, T. Nishimura, Y. Bando, *J. Am. Ceram. Soc.* 80 (1997) 1213.
- [228] G.D. Zhan, M. Mitomo, Y. Ikuhara, T. Sakuma, *J. Mater. Res.* 15 (2000) 1551.
- [229] N. Kondo, Y. Inagaki, J.F. Yang, T. Ohji, *J. Am. Ceram. Soc. Jpn.* 111 (2003) 285.
- [230] Y. Shigegaki, M.E. Brito, K. Hirao, M. Toriyama, S. Kanzaki, *J. Am. Ceram. Soc.* 80 (1997) 495.
- [231] Y. Inagaki, T. Ohji, S. Kanzaki, Y. Shigegaki, *J. Am. Ceram. Soc.* 83 (2000) 1807.
- [232] J.T. Luo, K.F. Zhang, G.F. Wang, W.B. Han, *Mater. Sci. Forum* 475–479 (2005) 2987.
- [233] K.T. Kim, Y.C. Jeon, *Mater. Sci. Eng. A* 245 (1998) 64.
- [234] K.T. Kim, Y.C. Jeon, *Acta Mater.* 46 (1998) 5745.
- [235] J. Besson, M. Abouaf, *J. Am. Ceram. Soc.* 75 (1992) 2165.
- [236] J.G. Noudem, E. Guilmeau, D. Chateigner, B. Ouladdiaf, D. Bourgault, *Physica C* 408–410 (2004) 862.
- [237] D. Kadau, G. Bartels, L. Brendel, D.E. Wolf, *Comp. Phys. Commun.* 147 (2002) 190.
- [238] D.C. Hague, M.J. Mayo, *J. Am. Ceram. Soc.* 82 (1999) 545.
- [239] Z. He, J. Ma, *J. Phys. D: Appl. Phys.* 35 (2002) 2217.
- [240] S. Singh, A.K. Jha, *J. Mater. Proc. Technol.* 112 (2001) 53.
- [241] [http://www.isc.fraunhofer.de/german/improfil/kompetenzfelder/media/projekt1\\_kf7\\_3\\_gross.jpg](http://www.isc.fraunhofer.de/german/improfil/kompetenzfelder/media/projekt1_kf7_3_gross.jpg).
- [242] M.N. Ritter, *Am. Ceram. Soc. Bull.* 81 (2002).
- [243] J.R. Groza, *Nanostruct. Mater.* 12 (1999) 987.
- [244] D.D. Upadhyaya, A. Ghosh, G.K. Dey, R. Prasad, A.K. Suri, *J. Mater. Sci.* 36 (2001) 4707.
- [245] J. Cheng, D. Agrawal, Y. Zhang, R. Roy, *Mater. Lett.* 56 (2002) 587.
- [246] Y. Bykov, A. Ereemeev, S. Egorov, V. Ivanov, Y. Kotov, V. Khrustov, A. Sorokin, *Nanostruct. Mater.* 12 (1999) 115.
- [247] E. Brevall, J.P. Cheng, D.K. Agrawal, P. Gigl, M. Dennis, R. Roy, A.J. Papworth, *Mater. Sci. Eng. A* 391 (2005) 285.
- [248] A. Goldstein, W.D. Kaplan, A. Singurindi, *J. Eur. Ceram. Soc.* 22 (2002) 1891.
- [249] M. Yoshimura, T. Ohji, M. Sando, Y. Choa, T. Sekino, K. Niihara, *Mater. Lett.* 38 (1999) 18.
- [250] P. Duran, F. Capel, J. Tartaj, C. Moure, *J. Am. Ceram. Soc.* 86 (2001) 1661.
- [251] F.J.T. Lin, L.C.D. Jonghe, M.N. Rahaman, *J. Am. Ceram. Soc.* 80 (1997) 2891.
- [252] B. Vaidyanathan, J.P.G. Binner, *Key Eng. Mater.* 264–268 (2004) 2339.
- [253] R. Wroe, *Met. Powder Rep.* 54 (1999) 24.
- [254] S. Vijayan, H. Varma, *Mater. Lett.* 56 (2002) 827.
- [255] X.L. Wang, Z. Wang, H.S. Fan, Y.M. Xiao, X.D. Zhang, *Key Eng. Mater.* 288–289 (2005) 529.
- [256] D. Menzies, Q. Dai, Y.B. Cheng, G. Simon, L. Spiccia, *J. Mater. Sci.* 39 (2004) 6361.
- [257] J.B. Li, Y. Huang, Z.P. Xie, *Ceram. Trans.* 71 (1996) 259.
- [258] C. Gabriel, S. Gabriel, E.H. Grant, B.S.J. Halstead, D.M.P. Mingos, *Chem. Soc. Rev.* 27 (1998) 213.
- [259] M. Gupta, W.L.E. Wong, *Scripta Mater.* 52 (2005) 479.
- [260] M.I. Jones, M.C. Valecillos, K. Hirao, Y. Yamauchi, *J. Eur. Ceram. Soc.* 22 (2002) 2981.
- [261] V.P. Paranosenkov, I.Y. Kelina, L.A. Plyasunkova, Y.Y. Bykov, *Refract. Ind. Ceram.* 44 (2003) 223.
- [262] M. Panneerselvam, A. Agrawal, K.J. Rao, *Mater. Sci. Eng. A* 356 (2003) 267.
- [263] Z.P. Xie, J.B. Li, Y. Huang, X.Y. Kong, *J. Mater. Sci. Lett.* 15 (1996) 1158.
- [264] T.T. Meek, R.D. Blake, J.J. Petrovic, *Ceram. Eng. Sci. Proc.* 8 (1987) 861.
- [265] A. De, I. Ahmad, E.D. Whitney, D.E. Clark, *Mater. Res. Soc. Symp. Proc.* 189 (1990) 283.
- [266] Z. Xie, C. Wang, X. Fan, Y. Huang, *Mater. Lett.* 38 (1999) 190.
- [267] Z. Xie, J. Yang, Y. Huang, *Mater. Lett.* 37 (1998) 215.
- [268] B.O. Regan, M. Gratzel, *Nature* 353 (1991) 737.
- [269] B.A. Gregg, A. Zaban, S. Ferrere, *Z. J. Phys. Chem.* 212 (1999) 11.
- [270] A. Hagfeldt, M. Gratzel, *Acc. Chem. Res.* 33 (2000) 269.
- [271] R.B. Goldner, R.L. Chapman, G. Foley, E.L. Goldner, T. Haas, P. Norton, G. Seward, K.K. Wong, *Sol. Energy Mater.* 14 (1986) 195.
- [272] K.Y. Lee, E.D. Case, *J. Mater. Sci. Lett.* 18 (1999) 201.
- [273] S.T. Oh, K.I. Tajima, M. Ando, T. Ohji, *Mater. Lett.* 48 (2001) 215.
- [274] V.V. Ivanov, S.N. Ivanov, O.K. Karban, A.V. Taranov, E.N. Khazanov, V.R. Khrustov, *Inorg. Mater.* 40 (2004) 1233.
- [275] S. Singh, O.P. Thakur, D.S. Rawal, C. Prakash, K.K. Raina, *Mater. Lett.* 59 (2005) 768.
- [276] K.S. Kumar, T. Mathews, *J. Alloys Compd.* 391 (2005) 177.
- [277] K.S. Kumar, T. Mathews, N.P. Bhat, *Thermochim. Acta* 427 (2005) 27.
- [278] Y. Yang, J.L. Ong, J. Tian, *J. Mater. Sci. Lett.* 21 (2002) 67.
- [279] D.D. Upadhyaya, A. Ghosh, K.R. Gurumurthy, R. Prasad, *Ceram. Int.* 27 (2001) 415.
- [280] W. Lin, X. Bai, Y. Ling, Z. Jiang, Z. Xie, *Mater. Sci. Forum* 423–425 (2003) 55.
- [281] D.L. Johnson, *Ceram. Int.* 17 (1991) 295.
- [282] P. Fauchais, A. Vardelle, B. Dussoubs, *J. Thermal Spray Technol.* 10 (2001) 44.
- [283] H. Herman, S. Sampath, *Metallurgical and Protective Coatings*, Chapman and Hall, London, 1996.
- [284] M.L. Thorpe, *Adv. Mater. Proc.* 143 (1993) 50.
- [285] M. Vardelle, A. Vardelle, A.C. Leger, P. Fauchais, D. Gobin, *J. Thermal Spray Technol.* 4 (1995) 50.
- [286] H. Herman, *Mater. Res. Soc. Bull.* 13 (1998) 60.

- [287] R.C. Dykhuizen, J. Thermal Spray Technol. 4 (1994) 351.
- [288] A. Geibel, L. Froyen, L. Delaey, J. Thermal Spray Technol. 5 (1996) 419.
- [289] A. Agarwal, T. McKechnie, S. Seal, J. Thermal Spray Technol. 12 (2002) 350.
- [290] A. Devasenapathi, H.W. Ng, S.C.M. Yu, A.B. Indra, Mater. Lett. 57 (2002) 882.
- [291] T. Laha, K. Balani, A. Agarwal, S. Patil, S. Seal, Met. Mater. Trans. A 36A (2005) 301.
- [292] A.V. Zagorski, F. Stadelmaier, Surf. Coat. Technol. 146–147 (2001) 162.
- [293] J. Mostaghimi, S. Chandra, R. Ghafouri-Azar, A. Dolatabadi, Surf. Coat. Technol. 163–164 (2003) 1.
- [294] G. Montavon, C. Coddet, Mater. Charac. 36 (1996) 257.
- [295] B.H. Kear, G. Skandan, Nanostruct. Mater. 8 (1997) 765.
- [296] J. Gang, J. Momioli, T. Grosdidier, Scripta Mater. 48 (2003) 1599.
- [297] T. Laha, A. Agarwal, T. McKechnie, K. Rea, S. Seal, Acta Mater. 53 (2005) 5429.
- [298] J. Kim, H. Yang, K. Baik, B.G. Seong, C. Lee, S.Y. Hwang, Curr. Appl. Phys. 6 (2006) 1002.
- [299] R.C. McCune, A.N. Papyrin, J.N. Hall, W.L. Riggs, P.H. Zajchowski, in: Proceedings of 8th National Thermal Spray Conference, Houston, TX, September 11–15, (1995), p. 1.
- [300] A.N. Papyrin, A.P. Alkimov, V.F. Kosarev, United Thermal Spray Conference, Dusseldorf, Germany, (1999), pp. 288–290.
- [301] M.F. Smith, J.E. Brockmann, R.C. Dykhuizen, D.L. Gilmore, R.A. Neiser, T.J. Roemer, Mater. Res. Soc. Symp. Proc. 542 (1999) 65.
- [302] S.V. Klinkov, V.F. Kosarev, M. Rein, Aerospace Sci. Technol. 9 (2005) 582.
- [303] K. Sakaki, Mater. Sci. Forum 449–452 (2004) 1305.
- [304] P.J. Meyer, D. Hawley, Thermal Spray Coatings: Properties, Processes and Application, ASM International, Materials Park, Ohio, 1995.
- [305] P. Fauchais, M. Vardelle, A. Vardelle, L. Bianchi, Ceram. Int. 22 (1996) 295.
- [306] R. McPherson, Surf. Coat. Technol. 34–40 (1989) 173.
- [307] P. Fauchais, A. Vardelle, Int. J. Thermal Sci. 39 (2000) 852.
- [308] S. Beauvais, V. Guipont, F. Borit, M. Jeandin, M. Español, K.A. Khor, A. Robisson, R. Saenger, Surf. Coat. Technol. 183 (2004) 204.
- [309] S. Sodeoka, M. Suzuki, T. Inoue, Y. Ono, K. Ueno, Thermal Spraying: Current Status and Future Trends, High Temperature Society of Japan, Kobe, Japan, 1995, p. 283.
- [310] E. Lugscheider, C. Barimani, P. Eckert, U. Eritt, Comput. Mater. Sci. 7 (1996) 109.
- [311] G.F. Degtev, B.M. Solov'ev, F.F. Vashkevich, V.I. Zhuravel, High Temperature Protective Coatings, Khar'kov, Moscow, USSR, 1970, p. 394.
- [312] D.M. Karpinos, V.G. Zilberberg, V.K. Kadyrov, V.P. Moroz, V.V. Gorsky, Powder Met. 13 (1974) 636.
- [313] M.E. Smagorinski, P.G. Tsantrizos, S. Grenier, A. Cvasin, T. Brzezinski, G. Kim, Mater. Sci. Eng. A 224 (1998) 86.
- [314] H. Kang, Surf. Coat. Technol. 193 (2005) 448.
- [315] H. Wang, W. Xia, Y. Jin, Wear 195 (1996) 47.
- [316] M.B. Karamış, K. Yıldızlı, H. Çakırer, Wear 258 (2005) 744.
- [317] G. Pintsuk, S.E. Brünings, J.E. Döring, J. Linke, I. Smid, L. Xue, Fusion Eng. Des. 66–68 (2003) 237.
- [318] J.E. Döring, R. Vaßen, G. Pintsuk, D. Stöver, Fusion Eng. Des. 66–68 (2003) 259.
- [319] S.O. Chwa, D. Klein, H. Liao, L. Dembinski, C. Coddet, Surf. Coat. Technol. 200 (2006) 5682.
- [320] J. Lee, S. Kang, T. Sato, H. Tezuka, A. Kamio, Mater. Lett. 57 (2002) 812.
- [321] J. Lee, S. Kang, T. Sato, H. Tezuka, A. Kamio, Mater. Sci. Eng. A 343 (2003) 199.
- [322] Y. Dong, D. Yan, J. He, X. Li, W. Feng, H. Liu, Surf. Coat. Technol. 179 (2004) 223.
- [323] P.V. Ananthapadmanabhan, P.R. Taylor, J. Alloys Compd. 287 (1999) 121.
- [324] R. Licheri, R. Orrù, G. Cao, A. Crippa, R. Scholz, Ceram. Int. 29 (2003) 519.
- [325] T. Valente, F.P. Galliano, Surf. Coat. Technol. 127 (2000) 86.
- [326] A. Edelstein, R. Cammarata, Nanomaterials: Synthesis, Properties and Applications, IOP Publishing Ltd., Bristol, 1996, p. 596.
- [327] A. Sergueeva, N. Mara, A. Mukherjee, Dislocations and Deformation Mechanisms in Thin Films and Small Structures, MRS Spring Meeting, San Francisco, (2001), p. 17.
- [328] W. Hofmeister, M. Wert, J. Smugeresky, J.A. Philliber, M. Griffith, M. Ensz, J. Min. Met. Mater. Soc. 51 (1999) 32.
- [329] C. Dumanidis, IEEE Control Systems 17 (1997) 46.
- [330] W.W. Duley, Laser Processing and Analysis of Materials, Plenum, New York, 1983.
- [331] P.C. Mathur, S. Annavarapu, D. Apelian, A. Lawley, J. Min. Met. Mater. Soc. 41 (1989) 23.
- [332] P.S. Grant, Prog. Mater. Sci. 39 (1995) 497.
- [333] B.J. McDonald, M.S.J. Hashmi, Mater. Proc. Technol. (2002).
- [334] S. Anand, Y. Wu, T. Srivatsan, E. Lavernia, International Symposium on Processing and Fabrication of Advance Materials VI, Singapore, (1997), p. 113.
- [335] T. Laha, A. Agarwal, T. McKechnie, Surface Engineering in Materials Science III, TMS Annual Meeting, 2005, p. 49.
- [336] R.B. Pipes, P. Hubert, Compos. Sci. Technol. 62 (2002) 419.
- [337] J. Salvétat-Delmotte, A. Rubio, Carbon 40 (2002) 1729.
- [338] P.M. Ajayan, L.S. Schadler, C. Giannaris, A. Rubio, Adv. Mater. 12 (2000) 750.
- [339] R. Andrews, M.C. Weisenberger, Curr. Opin. Solid State Mater. Sci. 8 (2004) 31.
- [340] Z. Balázs, F. Kónya, L. Wéber, L. Biró, P. Arató, Mater. Sci. Eng. C 23 (2003) 1133.
- [341] A. Agarwal, K. Rea, S. Wannaparhun, S. Seal, N.B. Dahotre, T. McKechnie, Surface Engineering in Materials Science II, TMS Annual Meeting, San Diego, CA, USA, 2003.
- [342] R. Goswami, H. Herman, S. Sampath, X. Jiang, Y. Tian, G. Halada, Surf. Coat. Technol. 141 (2001) 220.
- [343] B. Liang, H. Liao, C. Ding, C. Coddet, Thin Solid Films 484 (2005) 225.

- [344] S.J. Hong, V. Viswanathan, K. Rea, S. Patil, S. Deshpande, P. Georgieva, T. McKechnie, S. Seal, *Mater. Sci. Eng. A* 404 (2005) 165.
- [345] V. Viswanathan, A. Agarwal, V. Ocelik, J.D. Hosson, N. Sobczak, S. Seal, *J. Nanosci. Nanotechnol.* 6 (2006) 651.
- [346] K. Balani, T. Laha, A. Agarwal, TMS Annual Meeting and Conferences, 2006.
- [347] S.C. Mishra, K.C. Rout, P.V.A. Padmanabhan, B. Mills, *J. Mater. Proc. Technol.* 102 (2000) 9.
- [348] T. Laha, A. Agarwal, T. McKechnie, *J. Min. Met. Mater. Soc.* 1 (2004) 54.
- [349] E. Turunen, T. Varis, T.E. Gustafsson, J. Keskinen, T. Fält, S.-P. Hannula, *Surf. Coat. Technol.* 200 (2006) 4987.
- [350] N. Eigen, F. Gärtner, T. Klassen, E. Aust, R. Bormann, H. Kreye, *Surf. Coat. Technol.* 195 (2005) 344.
- [351] H. Li, K.A. Khor, R. Kumar, P. Cheang, *Surf. Coat. Technol.* 182 (2004) 227.
- [352] P.B. Messersmith, E.P. Giannelis, *Chem. Mater.* 6 (1994) 1719.
- [353] M. Sumita, T. Shizuma, K. Miyasaka, K. Ishikawa, *Macromol. Sci. Phys. B* 22 (1983) 601.
- [354] E. Petrovicova, R. Knight, L.S. Schadler, T.E. Twardowski, *J. Appl. Polym. Sci.* 77 (2000) 1684.
- [355] E. Petrovicova, R. Knight, L.S. Schadler, T.E. Twardowski, *J. Appl. Polym. Sci.* 78 (2000) 2272.
- [356] F. Gartner, C. Borchers, T. Stoltenhoff, H. Kreye, H. Assadi, *Adv. Sci. Appl. Technol.* (2003) 1.
- [357] M. Grujicic, J.R. Saylor, D.E. Beasley, W.S. DeRosset, D. Helfritsch, *Appl. Surf. Sci.* 219 (2003) 211.
- [358] R.S. Lima, J. Karthikeyan, C.M. Kay, J. Lindemann, C.C. Berndt, *Thin Solid Films* 416 (2002) 129.
- [359] T.H.V. Steenkiste, J.R. Smith, R.E. Teets, *Surf. Coat. Technol.* 154 (2002) 237.
- [360] T.H.V. Steenkiste, J.R. Smith, R.E. Teets, J.J. Moleski, D.W. Gorkiewicz, R.P. Tison, D.R. Marantz, K.A. Kowalsky, W.L. Riggs II, P.H. Zajchowski, B. Pilsner, R.C. McCune, K.J. Barnett, *Surf. Coat. Technol.* 111 (1999) 62.
- [361] R.C. Dykhuizen, M.F. Smith, D.L. Gilmore, R.A. Neiser, X. Jiang, S. Sampath, *J. Thermal Spray Technol.* 8 (1999) 559.
- [362] J. Vlcek, L. Gimeno, H. Huber, E. Lugscheider, *J. Thermal Spray Tech.* 14 (2005) 125.
- [363] S. Saji, *Powder Met.* 43 (1996) 1198.
- [364] R. Kumar, P. Cheang, K.A. Khor, *J. Mater. Process. Technol.* 140 (2003) 420.
- [365] C.C. Jia, H. Tang, X.Z. Mei, F.Z. Yin, X.H. Qu, *Mater. Lett.* 59 (2005) 2566.
- [366] Y. Zheng, S. Wang, M. You, H. Tan, W. Xiong, *Mater. Chem. Phys.* 92 (2005) 64.
- [367] L. Gao, H. Wang, H. Kawaoka, T. Sekino, K. Niihara, *J. Eur. Ceram. Soc.* 22 (2002) 785.
- [368] L. Gao, Z.J. Shen, H. Miyamoto, M. Nygren, *J. Am. Ceram. Soc.* 82 (1999) 1061.
- [369] T. Murakami, A. Kitahara, Y. Koga, M. Kawahara, H. Inui, M. Yamaguchi, *Mater. Sci. Eng. A* 239–240 (1997) 672.
- [370] R. Chaim, M. Margulis, *Mater. Sci. Eng. A* 407 (2005) 180.
- [371] G.D. Zhan, J.D. Kuntz, J.E. Garay, A.K. Mukherjee, *Appl. Phys. Lett.* 83 (2003) 1228.
- [372] R.G. Duan, G.D. Zhan, J.D. Kuntz, B.H. Kear, A.K. Mukherjee, *Mater. Sci. Eng. A* 373 (2004) 180.
- [373] M.O.J.W. Lee, Z.A. Munir, *Mater. Sci. Eng.* 325 (2002) 221.
- [374] U.A. Tamburini, J.E. Garay, Z.A. Munir, *Mater. Sci. Eng. A* 407 (2005) 24.
- [375] E.M. Heian, J.C. Gibeling, Z.A. Munir, *Mater. Sci. Eng. A* 368 (2004) 168.
- [376] C. Gras, F. Bernard, F. Charlot, E. Gaffet, Z.A. Munir, *J. Mater. Res.* 17 (2002) 542.
- [377] S. Kawano, J. Takahashi, S. Shimada, *J. Eur. Ceram. Soc.* 24 (2004) 309.
- [378] J. Wan, R.G. Duan, A.K. Mukherjee, *Scripta Mater.* 53 (2005) 663.
- [379] G.D. Zhan, J.D. Kuntz, H. Wang, C.M. Wang, A.K. Mukherjee, *Philos. Mag. Lett.* 84 (2004) 419.
- [380] R.G. Duan, G.D. Zhan, J.D. Kuntz, B.H. Kear, A.K. Mukherjee, *Scripta Mater.* 51 (2004) 11135.
- [381] G.D. Zhan, J.D. Kuntz, J. Wan, A.K. Mukherjee, *Nat. Mater.* 2 (2003) 38.
- [382] G.D. Zhan, A.K. Mukherjee, *Int. J. Appl. Ceram. Technol.* 1 (2004) 161.
- [383] G.D. Zhan, J. Kuntz, J. Wan, J. Garay, A.K. Mukherjee, *J. Am. Ceram. Soc.* 86 (2003) 200.
- [384] G.D. Zhan, J. Kuntz, J. Wan, J. Garay, A.K. Mukherjee, *J. Am. Ceram. Soc.* 86 (2002) 200.
- [385] [www.chemweek.com](http://www.chemweek.com).
- [386] H.C. Kim, I.J. Shon, J.E. Garay, Z.A. Munir, *Int. J. Ref. Met. Hard Mater.* 22 (2004) 257.
- [387] S.H. Lee, K.I. Moon, K.S. Lee, *Intermetallics* 14 (2006) 1.
- [388] J.S. Hong, L. Gao, S.D.D.L. Torre, H. Miyamoto, K. Miyamoto, *Mater. Lett.* 43 (2000) 27.
- [389] H.S. Jang, C.W. Kang, Y. Kim, K.T. Hong, S.J. Kim, *Intermetallics* 12 (2004) 477.
- [390] M. Omori, *Mater. Sci. Eng. A* 287 (2000) 183.
- [391] C. Shearwood, Y.Q. Fu, L. Yu, K.A. Khor, *Scripta Mater.* 52 (2005) 455.
- [392] S. Dong, G. Zou, H. Yang, *Scripta Mater.* 50 (2003) 319.
- [393] U.A. Tamburini, J.E. Garay, Z.A. Munira, A. Tacca, F. Spinolo, A.G. Maglia, *J. Mater. Res.* 19 (2004) 3255.
- [394] U.A. Tamburini, J.E. Garay, Z.A. Munira, A.T.A.F. Maglia, G. Chiodelli, G. Spinolo, *J. Mater. Res.* 19 (2004) 3263.
- [395] R. Kumar, K.H. Prakash, P. Cheang, K.A. Khor, *Acta Mater.* 53 (2005) 2327.
- [396] S. Palmqvist, *Arch. Eisenhüttenwesen* 9 (1962) 1.
- [397] W. Li, L. Gao, *J. Biomater.* 24 (2003) 937.
- [398] J. Kanters, U. Eiselle, J. Rodell, *J. Acta Mater. Sci.* 48 (2000) 1239.
- [399] P.V. Krakhmalev, E. Strom, M. Sundberg, C. Li, *Mater. Lett.* 57 (2003) 3387.
- [400] K.I. Moon, S.C. Kim, K.S. Lee, *Intermetallics* 10 (2002) 185.
- [401] F. Zhang, J. Shen, J. Sun, *J. Alloys Compd.* 385 (2004) 96.
- [402] F. Zhang, J. Shen, J. Sun, *Mater. Sci. Eng. A* 381 (2004) 86.
- [403] L. Gao, H.Z. Wang, J.S. Hong, H. Miyamoto, Y. Nishikawa, S.D.D.L. Torre, *Nanostruct. Mater.* 11 (1999) 43.
- [404] L. Gao, H.Z. Wang, J.S. Hong, H. Miyamoto, K. Miyamoto, Y. Nishikawa, S.D.D.L. Torre, *J. Eur. Ceram. Soc.* 19 (1999) 609.

- [405] F. Zhang, J. Shen, J. Sun, Y.Q. Zhu, G. Wang, G. McCartney, Carbon 43 (2005) 1254.
- [406] X. Wang, N.P. Padture, H. Tanaka, Nat. Mater. 3 (2004) 539.
- [407] [www.ceramicbulletin.org](http://www.ceramicbulletin.org).
- [408] R.S. Dohedoe, G.D. West, M.H. Lewis, Adv. Appl. Ceram. 104 (2005) 110.
- [409] H. Kogelnik, T. Li, J. Appl. Phys. 5 (1966) 1550.
- [410] X.C. Yang, W. Riehemann, Scripta Mater. 45 (2001) 435.
- [411] S. Neralla, D. Kumar, S. Yarmolenko, J. Sankar, Composites, Part B (2004) 157.
- [412] A.M. El-Sherik, U. Erb, G. Palumbo, K.T. Aust, Scripta Met. Mater. 27 (1992) 1185.
- [413] Y. Wang, N. Herron, J. Phys. Chem. 95 (1991) 525.
- [414] S. Zhang, D. Sun, Y. Fu, H. Du, Surf. Coat. Technol. 167 (2003) 113.
- [415] W.M. Steen, Laser Material Processing, Springer Verlag, London, 1991.
- [416] W.W. Duley, Laser Processing and Analysis of Materials, Plenum Press, NY and London, 1983.
- [417] <http://www.lasers.org.uk>.
- [418] V. Abdelsayed, Y. Ibrahim, M.S. El-Shall, S. Deevi, Appl. Surf. Sci. (2005) <http://www.lasers.org.uk/Liv/papers/cleaning3.html>.
- [419] C.N. Afonso, R. Serna, J.M. Ballesteros, A.K. Petford-Long, R.C. Doole, Appl. Surf. Sci. (1998) 339.
- [420] J. Gonzalo, R. Serna, J.M. Requejo, J. Solis, C.N. Afonso, A. Naudon, Appl. Surf. Sci. 154–155 (2000) 449.
- [421] S.C. Kuiry, S. Wannaparhun, N.B. Dahotre, S. Seal, Scripta Mater. 50 (2004) 1237.
- [422] R.J. Narayan, Diamond Relat. Mater. 14 (2005) 1319.
- [423] F.Z. Cui, D.J. Li, Surf. Coat. Technol. 131 (2001) 481.
- [424] T. Sasaki, K.M. Beck, N. Koshizakai, Appl. Surf. Sci. 197–198 (2002) 619.
- [425] T. Sasaki, N. Koshizaki, S. Terauchi, H. Umehara, Y. Matsumoto, M. Koinuma, Nanostruct. Mater. 8 (1997) 1077.
- [426] K.M. Beck, T. Sasaki, N. Koshizaki, Chem. Phys. Lett. 301 (1999) 366.
- [427] J.J. Hu, A.A. Voevodin, J.G. Jones, T.A. Fitz, J.S. Zabinski, Thin Solid Films 401 (2001) 187.
- [428] N. Benchikh, F. Garrelie, K. Wolski, C. Donnet, R.Y. Fillit, F. Rogemond, J.L. Subtil, J.N. Rouzaud, J.Y. Laval, Thin Solid Films 494 (2006) 98.
- [429] R. Dez, F. Tenegal, C. Reynaud, M. Mayne, X. Armand, N. Herlin-Boime, J. Eur. Ceram. Soc. 22 (2002) 2969.
- [430] A.A. Voevodin, J.S. Zabinski, Diamond Relat. Mater. 7 (1998) 463.
- [431] Y. Chen, C. Gan, T. Zhang, G. Yu, P. Bai, A. Kaplan, Appl. Phys. Lett. 86 (2005) 251905.
- [432] Y. Chen, Y.Q. Zhang, T.H. Zhang, C.H. Gan, C.Y. Zheng, G. Yu, Carbon 44 (2006) 37.
- [433] D. Tadic, F. Peters, M. Epple, Biomaterial 23 (2002) 2553.
- [434] F. Antolini, A. Ghezelbash, C. Esposito, E. Trave, L. Tapfer, B.A. Korgel, Mater. Lett. (2005).
- [435] T.D. Luccio, B. Nickel, F. Antolini, M. Pentimalli, L. Tapfer, Mater. Res. Soc. Symp. Proc. 847 (2005) EE13.22.1.
- [436] Y.M. Lin, M.M. Hsich, C.P. Liu, H.T. Chang, Langmuir 21 (2005) 728.
- [437] U. Erb, Nanostruct. Mater. 6 (1995) 533.
- [438] N.S. Qu, K.C. Chan, D. Zhu, Scripta Mater. 50 (2004) 1131.
- [439] B. Cai, Q.P. Kong, L. Lu, K. Lu, Mater. Sci. Eng. A 286 (2000) 188.
- [440] F. Ebrahimi, D. Kong, Scripta Mater. 40 (1999) 609.
- [441] G. Hibbard, K.T. Aust, G. Palumbo, U. Erb, Scripta Mater. 44 (2001) 513.
- [442] C.A. Moyna, M. Vazdar, Electrochem. Commun. 3 (2001) 159.
- [443] C.B. Wang, D.L. Wang, W.X. Chen, Y.Y. Wang, Wear 253 (2002) 563.
- [444] J. Li, Y. Sun, X. Sun, J. Qiao, Surf. Coat. Technol. 192 (2005) 331.
- [445] G. Palumbo, F. Gonzalez, A.M. Brennenstuhl, U. Erb, W. Shmayda, P.C. Lichtenberger, Nanostruct. Mater. 9 (1997) 737.
- [446] G. Palumbo, D.M. Doyle, A.M. Elsherik, U. Erb, K.T. Aust, Scripta Met. Mater. 25 (1991) 679.
- [447] M.J. Aus, B. Szpunar, U. Erb, A.M. Elsherik, G. Palumbo, K.T. Aust, J. Appl. Phys. 75 (1994) 3632.
- [448] <http://www.heilscher.com>.
- [449] [www.dynatronix.com](http://www.dynatronix.com).
- [450] [www.microlink.co.uk](http://www.microlink.co.uk).
- [451] A.M. Elsherik, U. Erb, G. Palumbo, K.T. Aust, Scripta Met. Mater. 27 (1992) 1185.
- [452] T. Yamasaki, P. Schlossmacher, K. Ehrlich, Y. Ogino, Nanostruct. Mater. 10 (1998) 375.
- [453] A. Moller, H. Hahn, Nanostruct. Mater. 12 (1999) 259.
- [454] W. Wang, F.Y. Hou, H. Wang, H.T. Guo, Scripta Mater. 53 (2005) 613.
- [455] J. Davis, ASM Handbook, ASM, Metals Park, 1990, p. 437.
- [456] T. Moffat, Mater. Res. Soc. Symp. Proc. 451 (1997) 413.
- [457] D. Tench, J. White, Met. Trans. A 15 (1984) 2039.
- [458] D.M. Tench, J.T. White, J. Electrochem. Soc. 138 (1991) 3757.
- [459] S. Menezes, D.P. Anderson, J. Electrochem. Soc. 137 (1990) 440.
- [460] R.R. Oberle, R.C. Cammarata, Scripta Met. Mater. 32 (1995) 583.
- [461] M.J. Aus, C. Zheung, B. Szpunar, U. Erb, J. Szpunar, J. Mater. Sci. Lett. 17 (1998) 1949.
- [462] J. Shi, S. Gider, K. Babcock, D.D. Awschalom, Science 271 (1996) 937.
- [463] H.N. Lin, Y.H. Chiou, B.M. Chen, H.P.D. Shieh, C.R. Chang, J. Appl. Phys. 83 (1998) 4997.
- [464] M. Hehn, K. Ounadjela, J.P. Bucher, F. Rousseaux, D. Decanini, B. Bartenlian, C. Chappert, Science 272 (1996) 1782.
- [465] S. Evoy, D.W. Carr, L. Sekaric, Y. Suzuki, J.M. Parpia, H.G. Craighead, J. Appl. Phys. 87 (2000) 404.

- [466] J. Steinbach, H. Ferkel, *Scripta Mater.* 44 (2001) 1813.
- [467] G.Y. Qiao, T.F. Jing, N. Wang, Y.W. Gao, X. Zhao, J.F. Zhou, W. Wang, *Electrochim. Acta* 51 (2005) 85.
- [468] D.H. Jeong, F. Gonzalez, G. Palumbo, K.T. Aust, U. Erb, *Scripta Mater.* 44 (2001) 493.
- [469] Y.Y. Chen, H.J. Tzeng, L.I. Wei, L.H. Wang, J.C. Oung, H.C. Shih, *Corros. Sci.* 47 (2005) 1001.
- [470] L. Shi, C.F. Sun, F. Zhou, W.M. Liu, *Mater. Sci. Eng. A* 397 (2005) 190.
- [471] L. Shi, C. Sun, P. Gao, F. Zhou, W. Liu, *Appl. Surf. Sci.* 252 (2006) 3591.
- [472] H.Q. Li, F. Ebrahimi, *Mater. Sci. Eng. A* 347 (2003) 93.
- [473] K. Saber, C.C. Koch, P.S. Fedkiw, *Mater. Sci. Eng. A* 341 (2003) 174.
- [474] M. Park, C. Harrison, P.M. Chaikin, R.A. Register, D.H. Adamson, *Science* 276 (1997) 1401.
- [475] A.K. Boal, F. Ilhan, J.E. DeRouchey, T. Thurn-Albrecht, T.P. Russell, V.M. Rotello, *Nature* 404 (2000) 746.
- [476] A.M. Higgins, R.A.L. Jones, *Nature* 404 (2000) 476.
- [477] C.T. Black, C.B. Murray, R.L. Sandstrom, S. Sun, *Science* 290 (2000) 1131.
- [478] H. Gau, S. Herminghaus, P. Lenz, R. Lipowsky, *Science* 283 (1999) 46.
- [479] T. Thurn-Albrecht, J. Schotter, G.A. Kastle, N. Emley, T. Shibauchi, L. Krusin-Elbaum, K. Guarini, C.T. Black, M.T. Tuominen, T.P. Russell, *Science* 290 (2000) 2126.
- [480] J.P. Spatz, S. Mossmer, C. Hartmann, M. Moller, T. Herzog, M. Krieger, H.G. Boyen, P. Ziemann, B. Kabius, *Langmuir* 16 (2000) 407.
- [481] G.M. Whitesides, J.P. Mathias, C.T. Seto, *Science* 254 (1991) 1312.
- [482] R. Kelsall, I.W. Hamley, M. Geoghegan, *Nanoscale Science and Technology*, Wiley, 2005, p. 472.
- [483] W.A. Lopes, H.M. Jaeger, *Nature* 414 (2001) 735.
- [484] Y.A. Vlasov, X.Z. Bo, J.C. Sturm, D.J. Norris, *Nature* 414 (2001) 289.
- [485] T. Lan, P.D. Kaviratna, T.J. Pinnavaia, *Chem. Mater.* 7 (1995) 2144.
- [486] E.P. Giannelis, R. Krishnamoorti, E. Manias, *Polymer–Silicate Nanocomposites: Model Systems for Confined Polymers and Polymer Brushes*, *Polymers in Confined Environments* 138 (1999) 107.
- [487] B. Wowk, *Nanotechnology*, MIT Press, Cambridge, 1996.
- [488] I.W. Hamley, V. Castelletto, J. Fundin, Z. Yang, M. Crothers, D. Attwood, Y. Talmon, *Colloid Polym. Sci.* 282 (2004) 514.
- [489] M. Estermann, L.B. McCusker, C. Baerlocher, A. Merrouche, H. Kessler, *Nature* 352 (1991) 320.
- [490] D.Y. Zhao, J.L. Feng, Q.S. Huo, N. Melosh, G.H. Fredrickson, B.F. Chmelka, G.D. Stucky, *Science* 279 (1998) 548.
- [491] T. Goldacker, V. Abetz, R. Stadler, I. Erukhimovich, L. Leibler, *Nature* 398 (1999) 137.
- [492] R. Stadler, C. Auschra, J. Beckmann, U. Krappe, I. Voigtmartin, L. Leibler, *Macromolecules* 28 (1995) 3080.
- [493] U. Breiner, U. Krappe, E.L. Thomas, R. Stadler, *Macromolecules* 31 (1998) 135.